CONTROLLABLE ELECTRORHEOLOGICAL AND MAGNETORHEOLOGICAL MATERIALS

EDITED BY: Seung-Bok Choi, Norman M. Wereley and Weihua Li
PUBLISHED IN: Frontiers in Materials

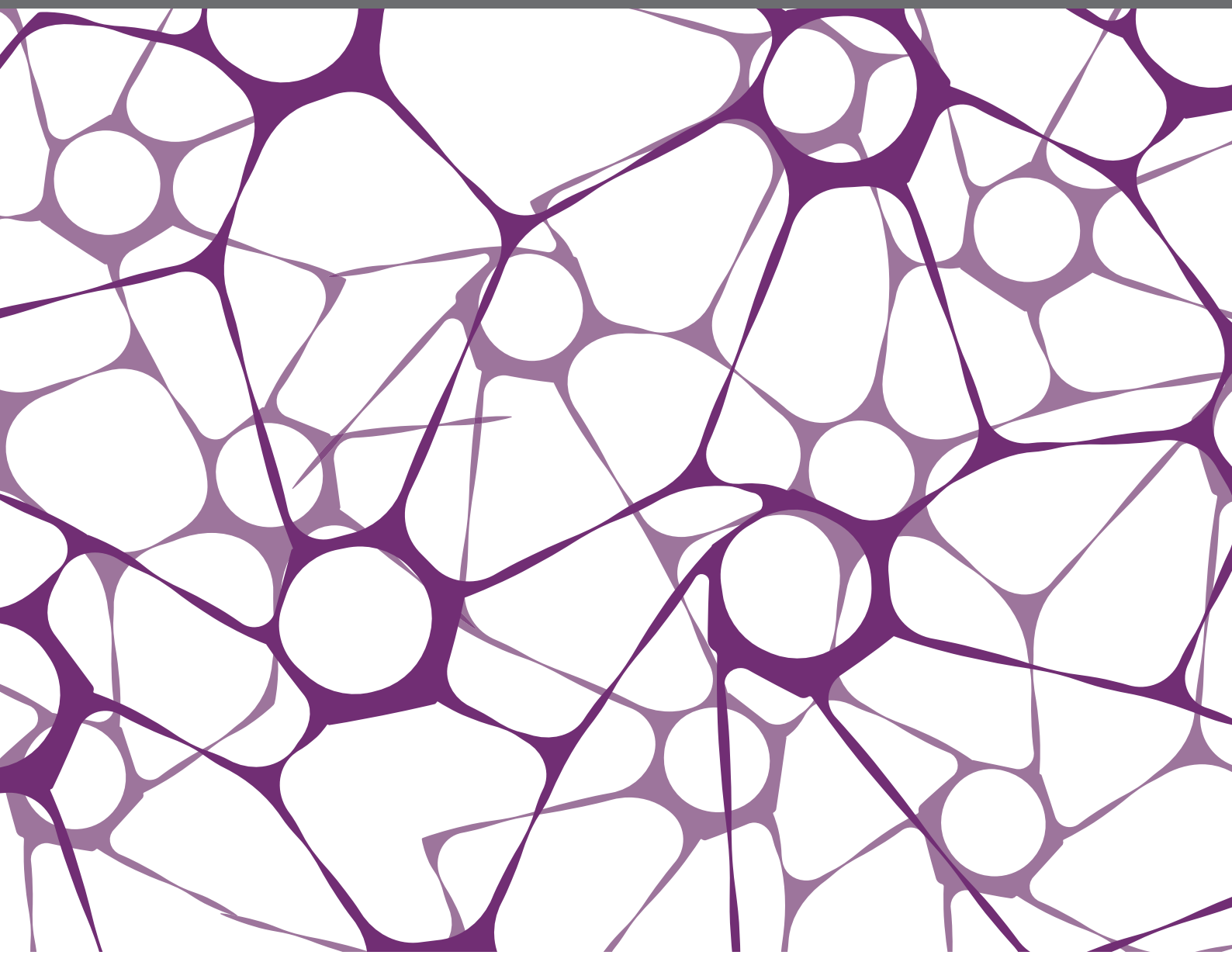

frontiers Research Topics

frontiers

ISSN 1664-8714
ISBN 978-2-88963-070-7
DOI 10.3389/978-2-88963-070-7

About Frontiers

Frontiers is more than just an open-access publisher of scholarly articles: it is a pioneering approach to the world of academia, radically improving the way scholarly research is managed. The grand vision of Frontiers is a world where all people have an equal opportunity to seek, share and generate knowledge. Frontiers provides immediate and permanent online open access to all its publications, but this alone is not enough to realize our grand goals.

Frontiers Journal Series

The Frontiers Journal Series is a multi-tier and interdisciplinary set of open-access, online journals, promising a paradigm shift from the current review, selection and dissemination processes in academic publishing. All Frontiers journals are driven by researchers for researchers; therefore, they constitute a service to the scholarly community. At the same time, the Frontiers Journal Series operates on a revolutionary invention, the tiered publishing system, initially addressing specific communities of scholars, and gradually climbing up to broader public understanding, thus serving the interests of the lay society, too.

Dedication to Quality

Each Frontiers article is a landmark of the highest quality, thanks to genuinely collaborative interactions between authors and review editors, who include some of the world's best academicians. Research must be certified by peers before entering a stream of knowledge that may eventually reach the public - and shape society; therefore, Frontiers only applies the most rigorous and unbiased reviews.
Frontiers revolutionizes research publishing by freely delivering the most outstanding research, evaluated with no bias from both the academic and social point of view. By applying the most advanced information technologies, Frontiers is catapulting scholarly publishing into a new generation.

What are Frontiers Research Topics?

Frontiers Research Topics are very popular trademarks of the Frontiers Journals Series: they are collections of at least ten articles, all centered on a particular subject. With their unique mix of varied contributions from Original Research to Review Articles, Frontiers Research Topics unify the most influential researchers, the latest key findings and historical advances in a hot research area! Find out more on how to host your own Frontiers Research Topic or contribute to one as an author by contacting the Frontiers Editorial Office: researchtopics@frontiersin.org

CONTROLLABLE ELECTRORHEOLOGICAL AND MAGNETORHEOLOGICAL MATERIALS

Topic Editors:
Seung-Bok Choi, Inha University, South Korea
Norman M. Wereley, University of Maryland, College Park, United States
Weihua Li, University of Wollongong, Australia

Citation: Choi, S.-B., Wereley, N. M., Li, W., eds. (2019). Controllable Electrorheological and Magnetorheological Materials. Lausanne: Frontiers Media.
doi: 10.3389/978-2-88963-070-7

Table of Contents

frontiers in Materials

ORIGINAL RESEARCH
published: 25 June 2019
doi: 10.3389/fmats.2019.00142

Influence of the Various Deformation Modes on Rheology of High-Concentrated Magnetorheological Fluids of Complex Composition for Controlled Layered Structures

Evguenia Korobko, Mikalai Zhurauski and Zoya Novikova*

Laboratory of Rheophysics and Macrokinetics, A. V. Luikov Heat and Mass Transfer Institute, National Academy of Sciences of Belarus, Minsk, Belarus

OPEN ACCESS

Edited by:
Weihua Li,
University of Wollongong, Australia

Reviewed by:
Tianhong Yan,
China Jiliang University, China
Xianzhou Zhang,
Independent Researcher, Australia

****Correspondence:***
Evguenia Korobko
evkorobko@gmail.com

Specialty section:
This article was submitted to Smart Materials, a section of the journal Frontiers in Materials

Received: *29 October 2018*
Accepted: *03 June 2019*
Published: *25 June 2019*

Citation:
Korobko E, Zhurauski M and Novikova Z (2019) Influence of the Various Deformation Modes on Rheology of High-Concentrated Magnetorheological Fluids of Complex Composition for Controlled Layered Structures. Front. Mater. 6:142. doi: 10.3389/fmats.2019.00142

The results of an experimental study of the rheological behavior of highly concentrated magnetorheological fluids of complex composition containing the main magnetosensitive filler—carbonyl iron and additives—particles of aerosil, chromium dioxide, and bentonite clay are presented. The modes of continuous shear deformation, linear increase of shear stress, and harmonic shear oscillations are considered. The influence of the additive material on shear stress, yield stress, components of the complex shear modulus of magnetorheological fluids in a magnetic field is determined.

Keywords: magnetorheological fluid, complex composition, deformation mode, viscoelasticity, vibration damping

INTRODUCTION

In various industries (machine building and shipbuilding, aviation, rocket and space technology, etc.), flat thin-walled elements (beams, plates, and shells) of a layered structure are used in order to reduce material consumption while maintaining the required strength and rigidity of products. The most important requirement at the stage of development of such structures, which experience dynamic loads of a wide range of frequencies and strains, is to ensure their vibration protection while maintaining the rigidity of objects (Librescu and Hause, 2000).

Existing vibration protection methods divide into two groups (Chu et al., 2005; Fu et al., 2018). "Passive" methods are based on the use of inertial, elastic, and dissipative elements. They are implemented by introducing damping elements made of elastic or viscoelastic materials placed between the bounding layers into the object structure. Active or semi-active vibration damping systems use an external energy source to automatically adjust the dynamic characteristics of the structure (for example, hydropneumatic systems) (Song, 2009; Akhtar et al., 2015).

To solve the problems of semi-active and active damping of oscillations of flat elements, magnetosensitive materials which, in a controlled manner, change their elastic-viscous-plastic characteristics in external magnetic fields can be used as interlayers. The influence of the field causes a change in the structural state of the material from fluid to quasi-solid. It allows to create the

necessary mode of material resistance to shear effects depending on the mechanical load. Outside the field, materials can be different consistencies and retain different degrees of fluidity, which are mainly determined by the concentration and physico-chemical characteristics of the particles of the dispersed phase. Such magnetosensitive quasi-solid materials as elastomers are known. They are a rubber-like matrix into which magnetic particles, for example iron, are introduced and oriented along the magnetic field strength vector (Zhou, 2003; Nayak et al., 2013; Tian et al., 2013; Li et al., 2014; Megha et al., 2016). It is shown that when exposed to an external magnetic field, the storage modulus G' and the loss modulus G'' of such materials increase, and the resonant frequency of the vibrations of the layered structures changes. It is shown in previous studies (Megha et al., 2016) that due to the increase in the loss modulus, a decrease in the amplitude of forced and free oscillations is achieved both in a uniform and non-uniform magnetic field. However, it is established that the increase in the storage modulus in a magnetic field did not exceed two to three times, and the loss modulus did not exceed one and a half to two times. An increase in the concentration of magnetic filler leads to an increase in the rigidity of the object (storage modulus) and the value of the static yield stress. However, it was noted that this reduces the range of deformations, in which a linear relationship between shear stress and deformation (elastic zone) occurs, which complicates the implementation of controllability of these systems (Tian et al., 2013). A number of constructions of vibroprotective devices using magnetically sensitive elastomers have been developed (Li et al., 2014). A significant problem of their wide use is the poor adhesion of the elastomer to the surfaces of the limiting elements and the small range of regulation of the viscoelastic characteristics due to the initial high rigidity of the rubber-like matrix, as well as a slow structural response to the action of a magnetic field (Ahamed et al., 2018).

The use of magnetorheological fluid materials in flat thin-walled structural elements as controlled layers could solve these problems. Well-known studies (Dong et al., 2018) showed that increasing the concentration of the dispersed phase and using additives of ferrimagnetic particles can reduce unwanted separation and spreading of magnetorheological fluids. For example, the addition of 0.1 wt. % ferrimagnetic $CoFe_2O_4$ nanoparticles (about 100 nm in size) to a fluid with 50 wt. % carbonyl iron allowed to halve the sedimentation and increase the shear stress (up to three times in small fields) compared with the composition without nanoparticles. A significant increase in shear stress was also obtained when adding 1% of γ-Fe_2O_3 (Leong et al., 2016). The magnetorheological effect can be enhanced by several times with the use of magnetite additives (Ashtiani and Hashemabadi, 2015). A multiple increase in the components of the complex shear modulus and shear stress was also noted with the addition of non-magnetic particles of poly(methylmethacrylate) (Iglesias et al., 2015).

Previously, we studied the rheology of high-filled (mass concentration of carbonyl iron was 68.5% and of aerosil was 3%) composite fluid magnetorheological materials. Such materials that do not contain a rubber-like matrix (Korobko et al., 2014), have a significant yield stress in the absence of a magnetic field. An increase of almost two orders of value of the shear resistance of the MRF in a magnetic field was obtained. The optimal range of the magnetic field induction, in which the largest increase in the loss modulus takes place, is determined. The results obtained allowed to suggest that by using a higher concentration of the dispersed phase, as well as by adding both an ferrimagnetic component and non-magnetic additives of oxide particles, it is possible to achieve an increase in the growth of rheological parameters in the field and the necessary damping response in a given strain range.

In connection with the foregoing, the aim of this work is to establish the influence of different deformation modes on the change in the magnetic field of the rheological characteristics of the magnetorheological fluids of a complex composition containing magnetic and non-magnetic components.

TABLE 1 | The content of the components in the MRF samples.

No.	Component (wt. %)	MRF-1	MRF-2	MRF-3	MRF-4	H_r, kA/m
1	Carbonyl iron	77	77	77	77	1730
2	Aerosil	4	2	–	–	–
3	CrO_2	–	2	8	–	440
4	Bentonite clay	–	–	–	10	–
5	Dispersion medium	19	19	15	13	–

MATERIALS AND EQUIPMENT

This paper presents the results of experimental studies of the developed compositions of highly concentrated magnetorheological composite fluids (MRF), which are high-filled pastes containing two types of particles as the dispersed phase.

The component of the composite dispersed phase of MRF, which has a high magnetorheological sensitivity, was particles of magnetically soft carbonyl iron (main diameter is about 3 μm). Samples containing 77 wt.% carbonyl iron and finely dispersed materials of a different nature to create a thixotropic matrix were investigated. Mobil synthetic oil was used as a dispersion medium. The compositions of the MRF samples and the values of the saturation magnetization of the magnetic components H_r are given in **Table 1**.

Aerosil particles (brand A-380) have a spherical shape and size of 5–15 nm, CrO_2 particles differ in a needle shape with a ratio of sizes of 15:1 and a length of 500 nm, and particles of bentonite clay have a plate shape and a size of 1–10 μm.

The rheological characteristics of the prepared MRF samples both without the influence of a magnetic field and under its influence in the magnetic induction range B 0–1 T are investigated. A Physica MCR 301 rheometer of Anton Paar with a measuring cell MRD 70/1T plate–plate type with a diameter of 20 mm (the gap between the plates is 0.7 mm) was used.

The measurements were carried out with the deformation of the MRF in three different modes. The first mode (1): tangential continuous shear of the upper plate with a constant shear rate

TABLE 2 | The values of the rheological parameters of MRF at $B = 0$.

Shear mode	Parameter (kPa)	MRF-1	MRF-2	MRF-3	MRF-4
(1)	τ_{100}	5.8	0.7	0.92	2.49
(2)	τ_0	1.6	0.27	0.033	0.015
(3)	G'	366.4	25.41	7.25	9.7
	G''	36.24	8.4	4.52	7.04

in the range of change from 0.01 to 100 s^{-1}. The dependences of shear stress τ on shear rate γ (flow curves) are obtained. The second mode (2) is a linear increase of external shear stress τ. The value of τ increases linearly up to a given maximum value within 400 s. The dependences of τ on the strain ε and the static yield stress τ_0 were obtained. The third mode (3) is sinusoidal tangential oscillations of the upper plate with a constant frequency $f = 10$ Hz and strain amplitude ε_a in the range of changes in its values from 0.0001 to 1. The components of the complex shear modulus $G^* = G' + iG''$ were measured (where G' is the storage modulus (elastic modulus) and G'' is the loss modulus). All measurements were performed at a constant temperature 20°C.

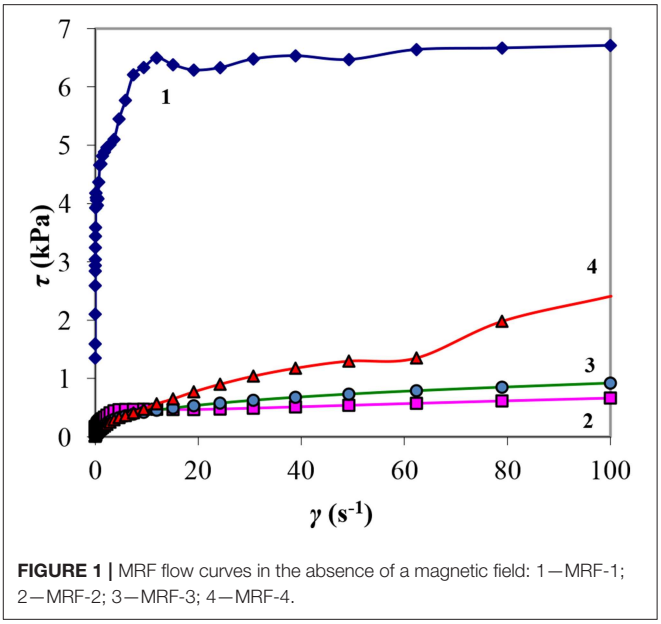

FIGURE 1 | MRF flow curves in the absence of a magnetic field: 1—MRF-1; 2—MRF-2; 3—MRF-3; 4—MRF-4.

RESULTS AND DISCUSSION

Rheological Characteristics Without a Magnetic Field

Typical rheological parameters of the materials studied and obtained without a magnetic field, are presented in **Table 2**. It contains shear stress at $\gamma = 100$ s^{-1} (τ_{100}), yield stress τ_0, G' and G'' at $\varepsilon_a = 0.01\%$. The measurement results show that the values of the rheological parameters of the MRF depend on the additive material used (**Table 1**). Among the studied compositions, the material MRF-1, containing 4 wt. % aerosil, the finest component, shows the highest values of the given rheological parameters. Replacement in the composition of the filler of 2 wt. % aerosil by 2% chromium oxide CrO_2 (MRF-2) leads to a decrease in τ_0 values by almost 6 times, τ_{100} values by eight times, and G' decreases by 15 times in comparison with the MRF-1 sample.

For the composition of MRF-4, containing 10 wt. % of bentonite clay, as well as for the composition of MRF-3 with 8 wt. % of CrO_2, a greater decrease in the rheological characteristics in the plastic and viscoelastic states (τ_0, G' and G'') is observed. In addition, an increase in shear stress in the fluid state (τ_{100}) compared with the data for MRF-2 is fixed.

This is due to the fact that aerosil matrix has greater strength at rest, even at lower particle concentrations than in the sample with bentonite clay MRF-4 and in the sample with CrO_2 MRF-3. However, it easily collapses when shear rates are of the order of 10 s^{-1} (mode 1). With a further increase in γ, the shear stress remains almost unchanged. This is illustrated in **Figure 1** (curve 1).

It can be seen that the MRF-4 sample with bentonite clay, unlike other samples, shows an increase in τ with an increase in shear rate (curve 4), but reaches a value much smaller than that of MRF-1. Other MRF compositions have τ_0 and τ_{100} values even lower in the whole range of shear rates.

Rheological Characteristics in the Mode of Continuous Shear

Figure 2 shows the changes in $\tau(\gamma)$ with a change in the magnetic field induction B from 0 to 1000 mT in mode (1). It can be seen that as B increases the shear stress τ increases at all shear rates. The shear stress of the MRF-1, MRF-2, and MRF-3 samples does not change with increase of shear rate in the range of $\gamma > 20$ s^{-1} at $B < 300$ mT. The flow curves (curves 1–4, **Figures 2A–C**) are almost parallel to the axis of shear rates, i.e. flow is viscoplastic. Only in the MRF-4 sample, an increase in τ was observed with an increase in the shear rate in the entire range of changes in the magnetic field induction (**Figure 2D**), which is characteristic of a pronounced viscoplastic flow. In this case, the shear stress is lower than that of the MRF-1.

This rheological behavior can be explained by the fact that, as in the absence of a magnetic field, the thixotropic matrix created by particles of bentonite clay (MRF-4) gradually collapses as the shear rate increases. The matrix of aerosil particles, as compared to bentonite one, is destroyed at lower shear rates. At the same time, the fine particles of aerosil do not prevent ferromagnetic particles from easily structuring in a magnetic field, unlike larger particles of bentonite clay, which prevent the interaction of particles, which reduces the magnetorheological effect. The thixotropic matrix of chromium dioxide particles in MRF-3 and MRF-2 also collapses at low shear rates. However, chromium dioxide particles have magnetic properties and are involved in the construction of bridge structures when influenced to a magnetic field, which leads to an increase in the shear resistance of the MRF-3 in a magnetic field compared to MRF-1 and MRF-4.

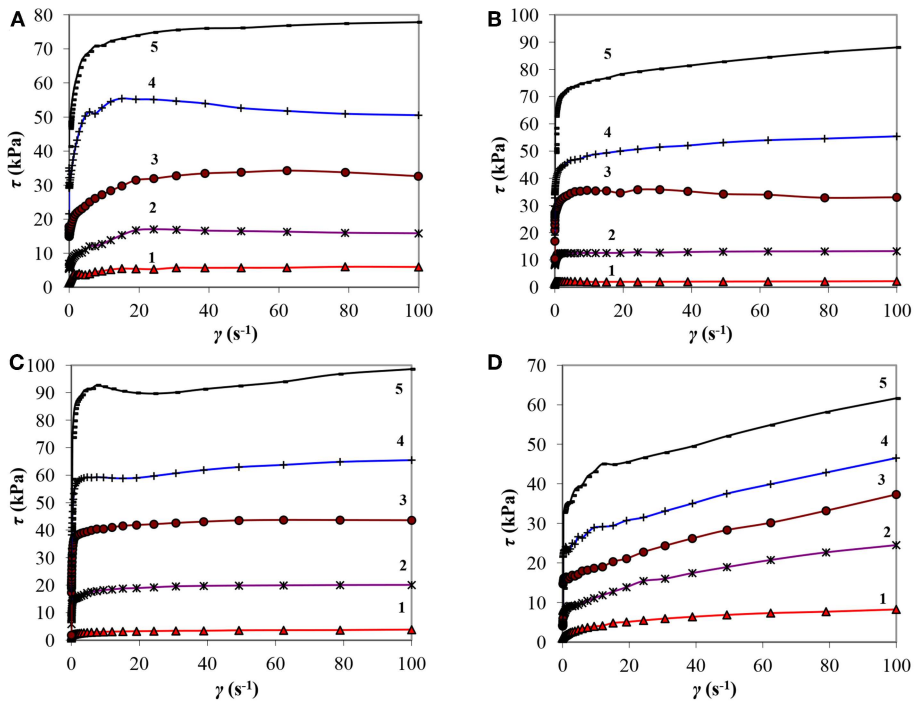

FIGURE 2 | MRF flow curves in a magnetic field (**A**—MRF-1, **B**—MRF-2, **C**—MRF-3, **D**—MRF-4): 1-*B* = 100 mT, 2-300, 3-500, 4-700, 5-1,000.

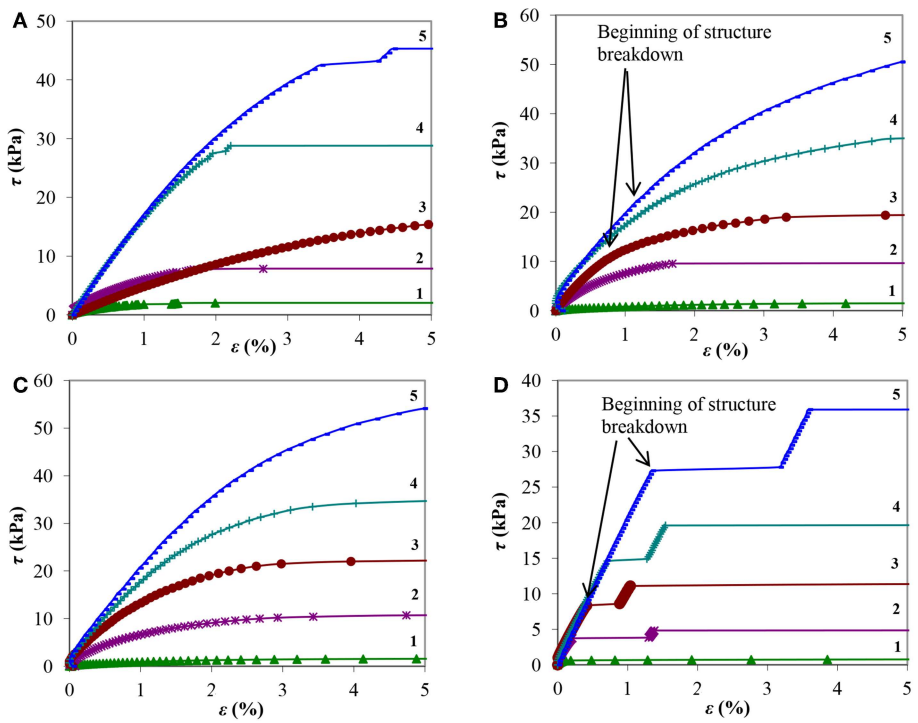

FIGURE 3 | Dependences of the shear stress τ on strain ε of MRF at different magnetic field induction (**A**—MRF-1, **B**—MRF-2, **C**—MRF-3, **D**—MRF-4): 1-*B* = 100 mT, 2-300, 3-500, 4-700, 5-1,000.

Rheological Characteristics in the Mode of Linear Increase of Shear Stress

Figure 3 shows the dependences of shear stress on strain $\tau(\varepsilon)$, obtained in mode (2) by the method of linear increase of shear stress, with the induction of a magnetic field $B = 0 \div 1{,}000$ mT.

From **Figure 3D** it can be seen that, prior to the beginning of the structure destruction, the composition of MRF-4 with bentonite clay is characterized by the presence of a significant region in the $\tau(\varepsilon)$ dependence, in which the shear stress and strain are proportional. For MRF compositions with aerosil and chromium dioxide (**Figures 3A–C**), the deviation of the dependence $\tau(\varepsilon)$ from linearity appears even at small strains. With increasing magnetic field induction, the transition limit to the non-linear dependence of shear stress on strain, corresponding to the onset of destruction of the MRF structure, shifts to the region of large strains. The destruction of the structure of the sample containing bentonite clay (MRF-4) in a magnetic field with induction $B > 200$ mT begins abruptly, the deformation increases with a jump when τ reaches the yield stress (**Figure 3D**). Probably, there is a rupture of the structure and sliding along a certain surface of the rupture. In this case, after a jump in the deformation due to particle rearrangement, the gap is eliminated and a slight increase in the structure strength is occurred. The resulting structure is again destroyed with further increase of τ (steps in **Figure 3D**, MRF-4). This sample shows the fragility of the structure in comparison with the sample containing as an additional component only aerosil (MRF-1), which collapses more smoothly with increasing deformation. The substitution of aerosol, partially with chromium dioxide (MRF-2) or completely (MRF-3), increases not only the zone of the linear dependence $\tau(\varepsilon)$, but also the value of τ_0 compared to the MRF-1 sample.

Figure 4 shows the dependences of the static yield stress τ_0 of MRF on magnetic field induction B, obtained in mode (2).

With the introduction of CrO_2 into MRF-3 and MRF-2, compared with MRF-1, τ_0 increases by 15–20%. The combination of 2% of aerosil and 2% of chromium dioxide provides the yield stress values that are the same with MRF-3, which uses 8% of chromium dioxide.

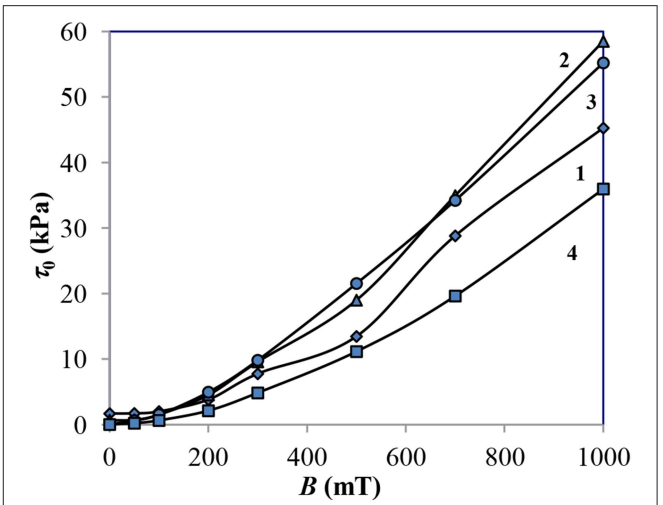

FIGURE 4 | Dependences of yield stress τ_0 on magnetic induction B: 1—MRF-1; 2—MRF-2; 3—MRF-3; 4—MRF-4.

Rheological Characteristics in the Mode of Sinusoidal Shear Oscillations

Figure 5 shows the dependences of the components of the complex shear modulus on the amplitude of the deformation at the magnetic field induction $B = 0 \div 1000$ mT obtained in mode (3).

At small strains (up to 1%), the storage modulus G' does not change with an increase in the amplitude of the strain (linear range). In a magnetic field with an induction $B = 1{,}000$ mT, G' is 2,000–2,300 kPa for all samples, increasing by 1–2 orders of magnitude compared with the values in the absence of a field. As the strain amplitude increases, the values of G' fall sharply, decreasing by more than an order of magnitude. The MRF-1 has a less sharp fall. G'' with increasing of ε_a increases to the value of the deformation amplitude, at which the most rapid decrease in the value of G' takes place. With increasing magnetic field induction, the values of the loss modulus G'' for all MRF samples increase by 1–2 orders of magnitude. The values of the maxima of G''_{max} at that move in the region of large deformation amplitudes. The maximum values of the loss modulus G''_{max} are characteristic for all samples at $B = 1{,}000$ mT and $\varepsilon_a \approx 3\%$. The smallest values of $G''_{max} \approx 300$–350 kPa for MRF-1 and MRF-2, containing aerosil, the highest (almost 1,000 kPa) are for MRF-4, containing bentonite clay.

Let us consider the dependences of the components of the complex shear modulus on the magnetic field induction at a certain constant amplitude of the shear strain. **Figure 6** shows such a relationship with ε_a equal to 0.01%. The loss modulus (**Figure 6B**) has a maximum at some intermediate value B, then decreases. With increasing magnetic field induction, the size of the structured aggregates of particles of the dispersed phase increases and the viscous resistance to shear grows. With a further increase in B, almost all the aggregates are connected in solid structures, the MRF is in a solid-like state with a predominantly elastic shear resistance, which corresponds to an increase in G' to maximum values for different B for each MRF.

With increasing magnetic field induction in the region of small deformations, an increase in the storage modulus of MRF-1 and MRF-2, containing aerosil particles, occurs in all range of B, unlike other samples, where G' increases in the range up to 200 mT and at higher induction reaches its maximum. In this case, the loss modulus reaches a maximum at induction of 200–300 mT, greater than that of other samples (up to 100 mT), which is apparently caused by the resistance of the aerosil matrix to structuring magnetic particles, which is achieved only in strong fields, at $B > 500$ mT. So, with an increase in the magnetic field induction up to 200 mT, the values of G' reach 2,000 kPa for MRF-4, for MRF-3 $G'' \approx 1{,}500$ kPa, for MRF-1 $G' \approx 880$ kPa, for MRF-2 $G'' \approx 620$ kPa.

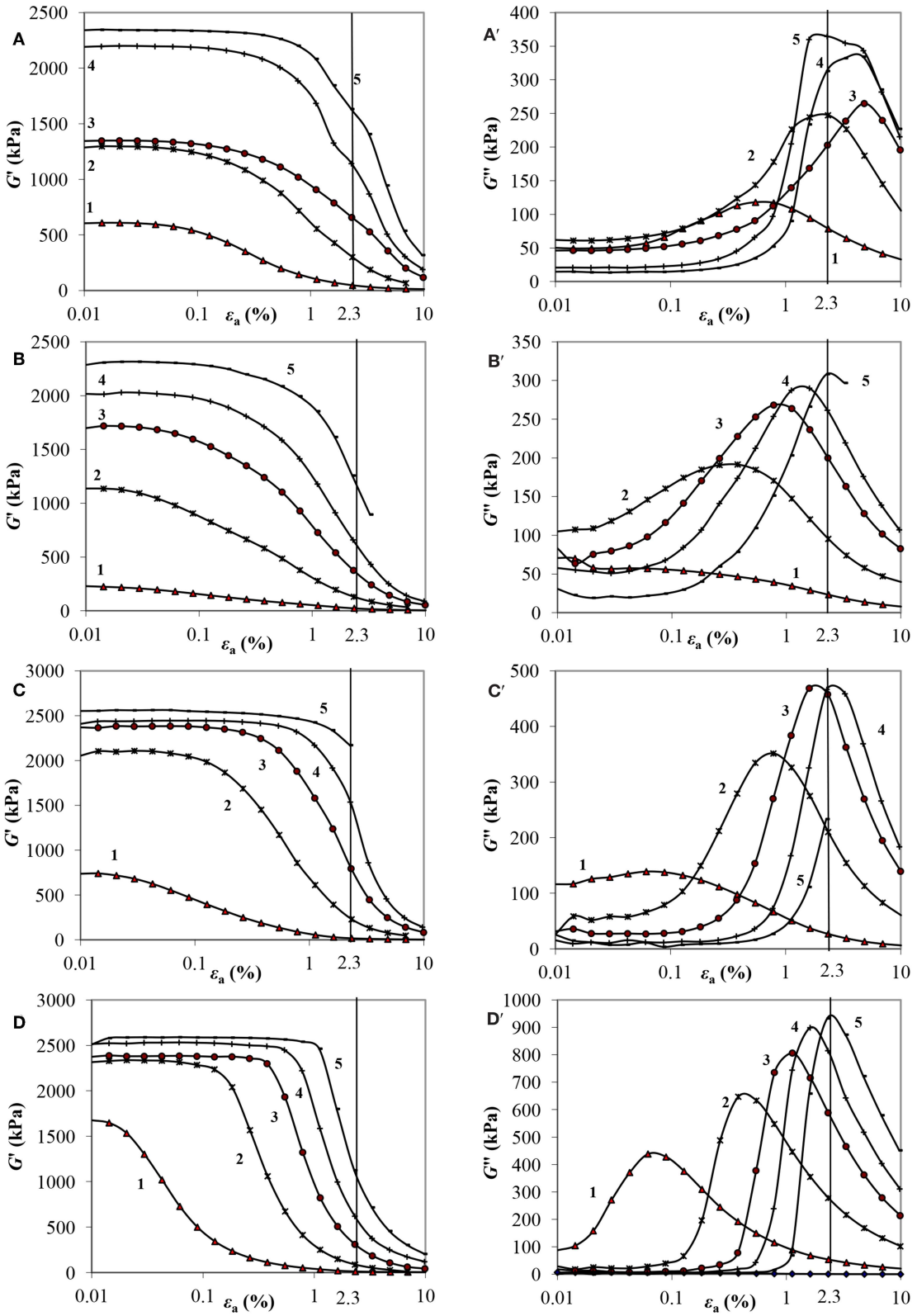

FIGURE 5 | Dependences of the components of the complex shear modulus on the deformation amplitude at different magnetic field induction (**A**,**A′**—MRF-1; **B**,**B′**—MRF-2; **C**,**C′**—MRF-3; **D**,**D′**—MRF-4): 1-*B* = 100 mT, 2-300, 3-500, 4-700, 5-1,000.

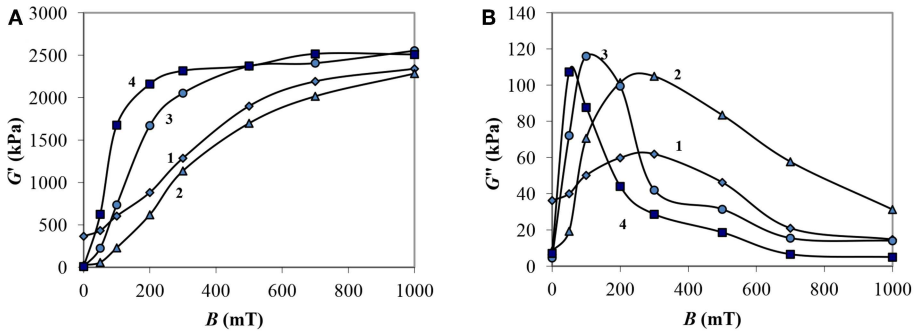

FIGURE 6 | Dependencies of the storage modulus G' **(A)** and loss modulus G'' **(B)** of MRF on the magnetic field induction at the strain amplitude $\varepsilon_a = 0.01\%$: 1—MRF-1; 2—MRF-2; 3—MRF-3; 4—MRF-4.

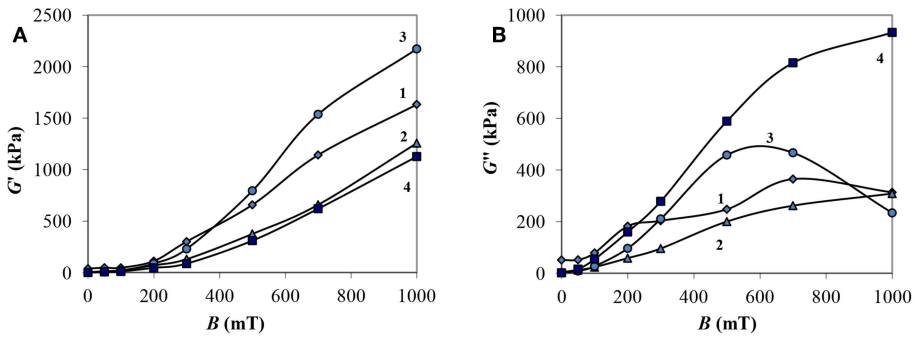

FIGURE 7 | Dependencies of the storage modulus G' **(A)** and loss modulus G'' **(B)** of MRF on the magnetic field induction at the strain amplitude $\varepsilon_a = 2{,}3\%$: 1—MRF-1; 2—MRF-2; 3—MRF-3; 4—MRF-4.

In **Figure 7** the dependence of the components of the complex shear modulus on the induction of the magnetic field at a strain amplitude of 2.3%, corresponding to the intensive destruction of the structure as a result of external influence is shown.

It can be seen that the storage modulus increases smoothly with an increase in the intensity of the external field for all MRF compositions. The storage modulus reaches greatest value in MRF-3, containing chromium dioxide. The loss modulus of this material has a maximum at a value of B ~600–700 mT, with greater induction it decreases. In other MRF samples, an increase in G'' values was observed in the entire range of magnetic induction. The smallest values of G' and the largest ones of G'' are in MRF-4 containing bentonite clay. At the same time, with small deformations, MRF-4, on the contrary, has the largest values of G'. The composition with bentonite clay has the strongest structure at rest, however, when subjected to shear deformations, it reveal a sharp destruction with the greatest energy losses among the materials studied. The presence of fine ferrimagnetic particles of chromium dioxide (MRF-3) prevents deformation fracture and increases the role of the elastic component of the material.

In **Figure 8** the dependences of the strain amplitude ε_l, at which the loss moduli are maximal, that is, at this strain, the greatest viscous losses are recorded (**Figure 5**), on the magnetic field induction are shown.

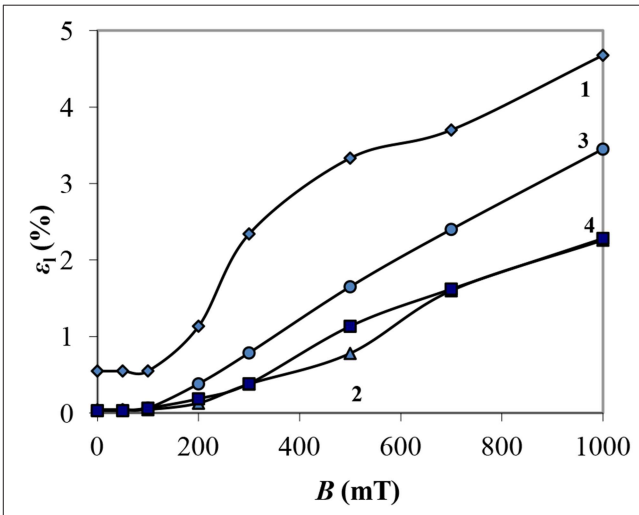

FIGURE 8 | Dependences of the strain amplitude ε_l at the maximum value of the loss modulus from the magnetic field induction B: 1—MRF-1; 2—MRF-2; 3—MRF-3; 4—MRF-4.

It can be seen that with the induction of a magnetic field up to 100 mT, ε_l practically does not change, then grows with increasing B. MRF-1, containing aerosil, experiences intense

structural destruction with large vibration amplitudes than other samples (curve 1) in the entire range *B*. Aerosil particles contribute to the formation of a more elastic structure capable of elastically deforming to large deformations.

CONCLUSION

For the purpose of application for controlled damping of layered structures with MRF in various shear modes, four compositions with additions of aerosil, chromium dioxide, and bentonite clay were investigated. The features of the rheological behavior of the MRF at continuous shear, linear increase of shear stress, sinusoidal tangential oscillations depending on the material of additives and magnetic field induction are established.

It has been established that in the continuous shear mode, the composition of MRF with bentonite clay shows a smooth increase in the shear stress with increasing shear rate, thus providing a greater range of its regulation.

In the mode of linear increase of shear stress when chromium dioxide is added to the carbonyl iron, the material shows greater structure strength compared to other compositions.

It is determined in the mode of shear oscillations that the optimal range of the magnetic field induction, in which the greatest change in the viscoelastic characteristics of the MRF takes place, is up to 300 mT. The use of bentonite clay in MR fluid provides the largest increase in loss modulus (from 1 to almost 1,000 kPa) in a magnetic field with strain amplitude in the non-linear region compared with other additives. This allows to recommend this composition for the creation of controlled damping of flat structural elements. The addition of chromium dioxide to the carbonyl iron into MRF allows one to achieve the greatest increase in the elasticity of the material in a magnetic field and, consequently, increase the rigidity of the structure with its use. MRF using bentonite clay in a linear zone of elasticity shows the values of the modulus of elasticity, close to the values for MRF with chromium dioxide.

The possibility of making a more targeted adjustment of the complex composition of the MRF by introducing additional particles of magnetic and non-magnetic nature makes it possible, for all the considered shear modes, to determine the features of their use in layered structural elements depending on the assigned tasks—increasing rigidity or damping, as well as yield stress.

AUTHOR CONTRIBUTIONS

EK proposed the idea and supervised the work. MZ performed the experiments. They also wrote the manuscript. ZN prepared the MRF samples. All authors performed data analysis.

REFERENCES

Ahamed, R., Choi, S.-B., and Ferdaus, M. M. (2018). A state of art on magneto-rheological materials and their potential applications. *J. Intell. Mater. Syst. Struct*. 29, 2051–2095. doi: 10.1177/1045389X18754350

Akhtar, M., Alam, S., and Mohd, F. (2015). Fuzzy rules incorporated skyhook theory based vehicular suspension design for improving ride comfort. *Int. J. Eng. Res. Appl*. 5, 30–36.

Ashtiani, M., and Hashemabadi, S. H. (2015). The effect of nano-silica and nano-magnetite on the magnetorheological fluid stabilization and magnetorheological effect. *J. Intell. Mater. Syst. Struct*. 26, 1887–1892. doi: 10.1177/1045389X15580659

Chu, S. Y., Soong, T. T., and Reinhorn, A. M. (2005). *Active, Hybrid and Semi-Active Structural Control*. New York, NY: John Wiley and Sons.

Dong, Y. Z., Hao, P. S., Zhang, K., and Choi, H. J. (2018). Effect of $CoFe_2O_4$ nanoparticles on a carbonyl iron based magnetorheological suspension. *Colloids Surf. A* 537, 102–108. doi: 10.1016/j.colsurfa.2017.10.017

Fu, J., Li, P., Liao, G., Lai, J., and Yu, M. (2018). Active/semi-active hybrid isolation system with fuzzy switching controller. *J. Intell. Mater. Syst. Struct*. 29, 101–115. doi: 10.1177/1045389X17733054

Iglesias, G. R., Roldán, A., Reyes, L., Rodríguez-Arco, L., and Durán, J. D. G. (2015). Stability behavior of composite magnetorheological fluids by an induction method. *J. Intell. Mater. Syst. Struct.* 26, 1836–1843. doi: 10.1177/1045389X15577656

Korobko, E., Novikova, Z., Zhurauski, M., Kazak, H., and Dragašius, E. (2014). Investigation of elasticity of magnetosensitive adaptive materials for laminated composite structures. *Mechanika* 20, 466–470. doi: 10.5755/j01.mech.20.5.7080

Leong, S. A. N., Samin, P. M., Idris, A., Mazlan, S. A., and Rahman, A. H. A. (2016). Synthesis, characterization and magnetorheological properties of carbonyl iron suspension with superparamagnetic nanoparticles as an additive. *Smart Mater. Struct*. 23:123001. doi: 10.1088/0964-1726/25/2/025025

Li, Y., Li, J., Li, W., and Du, H. (2014). A state-of-the-art review on magnetorheological elastomer devices. *Smart Mater. Struct*. 23:123001. doi: 10.1088/0964-1726/23/12/123001

Librescu, L., and Hause, T. (2000). Recent developments in the modeling and behavior of advanced sandwich constructions: a survey. *Composite Struct*. 48, 1–17. doi: 10.1016/S0263-8223(99)00068-9

Megha, S., Kumar, S., and D'Silva, R. (2016). Vibration analysis of magnetorheological elastomer sandwich beam under different magnetic fields. *J. Mech. Eng. Autom*. 6, 75–80. doi: 10.5923/c.jmea.201601.14

Nayak, B., Dwivedy, S. K., and Murthy, K. S. R. K. (2013). Vibration analysis of a three-layer magnetorheological elastomer embedded sandwich beam with conductive skins using finite element method. *Proc. Inst. Mech. Eng. Part C J. Mech. Eng. Sci*. 227, 714–729. doi: 10.1177/0954406212451812

Song, S. (2009). Cost-effective skyhook control for semiactive vehicle suspension applications. *Open Mech. Eng. J*. 3, 17–25. doi: 10.2174/1874155X00903010017

Tian, T. F., Zhang, X. Z., Li, W. H., Alici, G., and Ding, G. (2013). Study of PDMS based magnetorheological elastomers. *J. Phys. Conf. Ser*. 412:012038. doi: 10.1088/1742-6596/412/1/012038

Zhou, G. Y. (2003). Shear properties of a magnetorheological elastomer. *Smart Mater. Struct*. 12, 139–146. doi: 10.1088/0964-1726/12/1/316

Conflict of Interest Statement: The authors declare that the research was conducted in the absence of any commercial or financial relationships that could be construed as a potential conflict of interest.

frontiers in Materials

ORIGINAL RESEARCH
published: 20 June 2019
doi: 10.3389/fmats.2019.00139

Selection of Materials Used in Viscous Clutch With ER Fluid Working in Special Conditions

*Artur Olszak[1], Karol Osowski[2], Przemysław Motyl[2], Grzegorz Mędrek[2], Jan Zwolak[3], Andrzej Kęsy[2], Zbigniew Kęsy[2] and Seung-Bok Choi[4]**

[1] Technical Department, New Chemical Syntheses Institute, Puławy, Poland, [2] Faculty of Mechanical Engineering, Institute of Applied Mechanics and Energetics, Kazimierz Pulaski University of Technology and Humanities, Radom, Poland, [3] Department of Mechanics and Mechanical Engineering, University of Rzeszów, Rzeszów, Poland, [4] Inha University, Incheon, South Korea

OPEN ACCESS

Edited by:
Marcelo J. Dapino,
The Ohio State University,
United States

Reviewed by:
Yu Tian,
Tsinghua University, China
Rongjia Tao,
Temple University, United States
Jianbo Yin,
Northwestern Polytechnical University, China

***Correspondence:**
Seung-Bok Choi
seungbok@inha.ac.kr

Specialty section:
This article was submitted to Smart Materials, a section of the journal Frontiers in Materials

Received: *30 October 2018*
Accepted: *29 May 2019*
Published: *20 June 2019*

Citation:
Olszak A, Osowski K, Motyl P, Mędrek G, Zwolak J, Kęsy A, Kęsy Z and Choi S-B (2019) Selection of Materials Used in Viscous Clutch With ER Fluid Working in Special Conditions. Front. Mater. 6:139. doi: 10.3389/fmats.2019.00139

This article presents considerations regarding materials used to fabricate a hydraulic clutch with an ER fluid operating in non-standard working conditions. The hydraulic clutch was a subassembly of the device used for exerting a controlled force on the stationary object. This clutch was driven by an electric motor. The force was controlled by changing the shear stresses in the ER fluid. Shear stresses were changed in two ways: by changing the angular velocity of the electric motor and by changing the high voltage applied to the electrodes located on the driving part and the driven part of the clutch. The increase in these stresses caused an increase in the torque transmitted and an increase in the pressure force. In order to construct the clutch, mathematical models based on the Bingham model were developed, which took into account the influence of temperature and humidity on the shear stress in the ER fluid, allowing calculation of the clutch performance. In addition, numerical calculations of the temperature distribution inside the clutch were carried out using the ANSYS program because of the intense heat generation during the clutch operation. The developed mathematical models were used to optimize the clutch. The aim of the optimization was to obtain a high transmitted torque with small dimensions of the clutch, taking into account the thermal capacity of the clutch. Based on the optimization results, a prototype of a hydraulic clutch with an ER fluid was designed and made, assuming that for metal materials their anti-corrosion properties are the most important, since the presence of conductive metal oxides causes electrical breakdowns. The plastics used in the clutch prototype were mainly evaluated for insulating properties and high temperature resistance. When choosing the ER fluid, its sensitivity to temperature and humidity as well as durability were taken into account. The clutch prototype has been tested on a specially built test rig. The test results confirmed the proper selection of both construction materials and ER fluids. Based on the results of these tests, guidelines for the construction of clutches with ER fluids were formulated.

Keywords: viscous clutch, smart fluids, ER fluids, optimization, numerical calculations

INTRODUCTION

The most important factors that have recently contributed to mechanical devices' better results and which have increased the devices' reliability are the implementation of new materials and integration with digital electronics. In viscous clutches and brakes, both of these factors are combined by using new construction materials and hydraulic working fluids of a new type, i.e., smart fluids which react to a physical field by altering their rheological properties.

Two types of smart fluids are in use: electrorheological fluids (ER) and magnetorheological fluids (MR), activated, respectively with an electrical or magnetic field. ER and MR fluids are divided into two groups, according to their composition: monophasic and biphasic. Monophasic fluids are homogeneous while biphasic fluids consist of two phases: solid and liquid.

Viscous clutches consist of the driving part connected to input shaft and the driven part connected to the output shaft. Immobilizing the driven part causes the clutch to become a brake. In these clutches the torque is transmitted as a result of friction caused by shear stress in the working fluid between the driving part and the driven part. Two main types of viscous clutches can be distinguished, according to the shape of driving and driven part: cylindrical and disc clutches.

Due to the necessity to create an electric or magnetic field in the gap containing working fluid, building clutches and brakes with smart fluids proves much more complex than building clutches and brakes with typical working fluids. In viscous clutches with ER fluids, the electric field is usually created between two electrodes, one of which is situated in the driving part and the other in the driven part of the clutch. In such clutches, in order to convey the voltage to electrodes connected with the movable part of the clutches, additional electrical wires and sliding rings are used. However, in the viscous clutches with MR fluid, electromagnet cores and coils must be installed in addition to electrical wires and sliding rings. Due to these reasons, viscous clutches with MR fluids weigh more, and there is consequently more inertia of the rotating parts, which is unfavorable for the control of the clutches. The complicated structure of the clutches and brakes with smart fluids makes it necessary to select materials with proper properties as well as to choose design methods based on mathematical modeling and numerical calculations.

So far, to control the torque, a vital feature of viscous clutches and brakes was used: the dependence of torque on angular velocity of the input shaft. Altering the angular velocity enables the control of the transmitted torque. The torque can also be controlled by changing temperature, pressure or volume of the working fluid within the clutch. For viscous clutches and brakes built with new materials such as smart fluids, the control is achieved by causing changes in shear stress, influencing the ER or MR fluid with an appropriate field with regulated voltage. The change in electric or magnetic field is achieved by changing voltage or current with electronically controlled electric power supplies. Increase in shear stress within the working fluid causes increase in the torque transmitted by viscous clutches or brakes.

The paper presents the results of design optimization and experimental research of a viscous disc clutch with an ER fluid, working in unusual thermal conditions. The aim of the design optimization was to achieve a large torque of the clutch, with a small size of the clutch, and at the same time a small area of heat dissipation. However, the working fluid temperature of the clutch was kept close to the temperature of the surroundings. The multi-objective optimization was carried out based on mathematical models of the ER fluids and a disc viscous clutch. The multi-objective optimization of the viscous clutch with the ER fluid including the quality of materials had not been conducted in this way before. Subsequently, a prototype of a viscous clutch with the ER fluid was made and tested on a specially built test rig. The obtained results allowed the compilation of principles for constructing viscous clutches with ER fluid, including choice of materials.

LITERATURE STUDY

In the practically used biphasic ER and MR fluids, the solid phase is comprised of particles of polymer or iron, respectively, of diameter ranging from 5 to 10 μm, and the liquid phase—silicon oil (Fertman, 1990; Conrad, 1993; Weiss, 1993; Mikkelsen et al., 2017). The biphasic fluids also contain additives (up to 3%) that prevent sedimentation and aggregation of the solid phase and increase the electrorheological or magnetorheological effect. A percentage of contents of the solid phase in biphasic ER and MR fluids is, according to weight, 60–80% and according to volume, 20–30%. One limitation in the use of the ER fluid is its sensitivity to temperature changes and air humidity. MR fluid use is limited by the magnetic saturation phenomenon.

ER and MR fluids are used or predicted to use mainly as materials with controlled rheological properties in a variety of devices, such as haptic devices (Liu et al., 2006), energy absorbers (Milecki et al., 2005; Choi and Wereley, 2015), dampers (Sapiński et al., 2016), cantilever beams (Lara-Prieto et al., 2010), hydrodynamic clutches (Madeja et al., 2011; Olszak et al., 2018), discharge machines (Kim et al., 2002), or even robots (Saito and Ikeda, 2007; Jing et al., 2018) and seismic isolators (Li et al., 2013).

The most frequent uses of ER and MR fluids are in devices such as clutches and brakes (Olszak et al., 2016a; Raju et al., 2016; Gao et al., 2017). To achieve the assumed characteristics of clutches and brakes with ER and MR fluids, their architectures are taken into consideration by analyzing the shape and position of working space (Avraam et al., 2010), the way of producing the electric or magnetic field (Takesue et al., 2003; Böse et al., 2013; Sohn et al., 2018) as well as thermal working conditions (Chen et al., 2015; Song et al., 2018). Additionally taken into consideration are the smart fluids used for construction of clutches and brakes with ER and MR, mainly their composition (Sarkar and Hirani, 2013; Kumbhar et al., 2015; Mangal et al., 2016) and durability (Olszak et al., 2016b; Kim et al., 2017; Ziabska et al., 2017). Examples of design solutions for clutches and brakes with smart fluids can be found in publications (Papadopoulos, 1998; Kavlicoglu et al., 2002; Smith et al., 2007; Fernández and Chang, 2016).

The next vital step on the way to improving the construction of clutches and brakes with smart fluids is using the optimization methods. In the publications concerning this subject, the geometric dimensions are optimized while the authors assume different objective functions and different optimization methods.

The optimization objects are usually devices with the MR fluid, used in vehicles. In previous works (Park et al., 2006, 2008) the construction process involved multidisciplinary design optimization; the objective function takes into consideration brake weight as well-braking torque and uses scalar weighting factors. In these works the assumption was that in a car, the brake weight is more important than braking torque. To decrease calculation time, three optimization methods were used, the first two being less effective: built-in capabilities of ANSYS and then a random-search method, which gave the lowest objective function values. During the optimization, CFD analysis was also conducted and magnetic field intensity distribution along with steady-state temperature distribution were evaluated. Nguyen and Choi (2010), in the process of a car brake optimization and while defining the objective function, took into consideration the following aspects: required braking torque, temperature due to zero-field friction of MR fluid, mass of the brake system and geometric dimensions. The optimization method used there was based on finite element analysis. In the work (Assadsangabi et al., 2011), the objective function was assumed in a way which allowed the largest possible braking torque with the smallest possible weight of the car brake. The optimization was conducted with the use of finite element analysis and Genetic Algorithm. The aim of the work (Sohn et al., 2015) was the optimization of a motorcycle brake. In the objective function, factors taken into consideration were braking torque, weight and temperature. In the optimization process a tool based on finite element analysis was used. In research (Nguyen and Choi, 2010) concerning a passenger vehicle magnetorheological damper, the objective function included damping force, dynamic range and inductive time constant of the damper. In the optimization method based on finite element analysis, a golden-section analysis algorithm and a local quadratic fitting technique were used.

Dimension optimization of the clutches with MR fluid can be found in two previous articles (Horvath and Torőcsik, 2011; Bucchi et al., 2017). In both, the optimization was aimed to achieve the largest possible transmitted torque of the clutch, while in Bucchi et al. (2017) emphasis was put on the magnetorheological fluid gap shape, and the optimization was conducted while using the finite element method. However, in Horvath and Torőcsik (2011) the inner radius was emphasized, while the optimization was based on the simple analytical method and a simulation procedure. The article (Gao et al., 2017) depicts the optimization of a MR damper designed for smart prosthetic knees. In the objective function, factors taken into consideration were total energy consumption during one gait cycle and weight of the MR damper. The optimization was conducted based on the particle swarm optimization algorithm. The original optimization method called the Taguchi Method was used to optimize the magnetorheological brake actuator (Erol and Gurocak, 2011). In the objective function, torque-to-volume ratio was taken into consideration.

MATHEMATICAL MODEL

While defining the mathematical model of the ER fluid, it was assumed that rheological properties of the fluid can be described by the Bingham model:

$$\tau = \mu_p \dot{\gamma} + \tau_0 \tag{1}$$

while for $U = 0$, $\tau = \mu_0 \dot{\gamma}$, and the electric properties of the ER fluid can be described with the equation:

$$I = i_g S \tag{2}$$

where μ_p is plastic viscosity, τ_0 is electric field-dependent yield stress of ER fluid, μ_0 is the ratio of dynamic viscosity of fluid without an electric field, and i_g is the density of current leakage.

The relation of τ_0, μ_0, i_g to electric field E was described by formulas, in which temperature T, relative air humidity w and shear rate $\dot{\gamma}$ were taken into consideration:

$$\begin{aligned} \tau_0 &= a_0 \cdot a_1 \cdot a_2 \cdot a_3 \cdot E^2 \\ \mu_0 &= b_0 \cdot b_1 + b_2 E^2 \\ i_g &= c_0 \cdot c_1 \cdot c_2 \cdot c_3 \cdot E^{1,7} \end{aligned} \tag{3}$$

where a_0, b_0, c_0, a_2, b_2 are numerical coefficients; a_1, b_1, c_1 are coefficients depending linearly on temperature T; a_3, c_2 is coefficients depending linearly on relative air humidity w; and c_3 is coefficients depending linearly on shear rate $\dot{\gamma}$.

It was assumed that radiuses r in the mathematical model of the viscous clutch with ER fluid are described by a proportional enlargement of the model clutch whose geometry was determined based on the analysis of already existing clutches and brakes with smart fluid (Papadopoulos, 1998; Kavlicoglu et al., 2002; Smith et al., 2007; Nguyen and Choi, 2010; Erol and Gurocak, 2011) using the magnification factor s_k. The width of the model clutch is calculated depending on the number of discs n with a constant width of the gap h between discs. **Figure 1** shows a construction scheme of a model viscous clutch with ER fluid, and **Table 1** shows juxtaposed dimensions of the clutch, dependent on magnification factor s_k and number of working gaps n.

During the optimization process of the clutch, the following calculations were made: torque transmitted through the clutch M, the clutch's power P, the clutch's volume O, temperature of the ER fluid in clutch T_Z, and centripetal acceleration a_d. Calculations were made based on the following formulas:

$$\begin{aligned} M &= n\frac{\pi \mu_p}{2h}\omega\left({r_2}^4 - {r_1}^4\right) + n\frac{2\pi \tau_0}{3}\left({r_2}^3 - {r_1}^3\right) \\ P &= n\frac{\pi \mu_p}{2h}\omega^2\left({r_2}^4 - {r_1}^4\right) + n\frac{2\pi \tau_0}{3}\omega\left({r_2}^3 - {r_1}^3\right) \\ O &= \pi {r_z}^2 S_z \\ a_d &= \omega^2 r_z \\ T_z &= \frac{P}{\alpha S_z} + T \\ i_c &= n \cdot i_g \cdot S \end{aligned} \tag{4}$$

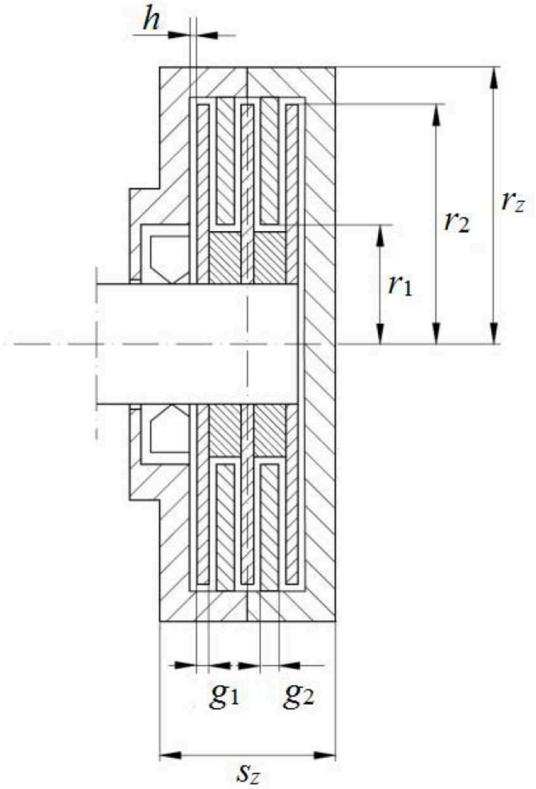

FIGURE 1 | Construction scheme of a model viscous clutch with ER fluid with 5 discs.

where T is the temperature of the surroundings and $S = \pi(r_2^2 - r_1^2)$ is the surface of the electrode's side.

The torque M transmitted through the viscous clutch with the ER fluid was calculated by integration of unit force occurring on the radius r, with the simplifying assumption that the shear stress τ does not change—neither along the disc radius nor along the gap height. The result was the following equation:

$$M = \int_{r_1}^{r_2} r\,dF = 2\pi \int_{r_1}^{r_2} \tau\, r^2 dr \tag{5}$$

where, subsequently, the formula (1) (Park et al., 2008; Erol and Gurocak, 2011) was taken into consideration.

The temperature T_Z was calculated from an equation describing heat Θ released into the surroundings in the moment Δt assuming that the clutch works with a constant power P in set conditions:

$$\Theta = P\,\Delta t = \alpha\, S_s\,(T_z - T)\,\Delta t \tag{6}$$

where α -is the heat transfer coefficient and T is the temperature of the surroundings.

TABLE 1 | Dimensions of the clutch with ER fluid assumed for optimization.

Dimension	Denomination	Unit	Formula
The inner radius of the friction surface	r_1	cm	$r_1 = 1{\cdot}s_k$
The outer radius of the friction surface	r_2	cm	$r_2 = 2.25{\cdot}s_k$
The inner radius of the clutch	r_z	cm	$r_z = r_2 + 1.75{\cdot}s_k$
The width of the working gap	h	cm	$h = 0.15$
The thickness of the inner disc	g_1	cm	$g_1 = 0.1{\cdot}s_k$
The thickness of the outer disc	g_2	cm	$g_2 = 0.1{\cdot}s_k$
The width of the clutch	s_z	cm	$s_z = n{\cdot}h{+}g_1(n\text{-}1){+}1.25{\cdot}\ s_k$
The volume of the clutch	O	cm^3	$O = \pi\ r_z^2{\cdot}s_z$
The side surface of the clutch	S_z	cm^2	$S_z = 2\pi\ r_z^2{+}2\pi\ r_z{\cdot}\ s_z$

The quantities described by formulas (4) are construction indicators of the viscous clutch with ER fluids, depicting its characteristic features, such as performance (P, M), dimensions (O) and working conditions (T, T_Z, a_d).

OPTIMIZATION OF THE VISCOUS CLUTCH WITH ER FLUID

The Way of Conducting the Optimization Calculations

The main goal of the optimization was to receive a viscous clutch with ER fluid with the smallest possible dimensions, transmitting the largest possible torque, but at the same time the amount of dissipated heat, dependent on the side surface of the clutch, ensured a possibly low temperature of the ER fluid during the constant work of the clutch.

Two objective functions were created, containing relations M/O and T_Z/T. Relation M/O should be as large as possible to receive the largest possible torque M from a construction with the smallest possible volume O. However, the relation T_Z/T should generate possibly small values to reduce temperature change, and consequently the temperature's influence on the ER fluid's attributes. The assumed limitations were the values of power P, centripetal acceleration a_d and current i_c.

The objective functions were as follows:

$$F_c = \frac{T_z}{T} \Big/ \frac{M}{O} \tag{7}$$

$$F_c = \left| w_1 \cdot T_z/T_r - w_2 \cdot \frac{O}{M} \Big/ \left(\frac{O}{M}\right)_r \right| \tag{8}$$

where: w_i $(i = 1, 2)$ is a weighting factor for the i th objective function.

Equation (8) was formulated based on the weighted sum method which is the most widely used method for multi-objective optimization. In this study it was assumed that $\sum_{i=1}^{i=2} w_i = 1$ and $0 \leq w_i \leq 1$. The coefficients w_1 and w_2 have no physical meanings.

The minimal values of these objective functions were needed:

- for allowed values from the scopes: $1 \leq s_k \leq 8$; $30 \leq \omega \leq 250$ rad/s; $5 \leq n \leq 13$;
- with the constraints: $P \leq 1000$ W; $a_d < 300$ rad/s^2; $i_c < 100$ mA.

For optimization calculations, an individual computer program was used, written in Delphi programming language. The calculations were conducted as follows:

- a random number generator was used, allowed values were drawn from the assumed ranges of allowed values;
- a check was conducted to ensure that constraints were met;
- if the drawn values of the allowed values met the constraints' conditions, objective functions were calculated; if not, the allowed values were drawn again;
- the calculated objective function was memorized and calculations were repeated;
- the objective functions' values from the former and current calculations step were compared;
- the smaller value was selected, and simultaneously the values calculated for the smaller value of the objective function were saved.

Based on several sets of geometric dimensions of viscous clutches with ER fluids (the sets that were deemed best), virtual solid models of the clutches were built. These models were subsequently used to calculate the distribution of temperature in the clutch with the aid of the ANSYS Fluent program. While calculating the heat created in working gaps of the clutch, the power emitted during electric current flow $P_1 = U \cdot i_c$ was taken into consideration, as well as power P_2 emitted as a result of shear stress τ occurrences. Due to different dimensions of the clutches obtained during the optimization process, power $P = P_1 + P_2$ was referred to the volume V of the ER fluids within the working gaps.

The relation of the power turned into heat to a unit of the fluid's volume P_2/V was calculated assuming that the power dP emitted in the fluid ring of dr thickness can be written as:

$$dP_2 = dF\,v = dS\tau\,v = 2\pi\,r\,dr\,\tau\,v \tag{9}$$

After complying with $dV = 2\pi\,r\,dr\,h$ and $v = \omega\,r = \dot{\gamma}\,h$ the result is:

$$dP_2 = 2\pi\,r\,dr\,\tau\,v = 2\pi\,r dr h\,\tau\dot{\gamma} = dV\tau\,\dot{\gamma} \tag{10}$$

and after integrating both sides of the equation and transforming:

$$\tau\,\dot{\gamma} = \frac{P_2}{V} \tag{11}$$

In order to render the ratio P_2/V dependent on the radius r it is taken into consideration that $\dot{\gamma} = \frac{v}{h} = \frac{\omega r}{h}$ and $\tau = \mu_p\dot{\gamma} + \tau_0$ which gives the result:

$$\frac{P_2}{V} = \left(\mu_p\dot{\gamma} + \tau_0\right)\,\dot{\gamma} = \mu_p\dot{\gamma}^2 + \tau_0\dot{\gamma} = \mu_p\frac{r^2}{h^2}\omega^2 + \tau_0\frac{r}{h}\omega \tag{12}$$

TABLE 2 | Basic information on ERF#6 fluid.

Coefficient of dynamic viscosity at 25°C	**μ = 60 mPa·s**
Kinematic viscosity at 25°C	$\mu = 56$ mm^2/s
Density	$\rho = 1.074$ g/cm^3
Coefficient of dynamic viscosity of liquid phase	μ_C =16 mPa·s
Density of liquid phase	ρ_C =0.98 g/cm^3
Density of solid phase	$\rho_S = 1.21$ g/cm^3
Proportion of solid phase by weight	$\varphi_W = 40\%$
Proportion of solid phase by volume	$\varphi_O = 35\%$
Temperature of ignition	$> 250^{O}$C
Temperature of solidification	$< -20^{O}$C
Size of solid particles	10 μm

Data for Optimization

It was assumed that in a viscous clutch with ER fluid, the ERF#6 fluid would be used. It consists of sulphonated styrene-divinylbenzene resin with sodium cation and silicon oil; its data is presented in **Table 2** (Płocharski et al., 1997; Bocińska et al., 2002) according to the producer's information. The ERF#6 fluid was selected mainly for its durability.

Coefficients a, b, and c of the ERF#6 fluid's mathematical model, described with formulas (3), were determined based on tests conducted by a measuring device. The device was built similarly to a cylindrical rheometer, but the cylinders' diameters were much larger. The basic element of the device was a viscous clutch built with mutually isolated cylinders, connected to electric poles of a high voltage power supply. One of the cylinders, with an inner radius of 122 mm, was set directly on a shaft of a vertically installed asynchronous motor controlled with a frequency converter which enabled a fluent regulation of angular velocity ω. However, the second cylinder, with an outer diameter of 120 mm and a height of 29 mm, was connected to a lever of length $l = 140$ mm, which pressed the strain gauge force sensor F. The gap between the cylinders was $h = 1$ mm. The temperature of the fluid T was measured with a resistive sensor placed on the wall of the non-rotating cylinder. The influence of relative air humidity on the rheological characteristics of the ERF#6 fluid was tested by placing a measuring device in a plastic tent in which a constantly increased humidity which kept increasing in accordance with the placement of vessels with steaming water. The building scheme of the measuring viscous clutch is presented in **Figure 2**.

During the research, a computer measuring system registered the value of force F depending on the angular velocity ω and leakage current I for various values of electric voltage U applied to the cylinders. Next, the value of the force F was calculated into shear stress τ, and the angular velocity ω into shear rate $\dot{\gamma}$ according to the following equation:

$$\tau = \frac{M}{r_2\,S} = \frac{F\,l}{r_2\,S} \quad [\text{Pa}] \tag{13}$$

$$\dot{\gamma} = \frac{\omega\,r_2}{h} \quad [1/s] \tag{14}$$

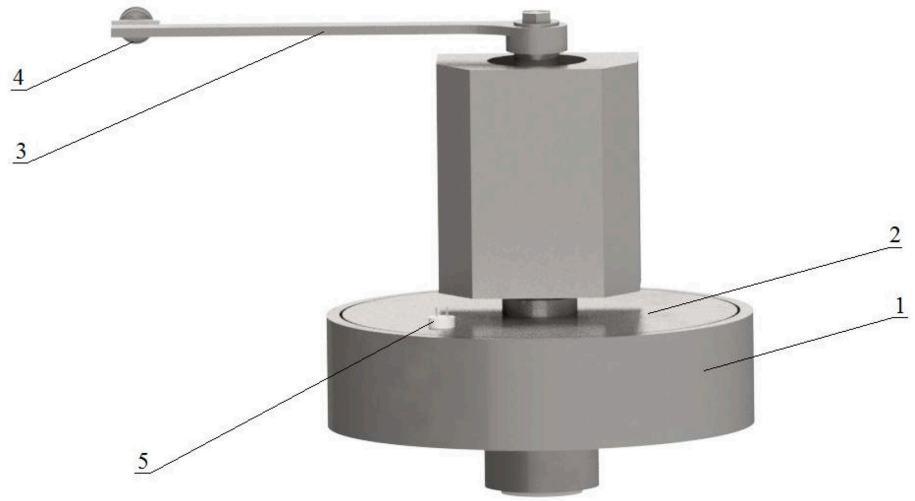

FIGURE 2 | Scheme of the viscous clutch of the measurement device: 1, cylinder set on the motor's shaft; 2, cylinder connected to a lever; 3, lever; 4, force sensor; 5, temperature sensor output.

where r_2 is the radius of the cylinder connected to the lever, h is the size of the gap, M is torque, $S = 2\pi r_2 b$ is shear area, l is the length of the force arm, and b is the height of the cylinder connected to the lever.

However, the electric field intensity was calculated basing on the formula:

$$E = U/h\,[kV/\mathrm{mm}] \tag{15}$$

The values of coefficients a, b, c of the ERF#6 fluid are juxtaposed in **Table 3**.

Value of the coefficient α, present in formulas (4) can be assumed from the scope 100 ÷ 150 W/(m^2 K) (Nakamura et al., 2003). In the optimization calculations it was assumed that $\alpha =$ 120 W/(m^2 K). The maximal value of the centripetal acceleration which can influence the ER fluid without causing degradation due to centrifugal force was assumed to equal 300 rad/s^2 based on a previous publication (Carlson, 1997).

Optimization Results

Table 4 shows juxtaposed results of optimizing calculations of geometric dimensions of the viscous clutch with ER fluid. The results were obtained from minimization of the objective function described by the equation (7) for predefined chosen values of angular velocity ω.

Table 5 shows the results of optimization calculations for the objective function described by equation (8) for different weighting factors w_1, w_2 chosen so that the magnification factor s_k was close to 2. Referential values $T_r = 37$ °C, $(O/M)_r =$ 1290 cm^3/Nm were assumed arbitrarily based on the results shown in **Table 4**.

Figure 3 depicts the results of calculations for objective function described by formula (8) for different weighting factors, received as a result of 2,500 draws.

TABLE 3 | Coefficients a, b, c appearing in mathematical model of ERF#6 fluid.

Coefficient	Units	Scope of the formula
$a_0 = 81.4$	kPa/(kV/mm)^2	
$a_1 = 1 + 2.9\,(T\text{-}20)/100$	–	T from 20 to 50°C
$a_2 = 1$	–	
$a_3 = 1 + 1.05\,(w - 30)/100$	–	w from 30 to 60 %
$b_0 = 0.068$	Pa·s	
$b_1 = 1 - 0.5\,(T - 20)/100$	–	T from 20 to 50°C
$b_2 = 0.011$	Pa·s/(kV/mm)^2	
$c_0 = 1.2$	(μA/cm^2)/(kV/mm)^{1,7}	
$c_1 = 1 + 95$ (T – 20)/100	–	T from 20 to 50°C
$c_2 = 1 + 10\,(w - 30)/100$	–	w from 30 to 60 %
$c_3 = (1 - 0.00014\dot{\gamma})$	–	$\dot{\gamma}$ from 0 to 4000 1/s

TABLE 4 | Calculation results for $T = 20$°C, $U = 2$ kV, $n = 12$, $w = 30\%$.

ω [rad/s]	50	100	150	180	200	250
s_k	6.14	3.39	2.43	2.09	1.93	1.62
T [°C]	35.1	37.2	39.0	39.9	40.1	41.7
O/M [cm^3/N·m]	1,285	1,282	1,287	1,290	1,292	1,304
r_1 [cm]	6.14	3.39	2.43	2.10	1.93	1.62
r_2 [cm]	13.82	7.63	5.47	4.72	4.35	3.64
r_z [cm]	24.58	13.57	9.73	8.39	7.73	6.47
s_z [cm]	15.64	9.17	6.92	6.13	5.74	5.00

Examples of diagrams showing dependence of P/V from radius r for angular velocity $\omega = 100$ rad/s is shown in **Figure 4**.

Figure 5 shows the geometry of the clutch with ER fluid for $s_k = 2$, while **Figure 6**. shows the calculated temperature distribution.

TABLE 5 | Calculation results for $U = 2$ kV, $30 \leq \omega \leq 250$ rad/s, $5 \leq n \leq 13$, $w = 30\%$.

	$w_1 = 0.3\ w_2 = 0.7$	$w_1 = 0.5\ w_2 = 0.5$	$w_1 = 0.7\ w_2 = 0.3$
ω [rad/s]	249	179	93
s_k	2.31	2.00	1.95
T_Z [°C]	62.0	38.4	26.1
O/M [cm^3/N·m]	926	1,339	2,119
N	12	8	12
F_C	$5.05 \cdot 10^{-4}$	$3.48 \cdot 10^{-4}$	$7.12 \cdot 10^{-6}$

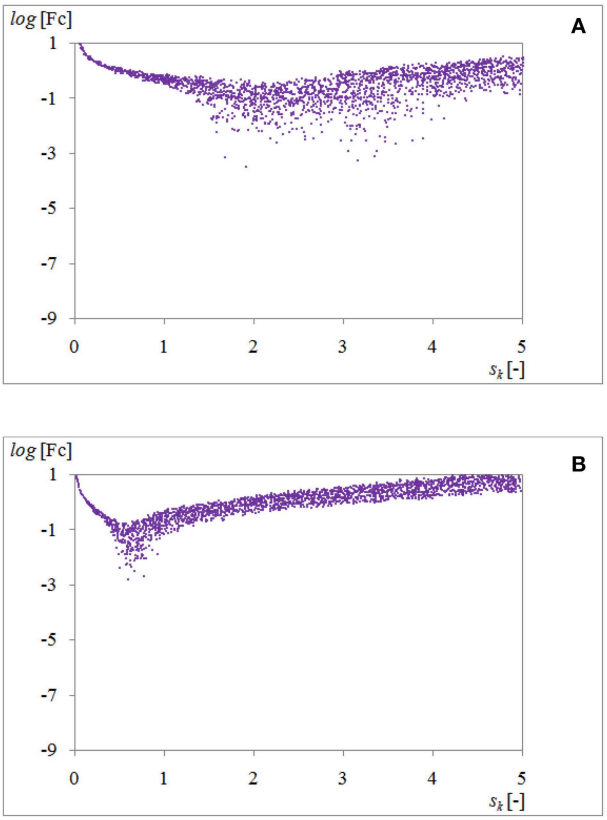

FIGURE 3 | A set of values of the objective function described by the formula (8) for $U = 2$ kV, $30 \leq \omega \leq 250$ rad/s, $5 \leq n \leq 13$, $w = 30\%$ and for: **(A)** $w_1 = 0.3$, $w_2 = 0.7$; **(B)** $w_1 = 0.7$, $w_2 = 0.3$.

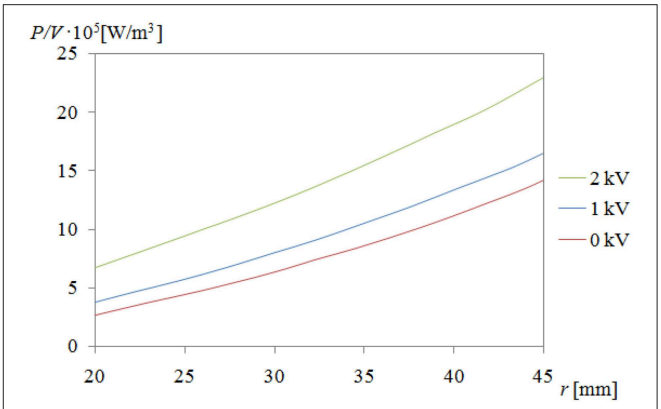

FIGURE 4 | Dependence of P/V from radius r for $\omega = 100$ rad/s and ERF#6 fluid.

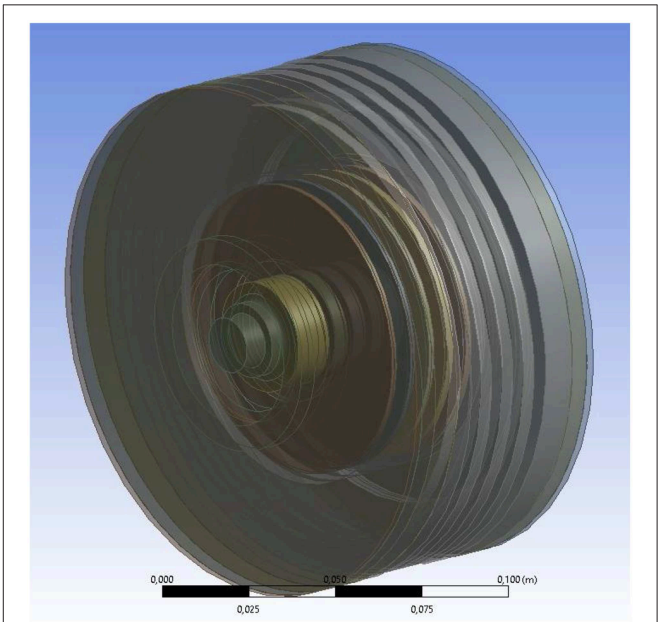

FIGURE 5 | View of the clutch's geometry for $s_k = 2$: brown color, discs; gray color, casing.

Discussion of the Results

As follows from the data in **Table 4**, for the objective function described with equation (7), for similar values of M/O ratio the increase of angular velocity ω of the driven part of the viscous clutch with ER fluid causes a decrease in the magnification factor s_k and an increase in mass temperature T of the clutch. A clutch working at higher angular velocity ω transfers more power P, as shown in the equations (4). On the other hand, the lower value of the magnification factor s_k means that the clutch has smaller dimensions and thus has smaller surfaces to dissipate heat, as can be seen from **Table 1**. Thus, the reason for the increase of the mass temperature T of the clutch with the increase of the angular velocity ω is the operation of the clutch at a higher power and a smaller area of heat dissipation.

By contrast, as follows from the data in **Table 5**, for similar values of the magnification factor s_k (close to 2.0) the clutch works with the larger angular velocity ω, with the smaller weighting factor w_1 determining the share of the temperature ratio T_Z/T_r in the objective function described with equation (8), so wherein the smaller weighting factor w_1 is, the higher the temperature T_Z.

As shown in **Figure 3**, depicting the dependence of the objective function described by the equation (8) on the magnification factor s_k, increasing the weighting factor w_1 from 0.3 to 0.7 causes minimal values of objective function, and therefore optimal solutions exist for smaller values of

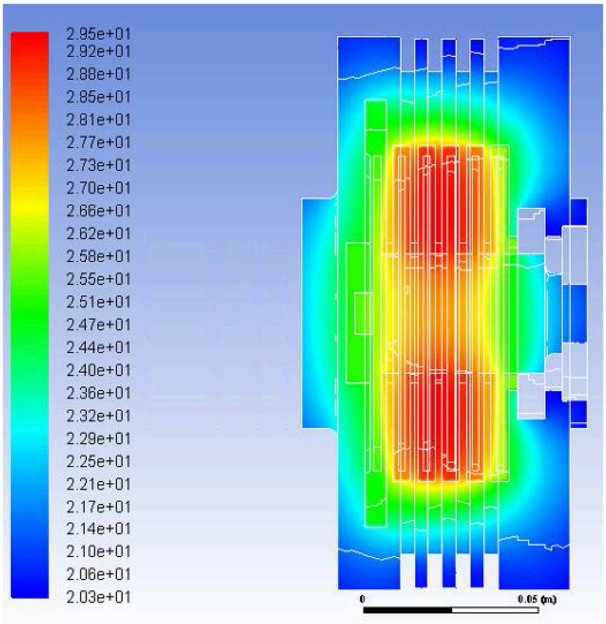

FIGURE 6 | Temperature distribution in °C in the cross-section of the clutch for $s_k = 2$, $\omega = 100$ rad/s, $U = 2$ kV.

magnification factor s_k, that is for smaller dimensions of the clutch with ER fluid.

It results from the conducted research that the most important parameter while optimizing the clutch with ER fluid is power P emitted in the viscous clutch with ER fluid, which is dependent on two values: U and ω. The range of changes in the high voltage U for all clutches with ER fluids is similar and in practice does not exceed values from 0 kV to 3 kV, mainly due to the possible occurrences of electric breakdowns between electrodes which generate electric field. Thus, selection of optimal dimensions of a viscous clutch with ER fluids should be preceded by selecting the value of angular velocity ω.

It was assumed that the clutch with ER fluid in a constructed device which serves to exert controlled force will usually be working in the velocity ω range from 100 rad/s to 180 rad/s. For such a range ω based on the results from the conducted calculations, mainly the results presented in **Tables 4**, **5**, and **Figure 3**, $s_k = 2$ was assumed.

In order to verify the optimization calculations for $s_k = 2$ for the following data: 100 rad/s $\leq \omega \leq$ 180 rad/s and T = 20°C, U = 2 kV, n = 12, w = 30%, calculations were made for the temperature of working fluid ER in a clutch based on both objective functions. For the objective function described by the equation (7), the received temperature was T = 28.3°C, and for the objective function described by the equation (8) and for $w_1 = 0.5$, $w_2 = 0.5$ the received temperature was $T_Z = 32.1$°C. The temperatures T and T_Z differ from the ER fluid's temperature of 29.5°C shown in **Figure 6** by no more than 6%, which indicates that the assumptions were correct.

CHOICE OF MATERIALS AND CONSTRUCTION OF A PROTOTYPE OF A VISCOUS CLUTCH WITH ER FLUID

Constructional Solution of the Clutch

After determining the dimension of the viscous clutch with ER fluid for $s_k = 2$, based on **Table 1**, a prototype was built. It was assumed that the clutch would work vertically, and the bearings would be placed on one side of the clutch, as presented in **Figure 7**.

Such a constructional solution is beneficial because of the sealing. Between the discs, spacer rings were used, and exchanging them enables changes in the width of the working gap. The "+" pole of the high voltage power supply was connected to the clutch's shaft by a brush and sliding ring, while the pole "–" was connected to the clutch's casing. In order to isolate the driving part from the driven part, the outer ring of the bearings fixed on the shaft were placed in the sleeves made of a material which is an excellent electrical insulator. To decrease the costs of producing the clutch, the discs were fixed with screws instead of typically used splines. In order to increase the thermal capacity and to facilitate dissipating the heat from the clutch's working gaps, the casing walls were made to be much thicker than would be necessary to ensure sufficient mechanical strength and rigidity.

Materials Used

Due to good electrical and thermal conductivity, most of the parts of the clutch's prototype were built with metal. Clutch discs were made of austenitic stainless steel with designation 304 according to the ASTM/AISI standard. The 304 stainless steel has approximately 19% chromium and 10% nickel as its major alloying additions and is resistant to corrosion while maintaining its strength at high temperatures. The starting material for the production of the clutch's discs was a cold-rolled sheet with a smooth surface. The discs were cut out of the sheet using abrasive water jet machining. Then, the discs were polished. Grinding of this material is not advised due to the fact that it is too soft for this process. The casing and shaft of the clutch were made by machining from steel designed as 403 by ASTM/AISI standards. The 403 stainless steel has 11% chromium and 1% manganese. A higher carbon content means that the 403 stainless steel has higher strength and higher wear resistance compared to the 304 stainless steel.

Isolating sleeves of the bearings and flexible coupling of the clutch's shaft with the motor shaft were made with a material called Poliamid (PA6). The sealing ring was 3D-printed with a material called ABS (Akrylonitrylo-Butadieno-Styren) (Kotlinski et al., 2013).

TESTS ON THE CLUTCH WITH ER FLUID

Building the Test Rig

The test rig used for the purpose of testing the prototypical clutch consisted of a controlled electric motor on whose shaft a driving part of the clutch with ER fluid was installed. The driven part was connected to the lever pressing on the force sensor. The accuracy

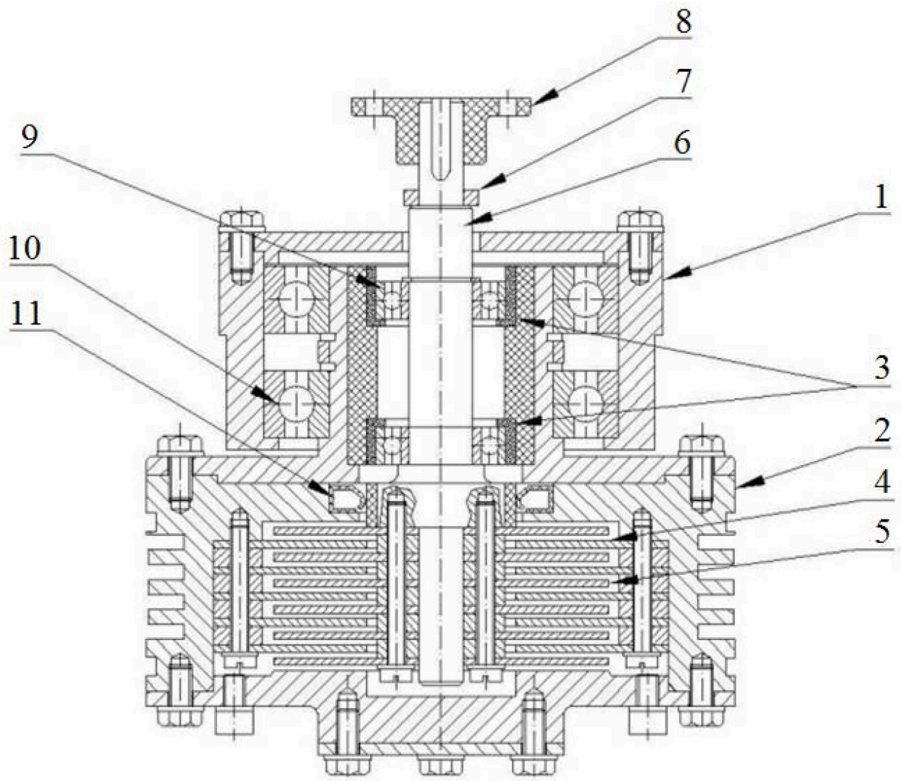

FIGURE 7 | Design solution of a prototype of the clutch: 1, bearings casing; 2, clutch casing; 3, insulating sleeves for shaft bearings; 4, discs fixed to the casing; 5, discs placed on the shaft; 6, shaft; 7, sliding ring; 8, flexible coupling; 9, shaft's bearing; 10, clutch's bearing; 11, sealing ring.

of the force sensor position relative to the lever was 0.1 mm, which resulted in an error of $< 0.1\%$.

The value of electric voltage was applied from the high voltage power supply, whose poles were connected interchangeably with discs of the prototypical clutch. The power supply also enabled the measurement of leakage current. In the casing of the viscous clutch with ER fluid, a thermometer was installed to enable measurements of ER fluid's temperature. Measurement of the relative air humidity was realized with a humidity transducer set in close proximity of the clutch. Angular velocity was read with the aid of an encoder of the electric motor. Accuracies of measuring devices used in the test rig are listed in **Table 6**. All measured values were recorded over time based on a computer measurement system. The scheme of the test rig is presented in **Figure 8**.

TABLE 6 | Accuracy of measuring devices.

Force sensor	**0.02 N**
Thermometer	0.1°C
Humidity transducer	2%
Encoder	0.3 degrees

Workplace Tests

The characteristics of the viscous clutch with the ER fluid as $\tau = f(\dot{\gamma})$ were determined based on formulas (13) and (14) for the read values of force F depending on the angular velocity ω for chosen constant values of electric voltage U, **Figure 9**. The measurements were performed in a constant temperature of the fluid and constant relative humidity w. In comparison, **Figure 9**. shows additionally characteristics $\tau = f(\dot{\gamma})$ made with a measurement device whose scheme can be seen in **Figure 2**.

As can be seen from the charts presented in **Figure 9**, differences between lines concerning measurement device and lines concerning the clutch with ER fluid are not large, even if there are substantial differences in dimensions and shape of working gaps. The average relative error was 12%. It is also essential to notice that the range of changes in shear stress τ caused by changing the voltage U from 0 to 2.5 kV is 30% larger than the range of changes in shear stress τ caused by changes in angular velocity ω.

Durability tests of the prototype clutch with ER fluid have shown that insulating material needs to be carefully selected, and so do materials for sliding ring and brush. Initially the insulating material was Tekstolit (TcF-1), characterized by a large electrical resistance and good machinability. To simplify the clutch's construction, a copper brush cooperating directly with the shaft was also used. However, during the tests it turned out that due to moisture deposited on the sleeve, exposed to high voltages, the material was partially charred on the surface,

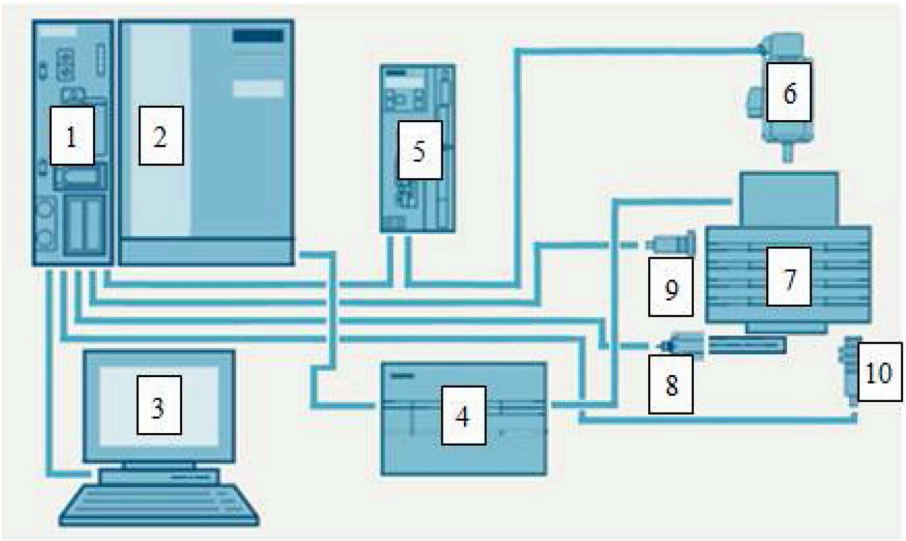

FIGURE 8 | Scheme of the test rig: 1, PLC; 2, input/output cards; 3, computer set with software; 4, high voltage power supply; 5, servo drive controller; 6, servo drive; 7, tested clutch with ER fluid; 8, force sensor; 9, humidity sensor; 10, temperature sensor.

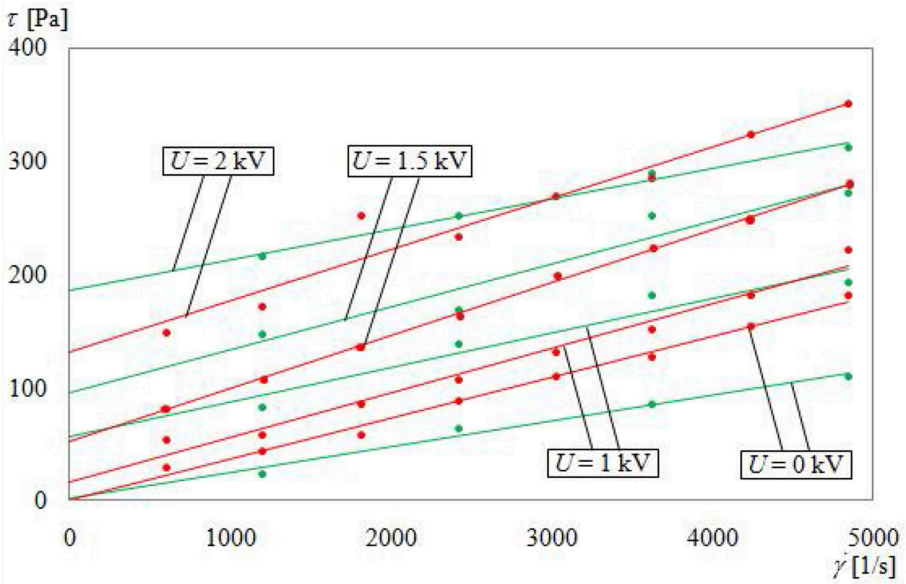

FIGURE 9 | Dependence of τ from $\dot{\gamma}$ for $T = 20\ ^{\circ}C$ and $w = 30\%$: green color, measurement devices; red color, viscous clutch with ER fluid.

and the conductive paths created this way largely decreased the insulating properties. After replacing Tekstolit (TcF-1) with Poliamid (PA6) material, there was no decrease in insulating properties. The tests have also shown that using the copper brush in cooperation directly with the shaft is the cause of electrical breakdowns occurring under a relatively low voltage, around 1.5 kV, due to the fact that the products of wear were getting inside the clutch with the ER fluid. To prevent this, the sliding ring was made of bronze and the brush was made of graphite, due to its good lubricating properties. After this change there were no occurrences of electrical breakdowns caused by products of wear.

Recommendations for the Selection of Materials

While choosing an ER fluid to use in a controlled clutch, one needs to select a fluid whose shear stress τ insignificantly depends on the shear rate $\dot{\gamma}$. As was shown in previous research (Nakamura et al., 2002, 2004), the larger the dependence, the more problematic the control of the device using the ER fluid is. The requirement is best met by heterogeneous ER fluids whose solid phase is chemically clean starch. The disadvantage of this type of fluid is a large sensitivity to humidity and low durability. While choosing the ER fluid to control viscous clutch, a factor

that needs to be taken into consideration is also the fact that the torque M, transmitted by the clutch, is the sum of two components, the first of which depends on $\mu_p \cdot \omega$ with the second depending on τ_0, being the function of voltage U. If the clutch is to be controlled by shifting the voltage U, the fluid that is chosen needs to have the largest τ_0/μ_0 ratio, while for a clutch controlled by changes in angular velocity ω needs to have the smallest possible τ_0/μ_0 ratio.

While choosing the materials for insulating elements for the viscous clutch with ER fluid, attention must be paid to their insulating strength, low thermal expansion ensuring shape stability when exposed to high temperature, good chemical resistance to oils, large mechanical durability and good machinability. It needs to be taken into consideration that plastics are good electrical insulators as well as thermal insulators. Using insulating materials hinders dissipation of the heat generated as a result of mutual friction of the particles, the friction between the particles and walls of the working gap, and electrical current in the ER fluid. When determining the thickness of the walls of the insulating elements, one needs to take into consideration the fact that the thicker the wall, the lesser the possibility of electrical breakdowns. However, this renders the heat dissipation conditions worse. Currently, a great facilitation is the possibility to create insulating elements of complicated shapes with 3D printing methods due to the fact that most plastics used in this technology have good insulating properties.

Using metal materials is connected to the possibility of corrosion of the metal parts of the clutch, especially the ones working in an increased temperature, whose products conducting electricity after getting into the ER fluids can cause an increase in leakage current and occurrences of electrical breakdowns. It is expedient to use metals and alloys resistant to corrosion. In the case of occurrences of frictional contacts of the clutch's elements, it is important to take notice of the fact that the wear products can hinder correct operation of the clutch.

CONCLUSIONS

Controlling force F by means of the clutch with the ER fluid can be realized by altering the angular velocity of the motor and by changing the high voltage of the electric current applied to the discs, because both the increase in the angular velocity and the increase in the electrical voltage cause an increase in shear stress in the ER fluids and an increase in the torque transmission to the lever. However, controlling by changes in voltage is faster and enables a control range that is 30% larger. The introduced way of controlling the force can be practically used, as it allows a fluent change of the force from zero to maximal value.

The designed mathematical models, although simple, are precise enough to be used for optimization of the construction of the clutch with ER fluid. Differences between the test results of the clutch with ER fluids and measurement device reach 12% on average, but they can be rendered acceptable due to significant differences in the dimensions and shapes of working gaps. It can be acknowledged that the test results gained with the aid of measurement devices can be used for designing clutches with ER fluid.

The assumed optimization methods for the dimensions of viscous clutch with ER fluids, consisting of a random proportional enlargement of the model clutch turned out to be useful for designing the viscous clutch with ER fluid. It is important to emphasize that the optimization conducted this way, by using two different objective functions, provided very similar results.

Due to the complex construction of the viscous clutch with ER fluids, it is vital to use construction materials with conducting properties as well as materials with insulating properties. However, not all materials with these abilities can be used in clutches with ER fluid. The introduced guidelines can be useful while choosing materials for construction of a viscous clutch with ER fluids. As shown by the conducted works, in practice it is vital to support the choice of materials by durability tests of the prototypical clutches.

Based on the results of the conducted tests it can be presumed that further works aiming to expand usage of viscous clutches with ER fluids in machines and devices need to focus especially not only on the optimal shape of the clutches with ER fluids, but also on proper choice of ER fluids as well as other construction materials.

AUTHOR CONTRIBUTIONS

AK and ZK contributed conception and design of the study. GM and JZ conducted optimization analysis. PM performed ANSYS calculations. AK, ZK, KO, and AO carried out tests. ZK, AO, and KO wrote the first draft of the manuscript. S-BC contributed to manuscript revision, read and approved the submitted version.

FUNDING

This research had received funding from the Polish-Taiwanese/Taiwanese-Polish Joint Research Project no. PBWLA/2016/019.

REFERENCES

Assadsangabi, B., Daneshmand, F., Vahdati, N., Eghtesad, M., and Bazargan-Lari, Y. (2011). Optimization and design of disk-type MR brakes. *Int. J. Auto. Tech-Kor.* 12, 921–932. doi: 10.1007/s12239-011-0105-x

Avraam, M., Horodinca, M., Romanescu, I., and Preumont, A. (2010). Computer controlled rotational MR-brake for wrist rehabilitation device. *J. Intel. Mat. Syst. Struct.* 21, 1543–1557. doi: 10.1177/1045389X10362274

Bocińska, M., Wyciślik, H., Osuchowski, M., and Płocharski, J. (2002). Influence of surfactans on properties of electrorheological fluids containing polyaniline. *Int. J. Mod. Phys. B.* 16, 2461–2467. doi: 10.1142/S0217979202012517

Böse, H., Gerlach, T., and Ehrlich, J. (2013). Magnetorheological torque transmission devices with permanent magnets. *J. Phys. Conf. Ser.* 412:012050. doi: 10.1088/1742-6596/412/1/012050

Bucchi, M. F., Forte, P., and Frendo, F. (2017). Geometry optimization of a magnetorheological clutch operated by coils. *P. I. Mech. Eng. LJ Mat.* 231, 100–112. doi: 10.1177/1464420716665650

Carlson, J. D. (1997). "Magnetorheological fluid actuators" in *Adaptronics and Smart Structures*, ed H. Janocha (Berlin; Heidelberg: Springer Verlag), 184–204.

Chen, S., Huang, J., Jian, K., and Ding, J. (2015). Analysis of influence of temperature on magnetorheological fluid and transmission performance. *Adv. Mater. Sci. Eng.* 2015, 1–7. doi: 10.1155/2015/583076

Choi, Y. T., and Wereley, N. M. (2015). Drop-induced shock mitigation using adaptive magnetorheological energy absorbers in corporating a time lag. *J. Vib. Acoust*. 137:7. doi: 10.1115/1.4028747

Conrad, H. (1993). Electrorheological fluids: characteristics, structure and mechanisms. *ASME Fluids Eng. Div. Electrorheol. Flows* 164, 99–113.

Erol, O., and Gurocak, H. (2011). Interactive design optimization of magnetorheological brake actuators using the Taguchi method. *Smart Mater. Struct.* 20:105027. doi: 10.1088/0964-1726/20/10/105027

Fernández, M. A., and Chang, J. Y. (2016). "Development of magnetorheological fluid clutch for robotic arm applications," in *IEEE 14th International Workshop on Advanced Motion Control*.

Fertman, V. E. (1990). *Magnetic Fluids Guidebook: Properties and Applications*. New York, NY; Washington, DC; Philadelphia, PA; London: Taylor and Francis Inc.

Gao, F., Liu, Y. N., and Liao, W. H. (2017). Optimal design of a magnetorheological damper used in smart prosthetic knees. *Smart Mater. Struct.* 26:035034. doi: 10.1088/1361-665X/aa5494

Horvath, P., and Torőcsik, D. (2011). Optimization of a disc-type magneto-rheological clutch. *Sci. Proc. Faculty Mech. Eng. STU Bratislava* 19, 106–111. doi: 10.2478/v10228-011-0018-8

Jing, Z., Sun, S., Ouyang, Y., Zhang, S., Li, W., and Zheng, J. (2018). Design and modeling analysis of a changeable stiffness robotic leg working with magnetorheological technology. *J. Intel. Mat. Syst. Struct.* 29, 3725–3736. doi: 10.1177/1045389X18798958

Kavlicoglu, B., Gordaninejad, F., Evrensel, C. A., Cobanogulu, N., Xin, M., Fuchs, A., et al. (2002). A high-torque magneto-rheological fluid clutch. *Proc. SPIE Conference Smart Mater. Struct.* 4697:472674. doi: 10.1117/12.472674

Kim, K. S., Choi, S. B., and Cho, M. S. (2002). Vibration control of a vire cut discharge machine using ER brake acuator. *J. Intel. Mat. Syst. Struct.* 13, 316–322. doi: 10.1177/1045389X02013010002

Kim, W. H., Park, J. H., Kim, G. W., Shin, C. S., and Choi, S. B. (2017). Durability investigation on torque control of a magnetorheological brake: experimental work. *Smart Mater. Struct.* 26:037001. doi: 10.1088/1361-665X/aa59d8

Kotlinski, J., Migus, M., Kesy, Z., Kesy, A., Hugo, P., Deez, B., et al. (2013). Fabrication of hydrodynamic torque converter impellers by using the selective laser sintering method. *Rapid Prototyping J.* 19, 430–436. doi: 10.1108/RPJ-04-2011-0043

Kumbhar, B. K., Patil, S. R., and Sawant, S. M. (2015). Synthesis and characterization of magneto-rheological (MR) fluids for MR brake application. *Eng. Sci. Technol. Int J.* 18, 432–438. doi: 10.1016/j.jestch.2015.03.002

Lara-Prieto, V., Parkin, R., Jackson, M., Silberschmidt, V., and Kęsy, Z. (2010). Experimental study of adaptive MR cantilever sandwich beams for vibration control applications. *Smart Mater. Struct.* 19:015005. doi: 10.1088/0964-1726/19/1/015005

Li, Y., Li, J., Li, W., and Samali, B. (2013). Development and characterization of a magnetorheological elastomer based adaptive seismic isolator. *Smart Mater. Struct.* 22:035005. doi: 10.1088/0964-1726/22/3/035005

Liu, B., Li, W. H., Kosasih, P. B., and Zhang, X. Z. (2006). Development of an MR-brake-based haptic device. *Smart Mater. Struct.* 15:1960. doi: 10.1088/0964-1726/15/6/052

Madeja, J., Kesy, Z., and Kesy, A. (2011). Application of electrorheological fluid in a hydrodynamic clutch. *Smart Mater. Struct.* 20:105005. doi: 10.1088/0964-1726/20/10/105005

Mangal, S. K., Munjal, K., and Sharma, V. (2016). On-state torque optimization for synthesized MR fluid. *Int. J. Eng. Res. Appl.* 6, 9–14(Pt 5). Available online at: www.ijera.com

Mikkelsen, A., Wojciechowski, J., Rajnak, M., Juraj Kurimsky, J., Khobaib, K., Kertmen, A., et al. (2017). Electric field-driven assembly of sulfonated polystyrene microspheres. *Materials* 10, 1–17. doi: 10.3390/ma10040329

Milecki, A., Sedziak, D., and Ortmann, J. (2005). Controllability of MR shock absorber for vehicles. *Int. J. Vehicle Des.* 38, 222–233. doi: 10.1504/IJVD.2005.007294

Nakamura, T., Saga, N., and Nakazawa, M. (2002). Impedance control of a single shaft-type clutch using homogeneous electrorheological fluid. *J. Intel. Mat. Syst. Struct.* 13, 465–469. doi: 10.1106/104538902029068

Nakamura, T., Saga, N., and Nakazawa, M. (2003). Thermal effects of a homogeneus ER fluid device. *J. Intel. Mat. Syst. Struct.* 14, 87–91. doi: 10.1142/9789812777546_0037

Nakamura, T., Saga, N., and Nakazawa, M. (2004). Variable viscous control of a homogeneous ER fluid device considering its dynamic characteristics. *Mechatronics* 14, 55–68. doi: 10.1016/S0957-4158(02)00095-8

Nguyen, Q. H., and Choi, S. B. (2010). Optimal design of an automotive magnetorheological brake considering geometric dimensions and zero-field friction heat. *Smart Mater. Struct.* 19:115024. doi: 10.1088/0964-1726/19/11/115024

Olszak, A., Osowski, K., Kęsy, A., and Kęsy, Z. (2016a). Experimental researches of hydraulic clutches with smart fluids. *Int. Rev. Mech. Eng.* 10, 364–372. doi: 10.15866/ireme.v10i6.8421

Olszak, A., Osowski, K., Kesy, Z., and Kesy, A. (2018). Investigation of hydrodynamic clutch with MR fluid. *J. Intel. Mat. Syst. Struct.* 30, 155–168. doi: 10.1177/1045389X18803463

Olszak, A., Ziabska, E., Osowski, K., Kęsy, A., and Kęsy, Z. (2016b). Durability of hydraulic clutches filled with electrorheological fluids. *Tech. Trans. Mech.* 113, 87–101. doi: 10.4467/2353737XCT.16.288.6120

Papadopoulos, C. A. (1998). Brakes and clutches using ER fluids. *Mechatronics* 8, 719–726.

Park, E. J., Falcao Da Luz, L., and Suleman, A. (2008). Multidisciplinary design optimization of an automotive magnetorheological brake design. *Comput. Struct.* 86, 207–216. doi: 10.1016/j.compstruc.2007.01.035

Park, E. J., Stoikov, D., Falcao da Luz, L., and Suleman, A. (2006). A performance evaluation of an automotive magnetorheological brake design with a sliding mode controller. *Mechatronics* 16, 405–416. doi: 10.1016/j.mechatronics.2006.03.004

Płocharski, J., Drabik, H., Wyciślik, H., and Ciach, T. (1997). Electrorheological properties of polyphenylene suspensions. *Synthet. Metals* 88, 139–145.

Raju, A., Md Meftahul, F., and Yancheng, L. (2016). Advancement in energy harvesting magneto-rheological fluid damper: a review. *Korea-Australia Rheol. J.* 28, 355–379. doi: 10.1007/s13367-016-0035-2

Saito, T., and Ikeda, H. (2007). Development of normally closed type of magnetorheological clutch and its application to safe torque control system of human-collaborative robot. *J. Intel. Mat. Syst. Struct.* 18, 1181–1185. doi: 10.1177/1045389X07084755

Sapiński, B., Rosół, M., and Węgrzynowski, M. (2016). Evaluation of an energy harvesting mr damper-based vibration reduction system. *J. Theor. App. Mech-Pol.* 54, 333–344. doi: 10.15632/jtam-pl.54.2.333

Sarkar, C., and Hirani, H. (2013). Synthesis and characterization of antifriction magnetorheological fluids for brake. *Defence Sci. J.* 63, 408–412. doi: 10.14429/dsj.63.2633

Smith, A. L., Ulicny, J. C., and Kennedy, L. C. (2007). Magnetorheological fluid fan drive for trucks. *J. Intel. Mat. Syst. Struct.* 18, 1131–1136. doi: 10.1177/1045389X07083136

Sohn, J. W., Gang, H. G., and Choi, S. B. (2018). An experimental study on torque characteristics of magnetorheological brake with modified magnetic core shape. *Adv. Mech. Eng.* 10, 1–8. doi: 10.1177/1687814017752222

Sohn, J. W., Jeon, J., Nguyen, Q. H., and Choi, S. B. (2015). Optimal design of disc-type magnetorheological brake for mid-sized motorcycle: experimental evaluation. *Smart Mater. Struct.* 24:085009. doi: 10.1088/0964-1726/24/8/085009

Song, W., Wang, S., Choi, S. B., Wang, N., and Xiu, S. (2018). Thermal and tribological characteristics of a disc-type magnetorheological brake

operated by the shear mode. *J. Intel. Mat. Syst. Struct.* 30, 722–733. doi: 10.1177/1045389X18770740

Takesue, N., Furushoa, J., and Inoue, A. (2003). Influence of electrode configuration and liquid crystalline polymer type on electrorheological effect. *J. App. Phys.* 94, 5367–5373. doi: 10.1063/1.1605811

Weiss, D. (1993). "High strength magneto and electro-rheological fluids," in *SAE Technical Paper, International Off-Highway & Powerplant Congress & Exposition* (Milwaukee, WI), 932451. doi: 10.4271/932451

Ziabska, E., Duchowski, J., Olszak, A., Osowski, K., Kęsy, A., Kęsy, Z., et al. (2017). Wear forms of heterogeneous electro-rheologicalfluids working in a hydraulic clutch system. *Smart Mater. Struct.* 26:095032. doi: 10.1088/1361-665X/aa78dc

Conflict of Interest Statement: The authors declare that the research was conducted in the absence of any commercial or financial relationships that could be construed as a potential conflict of interest.

frontiers in Materials

ORIGINAL RESEARCH
published: 12 June 2019
doi: 10.3389/fmats.2019.00125

Material Characterization of MR Fluid on Performance of MRF Based Brake

Nguyen Vien Quoc[1], Le Duy Tuan[1], Le Dai Hiep[2], Hung Nguyen Quoc[2] and Seung Bok Choi[3]**

[1] Industrial University of Ho Chi Minh City, Ho Chi Minh City, Vietnam, [2] Faculty of Engineering, Vietnamese-German University, Binh Duong, Vietnam, [3] Department of Mechanical Engineering, Inha University, Incheon, South Korea

This study focuses on material characterizations of Magneto-rheological fluid (MRF) on performance characteristics of magneto-rheological brake (MRB). In this study, three different types of MRF (low viscosity, medium viscosity, and high viscosity) are considered for several types of MRB. Firstly, the optimization solution of the MRB design is proposed based on the Bingham plastic model of the MRFs and finite element analysis of MRB magnetic circuit. From optimal design of the MRBs with different MRFs, performance characteristics of the MRBs such as braking torque, off-state torque, and power consumption are evaluated. In addition, the compact size of MRB using different MRFs is also studied. Finally, some observations and guidance on selection of MRFs in MRB design are summarized.

Keywords: magneto-rheological fluid (MRF), conventional MR brake, material characterization, optimal design, side-coil MR brake

OPEN ACCESS

Edited by:
Weijia Wen,
Hong Kong University of Science and Technology, Hong Kong

Reviewed by:
Xiaomin Dong,
Chongqing University, China
Xufeng Dong,
Dalian University of Technology (DUT), China

***Correspondence:**
Hung Nguyen Quoc
hung.nq@vgu.edu.vn
Seung Bok Choi
seungbok@inha.ac.kr

Specialty section:
This article was submitted to Smart Materials, a section of the journal Frontiers in Materials

Received: *01 November 2018*
Accepted: *14 May 2019*
Published: *12 June 2019*

Citation:
Quoc NV, Tuan LD, Hiep LD, Quoc HN and Choi SB (2019) Material Characterization of MR Fluid on Performance of MRF Based Brake. Front. Mater. 6:125. doi: 10.3389/fmats.2019.00125

INTRODUCTION

In last two decades, researches on the development and application of brake featuring magneto-rheological fluid (MRF) have interested many researchers. There have been numerous researches on improving performance of MRF based brake (MRB) with different configurations ad applications such as: disc-type MRB (An and Kwon, 2003; Liu et al., 2006; Park et al., 2006), drum-type MRBs (Huang et al., 2002; Smith et al., 2007), hybrid-type MRB with T-shaped rotor (Avraam et al., 2008; Nguyen and Choi, 2012; Mousavi and Sayyaadi, 2018). Avraam et al performed some analyses and comparisons of different types of MRB such as disc-type, drum type, and T-shape type in development of a rotational MRB for rehabilitation devices (Avraam et al., 2010). Inmaduddin et al. reviewed advances in MRBs, in terms of various innovations of structural and magnetic circuit designs, including disc-type, drum-type, and hybrid type as well as modeling techniques that have been involved with each innovation (Imaduddin et al., 2013). In order to have a more detailed comparison of different types of MRB, Nguyen and Choi (2011) investigated the optimal design of different types of MRB considering their maximum braking torque and specific volume. Later, Nguyen et al. (2014a) evaluated the effect of different shapes of envelope such as the rectangular, the polygonal and the spline to the performance and the mass of MRBs. Recently, Nguyen et al. (2014b, 2015) proposed a new configuration of MRB in which a magnetic coil is wound on each side of the housing of the MRB (in this research, it is named as side-coil MRB). The results showed that, with this configuration, some disadvantages of the traditional MRBs such as the "bottle-neck" problem of magnetic flux, the non-magnetic bobbin requirement, difficulties in manufacturing and maintenance can be eliminated or minimized. In addition, the optimal solutions showed that the mass of the side-coil MRB was significantly improved in producing the same braking torque as the conventional ones.

In the design of MRB, different types of MRF have been used. However, how the characterization of MRF's effects on the performance of MRB was not considered in detail. In order to fill this gap, this research investigates the effects of MRF characterizations on the performance of MRB through simulation results, from which guidelines on the selection of MRF types for MRBs are summarized. The remainder of the paper is arranged as follows. In section Conventional and Side-Coil MRBs, several configurations of MRB considered in this study are introduced. After that, in section Optimization of MRBs Based on Finite Element Analysis, the optimization solution of the MRB design is proposed based on the Bingham plastic model of the MRFs and finite element analysis of MRB magnetic circuit. In section Results and Discussions, optimal solutions of the MRBs with different MRFs are obtained, from which, performance characteristics of the MRBs such as braking torque, off-state torque, and power consumption are evaluated. Finally, some observations and guidance on selection of MRFs in MRB design are summarized.

CONVENTIONAL AND SIDE-COIL MRBs

As mentioned above, several types of MRB have been developed so far. In this study, two of the most typical types of MRB, the conventional disc-type MRB and the side-coil MRB, are considered. **Figure 1A** shows a typical conventional MRB and **Figure 1B** presents the side-coil one.

The first configuration represents conventional MRBs which use outside cylindrical coils such as disc-type, drum-type, while the second configuration represent for the MRBs which use side coils including T-shape MRBs. As shown in the figure, a disc (rotor) made of magnetic steel is fastened to the flange of the MRB shaft made of non-magnetic steel. The disc is embedded inside a stationary envelope (housing) made of magnetic steel. In **Figure 1A**, a wire-coil is wound on a non-magnetic bobbin which is fixed to the brake envelop while in **Figure 1B**, the coil is placed on each side housing of the brake. By using the side-coil configuration, it is observed that the coils can be placed directly on the housing. In addition, multiple coils can be implemented, especially for high braking torque MRBs.

It is obviously observed that the braking torque of the proposed MR brake comes from two sources: the friction of MRF acting on the two end-faces and on the outer annular face of the disc. Firstly, the friction between MRF and the end-faces of the disc is analyzed. The induced torque from MRF in radial duct acting on one end-face of a disc can be expressed as follows (Nguyen and Choi, 2012):

$$T_e = \int_A \tau_e r dA = 2\pi \int_{R_1}^{R_2} \tau_e r^2 dr \tag{1}$$

where A is the area of the end-face of the disc, r is the radius of an infinitesimal area of the disc, R_1 and R_2 are the inner and outer radius of the duct. τ_e is the shear stress of the MRF at the interface, which can be predicted from the Bingham-plastic model of the MRF as follows:

$$\tau_e = \tau_{ye} + \mu_e \dot{\gamma}_e \tag{2}$$

where, τ_{ye} and μ_e are, respectively, the yield stress and post yield viscosity of the MRF. $\dot{\gamma}_e$ is the shear rate of MR fluid at the interface. Because the gap size of the duct is very small, the shear rate of MRF in the gap is assumed to be linearly distributed which can be approximately determined as follows:

$$\dot{\gamma}_e = \frac{r\Omega}{d} \tag{3}$$

where d is the gap size and Ω is the angular velocity of the drum.

Plug Equations (2, 3) into Equation (1) the following equation can be obtained.

$$T_e = 2\pi \int_{R_1}^{R_2} r^2 \mu_e \left(\frac{r\Omega}{d}\right) dr + 2\pi \int_{R_1}^{R_2} r^2 \tau_{ye} dr \tag{4}$$

Generally, the magnetic density in the MRF gap is a function of radius r, thus the values of τ_{ye} and μ_e of the MRF in the gap are also functions of r. Equation (4) then have to be calculated by numerically integrating. In order to facilitate the calculation, it is assumed that the magnetic density in the MRF gap is constant and an average value of the magnetic density obtained from numerical integration is used. In this case, Equation (4) can be analytically integrated to yield

$$T_e = \frac{\pi \mu_e R_2^4}{2d}\left[1 - \left(\frac{R_1}{R_2}\right)^4\right]\Omega + \frac{2\pi\tau_{ye}}{3}(R_2^3 - R_1^3) \tag{5}$$

The torque due to MRF in annular gap acting on the outer circular face of the disc can be determined by

$$T_a = \int_{A_a} R_a \tau_a dA = \int_0^{L_a} R_a \tau_a 2\pi R_a dl = 2\pi R_a^2 \int_0^{L_a} (\tau_{ya} + \mu_a \dot{\gamma}) dl \tag{6}$$

where A_a is the area of the outer annular face of the disc, L_a and R_a are radius and length of annular duct, τ_a is the shear stress at the annular face of the disc, τ_{ya} and μ_a are the yield stress and post yield viscosity of the MRF in the annular duct. Similarly to MRF in the end-face gap, by using average magnetic density obtained from numerical integration and assuming a linear distribution of shear rate in the MRF gap, the following can be obtained

$$T_a = 2\pi R_a^2 L_a (\tau_{ya} + \mu_a \frac{R_a \Omega}{d}) \tag{7}$$

From Equations (5) to (7), by neglecting friction torque from sealing and bearing, the induced braking torque of the

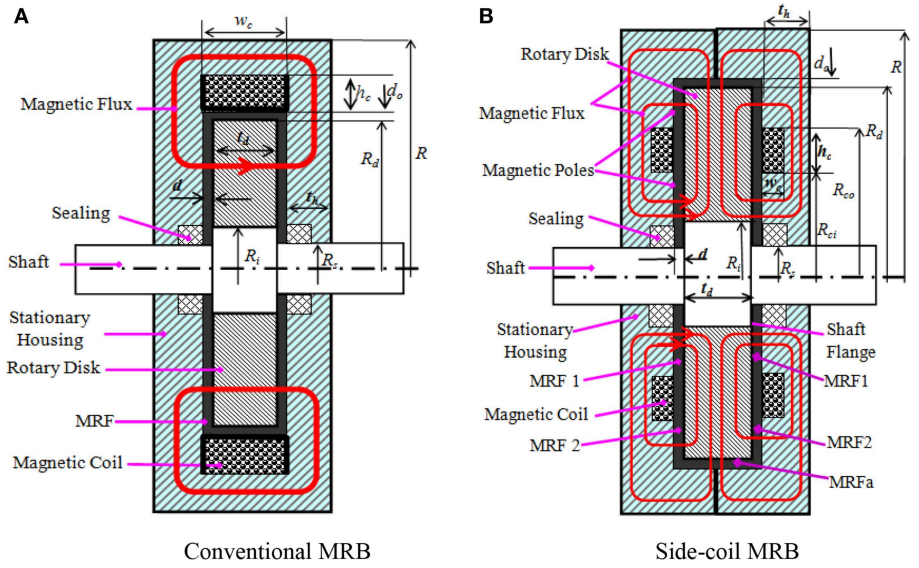

FIGURE 1 | Configurations of the conventional and the side-coil MRBs. **(A)** Conventional MRB. **(B)** Side-coil MRB.

conventional disc-type MRB and the side-coil ones can be correspondingly obtained

$$T_c = 2T_e + T_a = \frac{\pi \mu_e R_d^4}{d}[1 - (\frac{R_i}{R_d})^4]\Omega + \frac{4\pi \tau_{ye}}{3}(R_d^3 - R_i^3) + 2\pi R_d^2 t_d(\tau_{y0} + \mu_0 \frac{\Omega R_d}{d_o}) \quad (8)$$

$$T_s = 2(T_{e1} + T_{e2}) + T_a = \frac{\pi \mu_1 R_{ci}^4}{d}[1 - (\frac{R_i}{R_{ci}})^4]\Omega + \frac{4\pi \tau_{y1}}{3}(R_{ci}^3 - R_i^3) + \frac{\pi \mu_2 R_d^4}{d}[1 - (\frac{R_{co}}{R_d})^4]\Omega + \frac{4\pi \tau_{y2}}{3}(R_d^3 - R_{co}^3) + 2\pi R_d^2 t_d(\tau_{ya} + \mu_a \frac{\Omega R_d}{d_o}) \quad (9)$$

and the off-state force (the torque of the MRB when no magnetic field is applied to MRF) of both considered MRBs can be expressed as Nguyen et al. (2015).

$$T_0 = \frac{\pi \mu_0 R_d^4}{d}[1 - (\frac{R_s}{R_d})^4]\Omega + \frac{4\pi \tau_{y0}}{3}(R_d^3 - R_s^3) + 2\pi R_d^2 t_d(\tau_{y0} + \mu_0 \frac{\Omega R_d}{d_o}) + 2T_{sf} \quad (10)$$

where T_c is the braking torque of the conventional MRB, T_s is the braking torque of the side coil MRB, T_0 is the off-state torque of MRBs, T_{e1} and T_{e2} are the friction torque of MRF in region 1 (MRF1) and MRF in region 2 (MRF2) acting on the disc in case of the side coil MRB, R_d is the outer radius of the disc, R_i is the inner radius of the active MRF volume in the end-face duct, R_s is the shaft diameter, d is the gap size of the end-face MRF ducts between the disc and the housing, d_o is the gap size of the annular MRF duct at the outer cylindrical face of the disc, t_d is the thickness of the disc, R_{ci} and R_{co} are the inner and outer radii of the coil in the case of the side-coil MRB, Ω is the angular velocity of the rotor, μ_e and τ_{ye} are, respectively, the average post yield viscosity and yield stress of MRF in the end-face duct of the conventional MRB, μ_j is the average post yield viscosity of the j^{th} active MRF volume (denoted by MRFj) in the end-face duct of the side-coil MRBs while τ_{yj} is the corresponding yield stress, μ_a and τ_{ya} are, respectively, the average post yield viscosity and yield stress of MRF in the annular duct of the side-coil MRBs, τ_{y0} and μ_0 are the zero-field yield stress and viscosity of the MRF. The rheological properties of MRF such as the induced yield stress τ_{ye}, τ_{yj}, τ_{ya}, and the corresponding average post yield viscosity μ_e, μ_j, μ_a depend on the exerted magnetic flux density across the active MRF volumes and can be approximated by Zubieta et al. (2009).

$$Y = Y_\infty + (Y_0 - Y_\infty)(2e^{-B\alpha_{SY}} - e^{-2B\alpha_{SY}}) \quad (11)$$

where Y represents for a rheological parameters of MRF such as the yield stress and the post yield viscosity, Y_0 and Y_∞, respectively, represents for the value of Y in the absence of magnetic field and in saturated state of MRF, α_{SY} is the saturation moment index of the Y parameter, B is the applied magnetic density.

OPTIMIZATION OF MRBS BASED ON FINITE ELEMENT ANALYSIS

In this part, the optimal design problem of the conventional and the side-coil MRBs is constructed. In the design of MRBs, a required braking torque is usually given depending on the application. Therefore, the purpose of the MRB design is to determine geometric dimensions of the brake so that the brake can create a required braking torque while the mass of the brake

is as small as possible. In addition, the power consumption of the coils and the off-state torque are also important issues should be accounted for. The power consumption should be as small as possible to save energy and to accommodate with available power for each application. The off-state torque should be small to reduce the energy lost and also to reduce the heating problem. In this study, an objective function, which is a linear combination of the above issues, is proposed, which is mathematically expressed as the following:

$$Obj = \alpha_m \frac{m_b}{m_{ref}} + \alpha_p \frac{P}{P_{ref}} + \alpha_{To} \frac{T_0}{T_{0ref}} \quad (12)$$

In the above, m_b, P, and T_0 are, respectively, the mass, the power consumption and the off-state torque of the brake, m_{ref}, $P_{ref,}$ and T_{0ref} are, respectively, the reference mass, the power consumption and the off-state torque, and α_m, $\alpha_{P,}$ and α_{To} are the corresponding weighting coefficients determined based on the importance of the objectives. In this research, the reference values are obtained from the optimization problem in which the objective function is the mass of the MRB, Nguyen et al. (2014a, 2015). Generally, the MRB mass can be approximately calculated by Nguyen et al. (2015).

$$m_b = V_d\rho_d + V_h\rho_h + V_s\rho_s + V_{MR}\rho_{MR} + V_{bob}\rho_{bob} + V_c\rho_c \quad (13)$$

where V_d, V_h, V_s, V_{MR}, $V_{bob,}$and V_c are, respectively, the geometric volume of the disc, the housing, the shaft, the MRF, the bobbin and the coil of the brake, ρ_d, ρ_h, ρ_s, $\rho_{MR,}$ $\rho_{bob,}$ and ρ_c are correspondingly density of the discs, the housing, the shaft, the MRF, the bobbin in case of conventional MRB (in case of the side-coil MRBs, this term is eliminated) and the coil material.

Power consumption of the MRBs can be calculated by

$$P = I^2 R_w \quad (14)$$

where I is the electric current applied to the coils and R_w is the resistance of the coil wires, which can be approximately calculated as follows:

$$R_w = L_w r_w = 2\pi R_c N_c \frac{r}{A_w} = 2\pi R_c \varepsilon \frac{A_c}{A_w}\frac{r}{A_w} = \frac{2R_c \varepsilon w_c h_c r}{\pi d_w^2} \quad (15)$$

$$R_w = 2L_w r_w = 4\pi R_c N_c \frac{r}{A_w} = 4\pi R_c \varepsilon \frac{A_c}{A_w}\frac{r}{A_w} = \frac{4R_c \varepsilon w_c h_c r}{\pi d_w^2} \quad (16)$$

In the above, L_w is the length of the coil wire, r_w is the resistance per unit length of the coil wire, N_c is the number of coil turns, R_c is the average radius of the coil cross-sectional area, A_w is the cross sectional area of the wire, A_c is the cross sectional area of the coil, ε is the filling ratio of the coil which is assumed to be 0.8 in this study, r is the resistivity of the coil wire, $r = 0.017\,26\ (\Omega m)$ for copper wire.

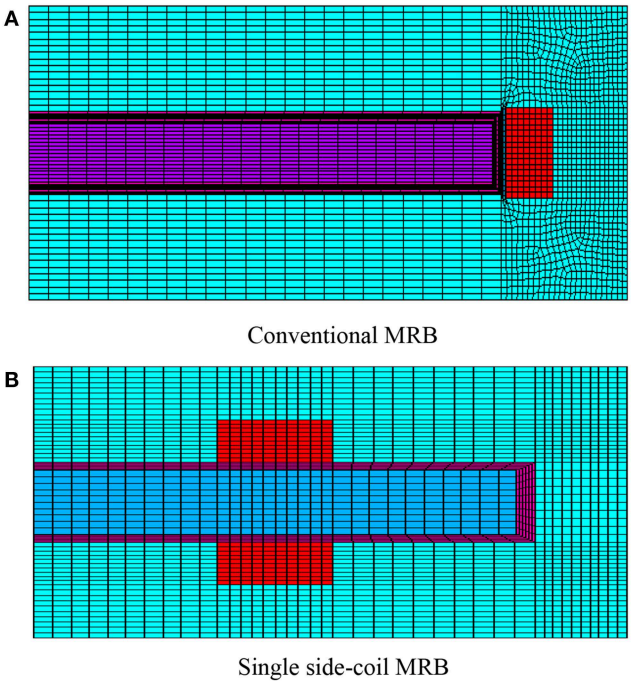

FIGURE 2 | Finite element models to analyze the magnetic circuit of the MRBs. **(A)** Conventional MRB. **(B)** Single side-coil MRB.

In order to determine the braking torque of the MRBs, firstly, finite element analysis (FEA) is used to evaluate the magnetic density across the ducts of MRF based on quasi-static analysis. This is reasonable because the purpose of this research is to investigate the effect of MRF on performance characteristics of MRB and this can be archived by quasi-static simulation. In detail, the finite element models generated by 2D-axisymmetric couple element (PLANE 13) of commercial ANSYS software, as shown in **Figure 2**, are applied to solve the magnetic circuits of the MRB. It is noted in **Figure 2** that the mesh size is specified by the number of elements per line rather than element size and the number of elements on the lines across the MR duct is specified as a parameter called the basic meshing number. The number of elements of other lines is chosen as a product of the basic meshing number and an appropriate scalar. It is well-known that the smaller the mesh size, the better the result is obtained. However, the small mesh size results in a high computational cost. When mesh size is reduced to a certain value, the convergence of solution is expected. In this study, the basic meshing number of 8 elements is sufficient to ensure the convergence of the FE solution.

From the FE solution of the magnetic circuit, the induced MRF rheological properties in the ducts such as the yield stress (τ_{ye}, τ_{yj}, $\tau_{ya,}$) and the post yield viscosity (μ_e, μ_{ej}, μ_a) are calculated by Equation (11) via the average induced magnetic density and its initial rheological parameters. From the obtained values of all abovementioned parameters, the on-state of each MRB can be then estimated by Equations (8, 9). From geometric dimensions, the off-state torque can be calculated by Equation

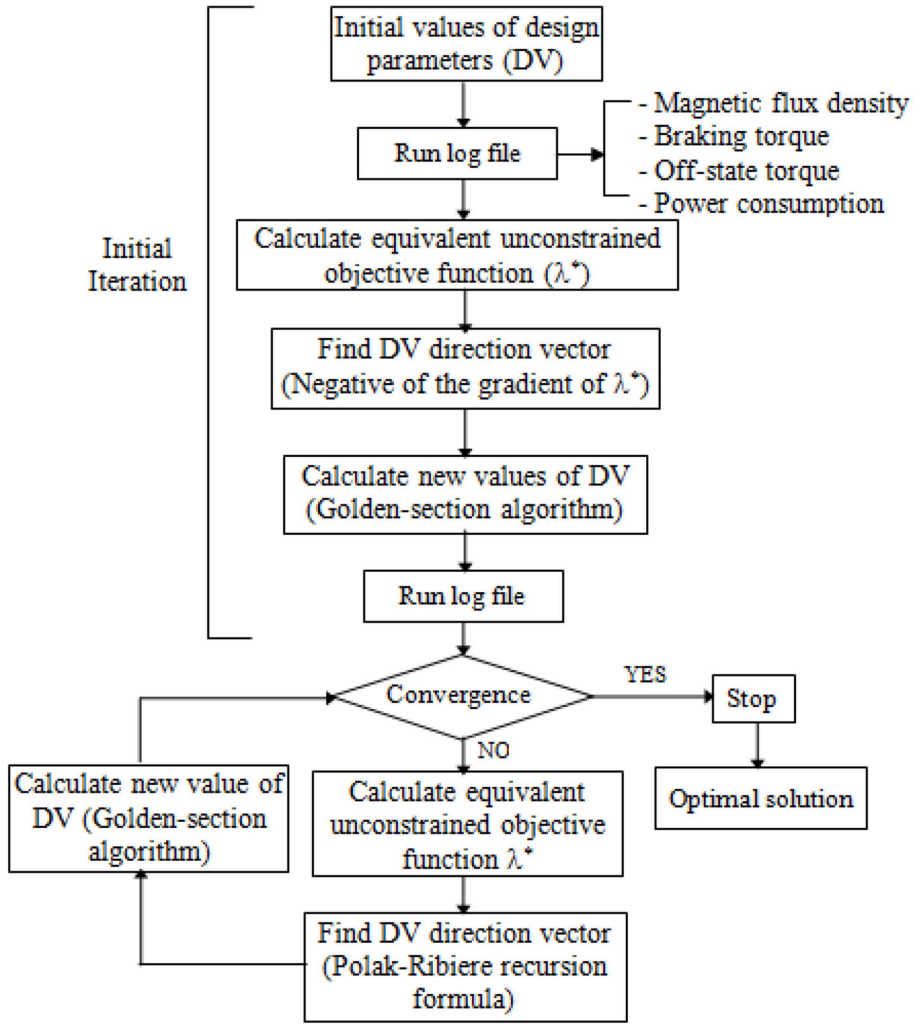

FIGURE 3 | Flow chart for optimal design using FEM.

(10) while the mass and the power consumption of the MRBs can be determined from Equations (13, 14), respectively. It is noted that these performance parameters are updated in each optimization loop. In this research, the optimization procedure is conducted by using the first order optimization method with the gradient decent algorithm. The procedures to achieve optimal design parameters of the MRBs using the first order method of ANSYS optimization tool is shown in **Figure 3**. Starting with initial value of design variables, by executing the ANSYS log-file, performance characteristics of the MRBs at the first iteration are calculated. The ANSYS optimization tool then transforms the constrained optimization problem to an unconstrained one via penalty functions. For the initial iteration, the search direction of DVs is assumed to be the negative of the gradient of the unconstrained objective function. In the subsequent iterations, the direction vectors are calculated according to Polak-Ribiere recursion formula. A detailed description of this algorithm integrated with ANSYS software is shown in previous research (Nguyen et al., 2007).

RESULTS AND DISCUSSIONS

In this section, the optimal results of the MRBs are obtained with different types of MRF and discussions on the effects of MRF types on performance parameters of the MRBs are presented. **Table 1** shows the materials selections for components of MRBs. As shown in the table, the commercial silicon steel is used for magnetic components of the MRB such as the housing and the disc, the bobbin is made of non-magnetic steel, the coil is made from copper wire sized as 24-gage (diameter = 0.511 mm) whose maximum working current is around 3 A and during the optimization process an applied current of 2.5 A is used. Three types of commercial MR fluid made by Lord Corporation: MRF-122-2ED (low yield stress), MRF-132-DG (medium yield stress) and MRF-140 CG (high yield stress) are considered. Parameters of the field dependent Bingham rheological model of the MRF are determined from experimental results using curve fitting method as shown in **Figure 5**. In this research work, a least square

TABLE 1 | Magnetic property of the brake components.

Brake components	Material	Relative permeability	Saturation flux density
Disc, Housing	Silicon Steel	B-H Curve (**Figure 4A**)	1.55 *Tesla*
Coil	Copper (24-gage)	1	X
MR Fluid	MRF-122-2ED MRF-132-DG MRF-140-CG	B-H curve (**Figure 4B**)	1.5 *Tesla* 1.65 *Tesla* 1.75 *Tesla*
Bobbin, Shaft	Non-magnetic Steel	1	X

curve fitting method is used, and the results are presented in **Table 2** (Nguyen and Choi, 2010).

In the optimization, the design variables are significant geometric dimensions of the MRBs such as the coil height h_c, the coil width w_c, the inner radius of the disc R_i, the outer radius of the disc R_d, the disc thickness t_d, outer radius of the brake R, the housing thickness t_h, the inner radius of the coils in case of the side-coil MRBs $R_{c,}$ and the gap size of the MRF ducts are also considered as design variables. It is noted that the shaft radius is set by R_s= 8 mm in the optimization.

Figures 6–**11** show optimal solutions of the MRB when the mass is considered as the objective function at different values of the constrained braking torque, ranging from 5 to 100 Nm. It is noted that this case is equivalent to the case when the weighting coefficients in the objective function in Equation (12) are chosen at α_m=1.0, α_P =α_{To} =0. The smaller value of the MRF gap size in the higher braking torque can be archived and the smaller mass of the MRB is. Therefore, during the optimization process, the MRF gap size is not considered as a design variable and fixed at a certain value. In these figures, three typical values of the gap size, which are 0.6, 0.8, and 1.0 mm, are considered. In **Figures 6**, **7**, the gap size is set by 0.6 mm. It is observed from the figure that when we consider only the mass of the MRBs in the optimization, MRBs employing the highest yield stress MRF have the smallest mass and power consumption at all values of the constrained braking torque. However, the off-state torque of the MRB with highest yield stress is significantly greater than the others. Therefore, if the brake normally works in off-state condition, this issue should be taken into account. It also observed from the figures that among the three MRFs, the medium yield stress MRF (MRF 132-DG) is the most compromised of the three mentioned performance parameters, the mass, the power consumption and the off-state force. The off-state torque in the case of MRB with MRF 132-DG is even smaller than the MRB with low yield stress MRF (MRF-122-2ED). The reason is that the MRB employing MRF-122-2ED has a larger disc radius to produce enough braking torque, which also results in corresponding higher off-state torque. By comparison at different values of the MRF gap size, it is observed that the smaller the gap size, the smaller the mass of the MRBs that can be archived, and the lower the power consumed by the coils. However, the off-state torque of the MRBs increases as the MRF gap size decreases and this should be taken into account especially when the MRBs work continuously such as in automotive application.

Figures 12, **13** show optimal solutions of the MRBs, when the weighting coefficients of the objective function in Equation (12) are chosen at α_m=α_P =α_{To} =1/3, at different values of the constrained braking torque ranging from 5 to 100 Nm. This means that the importance of the three performance parameters (the mass, the power consumption and the off-state torque) are assumed equal. It is noted that in this case the gap size of MRF is also considered as a design variable, ranging from 0.6 to 1.0 mm. The results show that by considering all three issues (multi-objective optimization) in the optimization, a compromised optimal result can be archived. By comparing **Figures 12**, **13** with the previous figures (**Figures 6**–**11**), it is observed that in case of multi-objective optimization, the mass of the MRBs is a bit greater than that in case of mass optimization; however the power consumption and off-state torque are significantly smaller. Again, the same comments can be obtained by considering different types of MRF from **Figures 12**, **13**, which mean that the medium yield stress MRF (MRF 132-DG) is the most compromised among the three considered MRFs. The gap size of MRBs at the optimum is equal to its lower limit, which is 0.6 mm.

Figures 14, **15** show optimal solutions of the MRBs, when the weighting coefficients of the objective function in Equation (12) are chosen at α_m= α_P = 0.5 and α_{To} = 0, which means that the importance of the mass and the power consumption are assumed equal while the off-state torque is not considered. The results show that the mass of the MRBs is a bit smaller than that in **Figures 12**, **13** and the power consumption of the MRBs is significantly reduced, especially for the MRBs employing MRF 132-DG, while the off-state of the MRBs are slightly increased. From **Figures 14**, **15**, again it is observed that the medium yield stress MRF (MRF 132-DG) is the most compromised among the three considered MRFs. The gap size of MRBs at the optimum is equal to its lower limit in this case, as well.

Figures 16, **17** show optimal solutions of the MRBs, when the weighting coefficients of the objective function in Equation (12) are chosen at α_m= 0.5, α_P = 0.0 and α_{To} = 0.5, which means that the importance of the mass and the off-state torque are assumed equal while the power consumption is not considered. The results show that the mass of the MRBs is almost the same as that in **Figures 14**, **15**. This is because the weighting coefficient is the same in both cases. However, the power consumption is much higher than that of the previous case, although the off-state torque is smaller. Similar to **Figures 14**, **15**, the medium yield stress MRF (MRF 132-DG) is the most compromised among the three considered MRFs. Again, the gap size of MRBs at the optimum is equal to its lower limit.

Figures 18, **19** show optimal solutions of the MRBs, when the weighting coefficients of the objective function in Equation (12) are chosen at α_m= 0.75, α_P = 0.0 (power consumption is not considered) and α_{To} = 0.25. By comparing with **Figures 16**, **17** it is observed that the mass of the MRBs is a bit smaller in this case while the off-state torque is a bit higher. However, the power consumption is much smaller than the previous case. Therefore, if the optimization considers only mass and off-state torque, it is recommended that the weighting coefficients should be set by

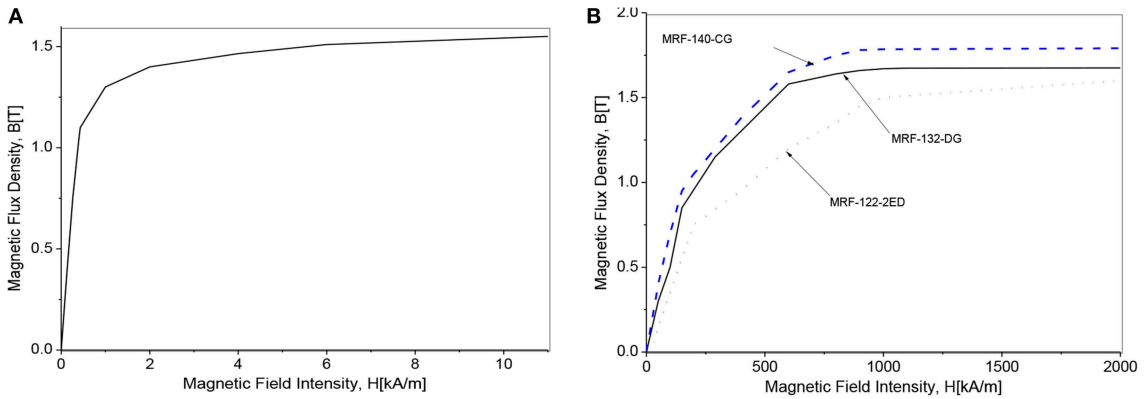

FIGURE 4 | Magnetic properties of silicon steel and MR fluids. **(A)** B-H curve of silicon steel. **(B)** B-H curve of MR Fluid.

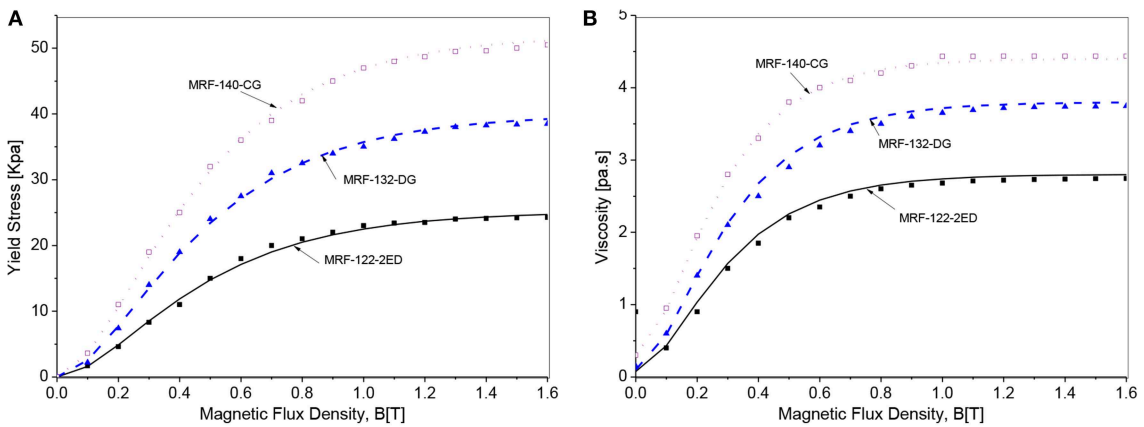

FIGURE 5 | Rheological properties of MR fluids. **(A)** Field dependent yield stress. **(B)** Field dependent post-yield viscosity.

TABLE 2 | Rheological properties of MR fluids.

MR fluid	Bingham model
MRF-122-2ED	$\mu_0 = 0.075pa \bullet s$; $\mu_\infty = 2.8pa \bullet s$; $\alpha_{s\mu} = 4.5T^{-1}$ $\tau_{y0} = 12pa$; $\tau_{y\infty} = 25200pa$; $\alpha_{st_y} = 2.9T^{-1}$
MRF-132DG	$\mu_0 = 0.1pa \bullet s$; $\mu_\infty = 3.8pa \bullet s$; $\alpha_{s\mu} = 4.5T^{-1}$ $\tau_{y0} = 15pa$; $\tau_{y\infty} = 40000pa$; $\alpha_{st_y} = 2.9T^{-1}$
MRF-140CG	$\mu_0 = 0.29pa \bullet s$; $\mu_\infty = 4.4pa \bullet s$; $\alpha_{s\mu} = 5T^{-1}$ $\tau_{y0} = 25pa$; $\tau_{y\infty} = 52000pa$; $\alpha_{st_y} = 3T^{-1}$

α_m= 0.75, α_P = 0.0, and α_{To} = 0.25 rather than α_m= 0.5, α_P = 0.0, and α_{To} = 0.5. The gap size of MRBs at the optimum is also equal to its lower limit.

From all of the above, it can be summarized as the following:

- An objective function which is a linear combination of the mass, the power consumption and the off-state torque can be used for multi-objective optimization of MRBs. By assigning different values of weighting coefficients in the objective function, different optimal solutions can be archived. To get the most compromised of the three objective performances, a real multiobjective algorithm to get Pareto front solution should be implemented.
- In the optimization, it is not necessary to consider the gap size of the MRF as a design variable. In most cases, the gap size of MRF should be selected to be as small as possible considering manufacturing convenience.
- At the optimum, the MRBs employing the highest yield stress MRF (MRF-140CG) always have the smallest mass and power consumption, however, the off-state torque is significantly larger than the others. Therefore, in case the off-state torque is not important for the brake, highest yield stress MRF (MRF-140CG) is recommended for MRB application.
- At the optimum, the MRBs employing the lowest yield stress MRF (MRF-122-2ED) have the largest mass and power consumption, while the off-state torque is larger than that in case of medium yield stress MRF (MRF132-DG). Therefore, lowest yield stress MRF (MRF-122-2ED) is not recommended for MRB application
- At the optimum, the MRBs employing the medium yield stress MRF (MRF-132DG) have the compromised performance when the off-state torque is considered in the objective

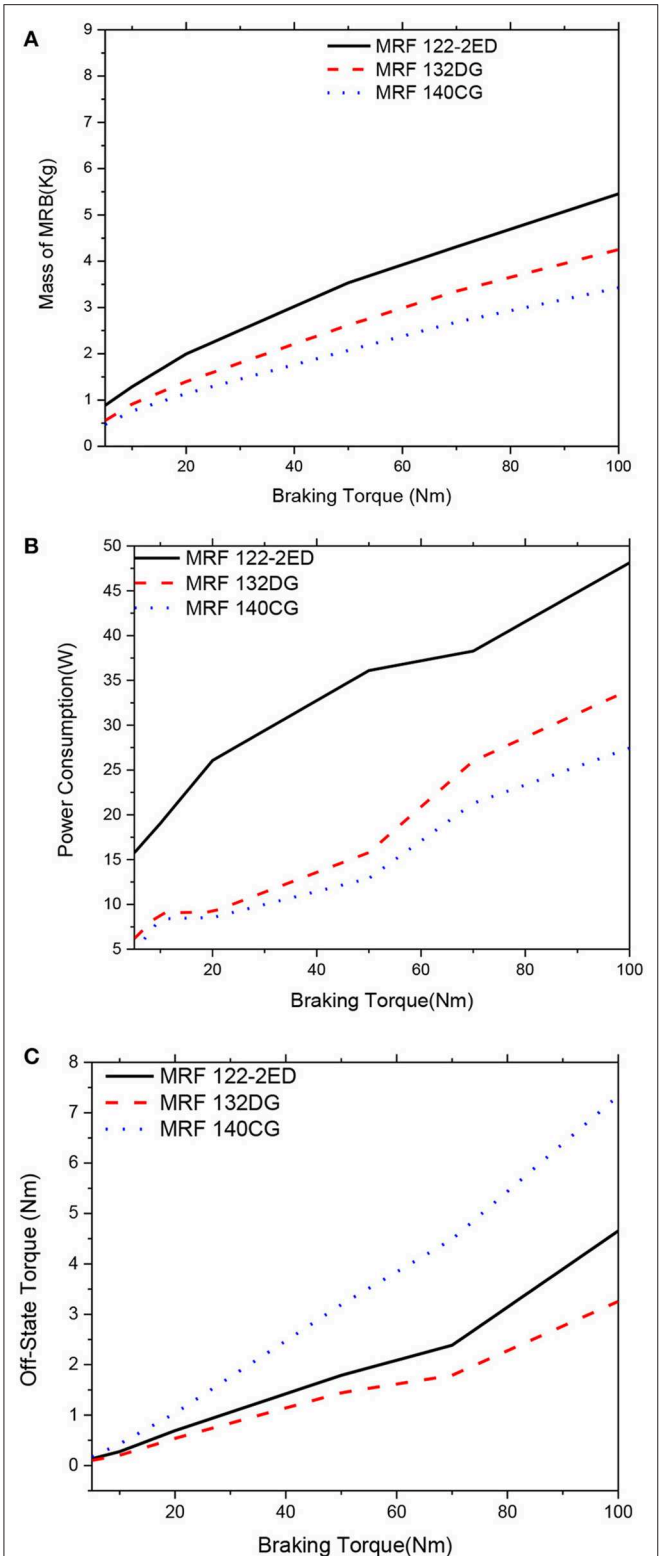

FIGURE 6 | Mass optimization results of the MRBs as a function of braking torque of conventional MRB, $d = 0.6$ mm. **(A)** Mass as a function of braking torque, **(B)** Power consumption as a function of braking torque, **(C)** Off-state torque as a function of braking torque.

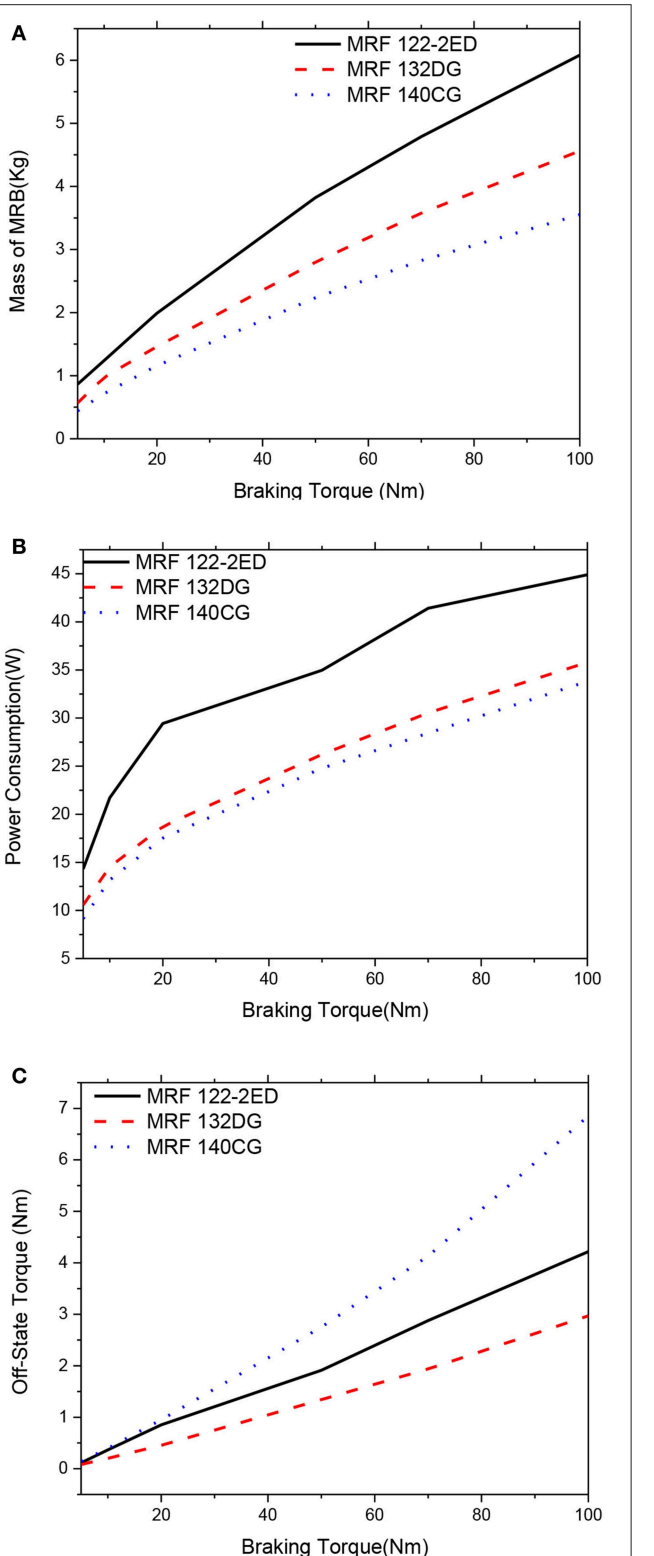

FIGURE 7 | Mass optimization results of the MRBs as a function of braking torque of side-coil MRB, $d = 0.6$ mm. **(A)** Mass as a function of braking torque, **(B)** Power consumption as a function of braking torque, **(C)** Off-state torque as a function of braking torque.

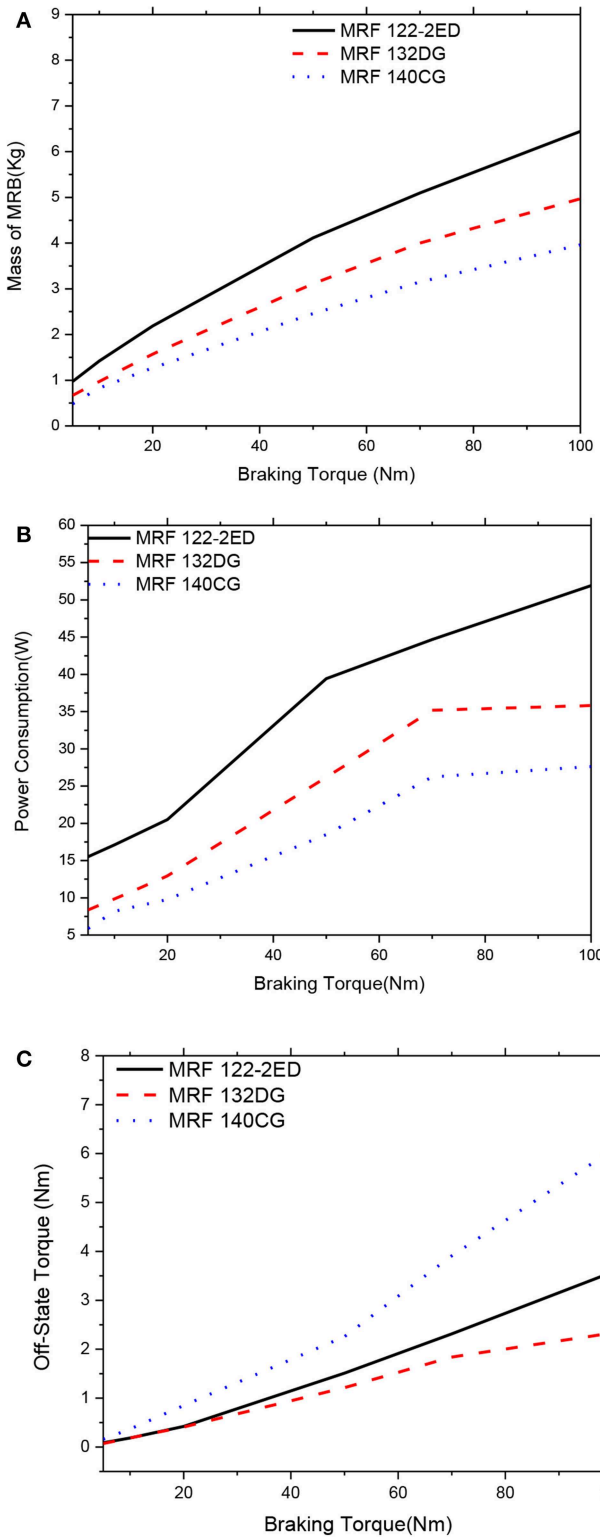

FIGURE 8 | Mass optimization results of the MRBs as a function of braking torque of conventional MRB, $d = 0.8$ mm. **(A)** Mass as a function of braking torque, **(B)** Power consumption as a function of braking torque, **(C)** Off-state torque as a function of braking torque.

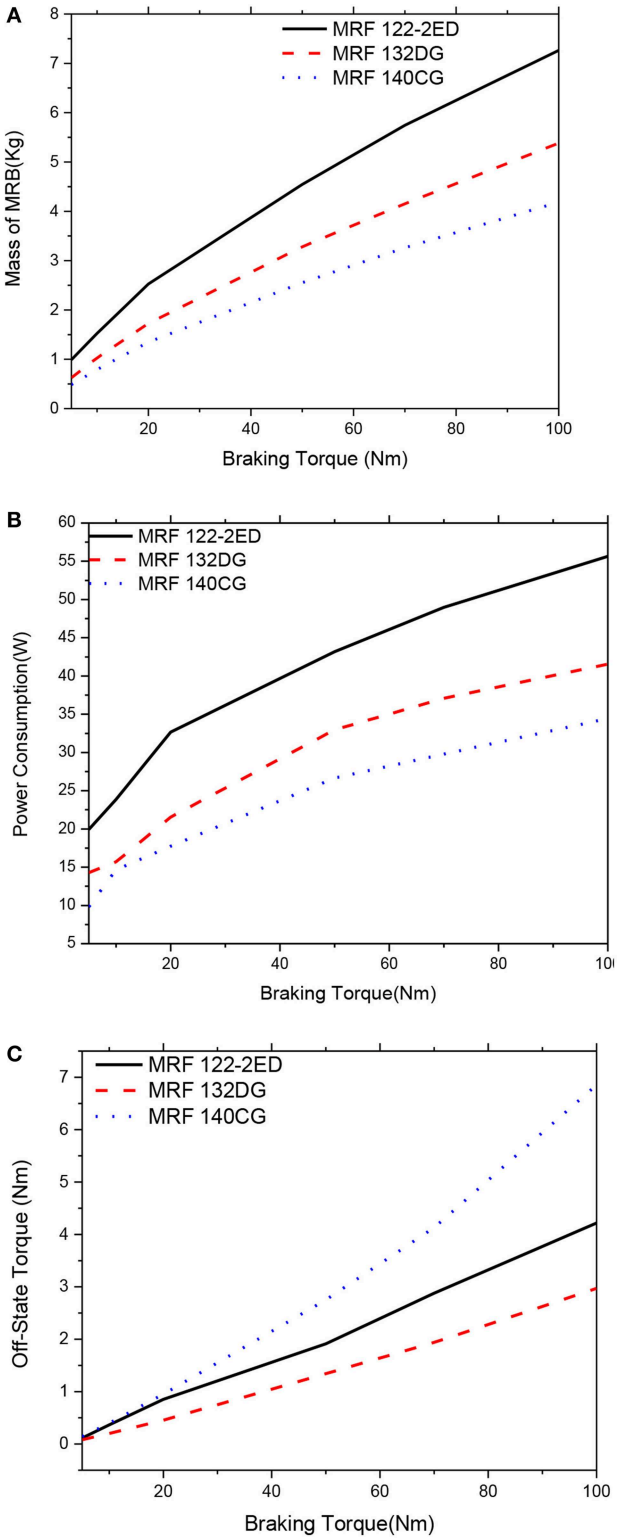

FIGURE 9 | Mass optimization results of the MRBs as a function of braking torque of side-coil MRB, $d = 0.8$ mm. **(A)** Mass as a function of braking torque, **(B)** Power consumption as a function of braking torque, **(C)** Off-state torque as a function of braking torque.

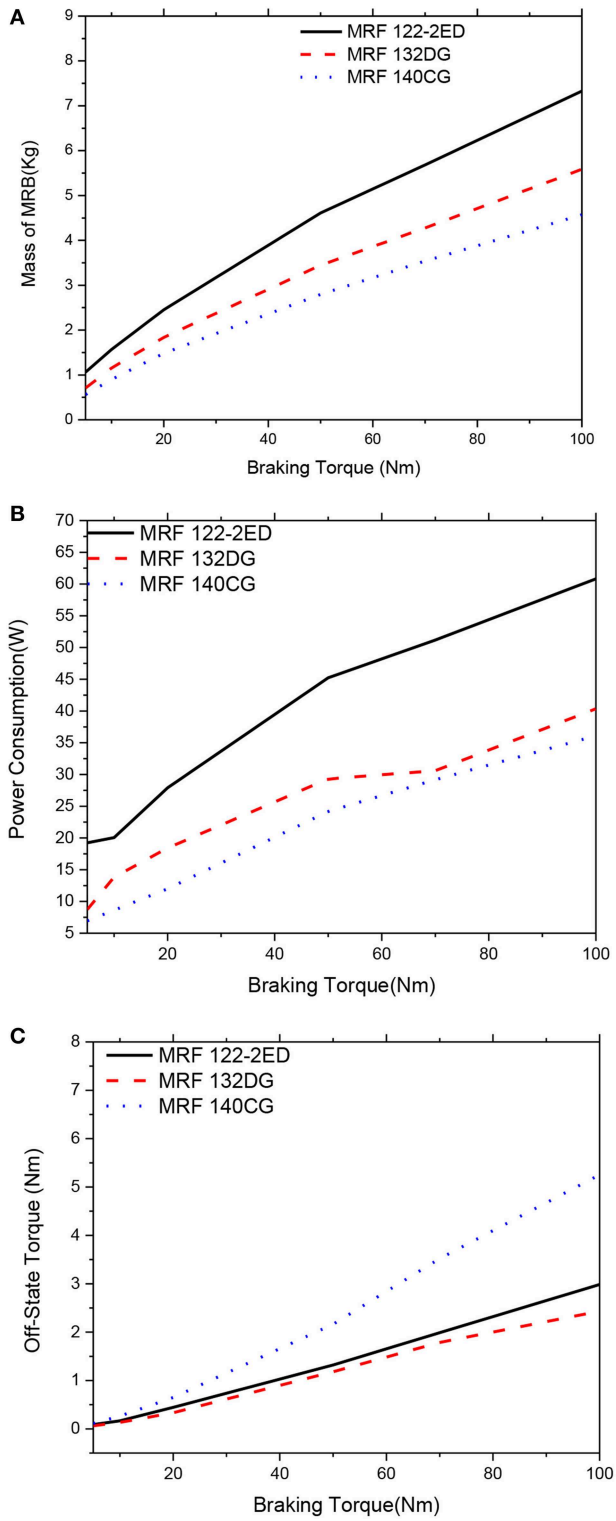

FIGURE 10 | Mass optimization results of the MRBs as a function of braking torque of conventional MRB, $d = 1.0$ mm. **(A)** Mass as a function of braking torque, **(B)** Power consumption as a function of braking torque, **(C)** Off-state torque as a function of braking torque.

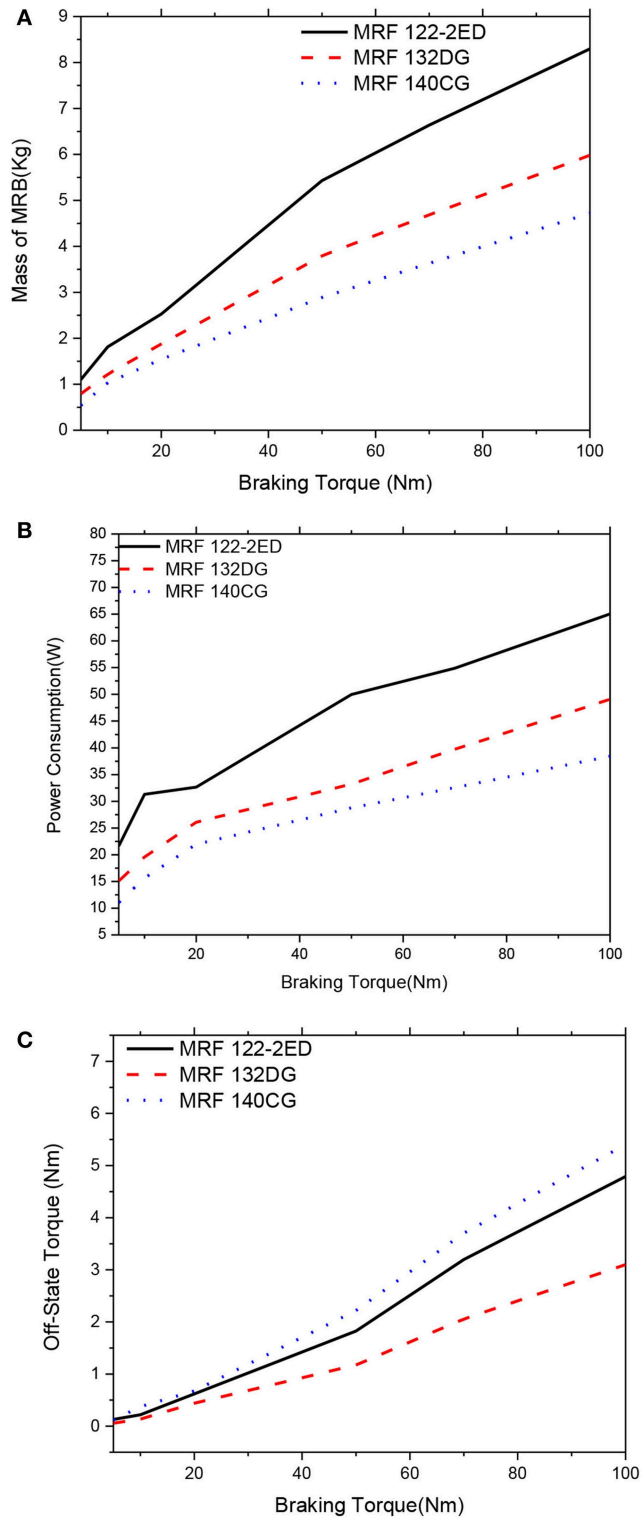

FIGURE 11 | Mass optimization results of the MRBs as a function of braking torque of side-coil MRB, $d = 1.0$ mm. **(A)** Mass as a function of braking torque, **(B)** Power consumption as a function of braking torque, **(C)** Off-state torque as a function of braking torque.

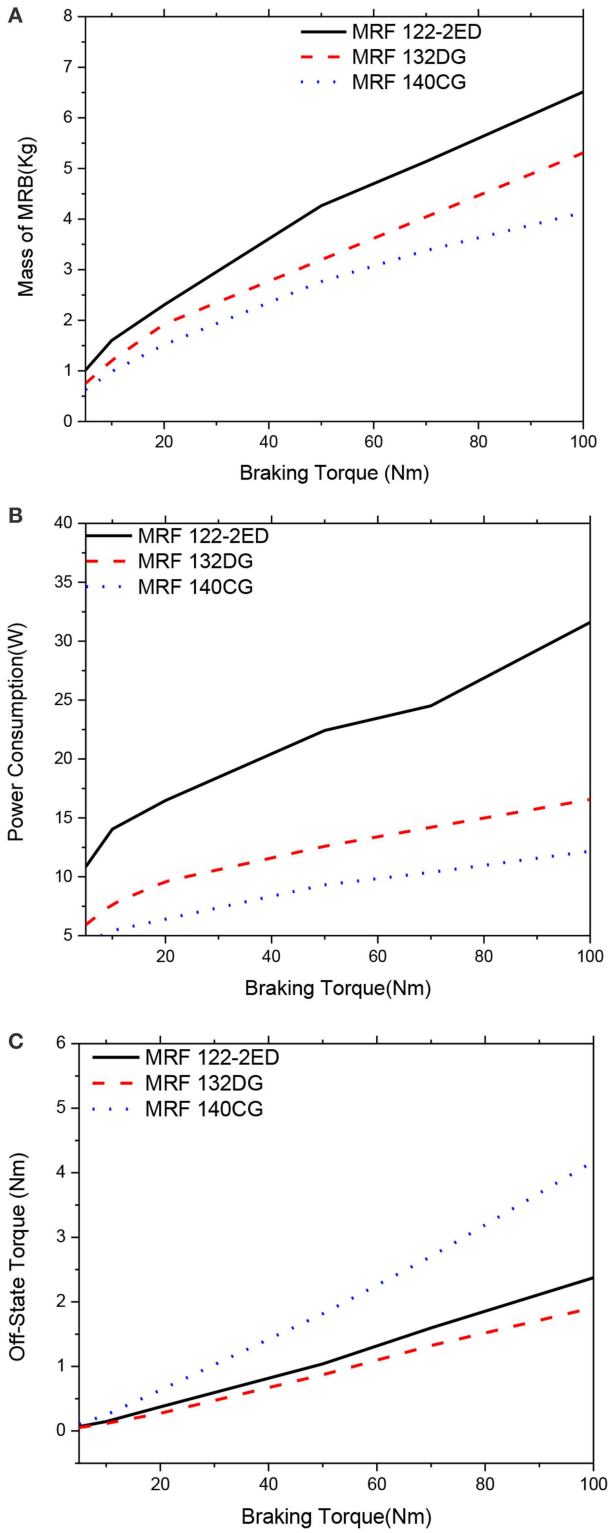

FIGURE 12 | Multi-objective optimization results of the MRBs as a function of braking torque of conventional MRB, $\alpha_m = \alpha_P = \alpha_{To} = 1/3$. **(A)** Mass as a function of braking torque, **(B)** Power consumption as a function of braking torque. **(C)** Off-state torque as a function of braking torque.

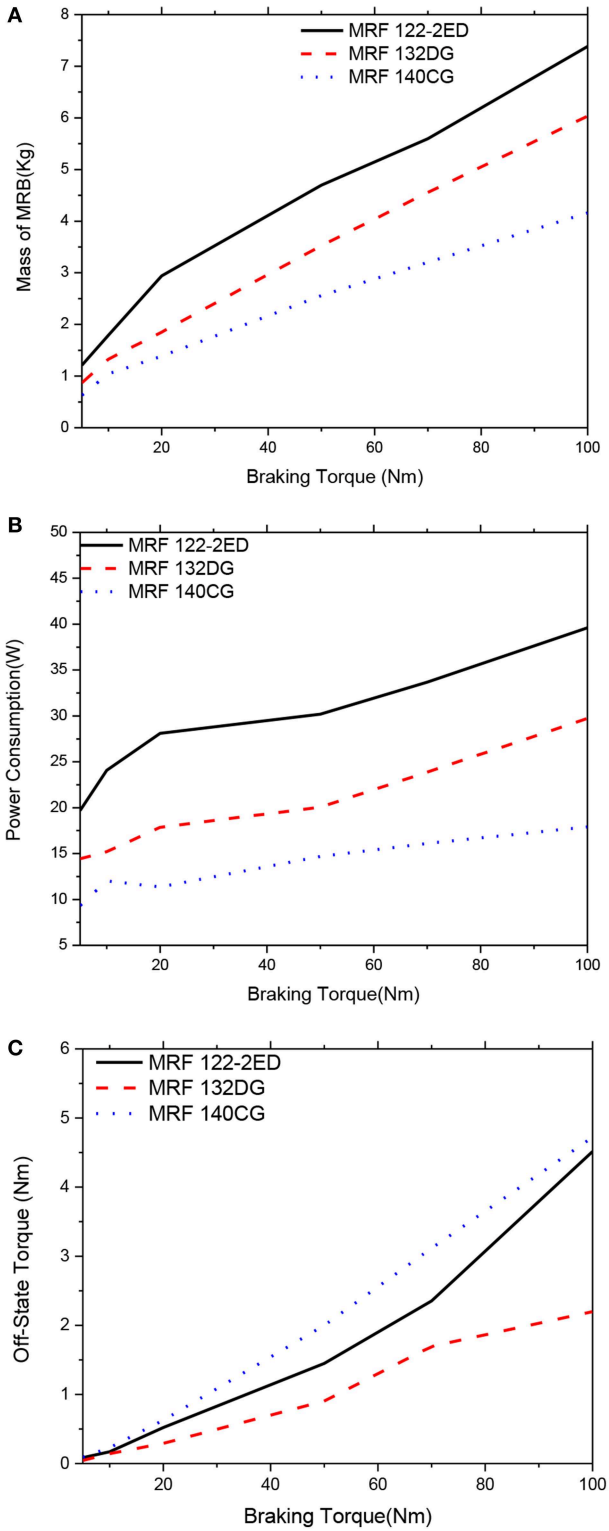

FIGURE 13 | Multi-objective optimization results of the MRBs as a function of braking torque of side-coil MRB, $\alpha_m = \alpha_P = \alpha_{To} = 1/3$. **(A)** Mass as a function of braking torque, **(B)** Power consumption as a function of braking torque, **(C)** Off-state torque as a function of braking torque.

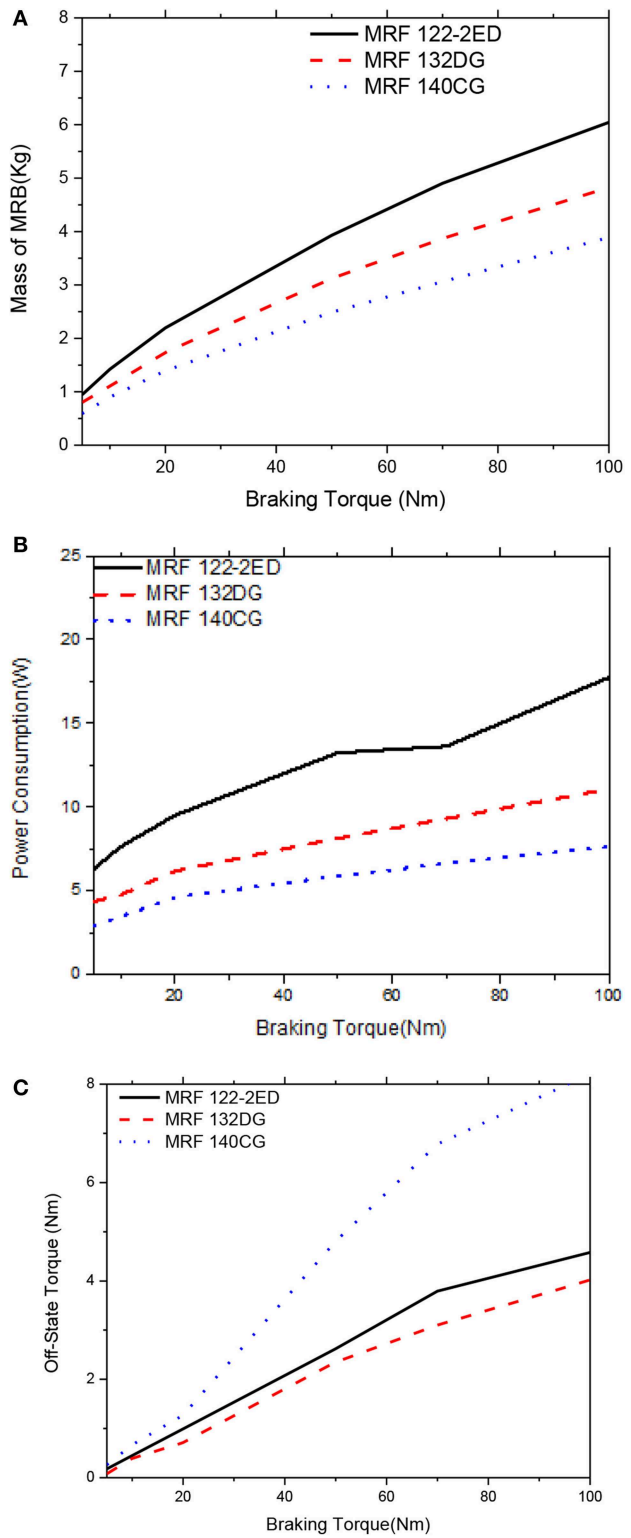

FIGURE 14 | Multi-objective optimization results of the MRBs as a function of braking torque of conventional MRB, $\alpha_m = \alpha_P = 0.5$, $\alpha_{To} = 0$. **(A)** Mass as a function of braking torque, **(B)** Power consumption as a function of braking torque, **(C)** Off-state torque as a function of braking torque.

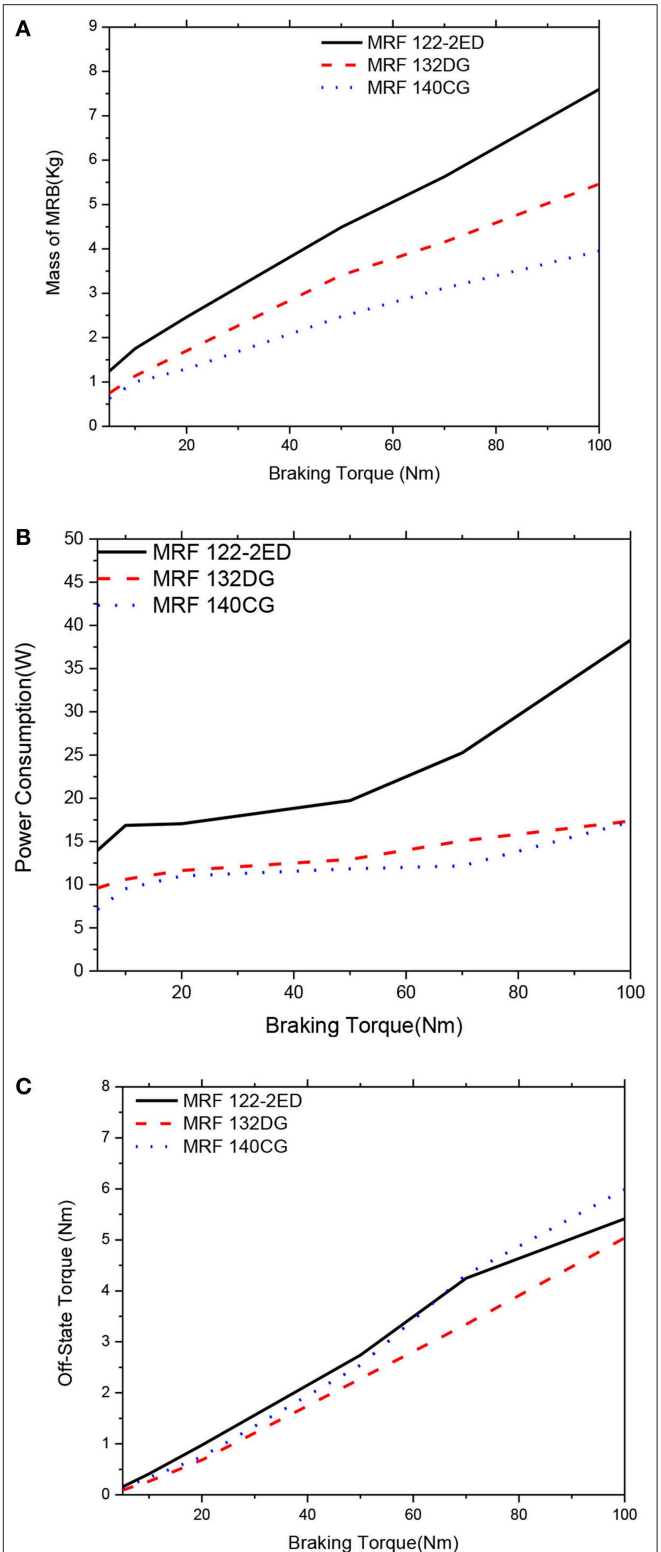

FIGURE 15 | Multi-objective optimization results of the MRBs as a function of braking torque of side-coil MRB, $\alpha_m = \alpha_P = 0.5$, $\alpha_{To} = 0$. **(A)** Mass as a function of braking torque, **(B)** Power consumption as a function of braking torque, **(C)** Off-state torque as a function of braking torque.

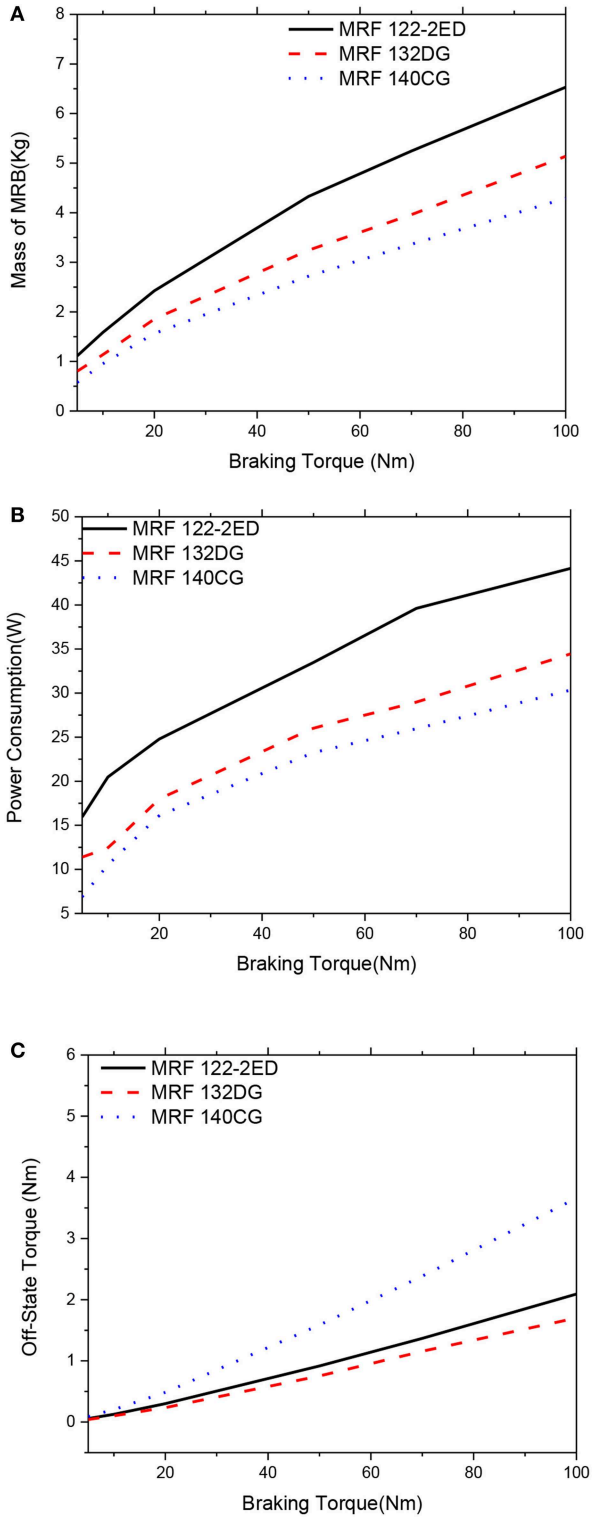

FIGURE 16 | Multi-objective optimization results of the MRBs as a function of braking torque of conventional MRB, $\alpha_m = 0.5$; $\alpha_P = 0.0$; $\alpha_{To} = 0.5$. **(A)** Mass as a function of braking torque, **(B)** Power consumption as a function of braking torque, **(C)** Off-state torque as a function of braking torque.

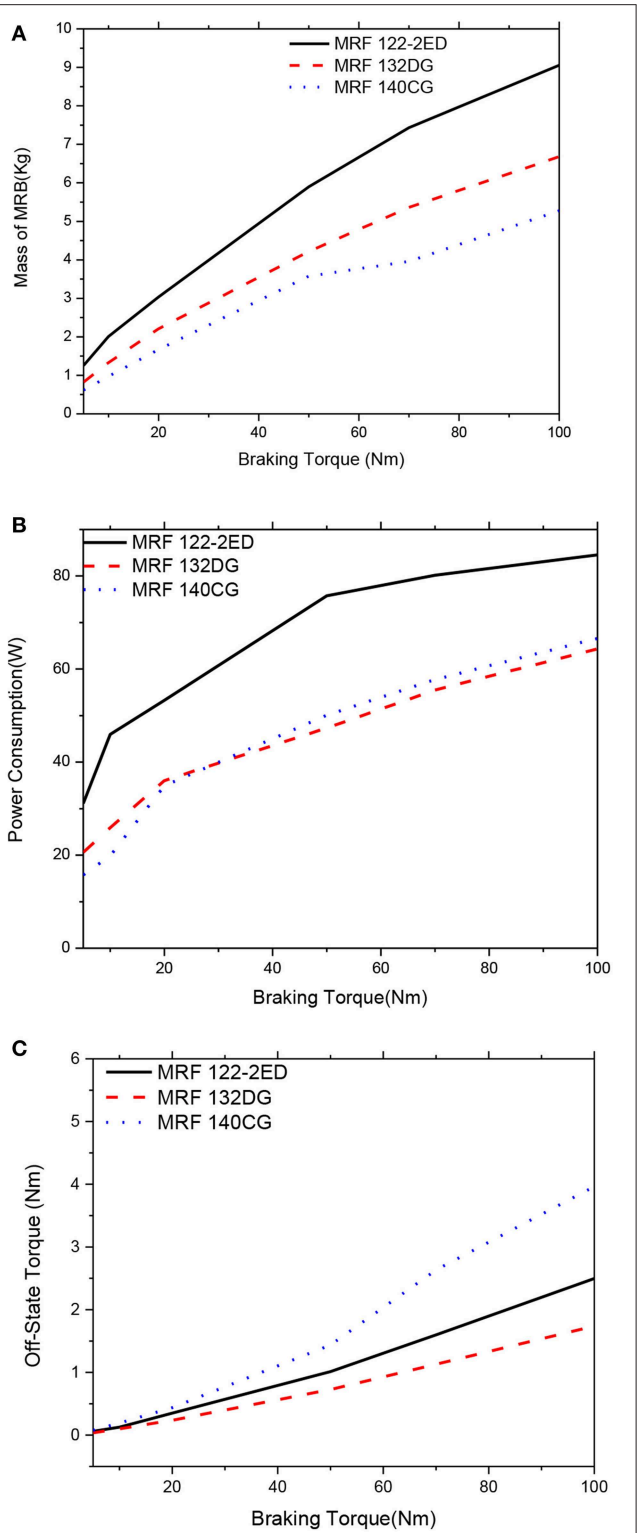

FIGURE 17 | Multi-objective optimization results of the MRBs as a function of braking torque of side-coil MRB, $\alpha_m = 0.5$; $\alpha_P = 0.0$; $\alpha_{To} = 0.5$. **(A)** Mass as a function of braking torque, **(B)** Power consumption as a function of braking torque, **(C)** Off-state torque as a function of braking torque.

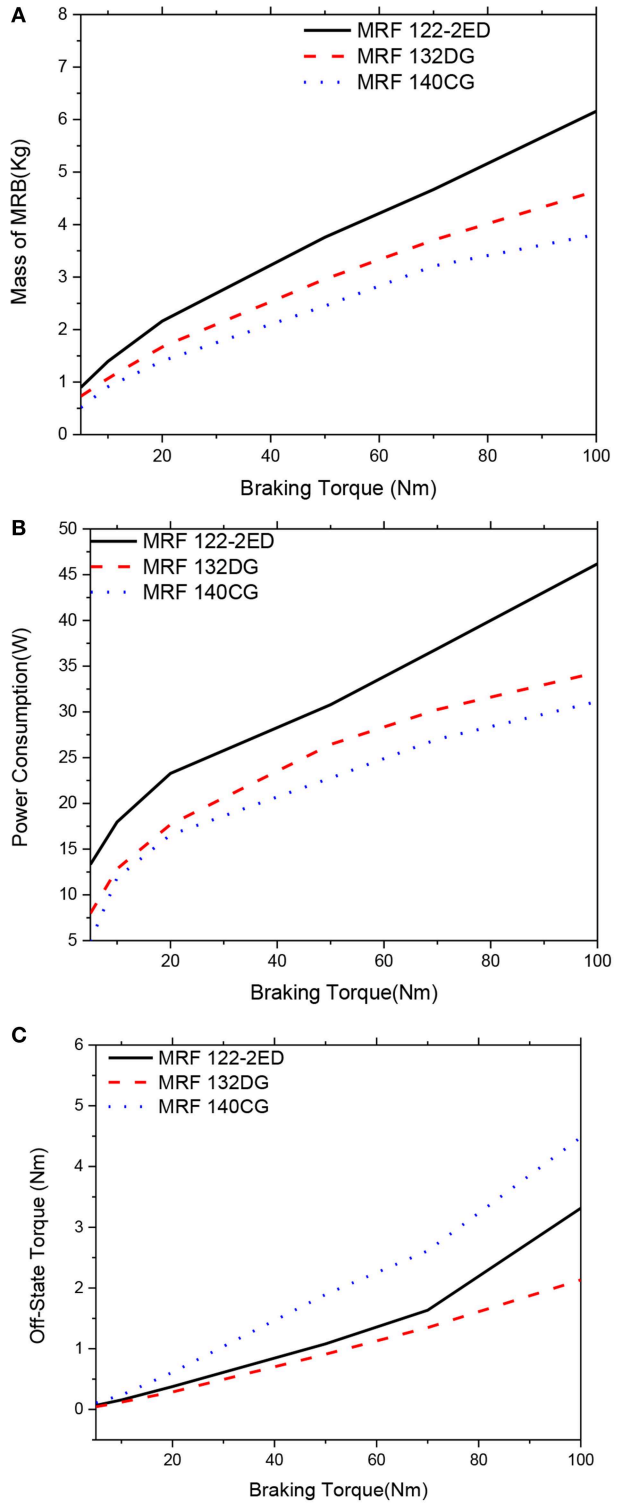

FIGURE 18 | Multi-objective optimization results of the MRBs as a function of braking torque of conventional MRB, $\alpha_m = 0.75$; $\alpha_P = 0.0$; $\alpha_{To} = 0.25$. **(A)** Mass as a function of braking torque, **(B)** Power consumption as a function of braking torque, **(C)** Off-state torque as a function of braking torque.

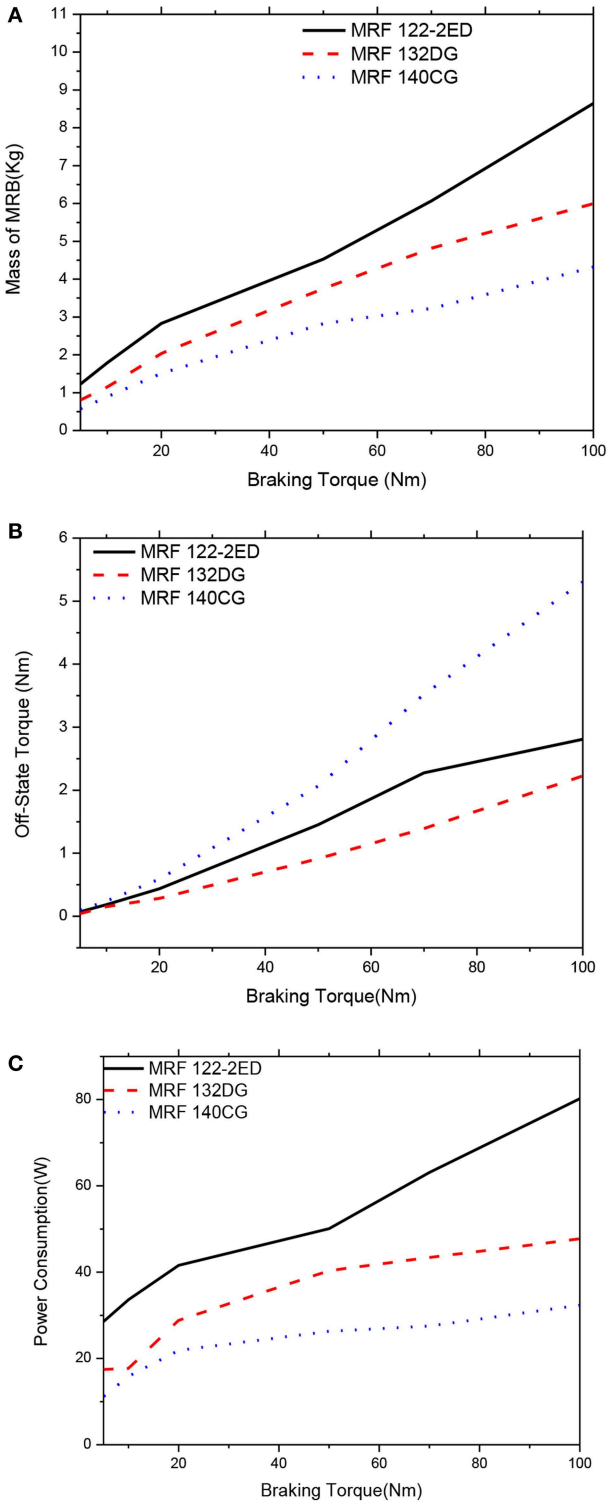

FIGURE 19 | Multi-objective optimization results of the MRBs as a function of braking torque of side-coil MRB, $\alpha_m = 0.75$; $\alpha_P = 0.0$; $\alpha_{To} = 0.25$. **(A)** Mass as a function of braking torque, **(B)** Off-state torque as a function of braking torque, **(C)** Power consumption as a function of braking torque.

function. Therefore, in most cases, the medium yield stress MRF (MRF-132DG) is the recommended MRB application.

CONCLUSIONS

In this research work, a multi-objective function considering mass, power consumption and off-state torque was proposed for the optimal design of MRBs. Based on the proposed optimization, material characterization of MRFs on the performance of the MRBs were investigated. Three different types of popular commercial MRFs: MRF-122-2ED (low yield stress), MRF-132-DG (medium yield stress) and MRF-140CG (high yield stress) and two typical disc type MRBs: the conventional and the side-coil MRB were considered. The simulation results show that, at the optimum, the MRBs employing MRF-140CG always have the smallest mass and power consumption, however, the off-state torque is significantly larger than the others. Therefore, in case the off-state torque is not important for the brake, MRF-140CG is recommended for MRB application. It is also found that performance of the MRBs employing MRF-122-2ED was always worse than the MRF132-DG. Therefore, the lowest yield stress MRF (MRF-122-2ED) is not recommended for MRB application. Among the three considered MRFs, MRF-132DG had the best compromised performance. Especially, in the case of $\alpha_m = 0.5$; $\alpha_P = 0.0$; $\alpha_{To} = 0.5$. Therefore, in the design of MRBs that need to compromise different conflict benefit performance characteristics, MRF-132DG is the recommended MRB application. Finally, it is found that, in the optimization, it is not necessary to consider the gap size of the MRF as a design variable. In most cases, the gap size of MRF should be selected as small as possible considering manufacturing convenience.

AUTHOR CONTRIBUTIONS

All authors listed have made a substantial, direct and intellectual contribution to the work, and approved it for publication.

ACKNOWLEDGMENTS

This research is funded by Vietnam National Foundation for Science and Technology Development (NAFOSTED) under grant number 107.01-2016.32.

REFERENCES

An, J., and Kwon, D.-S. (2003). Modeling of a magnetorheological actuator including magnetic hysteresis. *J. Intellig. Mater. Syst. Struct.* 14, 541–550. doi: 10.1177/1045389X03036506

Avraam, M., Horodinca, M., Letier, P., and Preumont, A. (2008). "Portable smart wrist rehabilitation device driven by rotational MR-fluid Brake actuator for telemedecine applications," in *IEEE/RSJ International Conference on Intelligent Robots and Systems,* (Nice).

Avraam, M., Horodinca, M., Romanescu, I., and Preumont, A. (2010). Computer controlled rotational MR-brake for wrist rehabilitation device. *J. Intellig. Mater. Syst. Struct.* 21, 1–15. doi: 10.1177/1045389X10362274

Huang, J., Zhang, J. Q., Yang, Y., and Wei, Y. Q. (2002). Analysis and design of a cylindrical magneto-rheological fluid brake. *J. Mater. Proc. Technol.* 129, 559–562. doi: 10.1016/S0924-0136(02)00634-9

Imaduddin, F., Mazlan, S. A., and Zamzuri, H. (2013). A design and modeling review of rotary magnetorheological damper. *Mater. Design*. 51, 575–591 doi: 10.1016/j.matdes.2013.04.042

Liu, B., Li, W. H., Kosasih, P. B., and Zhang, X, Z. (2006). Development of an MR-brake-based haptic device. *Smart Mater. Struct.* 15, 1960–1966. doi: 10.1088/0964-1726/15/6/052

Mousavi, S. H., and Sayyaadi, H. (2018). Optimization and testing of a new prototype hybrid MR brake with arc form surface as a prosthetic knee. *IEEE ASME Trans. Mechatron.* 23, 1204–1214. doi: 10.1109/TMECH.2018.2820065

Nguyen, Q. H., and Choi, S. B. (2010). Optimal design of an automotive magnetorheological brake considering geometric dimensions and zero-field friction heat. *Smart Mater. Struct.* 19:115024. doi: 10.1088/0964-1726/19/11/115024

Nguyen, Q. H., and Choi, S. B. (2011). Selection of magnetorheological brake types via optimal design considering maximum torque and constrained volume. *Smart Mater. Struct.* 21:15012. doi: 10.1088/0964-1726/21/1/015012

Nguyen, Q. H., and Choi, S. B. (2012). Optimal design of a novel hybrid MR brake for motorcycles considering axial and radial magnetic flux. *Smart Mater. Struct.* 21:55003. doi: 10.1088/0964-1726/21/5/055003

Nguyen, Q. H., Han, Y. M., Choi, S. B., and Wereley N. M. (2007). Geometry optimization of MR valves constrained in a specific volume using the finite element method. *Smart Mater. Struct.* 16, 2242–2252. doi: 10.1088/0964-1726/16/6/027

Nguyen, Q. H., Lang, V. T., Nguyen, N. D., and Choi S. B. (2014a). Geometric optimal design of a magneto-rheological brake considering different shapes for the brake envelope. *Smart Mater. Struct.* 23:15020. doi: 10.1088/0964-1726/23/1/015020

Nguyen, Q. H., Nguyen, N. D., and Choi, S. B. (2014b). "Design and evaluation of a novel configuration of MR brake with coils placed on the side housings," in *Proceedings of the SPIE.* doi: 10.1117/12.2044561

Nguyen, Q. H., Nguyen, N. D., and Choi, S. –B. (2015). Design and evaluation of a novel MR brake with coils placed on side housings. *Smart Mater. Struct.* 24:90590I. doi: 10.1088/0964-1726/24/4/047001

Park, E. J., Stoikov, D., Falcao da Luz, L., and Suleman A. (2006). A performance evaluation of an automotive magnetorheological brake design with a sliding mode controller. *Mechatronics* 16, 405–416. doi: 10.1016/j.mechatronics.2006.03.004

Smith, A. L., Ulicny, J. C., and Kennedy, L. C. (2007). Magnetorheological fluid fan drive for trucks. *J. Intellig. Mater. Syst. Struct.* 18, 1131–1136. doi: 10.1177/1045389X07083136

Zubieta, M., Eceolaza, S., Elejabarrieta, M. J., and Bou-Ali, M. M. (2009). Magnetorheological fluids: characterization and modeling of magnetization. *Smart Mater. Struct.* 18:95019. doi: 10.1088/0964-1726/18/9/095019

Conflict of Interest Statement: The authors declare that the research was conducted in the absence of any commercial or financial relationships that could be construed as a potential conflict of interest.

frontiers in Materials

ORIGINAL RESEARCH
published: 07 June 2019
doi: 10.3389/fmats.2019.00132

Features of the Mechanisms of Conductivity of the Electrorheological Fluids With Double Doped TiO_2 Particles Under External Temperature Effects

Evguenia V. Korobko and Zoya A. Novikova*

Laboratory of Rheophysics and Macrokinetics, A. V. Luikov Heat and Mass Transfer Institute, National Academy of Sciences of Belarus, Minsk, Belarus

Electrophysical and rheological characteristics of ER fluids with TiO_2 particles doped with aluminum and phosphorus and having anatase structure are considered in an extended temperature range (5–100°C). The mechanisms of leakage currents in the ER fluid in electric fields up to 3.5 kV/mm are determined. Conduction mechanisms such as thermionic ionization, electron injection from an electrode, thermal excitation of charges, field emission of electrons from an electrode, thermionic emission of electrons from an electrode, and field emission of electrons from traps are identified. Based on the analysis of the current-voltage characteristics of the ER fluid, the positive role of the additional doping of the dispersed phase particles with phosphorus compared with the known results for ER fluid with TiO_2/Al particles was established. The use of double doping of particles of the dispersed phase made it possible to obtain stable dependences of the shear stress of electrorheological fluids on the electric field strength in the range of the temperature effects under study.

Keywords: electrorheological fluids, conductivity, electric field, ER-effect, double doped particles TiO_2 particles

OPEN ACCESS

Edited by:
Miao Yu,
Chongqing University, China

Reviewed by:
Xufeng Dong,
Dalian University of Technology (DUT), China
Jianbo Yin,
Northwestern Polytechnical University, China

****Correspondence:***
Evguenia V. Korobko
evkorobko@gmail.com

Specialty section:
This article was submitted to Smart Materials, a section of the journal Frontiers in Materials

Received: *29 October 2018*
Accepted: *20 May 2019*
Published: *07 June 2019*

Citation:
Korobko EV and Novikova ZA (2019) Features of the Mechanisms of Conductivity of the Electrorheological Fluids With Double Doped TiO_2 Particles Under External Temperature Effects. Front. Mater. 6:132. doi: 10.3389/fmats.2019.00132

INTRODUCTION

A distinctive feature and the most important advantage of electrorheological fluids (ERF) is their controllability with the help of external electric fields, which allows their use for the creation of adaptive electromechanical devices of new generation. For the effective operation of such devices—heat exchangers, hydraulic systems, as well as devices used in dynamic conditions, for example, dampers and shock absorbers—fluids must exhibit a high ER-effect, stable in an extended temperature range. The main obstacle to obtaining the required results is the increase in conduction current in ER fluids with the temperature increase, which significantly reduces their rheological response. Due to the increase in the mobility of the charges and their quantity during heating, a breakdown situation arises, which does not allow for the application of an electric field of higher strength to obtain the required power indicators of the ER fluids. This is especially characteristic of ER fluids with particles of different oxides of an amorphous structure, in which there are bound charges at the interface and the characteristic Maxwell-Wagner type of polarization. In addition,

the non-linearity of the dependencies of the electrorheological characteristics on temperature, which have maximum values of the shear stress τ already at a temperature of 50–70°C and show their further reduction, does not allow to adaptively control ER fluids to maintain a stable ER effect in dynamic systems, for example, in vibroprotection devices.

The results of both early and more recent investigations (Xu et al., 1992; Böse and Trendler, 2001; Yin and Zhao, 2001, 2006; Shang et al., 2007; Tang et al., 2010; Korobko et al., 2012) on the use of semiconductor-type particles as fillers of ER fluids are known. In particular, TiO_2 particles with a crystalline structure ("anatase") and high dielectric constant ($\varepsilon = 90$), which belong to electronic semiconductors, are considered. Their surface and bulk properties are modified by researchers with the introduction of various impurities into the structure, which, however, has not yet yielded the expected results of the thermal stability of the rheological parameters of the ER fluid based on them.

When studying the ER-effect, the features of electrical conduction mechanisms (leakage currents) in electrorheological fluids are of key importance. Detection of the features of the occurrence and manifestation of these mechanisms will allow us to explain the physical nature of their effect on the ER fluids with dispersed particles of various types and to assess the level of stability of their rheological parameters during thermal exposure. So, for example, electrorheological fluids with particles of a semiconductor type, in particular TiO_2, showed a low rheological response to the influence of an external electric field (Yin and Zhao, 2001). The authors of this study showed that the ionic or atomic polarization of TiO_2 does not create the polarization conditions necessary for the manifestation of a high ER effect. However, modern possibilities of applying the methods of modifying the crystal structure of a semiconductor allow researchers to purposefully change the bulk and surface properties of TiO_2 particles to enhance their polarization and structural interaction, as well as optimize the number of charge carriers, including an extended temperature range.

The task of modifying the structure of TiO_2 in order to improve the rheological parameters of the ER fluids was taken up by many researchers. Thus, some studies (Yin and Zhao, 2001, 2006; Shang et al., 2007; Tang et al., 2010) showed that doping of the crystal structure of titanium oxide with metal ions allows the ER effect to be significantly increased. The best results were shown by ERF containing TiO_2 doped with Ce, La, Y, Al, Nb. The results of research by Tang et al. (2010) proved the effectiveness of ER fluids with particles of TiO_2 doped with Y^{3+}, Al^{3+}, Nb^{3+} cations with high ionic potential (z^2_{ion}/a_{ion}).

Most researchers studied the effect of modifying the structure of TiO_2 on the rheological parameters at room temperature. There are only a few papers devoted to the study of the rheology of electrorheological fluids with modified TiO_2 particles under the influence of temperature. The most complete studies of ER fluids with Ce-doped particles of TiO_2 in the extended temperature range 10–100°C were presented by Yin and Zhao (2001). Studying the dielectric spectra, electrical conductivity and rheological indices of ERF, the authors found that doping the structure of TiO_2 particles with cerium (Ce) not only increases the rheological response of the ERF, but also shifts the peak of the dependence τ (T) to a higher temperature (80°C) compared with the results obtained by using unmodified TiO_2 (40°C). These results were accompanied by a significant increase in conduction current and, according to the authors, can be explained by an increase in the number of charges thermally activated in the modified composition of the TiO_2 particles.

We have investigated the rheological and electrophysical properties of ERF with TiO_2 particles, doped with aluminum, annealed at different temperatures (Korobko et al., 2018). It was determined that the highest ER-activity in the electric field at strength of only up to 1.5 kV/mm has an ER fluid with TiO_2 particles doped by 7 mol.% aluminum annealed at a temperature of 600°C. However, a high leakage current does not allow an increase in the electric field strength of more than 1.5 kV/mm even at a temperature of 20°C.

Increasing the aluminum content to 12 moles% in doped TiO_2 particles and the annealing temperature up to 700°C contributed to a decrease in leakage current, which made it possible to increase the electric field strength to 3.0 kV/mm and increase the maximum value of the shear stress in the ER-fluid by two times. Analysis of the electrical conductivity of the investigated compositions of ER fluids containing TiO_2 particles doped with aluminum showed that high leakage currents in strong electric fields with strengths up to 3.0 kV/mm in the temperature range from 5 to 80°C are caused by mechanisms such as thermal excitation of charge carriers, thermoelectronic ionization, as well as the injection of electrons from the electrode and Schottky emission.

Possible ways of placing the impurity Al^{3+} cations in the TiO_2 lattice have been considered (Kofstad, 1972). Since the ionic radius of the Al^{3+} cation (0.054 nm) is smaller than the radius of the Ti^{4+} cation (0.061 nm), it is possible to partially replace the Ti^{4+} cation with Al^{3+} in the lattice sites of TiO_2. With the location of impurities in the lattice sites the concentration of free electrons decreases. If the impurity is in the interstices, the concentration of free electrons increases, however, with this method of introduction, Al^{3+} cations can play the role of scattering centers and cause a decrease in the mobility of charge carriers. Thus, when the substitution and interstitial impurities are present simultaneously in the anatase structure, the possible reason for the decrease in the electrical conductivity can be the reduction in the concentration and mobility of charge carriers.

The results of studies of the synthesis of mesoporous titanium dioxide doped with phosphorus and the determination of its protocatalytic activity (Yu et al., 2003) showed that phosphorus, when doped with TiO_2, can be incorporated into the crystal structure, either at the oxygen position or in the lattice interstitial sides.

FEATURES OF CHARGE TRANSFER MECHANISMS IN SEMICONDUCTOR MATERIALS

It is known that if both acceptor and donor impurities are introduced into the semiconductor, then impurities are compensated. Donor electrons spontaneously transfer to the level

of acceptor atoms. The need for these electronic transitions is due to the fact that in the absence of external exciting effects, electrons must occupy all lower energy levels, and since acceptor levels lie below donor levels, donor electrons move to free acceptor levels. Impurity atoms can be placed in the crystal lattice in two ways: either at the sites of the lattice—impurity substitutions, or in the interstitial site—intersitial impurity. The character of impurity substitutional atoms is determined by their valence, that is, aluminum is an acceptor, and phosphorus is a donor. If the impurity atoms are introduced into the interstices of the lattices, then the sign of the impurity conductivity is determined by their electronegativity. If the electronegativity of impurity atoms is greater than that of the main atoms of the lattice, then the impurity has acceptor properties; if it is smaller, then the impurities are donors (Mitrofanov and Phogel, 1965). According to Pauling, the relative electronegativity of Ti is 1.8, Al−1.5, P−2.1. Thus, aluminum and phosphorus atoms in the anatase structure can be both donors and acceptors, depending on their location in the crystal lattice of the material.

In the present work, in order to reduce the magnitude of conduction currents (leakage) and increase the effective strength of a constant electric field with increasing intensity of temperature effects, the characteristics of ERF containing semiconductor TiO_2 particles doped with aluminum and phosphorus are investigated and compared with similar indicators for ER fluids, containing TiO_2 particles doped with aluminum only.

The focus is on assessing the rheological and electrophysical characteristics of ER fluids, as well as identifying features of existing conduction mechanisms that create leakage currents under various external influences and as a result of modifying the crystal structure of TiO_2 particles.

It is known that a change in the conduction current (leakage current) of a semiconductor with a change in the electric field strength is due to the effect of the field on the mobility (μ) and the concentration of charge carriers in its volume. The change in charge mobility in an electric field, both in weak and strong fields, is determined, respectively, by the dependences $\mu \sim 1/\sqrt{E}$ and $\mu \sim E^{3/2}$. The concentration of charge carriers in semiconductors in strong fields, for which the linearity of the current-voltage characteristics (CVC) in the coordinates $I(U)$ is not typical, increases noticeably with increasing electric field strength.

A number of studies (Sze, 1981; Shalimova, 1985), described several different mechanisms for the emergence and movement of charge carriers in a semiconductor under the influence of an external electric field. The mechanism of thermoelectronic ionization, in which the electron is detached from the atom (the Poole-Frenkel effect), acts first in an external electric field. The magnitude of the potential barrier that an electron must overcome when moving to the conduction band decreases when exposed to an external electric field. The linear character of the current-voltage characteristics (CVC) in the coordinates ln (j/E) from $\sqrt{E}$ indicates that the conduction current is due to the Poole-Frenkel effect and can be calculated by the formula (1):

$$J = e\mu n_0 \frac{U}{L} \exp\left(\frac{\beta U^{\frac{1}{2}}}{kTL^{\frac{1}{2}}}\right), \quad (1)$$

where $\beta = \left(\frac{e^3}{\pi\varepsilon\varepsilon_0}\right)$, n_0 is the electron concentration in the conduction-band in the absence of the electric field, L is the semiconductor layer thickness, e is the electron charge, T is the absolute temperature, U is the voltage, ε is the relative permittivity, ε_0 is the electric constant, k is Boltzmann's constant ($k = 8.62 \cdot \times 10^{-5}$ eV/K), μ is charge mobility in the conduction-band, and J represents the current.

When exposed to strong electric fields in a semiconductor, a mechanism of excitation of charge carriers, caused by the impact of impact ionization, manifests itself. With external semiconductor heating, the change in the current value due to an increase in the number of charge carriers moved to the conduction-band is described by formula (2):

$$\ln J = \frac{\omega}{kT}, \quad (2)$$

where ω represents the activation energy of process of excitation, and k is the Boltzmann's constant. In the presence of this process, the CVC is constructed in the Arrhenius coordinate system ($\ln j - 1/kT$) and is approximated by a linear dependence.

The current flowing through thin layers of a semiconductor is determined not only by its own charge carriers. When an electric field is applied, the electrons injected from the electrode into the semiconductor are drawn deep into the semiconductor and, passing through it, cause a current to flow. Such a current is not associated with its own electrons in the conduction band of the material, but with charge carriers injected from the cathode. The presence levels capture of electrons (traps) leads to a strong decrease in current, since the capture levels, being initially empty, capture the overwhelming part of injected electrons, preventing them from moving when exposed to an electric field.

Thus, the electrons trapped in the traps create a space charge, but do not participate in the charge transfer through the semiconductor in the capacitor gap. The presence of traps significantly reduces the amount of spatial-charge-limited current (SCLC). Its dependence on the electric field is represented by the formula (3):

$$J = \frac{\theta\mu\varepsilon\varepsilon_0 E^2}{L}, \quad (3)$$

where θ represents the proportionality coefficient and depends on the depth of the traps.

The experimental dependences of the CVC are plotted in logarithmic coordinates ln$j$–ln$E$ and must be linear in the presence of a SCLC in a semiconductor.

The thermal emission of electrons from a heated metal into the conduction band of a semiconductor through a potential barrier in an electric field is called thermoelectron emission (Schottky emission). In this case, the value of the conduction current depends on the temperature, electric field strength, and the height

of the metal-semiconductor potential barrier. The current caused by the Schottky emission mechanism can be described by the Richardson-Dashman equation (Sze, 1981; Shalimova, 1985):

$$J = AT^2 \exp\left(\frac{1}{kT}\sqrt{\frac{e^3E}{4\pi\varepsilon_0\varepsilon}}\right), \quad (4)$$

where $A = C_{RD}\exp\left(\frac{\varphi_b}{kT}\right)$, C_{RD} *is the* Richardson constant and φ_b represent the potential barrier height.

The presence of current in a semiconductor caused by thermoelectronic emission is determined according to the linearity of the dependence of the experimental results of the CVC in the coordinate system ln$j$ –$\sqrt{E}$.

Electrons can enter the conduction band not only due to the kinetic energy of their thermal motion, which is observed during thermoelectronic emission, but as a result of the tunnel effect, in which the energy of the charge carrier is insufficient to overcome the potential barrier. In this case, the current caused by strong electric field strength (field emission) is described by the well-known Fowler-Nordheim equation (Fowler and Nordheim, 1928):

$$J = \alpha\varphi^{-1}E^2\exp\left(-\frac{b\varphi^{\frac{3}{2}}}{E}\right), \quad (5)$$

where $\alpha = \frac{e^3}{8\pi h}$, $b = \frac{4\sqrt{2m}}{eh}$, φ represents the electron work function of metal, m the electron mass, $h = \frac{h}{2\pi}$, where h–Planck's constant.

The linearity of the experimental results of the CVC in the coordinate system ln $j/E-1/\sqrt{E}$. determines the presence of current caused by the field emission mechanism in a semiconductor.

With strong electric fields or heating, the Poole-Frenkel effect transforms into trap tunneling or field emission of electrons from traps. The presence of current caused by the field emission of electrons from the traps is determined by the linearity of the experimental results of the CVC in the coordinates of the field emission ln (j/E^2) $-1/E$. The current caused by this conduction mechanism can be described by the following expression:

$$J = C_t E^2\exp\left(-\frac{\alpha\varphi^{\frac{3}{2}}}{E}\right), \quad (6)$$

$$\text{where } \alpha = \frac{8\pi\sqrt{2m_{ox}q}}{3h}.$$

Thus, the main, most typical mechanisms of charge transfer in semiconductors materials, that allow us to study the physical nature and estimate the values of the corresponding conduction currents in them are:

- thermoelectronic ionization–the Poole-Frenkel equation (coordinates ln(j/E)–$\sqrt{E}$);
- thermal excitation of charges (coordinates ln $j-1/kT$);
- impact ionization;
- injection from the electrode (SCLC) (coordinates ln$j$–ln$E$);
- thermoelectron emission (Schottky emission)–Richardson-Dashman equation, (coordinates ln j–$\sqrt{E}$);
- tunnel effect–the Fowler-Nordheim equation (coordinates ln$(j/E)-1/\sqrt{E}$);
- trap tunneling (field emission of electrons), coordinates ln $(j/E^2)-1/E$).

MATERIALS AND RESEARCH METHODS

Samples of double doping of aluminum and phosphorus TiO_2 and samples of doped-aluminum TiO_2 were synthesized by the sol-gel method. The alloying and structuring components were introduced into the freshly precipitated TiO_2 sol during the synthesis process. Dried samples were annealed at T_{an} =700°C (Murashkevich et al., 2017).

The ER-activity of the obtained samples of doped TiO_2 was determined from the change in shear stress and current density of the ER fluids containing 20 wt.% of the dispersed phase in the dielectric oil, with a change in the electric field strength of up to 3.5 kV/mm. The shear stress (τ) and the current density (j) of the ER fluids were determined using a Physica MCR 301 rheometer from Anton Paar in a coaxial-cylindrical measuring cell with an inner cylinder diameter of 26.7 mm and an external cylinder of 28.9 mm. The maximum value of the

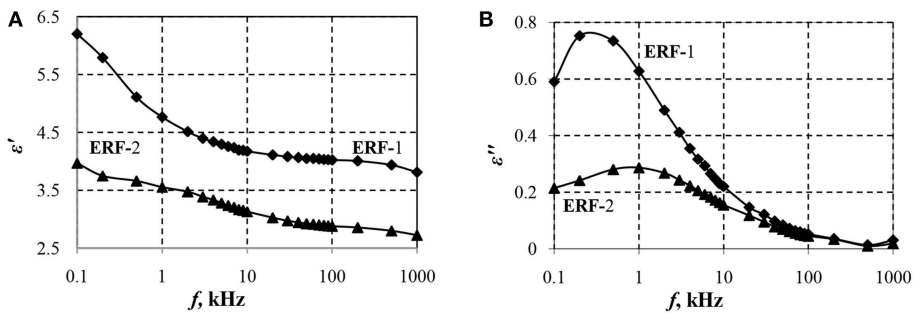

FIGURE 1 | Dependences of the real ε' **(A)** and imaginary ε'' **(B)** components of the dielectric constant of ERF-1 and ERF-2 on the field frequency.

permissible current density was 30 μA/cm^2, the temperature varied from 5 to 100°C, and the shear rate varied from 0.1 to 100.0 s^{-1}. The conduction mechanisms causing the leakage currents in the ER fluids were judged by the nature of the current-voltage characteristics (CVC) in the corresponding coordinates. Dielectric characteristics of ER fluids were determined using an E7-20 impedance meter, which allows measuring capacitance C and dielectric loss tangent tan δ_x in the frequency range of f from 25 Hz to 1 MHz (the measuring signal voltage used in the experiments is 1 V).

RESULTS AND DISCUSSION

Dielectric spectra $\varepsilon'(f)$ and $\varepsilon''(f)$, dependences of current density (j) and shear stress (τ) on electric field strength (E) from 0 to 3.5 kV/mm when the temperature changes (T) were considered in determining the effect of double doping of TiO_2 with aluminum and phosphorus on the electrophysical and rheological characteristics of the ER fluids. Sample ER fluid −1 (ERF-1) contains 20 wt.% TiO_2, doped with aluminum and phosphorus expressed as elements, respectively, 10 mol.% Al and 1 mol.% P. Sample ER fluid −2 (ERF-2) contains 20 wt.% TiO_2, doped with 10 mol.% Al.

The frequency dependences of the real (ε') and imaginary (ε'') components of the complex dielectric constant ($\varepsilon = \varepsilon' - i\varepsilon''$) determine the features of polarization of the material under consideration. The polarization ability of particles is determined by the difference between the relative dielectric constant (ε') at a frequency below and above the relaxation frequency f_r, at which the dielectric loss factor is maximum ($\Delta\varepsilon' = \varepsilon'_{0.1\text{kHz}} - \varepsilon'_{100\text{kHz}}$). Hao et al. (1998) determined that to achieve a high ER-effect, suspensions should have interfacial polarization, i.e., the

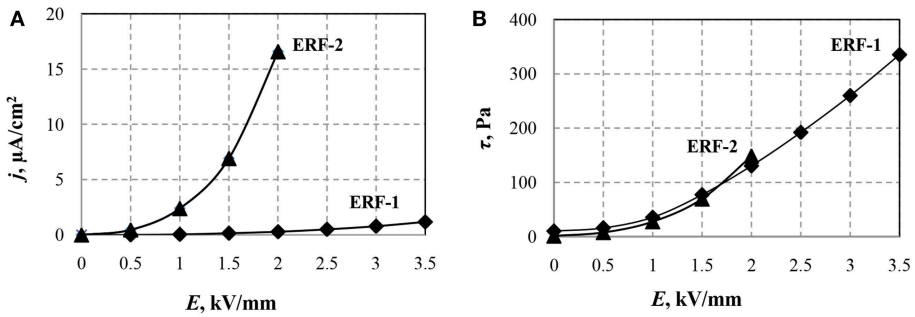

FIGURE 2 | Dependencies of current density **(A)** and shear stress **(B)** of ERF-1 and ERF-2 on the electric field strength at a temperature of 20°C and shear rate of 100 s^{-1}.

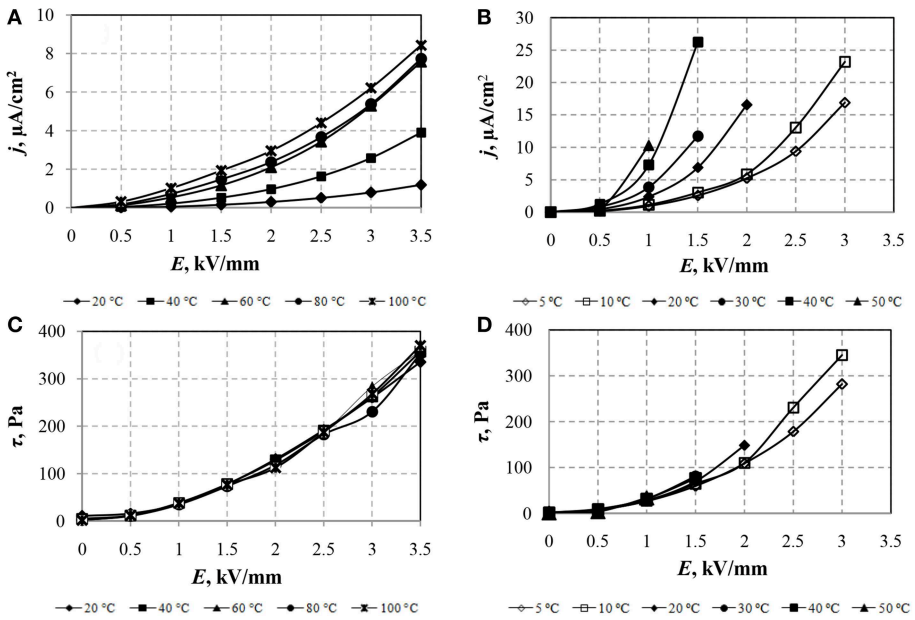

FIGURE 3 | Dependences of current density **(A,B)** and shear stress **(C,D)** of ERF-1 **(A,C)** and ERF-2 **(B,D)** on the electric field strength with temperature change. Shear rate 100 s^{-1}.

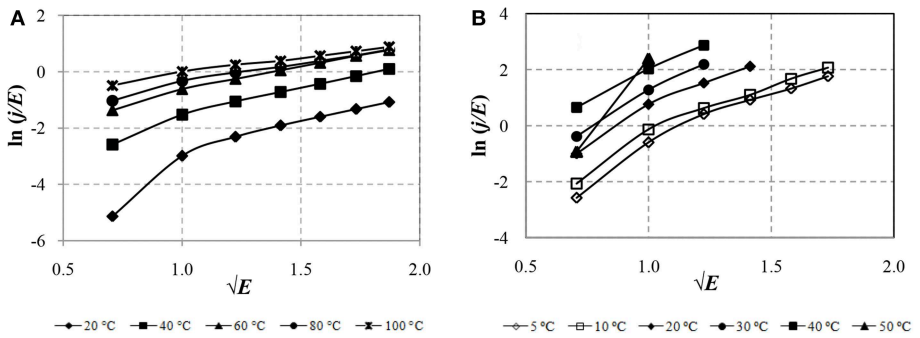

FIGURE 4 | CVC of ERF-1 **(A)** and ERF-2 **(B)** samples in the coordinates of Poole-Frenkel.

relaxation frequency should be in the range of 0.1 to 1,000 kHz and at large values of the dielectric loss factor, the ER effect will be higher.

Figure 1 shows the dependences of the real (ε') and imaginary (ε'') components of the dielectric constant of ERF-1 and ERF-2 on the frequency of the electric field.

Dependences ε' (f) and $\varepsilon''(f)$ confirm the presence of interfacial polarization in ERF-1 and ERF-2 (**Figure 1**). Double doping of aluminum and phosphorus TiO_2 (ERF-1) increases $\Delta\varepsilon'$ ($\Delta\varepsilon'_{ERF-1} = 2.4$; $\Delta\varepsilon'_{ERF-2} = 1.3$) and ε'' at the relaxation frequency ($\varepsilon''_{ERF-1} = 0.75$ for $f_{rERF-1} \approx 0.2$ Hz; $\varepsilon''_{ERF-2} = 0.29$ when $f_{rERF-2} \approx 1.0$ Hz), that increases the polarization ability of ERF-1 ($\Delta\varepsilon'_{ERF-1} > \Delta\varepsilon'_{ERF-2}$).

Figure 2 shows the dependences of the current density and shear stress ERF-1 and ERF-2 on the electric field strength.

It can be seen from the above dependences that even at $E > 2$ kV/mm, significant leakage currents in the ERF-2 do not allow an increase in the electric field strength. The shear stress of the ERF-1 with double doping of aluminum and phosphorus TiO_2 particles is two times greater than the maximum achievable for ERF-2 in the considered range of electric fields. The double doping leads to a significant decrease in the current ERF-1, which allows increasing the electric field strength.

The effect of the electric field strength on the current density and the shear stress of ERF-1 and ERF-2 with temperature changes are shown in **Figure 3**.

In **Figures 3A**,**B,** in which the CVC in the coordinates of the current density (j) from the electric field strength (E) are shown, it can be seen that heating the ER fluids samples increases the leakage current density in the entire range of variation of the electric field. Maximum value of current density in ERF-1 is three times less than in ERF-2. It is necessary to note the significant intensity of the current density increase in ERF-2 with increasing temperature at all electric field strengths compared with its smooth change for ERF-1.

Figure 3C shows that the shear stress of the ERF-1 almost does not change with increasing temperature, the current density of the ERF-1 decreases with a temperature decrease to 20°C (**Figure 3A**). The maximum value of the current density ERF-1 (8.8 μA/cm^2) obtained at $T = 100$°C and $E = 3.5$ kV/mm. According to previously collected data (Yin and Zhao, 2001), the shear stress of Ce-doped TiO_2 ER fluid increases with temperatures at 80°C and, with a further increase in temperature to 100°C, the shear stress of the ER fluid decreases.

To identify the conduction mechanisms causing the leakage currents of the ER fluids, the CVC constructed in different coordinates is to be considered. The presence of a mechanism of thermionic ionization in the formation of leakage currents can be determined by the type of dependences of the current—voltage characteristics in the coordinates ln (j/E) on $\sqrt{E}$, as shown in **Figure 4**.

Figure 4 shows that the currents of the ERF-1 are lower than the currents of the ERF-2. The CVCs in the coordinates ln (j /E) from $\sqrt{E}$ for ERF-1 and ERF-2 have a linear character in electric field strength $E \geq 1$ kV/mm. To determine the effect of heating on the increase in conductivity of the ER fluids, the experimental results are presented in the Arrhenius coordinate system ln J from $1/T$, as shown in **Figure 5**.

The decrease leakage currents in ERF-1 compared to ERF-2 due to thermoelectric ionization (**Figure 4**) and thermal excitation (**Figure 5**) confirms the assumption of a decrease conductivity due to a decrease in the concentration of charge carriers. This is due to the joint presence of donor and acceptor impurities, as well as impurities of interstitial and substitution in the structure of TiO_2. **Figure 5** shows that the increase in current in ERF-1 is significantly influenced by the thermal excitation of charge carriers and their transfer to the conduction band when heated to 60°C ($1/T = 0.003$). With a further increase in temperature to 100°C ($1/T = 0.00268$), the current increases weakens, and in electric field strength $E \geq 2.0$ kV/mm, the current increase is minor . The dependences in the Arrhenius coordinates for ERF-2 are linear in the whole range of variations of the electric field strength and temperature from 5 to 50°C.

To determine the space-charge-limited current (SCLC) created by electrons injected from the electrode in the ER fluid, the CVC in logarithmic coordinates ln$j$–ln$E$ is to be considered (**Figure 6**).

Figure 6 shows that the CVCs for ERF-1 and ERF-2 are linear in the whole range of the electric field strength and temperature. The CVC for ERF-1 has a piecewise linear approximation at 200°C.

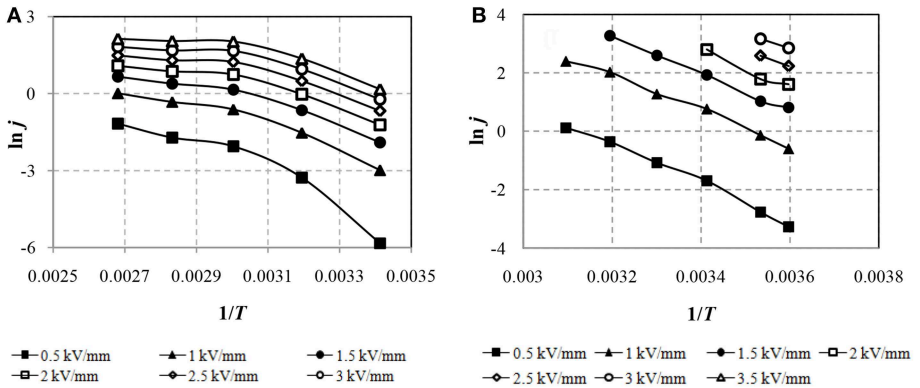

FIGURE 5 | CVC of samples ERF-1 **(A)** and ERF-2 **(B)** on temperature in Arrhenius coordinates.

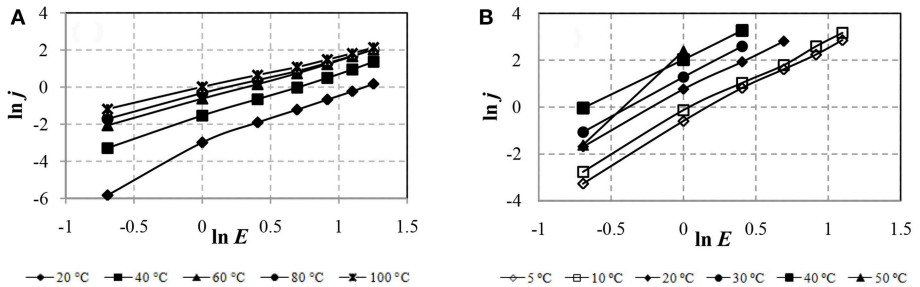

FIGURE 6 | CVC of the ERF-1 **(A)** and ERF-2 **(B)** samples in logarithmic coordinates ln*j*–ln*E*.

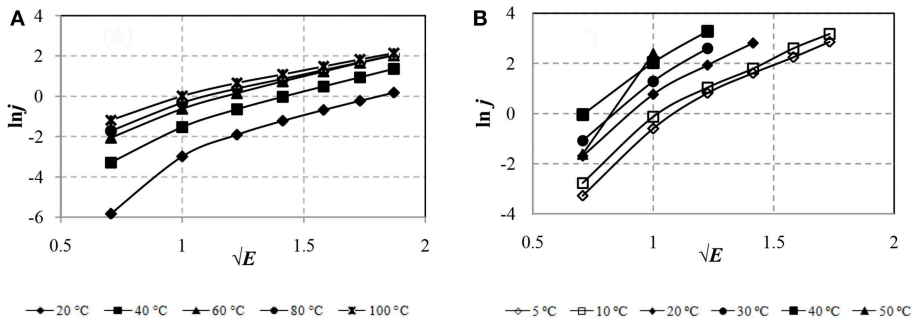

FIGURE 7 | CVC of ERF-1 **(A)** and ERF-2 **(B)** 2 samples in event thermoelectronic emission (Schottky mechanism).

The SCLC in the ERF-1, associated with the trapping of electrons on traps, is significantly lowwe than in the ERF-2 and slightly changes with a temperature increase from 60 to 100°C. This result can be explained by the presence of a larger number of acceptor traps and their faster filling with increasing temperature in ERF-1 compared to ERF-2.

To identify the mechanism of conductivity in the ER fluid due to the thermoelectronic emission of Schottky, the experimental results are graphically presented in the coordinate system ln *j* from $\sqrt{}$E in **Figure 7**.

Figure 7 shows that the leakage currents of ERF-1 and ERF-2 in electric field strength $E \geq 1.0$ kV / mm ($\sqrt{E} = 1$) are due to the Schottky mechanism (thermoelectronic emission), as the CVC is approximated by a linear dependence at E from 1.0 to 3.5 kV/mm (from $\sqrt{E} = 1$ to $\sqrt{E} = 1.87$) in the whole range of temperatures. ERF-1 currents are significantly lower than ERF-2 currents. It is possible that a decrease in the current due to the Schottky effect may be associated with an increase in the height of the metal-semiconductor interfacial potential barrier for aluminum and phosphorus double doped TiO_2 (ERF-1) compared with only aluminum doped TiO_2(ERF-2).

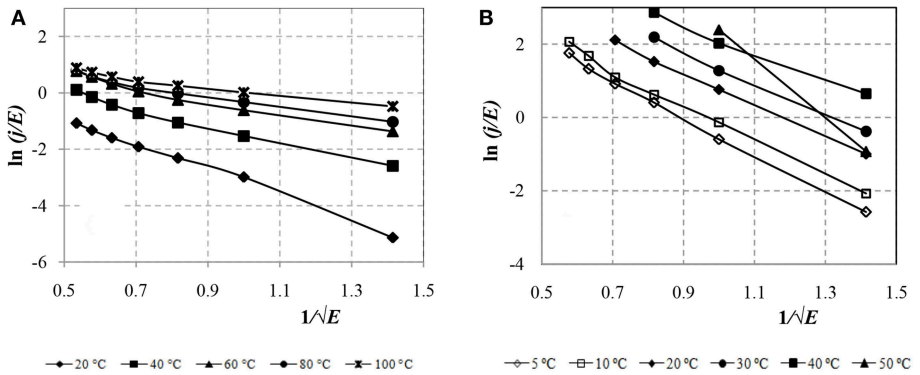

FIGURE 8 | CVC of the ERF-1 **(A)** and ERF-2 **(B)** samples in event of field emission of electrons from the electrode metal.

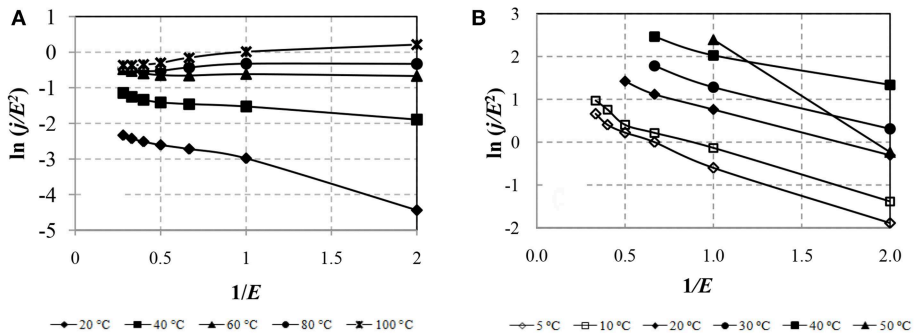

FIGURE 9 | CVC of samples ERF-1 **(A)** and ERF-2 **(B)** in the coordinates of the field emission from the traps.

To identify the mechanism of conductivity due to field emission of electrons from a metal, **Figure 8** presents the CVC of ERF-1 and ERF-2 in the Fowler-Nordheim coordinates.

Figure 8 shows that the conductivity of the ERF-1 and ERF-2 samples is due to the Fowler-Nordheim tunneling mechanism, since the CVC is approximated by a linear dependence. The double doping of TiO_2 with aluminum and phosphorus reduces the leakage current in ERF-1 caused by the field emission of electrons from a metal.

To identify the mechanism of conduction of the field emission of electrons from the traps, the CVC is constructed in the coordinates ln (j/E^2) from 1/E. **Figure 9** shows the CVC characteristics of the ERF-1 and ERF-2 samples in the field emission coordinates at different temperatures.

Figure 9 shows that the leakage currents of ERF-1 and ERF-2, are due to the conduction mechanism, known as field emission of electrons from traps, and the leakage currents of ERF-1 are much less at $T \geq 60°C$ and depend little on the electric field strength and temperature.

Analysis of the CVC of the materials under study made it possible to determine the mechanisms of formation (transfer) of charge (electron) in ER-fluids with semiconductor dispersed fillers with various modifications of their structure, which determine the rheological behavior of fluids on temperature changes (the impact mechanism is manifested with much stronger energy effects).

Double doping TiO_2 with aluminum and phosphorus significantly reduces leakage currents in ERF with TiO_2/Al/P compared to currents in ERF with TiO_2/Al caused by all the above mentioned conduction mechanisms. This may be due to an increase in the number of TiO_2 lattice defects during double doping, which are charge recombination centers, as well as an increase in the degree of recombination of electrons and holes, since the simultaneous introduction of donor and acceptor impurities leads to mutual compensation of charge carriers. In addition, the results obtained may be due to an increase in the metal-semiconductor interfacial potential barrier when using aluminum and phosphorus double doped TiO_2 compared with the use of aluminum doped TiO_2.

CONCLUSION

The results of the study of the rheological and electrophysical characteristics of the ER fluid with TiO_2 particles doped with aluminum and phosphorus and their comparison with the characteristics of the ER fluid with TiO_2 particles doped with aluminum alone, revealed the following regularities and behavioral features of ER fluids with semiconductor dispersed materials having modified crystal structures (anatase), in electric

fields of direct current up to 3.5 kV/mm in the temperature range of 5–100°C:

- Double doping of TiO_2/Al/P allowed to increase the value of ε' in the ERF by 1.5 times compared to ERF with TiO_2/Al, which indicates an increase in the polarization ability of the particles of the modified material of the dispersed phase.
- A comparison of the conduction currents of the considered EPF samples in the range of the electric field strength from 0 to 3.5 kV/mm showed that with double doping of TiO_2/Al /P the leakage current is 30 times lower. This made it possible to increase the value of the electric field strength to 3.5 kV/mm, in contrast to the maximum achievable value in the ERF with TiO_2/Al–only 2 kV/mm.
- Analysis of the results of measuring the shear stress in an electric field with a temperature change in the range from 20 to 100°C showed that all the dependences of the shear stress on the electric field strength τ (E) do not depend on temperature only for ERF with TiO_2/Al/P.
- The determination of the linearity of the dependences of the CVC in the corresponding coordinates, which are characteristic for the measurement of semiconductors of materials, made it possible to determine the main mechanisms charge transfer induce in leakage currents in the samples of ER fluids. It has been established that when exposed to a strong electric field taking into account heating in an extended temperature range, leakage currents are induced by conduction mechanisms such as thermoelectronic ionization, electron injection from an electrode, thermal excitation of charges, thermoelectronic emission, field emission from a metal (tunnel effect), field emission of electrons traps (trap tunneling).

AUTHOR CONTRIBUTIONS

EK conceived the study, revised the manuscript, and supervised the work. ZN performed the experiments, contributed to data analysis and manuscript review.

REFERENCES

Böse, H., and Trendler, A. (2001). Comparison of rheological and electric properties of ER fluids based on different materials. *Int. J. of Modern Phys. B.* 15, 626–633. doi: 10.1142/S0217979201005088

Fowler, R. H., and Nordheim, L. (1928). Electron emission in intense electric fields. *Proc. Roy. Soc.* 109, 173–181. doi: 10.1098/rspa.1928.0091

Hao, T., Kawai, A., and Ikazaki, F. (1998). Mechanism of the electrorheological effect: evidence from the conductive, dielectric, and surface characteristics of water-free Electrorheological fluids. *Langmuir* 14, 1256–1262. doi: 10.1021/la971062e

Kofstad, P. (1972). *Nonstoichiometry, Diffusion and Electrical Conductivity in Binary Metal Oxides*. New York, NY: Wiley.

Korobko, E., Novikova, Z., Murashkevich, A., and Kharlamova, I. (2018). Effect of the filler composition on the Electrorheological response of dielectric suspensions in an enlarged temperature range. *J. Intell. Mater. Syst. Struc.* 29, 242–249. doi: 10.1177/1045389X17704073

Korobko, E. V., Novikova, Z. A., and Kharlamova, I. M. (2012). *Structural and Rheological Features of the Behavior of Nanoscale Electrosensitive Dispersions. Preprint No. 1*. Minsk: A. V. Luikov Heat and Mass Transfer Institute, National Academy of Sciences of Belarus.

Mitrofanov, V., and Phogel, V. (1965). *Physics and Chemistry of Semiconductors*. Leningrad: Shipbuilding.

Murashkevich, A. N., Alisenok, O. A., Zharsky, M. I., Korobko, E. V., and Novikova, Z. A. (2017). The effect of the conditions for producing nano-sized titanium dioxide modified with aluminum on the effectiveness of its use in electrorheological dispersions. *Colloid J.* 79, 65–72. doi: 10.1134/S1061933X17010100

Shalimova, K. V. (1985). *Physics of Semiconductors*. Moscow: Energoatomizdat.

Shang, Y. L., Jia, Y. L., Liao, F. H., Li, J. R., Li, M. X., Wang, J., et al. (2007). Preparation, microstructure and electrorheological property of nanosized TiO_2 particle materials doped with metal oxides. *J. Mater. Sci.* 42, 2586–2590. doi: 10.1007/s10853-006-1336-5

Sze, S. M. (1981). *Physics of SemiconductorsDevices*. New York, NY: John Wiley & Sons, Inc.

Tang, H., He, J., and Jacques, P. (2010). Giant electrorheological effects of aluminum-doped TiO_2 nanoparticles. *Particuology* 8, 442–446. doi: 10.1016/j.partic.2010.07.007

Xu, Y. Z., Liang, R. F., Hao, T., Zhang, Q. Z., Xu, Z. M., and Chen, Y. H. (1992). "Design of high performance dry electrorheological fluid," in *Proceedings of the International Conference ERF*. (Singapore).

Yin, J. B., and Zhao, X. P. (2001). Temperature effect of rare earthdoped TiO_2 electrorheological fluids. *J. Phys. D Appl. Phys.* 34, 2063–2067. doi: 10.1088/0022-3727/34/13/317

Yin, J. B., and Zhao, X. P. (2006). Enhanced electrorheological activity of mesoporous Cr-doped TiO_2 from activated pore wall and high surface area. *J. Phys. Chem. B* 110, 12916–12925. doi: 10.1021/jp0554588

Yu, J. C., , Zhang, L., Zheng, Z., and Zhao, J. (2003). Synthesis and characterization of phosphated mesoporous titanium dioxide with high photocatalytic activity. *Chem. Mater.*15, 2280–2286. doi: 10.1021/cm0340781

Conflict of Interest Statement: The authors declare that the research was conducted in the absence of any commercial or financial relationships that could be construed as a potential conflict of interest.

frontiers in Materials

ORIGINAL RESEARCH
published: 17 May 2019
doi: 10.3389/fmats.2019.00111

Research on Ferromagnetic Hysteresis of a Magnetorheological Fluid Damper

Zhaochun Li and Yao Gong*

College of Mechanical and Electronic Engineering, Nanjing Forestry University, Nanjing, China

The inherent hysteresis of magnetorheological fluid dampers is one of the main reasons which limit their applications. The hysteresis mainly caused from two aspects. One part of the hysteresis is between the damping force and the piston velocity, which induced from the friction force of the damper, the compressibility of the fluid, rheological behavior etc. Another part of the hysteresis is between the damping force and the control current, which induced from the ferromagnetic materials inside the MR fluid damper. The ferromagnetic hysteresis of the MR fluid damper has been paid little attention to for a long time. Currently, the MR fluid damper is applying to the field of high velocity or shock and impact loadings where ferromagnetic hysteresis reduces the performance of the control current which leads to worse performances of vibration or buffer. Hall sensors are embedded to the MR fluid damper in this paper so that the magnetic flux density of the damping channels can be measured in real time. The hysteresis loops of the damping channels are obtained by measuring the relationships of the magnetic flux densities and the control currents. Furthermore, a Jiles-Atherton (J-A) hysteresis model based on differential equations for the MR fluid damper is established. The J-A hysteresis model is according to the domain-wall theory so that it has clear physical meaning with a small number of parameters. The hysteresis model is simulated utilizing MATLAB/SIMULINK. The particle swarm optimization (PSO) is adopted to identify the parameters of the J-A hysteresis model. The results show that the hysteresis loops identified by PSO is more similar to the measured hysteresis loops compared with the traditional parameter identification method. The research in this paper on the characteristic and model of the ferromagnetic hysteresis of the MR fluid damper is benefit to decrease or eliminate the effects of hysteresis which can improve the performances of the MR fluid dampers.

Keywords: MR fluid damper, hysteresis, Jiles-Atherton model, parameter identification, nonlinear system

OPEN ACCESS

Edited by:
Marcelo J. Dapino,
The Ohio State University,
United States

Reviewed by:
Luwei Zhou,
Fudan University, China
Xufeng Dong,
Dalian University of Technology (DUT), China

****Correspondence:***
Zhaochun Li
lzc.hn@163.com

Specialty section:
This article was submitted to Smart Materials, a section of the journal Frontiers in Materials

Received: *18 December 2018*
Accepted: *30 April 2019*
Published: *17 May 2019*

Citation:
Li Z and Gong Y (2019) Research on Ferromagnetic Hysteresis of a Magnetorheological Fluid Damper. Front. Mater. 6:111. doi: 10.3389/fmats.2019.00111

INTRODUCTION

Magnetorheological (MR) dampers have the advantages of continuous adjustable damping force, large and wide adjustable range, low energy consumption and wide dynamic range. Magnetorheological dampers have attracted wide attention in the field of Engineering Vibration reduction. Relevant research has been widely carried out in vehicle, civil engineering, household appliances, medical health, military engineering and other fields (Ahmadian et al., 2002; Carlson, 2002; Hiemenz et al., 2009; Gordaninejad et al., 2010). In recent years, the research results of MR dampers have gradually

penetrated into the field of shock buffer control (Singh et al., 2014; Shou et al., 2018; Li et al., 2019). It provides a new way of thinking for shock cushioning in engineering. However, the inherent hysteretic non-linearity of MR dampers is one of the main reasons that limit their wide application in engineering, especially in the field of shock buffering. The hysteretic non-linearity of MR dampers is particularly prominent because the shock buffering system requires rapid and accurate response control to achieve impact resistance.

The hysteretic non-linearity of MR dampers mainly comes from two aspects (Seong et al., 2009):

(1) Hysteretic non-linearity between damping force and velocity. This part of the hysteresis is caused by friction and fluid compression in the damper, as well as the non-linear rheological properties of magnetorheological fluid, such as yield stress and shear thinning. Hysteretic non-linearity between damping force and velocity can usually be described and eliminated by establishing hysteretic dynamic model.

(2) Hysteresis non-linearity (i.e., hysteresis characteristics) between adjustable damping force and control current. It is caused by the inclusion of ferromagnetic materials in the internal structure of MR damper. The hysteresis non-linearity between magnetic induction and magnetic field intensity is caused by the magnetization characteristics of ferromagnetic materials, which is commonly called hysteresis loop. The magnetic field intensity of the internal damping channel of MR damper is generated by the control current. The adjustable yield stress is a function of magnetic induction intensity. Therefore, the hysteretic non-linearity between magnetic induction and magnetic field intensity will greatly affect the relationship between damping force and control current.

On the one hand, most low-speed vibration systems do not require high real-time performance, so the hysteretic non-linearity between the adjustable damping force and the control current of MR dampers has little effect. For a long time, hysteresis non-linearity has not attracted enough attention. On the other hand, it is difficult to model this part of hysteresis with dynamic equation of the MR damper, so it is ignored by most researchers.

However, the magnetorheological materials and structures in shock buffer systems are greatly affected by the coupling of magnetic field, flow field, temperature field and other physical fields. The structural parameters of MR dampers change with time, which are unknown, time-varying and non-linear. This makes the hysteretic non-linearity between the adjustable resistance and current of MR dampers complicated and uncertain. For shock buffering system, the hysteresis characteristics of MR dampers greatly affect the accuracy of prediction and control of damping force. The hysteresis characteristics of MR dampers for impact buffering are tested experimentally and the model is established in this paper, which will provide a research basis for the compensation or elimination of the hysteresis of MR fluid dampers.

At present, there are three most commonly used methods for hysteresis modeling: Preisach hysteresis model, J-A hysteresis model and neural network hysteresis model. Preisach model is the most general operator-based model. It assumes that hysteresis can be modeled as the sum of a weighted hysteresis operator. However, the construction of weighting function and the experimental measurement of related parameters are more difficult, and the repeatability of a large number of data points and system behavior has a direct impact on the accuracy of the model (Joseph, 2001). On the other hand, the establishment of Preisach model needs to take into account the anisotropy and frequency factors (Ge and Jouaneh, 1997), which leads to a much too complication mathematical expression, so it is not convenient for numerical calculation. Neural network model has strong non-linear fitting ability, so it can map almost any complex non-linear relationship. At the same time, it has strong robustness, memory ability, non-linear mapping ability and strong self-learning ability. However, the approximation and generalization ability of network models are closely related to the typicality of learning samples, and neural network methods usually require at least thousands or even millions of labeled samples. It is difficult to select typical samples from the problem to form training set.

J-A mathematical model was presented by Jiles D C and Atherton D L to descript the hysteresis mechanism in ferromagnets (Jiles and Atherton, 1986). J-A hysteresis model is a typical differential equation-based model (Jiles and Atherton, 1986, 1998). It is based on the domain wall theory of ferromagnetic materials. J-A model theory holds that the existence of non-magnetic inclusions, internal stresses, grain boundaries, and other constraints hinders the irreversible magnetization process caused by domain wall substitution, resulting in hysteresis. This explanation accords with the physical law of hysteresis phenomenon. Moreover, J-A model has fewer parameters, and its physical meaning is clear and easy to implement. This model can truly describe the non-linear relationship between magnetic field intensity and magnetic induction intensity. The accurate hysteresis loop can be obtained by solving the differential equation of J-A model. Therefore, J-A model is widely used in the field of hysteresis modeling and simulation of ferromagnetic materials. In this paper, the magnetic circuit part of the MR fluid damper is composed of piston, cylinder and MR fluid. The materials of the piston and the cylinder of the MR fluid damper in this paper are both SAE1045 steel. And the MR fluid contains soft magnetic particles. Therefore, it is reasonable to use J-A model to descript the ferromagnetic hysteresis curve of the MR fluid damper.

Because of the complexity of hysteresis non-linearity, the calculation of model parameters is a key problem in the process of establishing J-A hysteresis model. Many non-linear optimization methods are used to calculate the parameters of J-A hysteresis model. However, these optimization methods are vulnerable to the selection of initial values of parameters. For example, Jiles and Thoelke proposed a classical algorithm to estimate the parameters of J-A model (Jiles et al., 1992). By iterating the parameters, they find the optimal combination of parameters. However, the initial values of the parameters and the iteration order of the parameters have great influence on the method, which leads to low identification accuracy. In recent years, many intelligent optimization algorithms have been developed rapidly, and have been increasingly introduced into J-A model parameter identification, including

particle swarm optimization, genetic algorithm, and neural network (Wilson et al., 2001; Salvini and Fulginei, 2002; Cao et al., 2004; Leite et al., 2004; Marion et al., 2008; Trapanese, 2011).

In this paper, the J-A model is used to describe the hysteresis non-linearity between the magnetic induction intensity and the current of the MR fluid damper for shock buffering. The J-A hysteresis model is simulated numerically. The hysteresis characteristics of MR fluid damper damping channel are obtained by embedding small size Hall sensors into the damping channels. Five parameters of J-A hysteresis model are identified by the particle swarm optimization.

THEORY OF JILES-ATHERTON MODEL

J-A model theory assumes that domains with the same orientation belong to the same magnetic phase. Therefore, the spatial distribution of magnetic domains with different orientations need not be considered. It can only be regarded as the thermodynamic statistical distribution of many domains with different orientations. At the same time, it is assumed that the angle of domain wall is 180 degrees, and the thickness of domain wall is not taken into account. In addition, it is assumed that all pinning points are uniformly distributed and have the same pinning energy (Jiles and Atherton, 1986). It is assumed that the irreversible magnetization component caused by domain wall substitution in J-A model is M_{irr}. The reversible magnetization component caused by domain wall bending is M_{rev}. So the total magnetization is

$$M = M_{irr} + M_{rev}, \tag{1}$$

where M_{irr} and M_{rev} can be obtained from the hysteresis-free intensity of magnetization M_{an}.

$$M_{rev} = c(M_{an} - M_{irr}), \tag{2}$$

where c is a reversible magnetization coefficient. It characterizes the relationship between the reversible and irreversible components of magnetization.

Weiss's "molecular field" theory holds that there exists a strong field effect in ferromagnetic materials. Under this effect, the magnetic moments of each atom tend to align spontaneously and produce spontaneous magnetization until saturation. Weiss calls this action a "molecular field" and expresses it in H_m. The expression is shown as,

$$H_m = \alpha M, \tag{3}$$

where α is the coefficient of the molecular field. According to Weiss molecular field theory, α can be expressed as $\alpha = \frac{\theta}{C}$, where θ is paramagnetic Curie temperature, and C is the Curie constant.

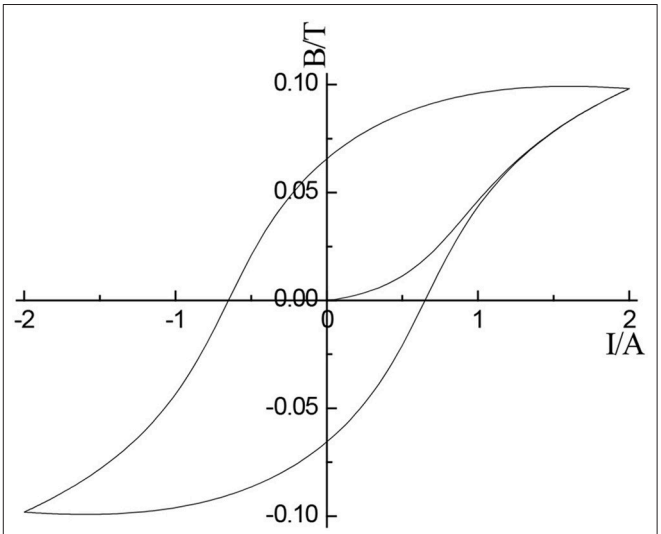

FIGURE 2 | J-A hysteresis loop by numerical simulation ($M_S = 1.6 \times 10^6$, $a =$ 1,100, $\alpha = 0.0017$, $c = 0.26$, $k = 400$).

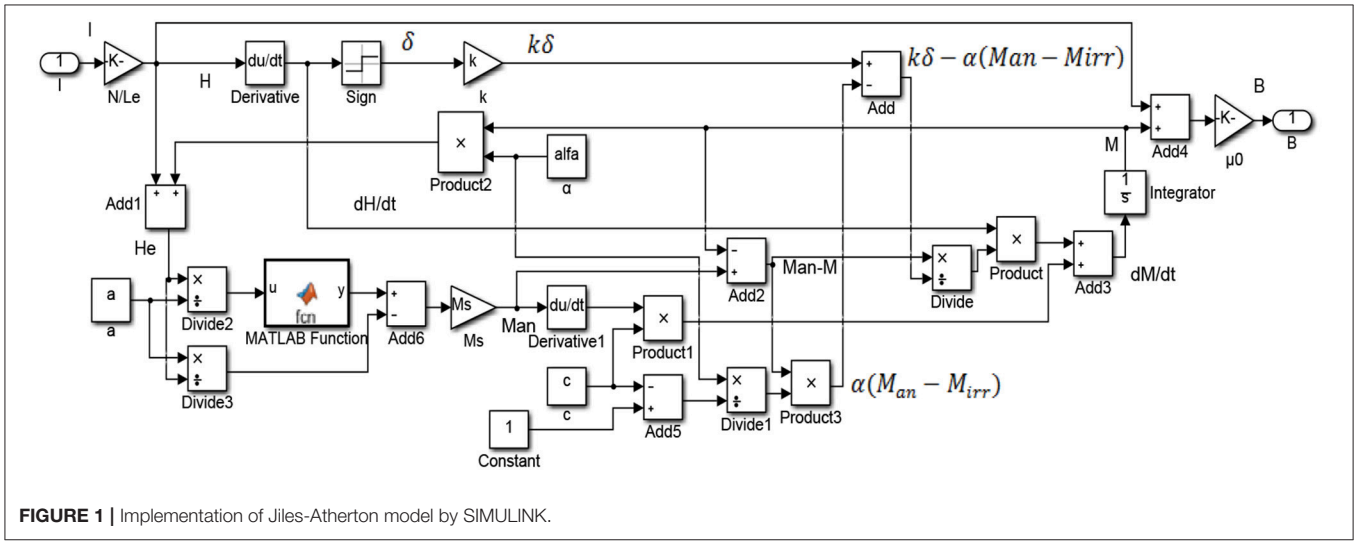

FIGURE 1 | Implementation of Jiles-Atherton model by SIMULINK.

Assuming that the direction of the external magnetic field H is the same as that of the magnetization intensity M, the effective magnetic field strength is

$$H_e = H + \alpha M. \tag{4}$$

The hysteresis-free magnetization M_{an} is described by an improved Langevin function shown as

$$M_{an} = M_s \left[\coth\left(\frac{H_e}{a}\right) - \frac{a}{H_e} \right], \tag{5}$$

where M_s is the saturated magnetization density. It is related to the material's own characteristics and temperature. a is a shape parameter of non-hysteresis magnetization curve.

The magnetization intensity M can be obtained by Equation (1) and (2).

$$M = (1 - c)\, M_{irr} + cM_{an}. \tag{6}$$

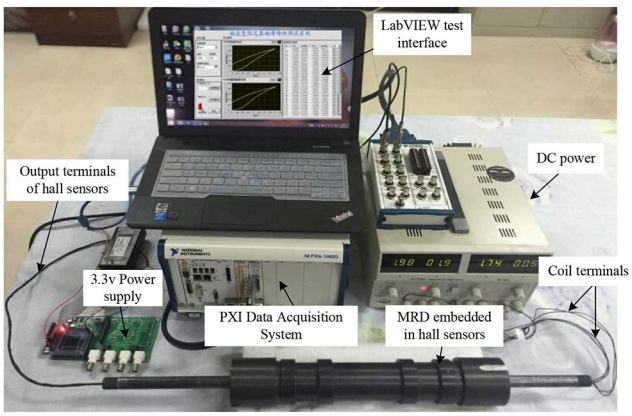

FIGURE 3 | Experimental setup of hysteresis characteristics of MR fluid damper.

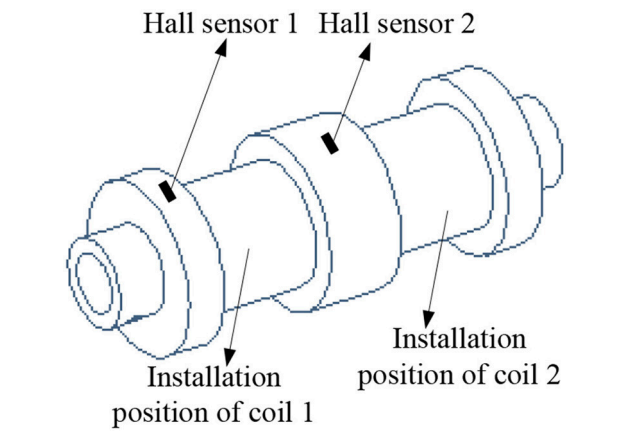

FIGURE 4 | The sketch of the piston of the MR fluid damper labeled the locations and installation of the two Hall sensors.

The following equation is obtained by the derivation of external magnetic field H on both sides of Equation (6).

$$\frac{dM}{dH} = (1 - c)\frac{dM_{irr}}{dH} + c\frac{dM_{an}}{dH}. \tag{7}$$

The differentiation of magnetic field strength H by irreversible component M_{irr} is expressed by the following equation

$$\frac{dM_{irr}}{dH} = \frac{M_{an} - M_{irr}}{k\delta - \alpha(M_{an} - M_{irr})}, \tag{8}$$

where k is the constraint parameter. It is multiplied by vacuum permeability μ_0 as hysteresis loss parameter K. K represents the change of energy loss in each element during magnetization, which is proportional to the number of pinning points and energy. δ is a parameter indicating the direction of magnetic field change. When $dH/dt > 0, \delta = 1$. When $dH/dt < 0, \delta = -1$.

The following equation is obtained by Equation (7) and (8)

$$\frac{dM}{dH} = (1 - c)\, \frac{(Man - Mirr)}{k\delta - \alpha\,(Man - Mirr)} + c\frac{dMan}{dH}, \tag{9}$$

or

$$\frac{dM}{dH} = \frac{(Man - M)}{k\delta - \alpha\frac{Man - M}{1 - c}} + c\frac{dMan}{dH}. \tag{10}$$

Simulation of Jiles-Atherton Model

Jiles-Atherton model describes the relationship between magnetization intensity M and magnetic field H. Because the magnetic induction intensity B is directly involved in the calculation of the electromagnetic energy conversion relationship of the MR fluid damper, the differential equation of M-H is transformed to obtain the B-H differential relationship as follows

$$B = \mu_0(H + M), \tag{11}$$

where, $\mu_0 = 4\pi \times 10^{-7} N/A^2$ is the vacuum permeability.

During the operation of MR fluid damper, the magnetic field strength H is determined by the current I loaded in the electromagnetic coil. The relationship between H and I is

$$H = \frac{NI}{L_e}, \tag{12}$$

where H is the intensity of the magnetic field, N is the number of turns of the excitation coil, I is the excitation current and Le is the effective length of the magnetic circuit.

Thus, the relationship between M-H can be transformed to B-I. In order to facilitate the numerical simulation, the two sides of Equation (8) are multiplied by dH/dt simultaneously and Equation (8) is transformed into a differential of time, as shown in the following formula.

$$\frac{dM}{dt} = (1 - c)\, \frac{(Man - Mirr)}{k\delta - \alpha\,(Man - Mirr)}\frac{dH}{dt} + c\frac{dMan}{dt}. \tag{13}$$

Equation (11), (12), and (13) is transformed into differential equation with current as input and magnetic induction as output.

Then the hysteresis model is established by using the simulation software MATLAB/SIMULINK. The simulation model is shown in **Figure 1**. Given five parameters of J-A hysteresis model (M_s, a, α, c, k), the hysteresis curve between magnetic induction intensity and current can be obtained. **Figure 2** is the hysteresis loop between magnetic induction B and current I when $M_s = 1.6 \times 10^6$, $a = 1{,}100$, $\alpha = 0.0017$, $c = 0.26$, $k = 400$.

TESTING OF HYSTERESIS CHARACTERISTICS OF MR FLUID DAMPER

The hysteresis characteristic test system of MR fluid damper designed in this paper is shown in **Figure 3**. The test system consists of DC power supply, MR fluid damper embedded in Hall sensors, PXI data acquisition system, LabVIEW test interface and 3.3 voltage power supply circuit board. The hardware of data acquisition system adopts PXIe-6363 module of PXI acquisition system produced by National Instruments Corporation. The test interface software is programmed by LabVIEW. The Hall sensors A1304ELHLX-05-T produced by Allegro Micro Systems is used in this paper. In order to measure the magnetic induction intensity of MR fluid passing vertically through the damping channel, two Hall sensors are embedded in the MR fluid damper and installed, respectively, on the circumferential surface of the two stages of the piston of the MR fluid damper. According to the structure of MR fluid damper, the circumferential area of the installation position of the second sensor is twice the circumferential area of the installation position of the first sensor. Every Hall sensor chip has three pins, which are 3.3 voltage power supply terminal, grounding terminal and output terminal, respectively. The power supply terminal and the ground terminal are connected to the power supply circuit board. The output terminal and the ground terminal are connected to the data acquisition module. According to the static output voltage and sensitivity coefficient of the sensor, the corresponding magnetic induction intensity is converted by the test interface software designed by LabVIEW. The DC power supplies current to the coil of MR fluid damper. The LabVIEW test interface software not only controls the acquisition hardware but also realizes the functions of saving experimental data and drawing and displaying hysteresis loop curve.

Figure 4 shows the exact locations and installation of the two Hall sensors and the installation position of the two coils. The two Hall sensors are installed on the surfaces of the circumferences of the piston of the MR fluid damper. In order to paste the two sensors on the surfaces tightly, the installed positions should be smoothed by a file before installation. As shown in **Figure 4**, the circumferential area where hall sensor 2 installed (area 2) is twice of the circumferential area where hall sensor 1 installed (area 1).

The hysteresis characteristics of the MR fluid damper for shock buffering are tested by using the experimental setup shown in **Figure 3**. The measurement of magnetic flux density is under the work of coil 1. The experimental scheme is to change the output current of DC power supply from 0 to 2 A. A total of 27 current values were selected to apply on the coils of the MR fluid damper. Then from 2 to 0 A, the corresponding 27 current values are also applied on the coils. The applied currents and the output voltage values of Hall sensor in the whole two processes are acquired by PXI data acquisition system. After a group of testing, the hysteresis curve is automatically drawn by the LabVIEW test interface. The test interface implemented by LabVIEW is shown in **Figure 5**. **Figure 6** are the hysteresis characteristic curves

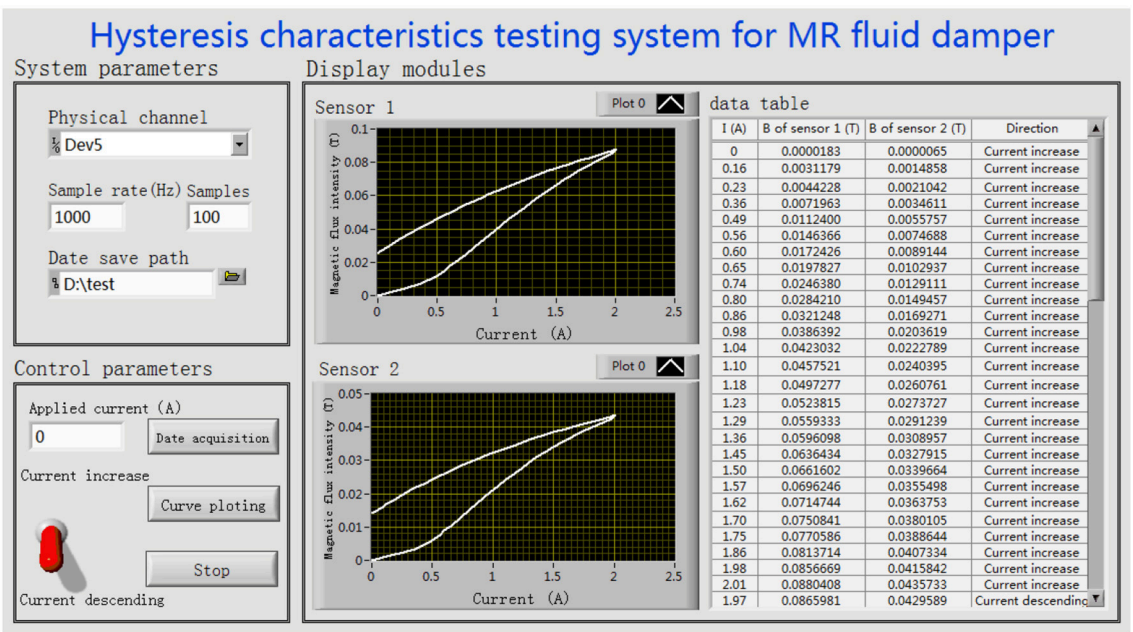

FIGURE 5 | Interface of hysteresis testing system for MR fluid damper utilizing LabVIEW.

measured by different Hall sensor on different stage of the piston of the MR fluid damper, respectively.

As can be seen from **Figure 6**, the magnetic flux intensity increases with the increase of the current. According to Kirchhoff's First Law of magnetic circuit, the magnetic flux density of area 1 theoretically is twice of that of area 2. **Figure 6** shows that the maximum magnetic flux density measured by sensor 1 is around 0.09 Tesla and the maximum magnetic flux density measured by sensor 2 is around 0.045 Tesla. The results are consistent with Kirchhoff's First Law of magnetic circuit. These results are consistent with the theoretical analysis. In the descending phase of current, the value of magnetic induction does not decrease to 0 with the input current being 0. The values measured by the two sensors are 0.026 and 0.015 tesla, respectively. The curve of magnetic flux intensity changing with current shows obvious hysteresis characteristics. The measured curves in **Figures 6A,B** show obvious hysteresis characteristic which is consistent with the J-A hysteresis loop by simulation shown in **Figure 2**.

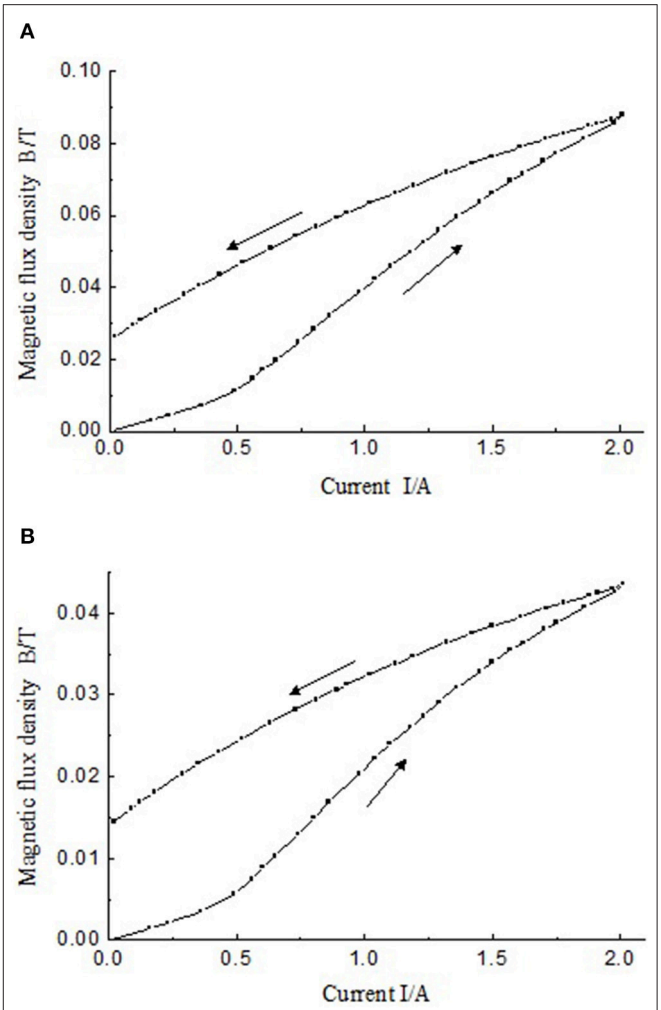

FIGURE 6 | Magnetic hysteresis curves measured by the sensors installed on circular surfaces of the piston of the MR fluid damper. **(A)** First sensor; **(B)** Second sensor.

PARAMETER IDENTIFICATION OF JILES-ATHERTON MODEL

Theory of Particle Swarm Optimization

Particle swarm optimization (PSO) is an intelligent optimization algorithm derived from the study of bird predation behavior. This algorithm was first proposed by American electrical engineer Eberhart and social psychologist Kennedy in 1995 (Kennedy, 2011). The quality of PSO solution is evaluated by fitness. It has no "crossover" and "mutation" operations of genetic algorithm, so its structure is simpler. In addition, PSO algorithm benefits from individual cooperation and information sharing to find the optimal solution. This algorithm has the advantages of easy implementation, less adjustment parameters and strong global optimization ability. PSO algorithm is widely used in the fields of electrical engineering, robot, and medical field (Yoshida et al., 2001; Bingul and Karahan, 2011; Hsieh et al., 2014).

Initialization of PSO algorithm generates a group of particles (random solutions) randomly, and the characteristics of particles are represented by three parameters: position, velocity, and fitness. The fitness value is calculated by fitness function. Whether it is good or not indicates the good or bad of particles. During the iteration, each particle moves in the search space. They update individual location by tracking individual extreme value and group extreme value. The individual extreme value P_{best} and the population extreme value G_{best} refer to the fitness value of the location experienced by the individual and the fitness value of the optimal location searched by all the particles in the population, respectively. The fitness value is calculated once the particle updates its position. After each update, the fitness and individual extremum of the new particle and the group extremum are compared, so that the position of individual extremum and group extremum is updated continuously.

Assume that the position and velocity of a particle are recorded as X_i and V_i, respectively. Assuming that the search space of the problem is a D-dimensional space, the position and velocity of particles can be expressed as $X_i = [x_{i1}, x_{i2}, \cdots, x_{id}]$ and $V_i = [v_{i1}, v_{i2}, \cdots, v_{id}]$. The individual extremum of the particle is denoted as $P_i = [p_{i1}, p_{i2}, \cdots, p_{id}]$. The extremum of the whole population is denoted as $P_g = [p_{g1}, p_{g2}, \cdots, p_{gd}]$. The velocity and the position of particles are updated according to the following equation

$$\begin{cases} v_{ij}(t+1) = wv_{ij}(t) + c_1 r_1 [p_{ij}(t) - x_{ij}(t)] + c_2 r_2 \\ \qquad \left[p_{gj}(t) - x_{ij}(t)\right] \\ x_{ij}(t+1) = x_{ij}(t) + v_{ij}(t+1) \\ 1 \le i \le n, 1 \le j \le D \end{cases}, \quad (14)$$

where t is the current iteration number and c_1 and c_2 are acceleration constants. It represents the weight of the statistical acceleration term that pushes each particle to the position of P_{best} and G_{best}. When the acceleration constant is small, particles are allowed to wander outside the target area before being pulled back. When the acceleration constant is large, the particle will

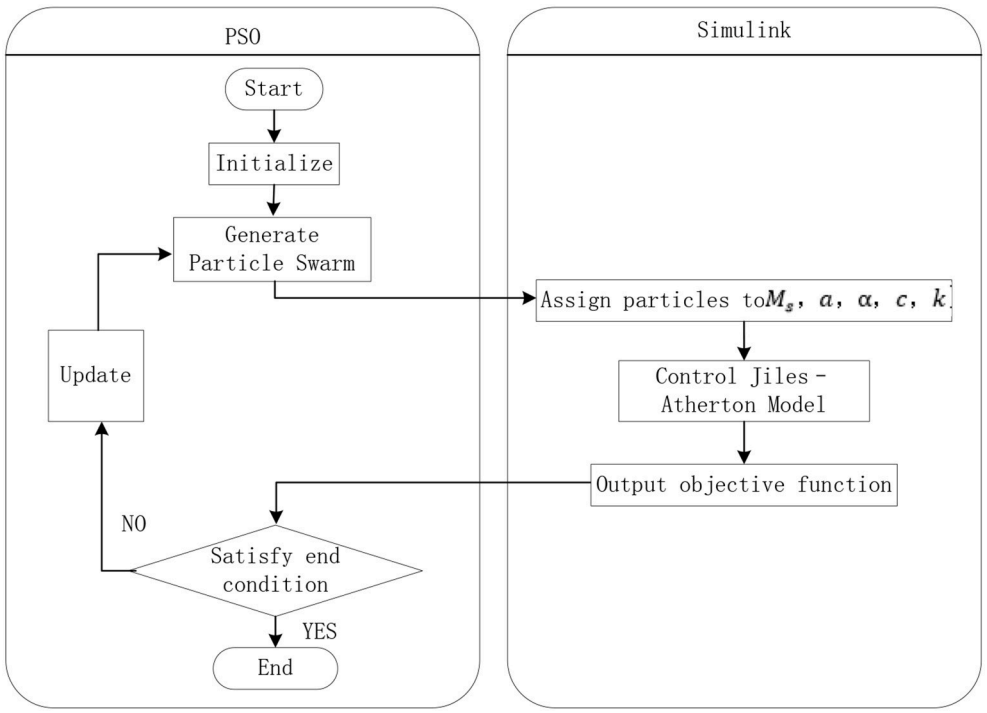

FIGURE 7 | Flow diagram of parameters optimization of Jiles-Atherton model using PSO.

suddenly exceed the target area, which will cause the fitness fluctuation. Usually, let $c_1 = c_2 = 2$. r_1 and r_2 are random numbers of [0,1], which are used to increase the randomness of search. w is called inertia factor. It is a non-negative number, which is used to adjust the search range of solution space. It represents global and local search capabilities. When w is large, it means the ability of global optimization is strong. On the contrary, it means that the local optimization ability is weak. In addition, the accuracy of the region between the current position and the optimal position is determined by the maximum velocity $v_{\max}$. If $v_{\max}$ is too large, the particle may cross the minimum point. On the contrary, the particle may fall into the local extremum region, which makes it impossible to explore the region beyond the local minimum. Therefore, the velocity of particle movement is limited to $[-v_{\max}, v_{\max}]$. That is, after each speed updates, if $v_{ij} < -v_{\max}$, then $v_{ij} = -v_{\max}$. If $v_{ij} > v_{\max}$, $v_{ij} = v_{\max}$.

Implementation of PSO

According to the experimental curve, the optimal values of five parameters in J-A hysteresis model are to solve the optimization problem. When the parameters of the model are obtained by PSO, the objective function shown in Equation (15) is used to evaluate the optimization performance.

$$J = \sqrt{\frac{\sum_{n=1}^{N} (B_m - B_d)^2}{N}} \tag{15}$$

TABLE 1 | Parameters optimization of J-A model for MR fluid damper.

Parameter	Group 1		Group 2	
	LSM	PSO	LSM	PSO
M_S(A/m)	1.5034×10^6	1.2456×10^6	0.9018×10^6	1.9332×10^6
a(A/m)	3.4340×10^4	2.6882×10^4	3.2706×10^4	3.4320×10^4
α	5.8263×10^{-3}	1.4697×10^{-4}	0.3414×10^{-2}	0.9021×10^{-2}
c	0.51524	0.5385	0.39107	0.2006
k(A/m)	6.4481×10^3	5.6943×10^3	1.1887×10^4	4.6041×10^4

where B_m is the measured value of magnetic flux intensity, B_d is the calculated value of the magnetic flux intensity, N is the number of measured value of the magnetic flux intensity.

When calculating the parameters of J-A model using PSO method, each particle in the population is regarded as a potential solution of the parameters of J-A model. The position of a particle can be expressed as $x_i(M_{si}, a_i, \alpha_i, c_i, k_i)$. That is to say, the position and velocity dimensions of each particle are 5-dimensional. In the calculation process, the objective function shown in Equation (15) is used as the fitness function of PSO algorithm. Five parameters are adjusted continuously by PSO algorithm to minimize the deviation between the experimental value of magnetic flux intensity and the calculated value. Thus, five parameters of J-A model will be identified and hysteresis loops will be obtained.

When the PSO optimization of J-A model is realized by using MATLAB/SIMULINK, the fourth-order Runge-Kutta method

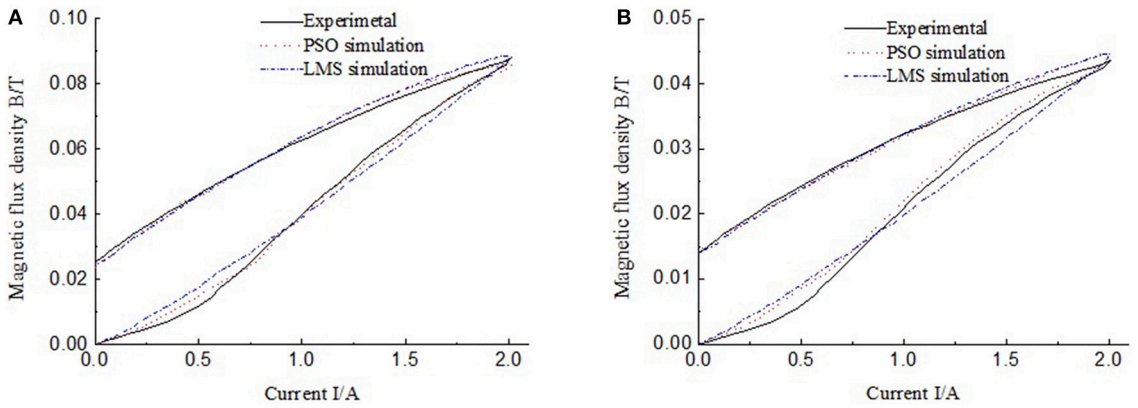

FIGURE 8 | Comparison of hysteresis curve using different optimization methods. **(A)** Group 1; **(B)** Group 2.

TABLE 2 | Accuracy comparison of PSO and LSM methods on parameter identification of Jiles-Atherton model.

Accuracy	Group 1		Group 2	
	LSM	PSO	LSM	PSO
Max absolute error (Tesla)	5.9×10^{-3}	3.3×10^{-3}	3.3×10^{-3}	2.8×10^{-3}
Max relative error	6.7%	3.4%	7.6%	6.4%
Average error (Tesla)	2.1×10^{-3}	1.0×10^{-3}	1.2×10^{-3}	0.8×10^{-3}
Average relative error	2.3%	1.2%	2.8%	1.9%

with fixed step size and high accuracy is selected to solve the problem. The time step is set to 0.01 s. PSO is used to optimize the parameters of J-A model. The steps are shown in **Figure 7**. The specific steps to achieve this are as follows.

(1) Setting the control variables of PSO algorithm, including inertia factor, acceleration constant, maximum number of iterations, particle swarm size, dimension of model parameters and search space.
(2) Initialization of particle swarm, i.e., random generation of initial values of model parameters.
(3) Call the J-A model in Simulink form, and then calculate the fitness of particles according to formula (15). If better p_{ij} and p_{gj} are obtained, the current optimal values are updated and saved.
(4) Update the velocity and position of each particle according to Equation (14).
(5) If the termination condition is not satisfied, the iteration is restarted from step 3. Otherwise, the operation is terminated and the optimal objective function value and corresponding model parameter value are displayed.

As shown in **Figure 7**, the PSO algorithm and J-A hysteresis model are connected by the five parameters of the model and the corresponding fitness of the particle. In the process of optimizing parameters of J-A model by PSO, PSO firstly generates particle swarm, and assigns the particles in the particle swarm to five parameters M_s, a, α, c, k of J-A model in turn. Then, utilizing the SIMULINK form of J-A model, the calculated values of the objective functions corresponding to these parameters are obtained. Finally, the calculated value is transferred to PSO as the fitness value of the particle to determine whether it can exit the algorithm.

During the simulation calculation of parameters of J-A model, the number of sampling points is set to 53. That means the number of sampling points equals to the number of measured magnetic flux density in this paper. The maximum value of current is set to 2A, which is the same condition with the experiment in this paper. For PSO simulation parameters, Swarm Size = 100. It indicates that there are 100 solution spaces. Maximum number of iterations MaxIter=100. The minimum fitness is 0.00001. The search space of the five parameters are set to the area within±100% near their true values. Inertial factor $w = 1$. The acceleration constant $c_1 = c_2 = 2$.

RESULTS AND DISCUSSIONS

Using the PSO parameter optimization method described above, the parameters of the hysteresis characteristic test results shown in **Figure 5** are identified. The parameters of J-A hysteresis model for two damping channels of the MR fluid damper can be obtained, respectively, as shown in **Table 1**. In order to compare, this paper also uses the traditional optimization method of least squares method (LSM) to optimize the model parameters. The results are listed in **Table 1** and compared with the optimization results of PSO method.

The results of group 1 and group 2 are the calculation results of the data measured by sensor 1 and sensor 2, respectively. The results of parameter estimation by the two methods are shown in **Table 1**.

According to the optimized parameters in **Table 1**, the J-A hysteresis model curve can be plotted. The hysteresis curves of J-A hysteresis model under the PSO parameters and the LMS parameters are compared with experimental hysteresis curves as shown in **Figure 8**.

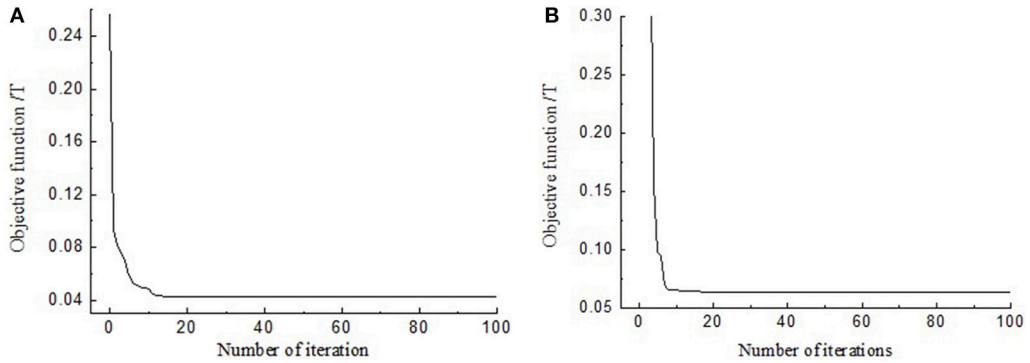

FIGURE 9 | Changes of the value of the objective function with the numbers of iteration using LMS. **(A)** Group 1; **(B)** Group 2.

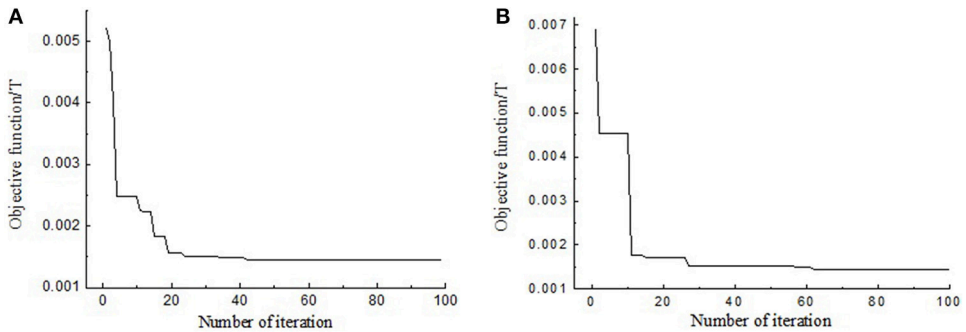

FIGURE 10 | Changes of the value of the objective function with the numbers of iteration using PSO. **(A)** Group 1; **(B)** Group 2.

TABLE 3 | Comparison of the value of objective function using LSM and PSO.

	Iteration times	Value of objective function using LSM (Tesla)	Value of objective function using PSO (Tesla)
Group 1	20	4.24×10^{-3}	0.156×10^{-3}
	50	4.24×10^{-3}	0.146×10^{-3}
Group 2	20	6.33×10^{-3}	0.171×10^{-3}
	50	6.33×10^{-3}	0.151×10^{-3}

Figures 8A,B show that, during the process of current increase, there are both small differences between the measured results and the curves drawn by J-A model under the LMS optimization method. In order to compare the accuracy of PSO and LSM methods, four kinds of errors are calculated from **Figure 8** and listed in **Table 2**. **Table 2** shows the max absolute errors, max relative errors, average errors and average relative errors of the two methods in prediction of ferromagnetic hysteresis curves of the MR damper. As we can see, the accuracy of PSO method is better than the LSM method on each position. The accuracy of the two methods is indicated by both the max relative error and the average relative error. Both the two relative errors show that the PSO method is better than the traditional LSM method in prediction of ferromagnetic hysteresis curves of the MR damper.

As we can see, for group 1, the relative errors of PSO are nearly half of those of LSM. For group 2, the relative errors of PSO are more than half of those of LSM. While, the variation of the magnetic flux density of group 1 is 0.09 Tesla and that of group 2 is 0.045 Tesla. The results in **Table 2** indicate that the larger the variation range of magnetic flux density, the better the PSO method works.

Figure 9 shows the change of objective function with the number of iterations using LMS optimization method. And **Figure 10** shows the change of objective function with the number of iterations using PSO optimization method.

In order to compare the convergence speed of PSO and LSM methods, the results of magnetic induction stabilization at the same iteration numbers are listed in **Table 3**. The iteration times of 20 and 50 are both selected to reveal the variation trend of the convergence speed. **Table 3** shows that when the iteration times reach to 20, the values of objective function using PSO are much smaller than that using LSM. Especially, for PSO, when the iteration times increases from 20 to 50, the values of objective function further decrease. However, for LSM, when the iteration times increases from 20 to 50, the values of objective function remain unchanged. The results indicate PSO has better global convergence ability than LSM on parameters optimization of hysteresis model of the MR damper.

J-A model is described by a differential equation as shown in Equation (9). The equation contains the parameter δ which has relation to the direction of the magnetic flied. That means J-A model equation is discontinuous and non-differentiable at some point. For PSO, the optimized function is not required to be differentiable, derivative and continuous. While, LSM is an identification method based on process gradient information. Its premise is differentiable cost function, differentiable performance index and smooth search space.

In addition, there is some orders of magnitude difference for the five parameters of J-A model of the MR damper. This determines that the search space is unknown and stochastic. As PSO algorithm is based on the stochastic solution to optimize iteratively, it will leads to better optimization parameters than LSM.

SUMMARY

In this paper, J-A hysteresis model is used to describe the hysteresis non-linearity of MR fluid dampers. According to the differential equation of J-A model, the numerical simulation model is established. The hysteresis characteristics test system of MR fluid damper is built. Then, the hysteresis loops of damping channels of the MR fluid damper in the working current range are obtained. The PSO optimization algorithm is applied to the parameter optimization of the model. Hence, five parameters of the model are optimized. The results of parameter optimization show that the hysteresis curves of MR fluid damper optimized by PSO algorithm is in good agreement with the experimental hysteresis loops compared with the traditional LMS optimization method. The hysteresis model and parameter identification of the MR fluid dampers in this paper provide support for eliminating or reducing the influence of hysteresis non-linearity on the performance of MR fluid dampers.

AUTHOR CONTRIBUTIONS

ZL research the theory of the hysteresis model, built the experimental setup and wrote the manuscript. YG realized the simulation of the hysteresis model, parameter identification, and hysteresis characteristic test.

FUNDING

This work is supported by National Natural Science Foundation of China (NSFC) grant funded by the Chinese Government (No. 51305207) and Natural Science Foundation of Jiangsu Provincial College (Nos. 13KJB460010 and 17KJB413002).

REFERENCES

Ahmadian, M., Appleton, R., and Norris, J. A. (2002). An analytical study of fire out of battery using magneto rheological dampers. *Shock Vibrat.* 9, 129–142. doi: 10.1155/2002/983140

Bingul, Z., and Karahan, O. (2011). "Tuning of fractional PID controllers using PSO algorithm for robot trajectory control," in *IEEE International Conference on Mechatronics,* (Istanbul), 955–960.

Cao, S., Wang, B., Yan, R., Huang, W., and Yang, Q. (2004). Optimization of hysteresis parameters for the Jiles-Atherton model using a genetic algorithm. *IEEE Trans. Appl. Superconduct.* 14, 1157–1160. doi: 10.1109/TASC.2004.830462

Carlson, J. D. (2002). "What makes a good MR fluid?" in *Electrorheological Fluids and Magnetorheological Suspensions*. 63–69. doi: 10.1142/9789812777546_0010

Ge, P., and Jouaneh, M. (1997). Generalized preisach model for hysteresis nonlinearity of piezoceramicactuators. *Precisi. Eng.* 20, 99–111. doi: 10.1016/S0141-6359(97)00014-7

Gordaninejad, F., Wang, X., Hitchcock, G., Bangrakulur, K., Ruan, S., Siino, M., et al. (2010). Modular high-force seismic magneto-rheological fluid damper. *J. Struct. Eng.* 136, 135–143. doi: 10.1061/(ASCE)0733-9445(2010)136:2(135)

Hiemenz, G. J., Hu, W., and Wereley, N. M. (2009). Adaptive magnetorheological seat suspension for the expeditionary fighting vehicle. *J. Phys. Con. Ser.* 149:012054. doi: 10.1088/1742-6596/149/1/012054

Hsieh, Y. Z., Su, M. C., and Wang, P. C. (2014). A PSO-based rule extractor for medical diagnosis. *J. Biomed. Inform.* 49, 53–60. doi: 10.1016/j.jbi.2014.05.001

Jiles, D. C., and Atherton, D. L. (1986). Theory of ferromagnetic hysteresis. *J. Magn. Magn. Mater.* 61, 48–60. doi: 10.1016/0304-8853(86)90066-1

Jiles, D. C., and Atherton, D. L. (1998). Theory of ferromagnetic hysteresis. *J. Appl. Phys.* 55, 2115–2120. doi: 10.1063/1.333582

Jiles, D. C., Thoelke, J. B., and Devine, M. K. (1992). Numerical determination of hysteresis parameters for the modeling of magnetic properties using the theory of ferromagnetic hysteresis. *IEEE Trans. Magn.* 28, 27–35. doi: 10.1109/20.119813

Joseph, D. S. (2001). *Parameter Identification for the Preisach Model of Hysteresis*. Blacksburg, VA: VirginiaTech.

Kennedy, J. (2011). Particle swarm optimization/ /Encyclopedia of machine learning. Boston, MA: Springer, 760–766.

Leite, J. V., Avila, S. L., Batistela, N. J., Carpes, W. P., Sadowski, N., Kuo-Peng, P., et al. (2004). Real coded genetic algorithm for Jiles-Atherton model parameters identification. *Magn. IEEE Trans.* 40, 888–891. doi: 10.1109/TMAG.2004.825319

Li, Z., Gong, Y., and Wang, J. (2019). Optimal control with fuzzy compensation for a magnetorheological fluid damper employed in a gun recoil system. *J. Intell. Mater. Syst. Struct.* 30, 677–688. doi: 10.1177/1045389X17754258

Marion, R., Scorretti, R., Siauve, N., Raulet, M. A., and Krahenbuhl, L. (2008). Identification of Jiles-Atherton Model Parameters Using Particle Swarm Optimization. *IEEE Trans. Magn.* 44, 894–897. doi: 10.1109/TMAG.2007.914867

Salvini, A., and Fulginei, F. R. (2002). Genetic algorithms and neural networks generalizing the Jiles-Atherton model of static hysteresis for dynamic loops. *Magn. IEEE Trans.* 38, 873–876. doi: 10.1109/20.996225

Seong, M. S., Choi, S. B., and Han, Y. M. (2009). Damping force control of a vehicle MR damper using a Preisach hysteretic compensator. *Smart Mater. Struct.* 18:074008. doi: 10.1088/0964-1726/18/7/074008

Shou, M., Liao, C., Zhang, H., Li, Z., and Xie, L. (2018). Modeling and testing of magnetorheological energy absorbers considering inertia effect with non-averaged acceleration under impact conditions. *Smart Mater. Struct.* 27:115028. doi: 10.1088/1361-665X/aae6a0

Singh, H. J., Hu, W., Wereley, N. M., Norman, M., and William, G., et al.(2014). Experimental validation of a magnetorheological energy absorber design optimized for shock and impact loads. *Smart Mater. Struct.* 23:125033. doi: 10.1088/0964-1726/23/12/125033

Trapanese, M. (2011). Identification of parameters of the Jiles-Atherton model by neural networks. *J. Appl. Phys.* 109:07D355. doi: 10.1063/1.3569735

Wilson, P. R., Ross, J. N., and Brown, A. D. (2001). Optimizing the Jiles-Atherton model of hysteresis by a genetic algorithm. *IEEE Trans. Magn.* 37, 989–993. doi: 10.1109/20.917182

Yoshida, H., Kawata, K., Fukuyama, Y., Takayama, S., and Nakanishi, Y. (2001). A particle swarm optimization for reactive power and voltage control considering voltage security assessment. *Power Syst. IEEE Trans.* 15, 1232–1239. doi: 10.1109/59.898095

Conflict of Interest Statement: The authors declare that the research was conducted in the absence of any commercial or financial relationships that could be construed as a potential conflict of interest.

frontiers in Materials

ORIGINAL RESEARCH
published: 01 May 2019
doi: 10.3389/fmats.2019.00095

Novel Spring-Buffered Variable Valve Train for an Engine Using Magneto-Rheological Fluid Technology

Yaojung Shiao, Mahendra Babu Kantipudi and Jing-Wen Jiang*

Department of Vehicle Engineering, National Taipei University of Technology, Taipei, Taiwan

Vehicle manufacturers have been attempting to increase engine efficiency and decrease pollution through various methods. Variable valve actuation technology is one of these methods. Several mechanisms have been established already and have been used to develop this technology. However, these systems have common problems such as complex design, large volume, low response rate, and high-energy consumption. In this study, a novel variable valve actuation device that is compact and requires less energy was developed using magnetorheological (MR) fluid technology. The main components used in this device are an MR valve, passive buffer spring, cam, and rocker arm. This study was divided into three parts. First, an MR valve train was designed. This valve train can be constructed easily, and has fewer hydraulic and mechanical components and consumes less energy than other technologies. Second, the magnetic plate block design was optimized to obtain the required control force at optimal volume and energy. Finally, dynamical simulations pertaining to the springs and the structure were executed to analyze the dynamic condition of the valve. The simulation results indicated that the proposed MR valve could effectively provide functions of variable valve timing and variable valve lift (VVL) by dynamically controlling the external current in the magnetic coil.

Keywords: magneto-rheological fluid, variable valve timing (VVT), variable valve lift (VVL), engine performance, valve actuation

OPEN ACCESS

Edited by:
Seung-Bok Choi,
Inha University, South Korea

Reviewed by:
Miao Yu,
Chongqing University, China
Jung Woo Sohn,
Kumoh National Institute of Technology, South Korea
Luwei Zhou,
Fudan University, China

****Correspondence:***
Yaojung Shiao
yshiao@ntut.edu.tw

Specialty section:
This article was submitted to Smart Materials, a section of the journal Frontiers in Materials

Received: *30 November 2018*
Accepted: *15 April 2019*
Published: *01 May 2019*

Citation:
Shiao Y, Kantipudi MB and Jiang J-W (2019) Novel Spring-Buffered Variable Valve Train for an Engine Using Magneto-Rheological Fluid Technology. Front. Mater. 6:95. doi: 10.3389/fmats.2019.00095

INTRODUCTION

Magnetorheological (MR) fluid is an intelligent fluid that can generate resistance corresponding to variations in a magnetic field. This liquid reacts quickly, can satisfy control operation requirements, and is reversible. MR fluid can be used in numerous types of machinery, such as resistance devices, brakes, and clutches. However, a various problems pertaining to the fluid must be addressed for its effective, practical application (Phu and Choi, 2019). These MR devices operate based on one of the three following resistance conditions—shear, flow, and mixed squeeze and flow resistances. Among these types, flow resistance is a promising concept for realizing intelligent devices for engineering applications. Devices using this concept are available, including dampers, shock absorbers, and MR valves.

Dampers are used in vehicles as shock absorbers for the operation of active and semi active suspension systems. Several mathematical models (Yao et al., 2002), experimental devices, and simulation studies have been achieved. Several studies have revealed the

potential of this technology in civil applications by developing an MR damper model (Dyke et al., 1996a,b, 1998). These studies clarify that compared with conventional devices, MR dampers are more effective, active, responsive, and consume less power.

Another flow mode for an MR device is an MR valve that can be used in hydraulic actuation systems. This valve is a valuable alternative to mechanical valves and exhibit many benefits such as low weight, ease of control, and no moving parts. Yoo and Wereley (2002) designed a high-efficiency MR valve with an optimal design. The analyzed its performance and verified it by conducting simulations and experiments. To enhance the performance of an MR valve, numerous MR valve structures have been established, such as a multistage structure, modular structure, and modular structure with meandering flow (Ichwan et al., 2016).

The adoption of this type of intelligent valve control in internal combustion (IC) engines to enhance engine performance is an innovative and valuable research approach. To improve the performance of an IC engine under certain speed and load conditions, the intake quantity and intake timing should be varied continuously (Lee et al., 2007). When suitable valve opening timing and valve lifts are selected, a 6% improvement in engine performance is possible (Sawant and Bari, 2018). Such an improvement cannot be obtained using the conventional cam-based fixed timing valve train control system. Therefore, engine developers have introduced various valve timing (VVT) and variable valve lift (VVL) systems with different actuators. Numerous devices with mechanical, hydraulic, and electronic actuators have been established to achieve such VVT and VVL systems.

Pierik and Burkhard (2000) developed an active mechanical valve and achieved a specific fuel consumption (SFC) improvement of 12% at low-to-medium load conditions. However, this device has drawbacks of a long response time, limited variations, and mechanical frictional elements.Flierl and Klüting (2000) from BMW group proposed electromechanical control that improved SFC by 11%. Sun and He (2007) presented an electrohydraulic valve circuit. However, the circuit requires considerable energy resources and has hydraulic fluid leakage problems. For MultiAir of FIAT, Bernard et al. (2009) used a hydraulic chamber as a clutch between the camshaft and valve. However, the structure of this system is complicated. Shiao and Dat (2013) proposed an electromagnetic valve device for a camless spark-ignition engine. All these devices have specific advantages and disadvantages. However, the common problems of the systems include mechanism complexity and high-energy consumption.

Therefore, this study aimed to fabricate a new valve train device by using the MR fluid technology, which can overcome those problems. It is hoped that the conventional valve-actuating mechanisms can be replaced with an intelligent MR-fluid-based valve to improve IC engine performance. The application of an MR valve in an IC engine is a novel concept. Recently, Smith (2018) invented an electromechanical hydraulic valve lifter based on MR technology for use in an IC engine.

A previous study by the author (Shiao and Cheng, 2016) introduced a new innovative valve device to realize this variable valve actuator, that is, the MR valve (MRV). This is a novel concept for IC engine valve actuation. The valve device has an active block, a magnetic plate block, and a buffer block. The viscosity of the MR fluid in the plate block can be controlled by using a magnetic field, and the lower piston motion is based on this viscosity. At a magnetic field intensity of zero, there is no resistance at the plate block, and thus, a full lift of the valve is obtained. When the field is activated, some of the motion is restricted by the plate block, thus opening the valve partially. The MRV device holds considerable value, but the large volume, low speed, and fluid leakage are major disadvantages.

Therefore, the objective of this study was to design a new, compact MR valve that can be easily fabricated for use in IC engines. This device was developed using the "compression distribution in parallel spring" concept, and this device has a straightforward mechanism and is easy to manufacture. This simple spring arrangement overcomes the leakage problems in the complex buffer block presented in Shiao and Cheng (2016). The primary block parameters were optimized by using magnetic simulations; thus, the volume of this device is lower than that of the previous model. The designed kinematic behavior was validated by conducting computer simulations. For manufacturing flexibility, the commercial MR fluid in the market was used for this device.

DESIGN OF NEW GENERATION MR VALVE

The model of the new magnetorheological fluid variable valve with a spring buffer is displayed in **Figure 1**. The cam and

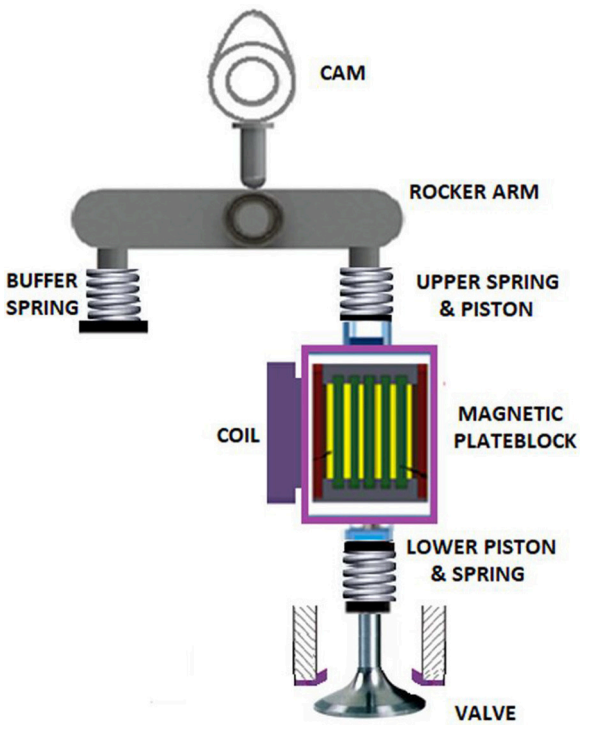

FIGURE 1 | The new magneto-rheological fluid variable valve.

follower set provide default valve actuation movement to the rocker arm. Then, the rocker arm transfers that motion to the side spring and the upper spring of the body simultaneously. The side spring, also called the buffer spring, compresses due to the rocker's motion. The upper spring is connected to the upper piston, which is connected to the plates in the magnetic plate block. The motion of the upper piston is transferred to the lower piston via these MR plates. The magnetic plate block has a series of MR fluid-filled plates and is surrounded by magnetic coils. The block changes the valve lift and timing by changing the MR fluid's flow resistance force. Finally, the lower piston is connected to the engine intake–exhaust valve with a return spring.

MRF-140CG (LORD Corporation, North Carolina, United States), which is an established and high-grade MR fluid, was used for this model. The properties of this fluid are as follows: the liquid viscosity at 40°C is 0.280 ± 0.070 Pa·s, the density is 3.54–3.74 g/cm3, the solid content by weight percent is 85.44%, the flash point is above 150°C, and the operation temperature is −40°C to 130°C (Lord-corporation, 2012). This fluid has favorable resistance to particle sedimentation; thus, it produces less sediment during short-time idle situations compared with other approaches. Moreover, sediment iron particles can be easily suspended in the MR fluid after only a few running cycles. Therefore, particle sedimentation is not a major problem for this device.

Working Modes

When the magnetic coils are energized, the magnetic field increases the flow resistance force in the MR fluid-filled plates. This force can be changed dynamically using magnetic field intensity control. By harnessing this flexibility, the required valve opening variations can be attained. This new MR fluid variable valve can control the required valve opening modes—fully open, fully closed, and adjustable.

Full Open Mode

When the new MR fluid variable valve is fully open, as shown in **Figure 2A**, the rocker pushes the upper piston body. Then, this force is transferred to the bottom side by the MR valve system to push the lower piston to open the valve. The upper and lower springs and the side-by-side springs are compressed simultaneously, and the rocker arm has a horizontal downward movement. At this time, the magnetic pole coils do not generate any current, that is, the MR fluid does not have any resistance except its natural viscosity, and the valve opens downwards smoothly.

Fully Closed

In the fully closed mode, as shown in **Figure 2B**, the coil current reaches its maximum value. Thus, a strong magnetic field is generated, and the resistance reaches its maximum value. When the rocker arm is pushed downward, the resistance of the magnetic pole region prevents the upper piston from being pressed downward. Thus, the valve lift is zero. At this time, the force on the side spring in this mode is larger than the forces in all other modes, and the rocker is in an inclined position.

Partially Open

In this mode, the resistance in the MR fluid can be controlled by varying the current in the coils. Based on this current control, as shown in **Figure 2D**, the resistance force against the piston motion varies. Thus, the side-by-side springs have different amounts of compression, as shown in **Figure 2C**. Therefore, the valve opens in proportion to the lift.

Moreover, by changing the timing of the applied current, the valve opening time can be delayed, as shown in **Figure 12**. When the valve is about to open based on the default cam timing, that is, at ∼117°, a maximum current of 0.6 A is applied. When the

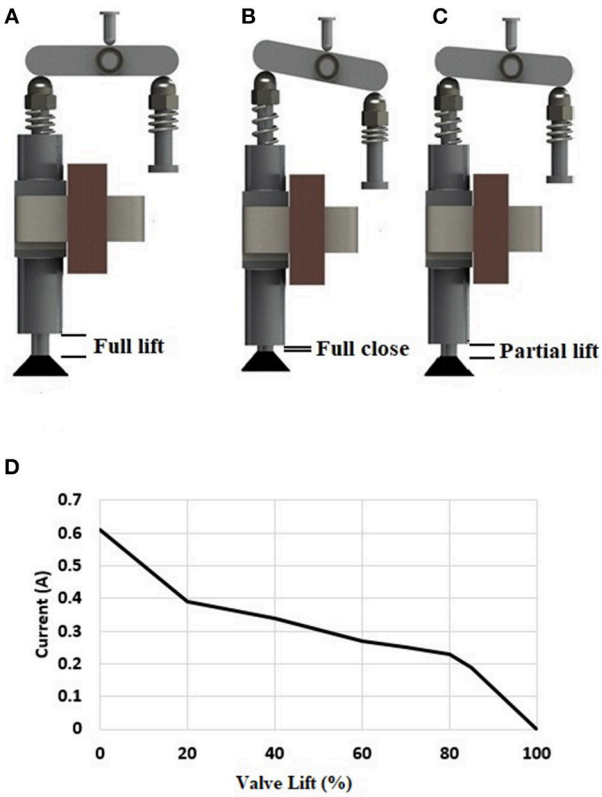

FIGURE 2 | Valve train mechanism at **(A)** fully open, **(B)** fully closed, **(C)** partial conditions, and **(D)** required current for different lifts.

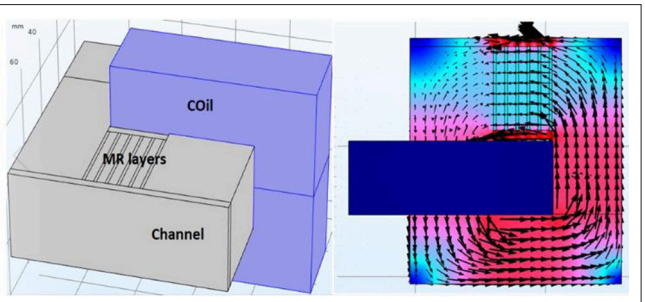

FIGURE 3 | Views of the resistance valve body.

required timing angle is attained, the current is reduced to zero immediately. Because of the design restriction, this device cannot provide valve closing variations, that is, an early valve closing option. Therefore, the valve closing timing is fixed based on the cam default angle.

OPTIMIZATION OF MAGNETIC PLATE BLOCK

The magnetic plate block is the most important part in this device as it provides the required resistance force. **Figure 3** presents the magnetic field flux direction and a top view and 3D diagram of the resistance valve (including the coil). The larger the magnetic field through the MR layers is, the greater is the resistance force generated by this block. By using a high-resistance force, greater spring stiffness can be obtained to achieve higher rotational speeds.

The main objective of this step is to maximize the resistance force in the given geometric constraints. Resistance force in a plate block is a cost function, which depends on the input ampere turn (AT), core material, magnetic channel width (w) and height (L), MR fluid layer thickness (h), partition plate thickness (s), and end wall thickness (d).

A magnetic analysis software program was used to achieve this optimized result. A 3D simulation model of the magnetic plate block was built, as shown in **Figure 3.** Parameters for optimization and governing equations were also included. After several magnetic simulations were conducted, these dimensions were optimized.

For the resistance force simulation of MR fluid, the MR fluid chaining force is as presented in Equation (1).

$$F_{dMR} = \frac{\dot{x}}{|\dot{x}|}\left(\frac{c_1 \tau_y L}{h}\right) A_p, \tag{1}$$

where, τ_y is the shear stress in the MR fluid and depends on the magnetic field (Equation 2).

$$\tau_y\,(B) = 0.98 * B^{1.61}. \tag{2}$$

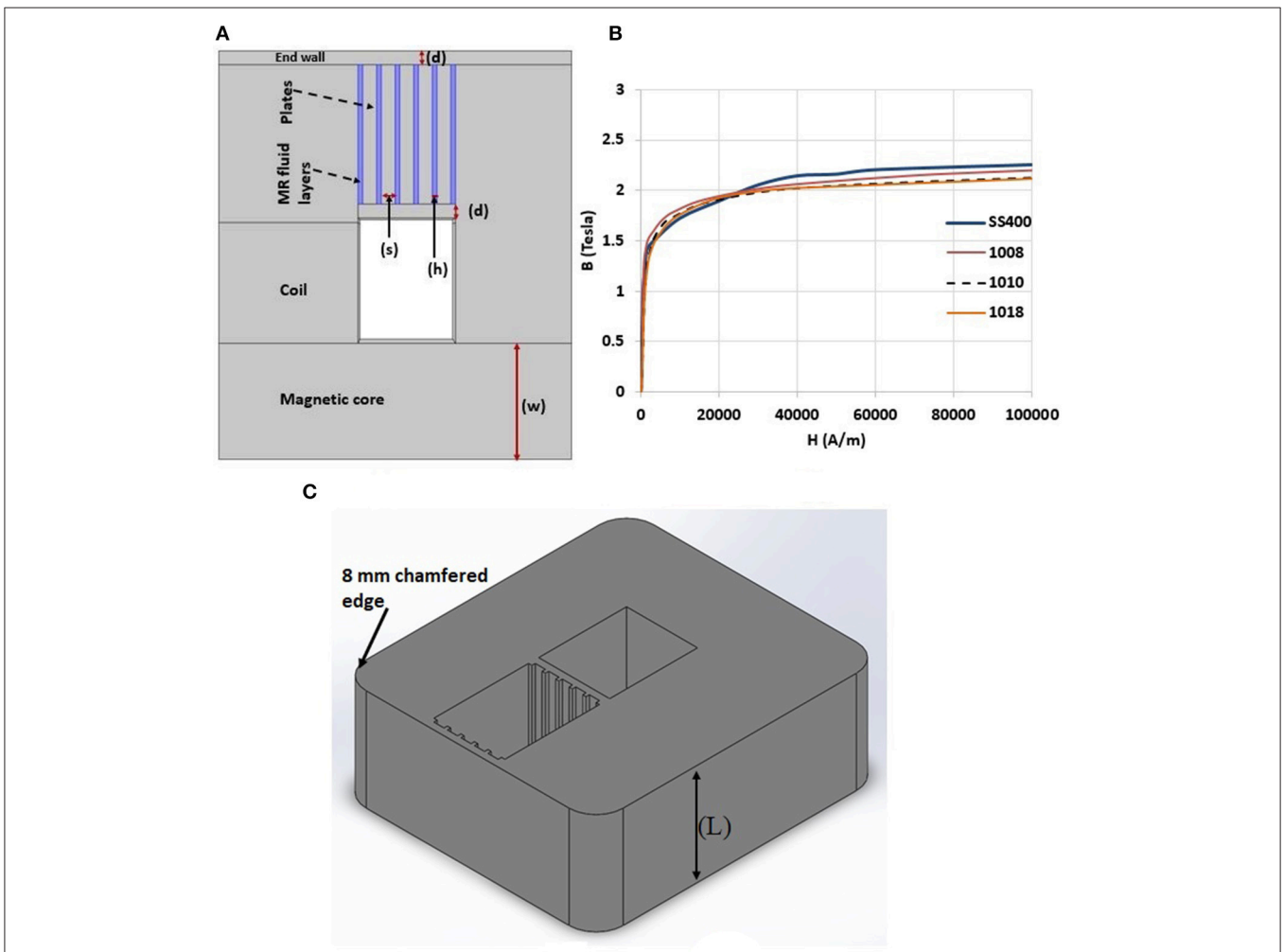

FIGURE 4 | (A) Schematic diagram of the thickness of the magneto-rheological fluid layer and the thickness of the separator **(B)** comparison of B-H curves of magnetic materials **(C)** 3D view of magnetic plate block.

MR fluid also contains viscous damping force as given in Equation (3).

$$F_{dn} = \left(1 + \frac{wh}{2A_p}\right)\frac{12\mu L{A_p}^2}{wh^3}\dot{x} = k\frac{12\mu L{A_p}^2}{wh^3}\dot{x}. \quad (3)$$

The total force can be calculated using the formula after the total number of partitions in Equation (4).

$$F_{total} = (n+1)(F_{dMR} + F_{dn}). \quad (4)$$

Here, B is the magnetic induction, L is the length of the magnetic field channel, h is the gap between the upper and lower plates, A_p

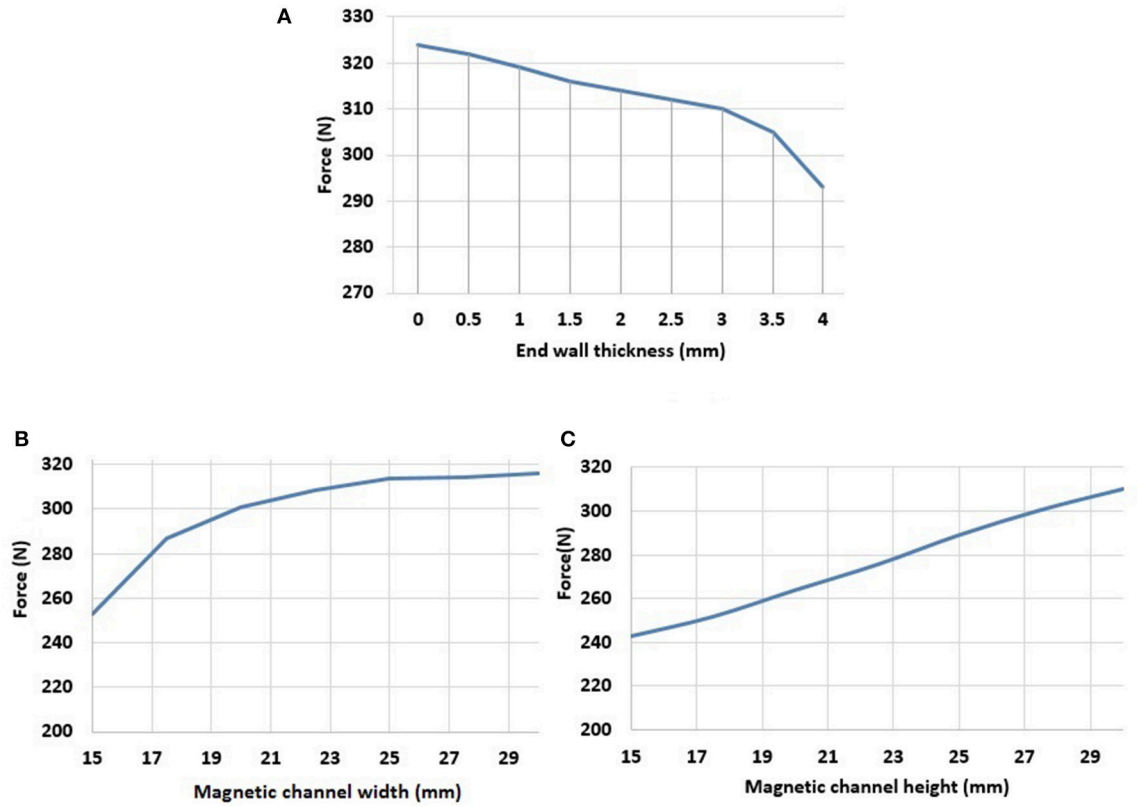

FIGURE 5 | (A) Maximum resistance force with different wall thicknesses **(B)** maximum resistance at different magnetic channel widths **(C)** maximum resistance at different magnetic channel height.

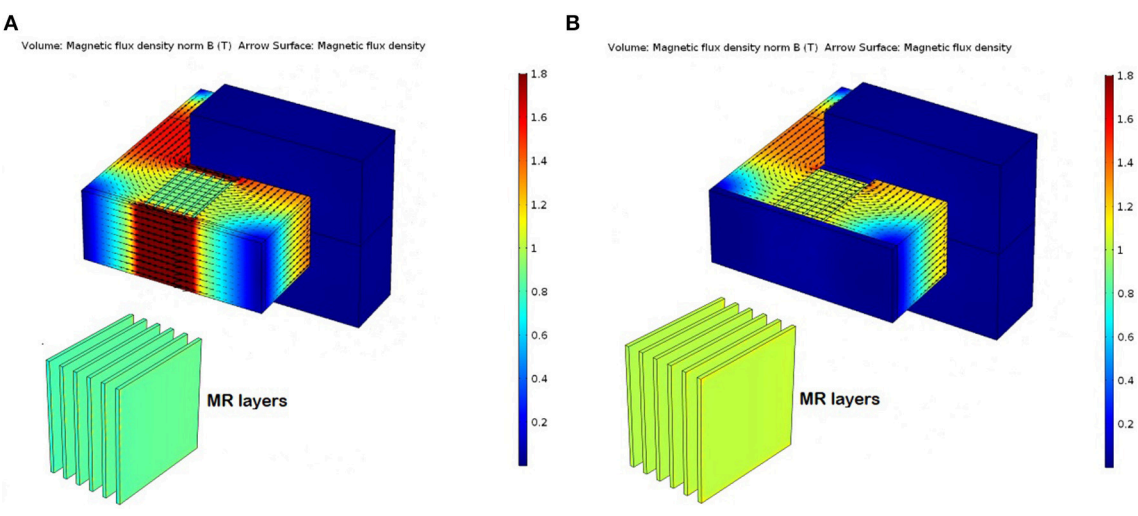

FIGURE 6 | Magnetic simulation results of the **(A)** final design **(B)** design with non-magnetic end wall.

is the effective area of the piston, x is the liquid flow rate, and c_1 is the parameter value in the range of 2.07–3.07 that is presented in Equation (5).

$$(c_1 = 2.07 + \frac{12Q\mu}{12Q\mu + 0.4wh^2\tau_y}), \quad (5)$$

where, μ is the MR fluid viscosity coefficient and k can be obtained using Equation (6).

$$k = 1 + (w*h)/2A_p. \quad (6)$$

This plate block design is not complicated; thus, the straightforward local optimization procedure was used. Because of volume restrictions on the engine and manufacturing aspects, the maximum possible resistance force must be achieved at the smallest plate block. Therefore, the designed parameters have limits, and the optimized results must be below those limits.

For design flexibility, the cross-sectional area of the magnetic channel is considered to be rectangular. The primary parameters of the design of the resistance valve include the thickness of the MR fluid layer and that of the separator. The thickness of the resistance valve affects the number of layers of the MR fluid. The greater the number of layers, the greater is the resistance of the resistance valve. However, the volume of the resistance valve is limited by the volume of the cylinder head. The thinner the MR fluid layer thickness is, the higher is the resistance. If the MR fluid layer is too thin, the MR fluid cannot pass fully through it, causing excessive resistance. Thus, a thickness of 1 mm was applied. The thinner the separator is, the greater is the resistance. However, an extremely thin separator causes the separator to deform when it is subject to force. Therefore, a thickness of 3 mm was applied. Finally, six layers and five partitions were used, as shown in **Figures 4A,C**.

Fixed parameters:

- Structure of core = rectangular;
- MR fluid layer thickness (h) = 1mm;
- Plates thickness (s) = 3mm.

Variables for the optimization

- Material selection,
- End wall thickness (d),
- Magnetic channel width (w) and height (L),
- Input current.

Due to the characteristics of the MR fluid, a material with high magnetic permeability must be used for the resistance valve body. The magnetic induction intensity B in different materials is different under different magnetic field strengths H. A comparison of the B–H magnetic induction curves of different materials revealed that pure iron has a high permeability of almost 100% but is difficult to manufacture. Steel 1008 is iron with 0.08% carbon content, steel 1010 is iron with 0.1% carbon content, and steel 1018 is iron with 0.18%

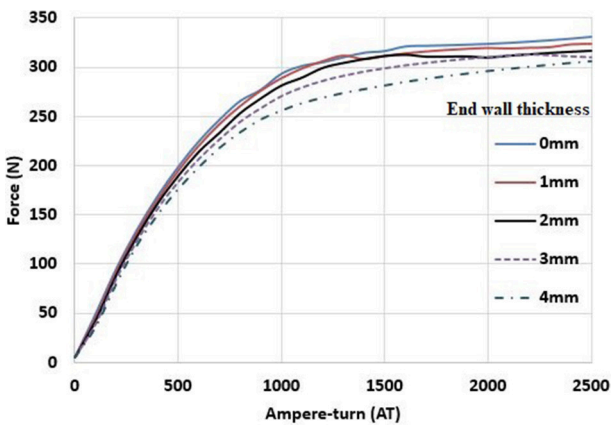

FIGURE 7 | Effect of different ampere-turns and siding thickness on maximum resistance.

TABLE 1 | Optimized magneto-plate block parameters.

Parameter	Possible limits	Optimized values
Core material	SS400,AISI1008,1018,&1010	SS400
Magnetic channel width (w)	15–30 mm	25 mm
Magnetic channel height (L)	15–30 mm	30 mm
MR fluid layer thickness (h)	0.5–2 mm	1 mm
Partition plate Thickness (s)	1–3 mm	3 mm
Ends wall thickness (d)	0–4 mm	3 mm
Input current * no of coil turn	500–2500 AT	1500 AT
Resistance force	Maximum possible	303.87N

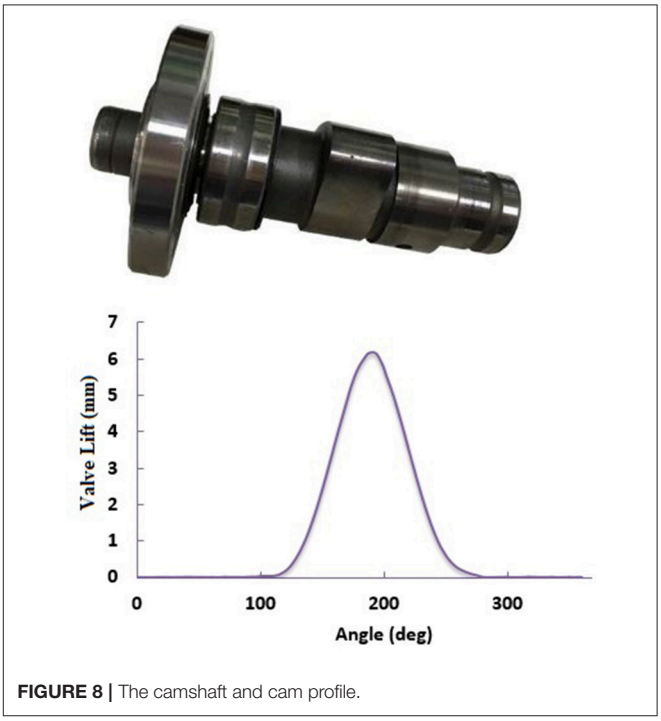

FIGURE 8 | The camshaft and cam profile.

carbon content. After a discussion was held on materials with processing plant personnel, SS400, which is a low carbon steel with a carbon content of 0.15–0.2%, was considered the most suitable material; its B–H curve is displayed in **Figure 4B**. B–H curve details can be obtained from the studies conducted by Lee et al. (2013) and Shiao and Dat (2013).

Figure 4B reveals that when the magnetic field strength is below 30 kA/m, steel 1008 has the highest magnetic flux density. Nevertheless, when H is in the range of >30 to 100 kA/m, SS400 superior better properties, as presented in its curve. The magnetic flux density of SS400 generated at a lower magnetic field strength increases slowly, which implies that resistance control is easier. Moreover, the maximum resistance of SS400 is better than that of other low carbon steels. Therefore, SS400 was selected as the material for the block and plates of the resistance valve body.

To prevent leakage of the MR fluid, the resistance valve wall plate was designed to block the MR fluid on both sides of the resistance valve. The thickness of the wall plate not only affects the strength of the resistance valve but also the maximum resistance of the valve. If the wall is thin, it can easily be magnetically saturated. Thus, most of the magnetic flux is forced to penetrate the MR fluid and plates. Thus, the magnetic field in the MR fluid is sufficiently strong to produce a high-resistance force. By contrast, if the wall is too thick, most of the magnetic flux penetrates the wall and does not penetrate the MR fluid and plates. Thus, the applied magnetic field in the MR fluid is weak, and thus, the produced resistance force is weak. The relationship between wall thickness and resistance at a coil input of 2000 AT is presented in **Figure 5A.**

Figure 5A proves that the thicker the wall plate is, the lower is the resistance force. As aforementioned, this is because a large wall allows more magnetic flux to pass through and causes less magnetic flux to pass through the MR fluid. Thus, less resistance force is produced. The appropriate thickness of this device was found to be 3 mm. As presented in the figure, the resistance force at a wall thickness of 3 mm was only 9 N lower than that at a

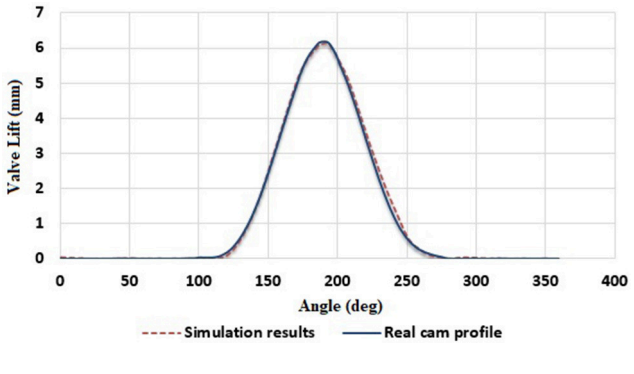

FIGURE 10 | Comparison of cam profiles.

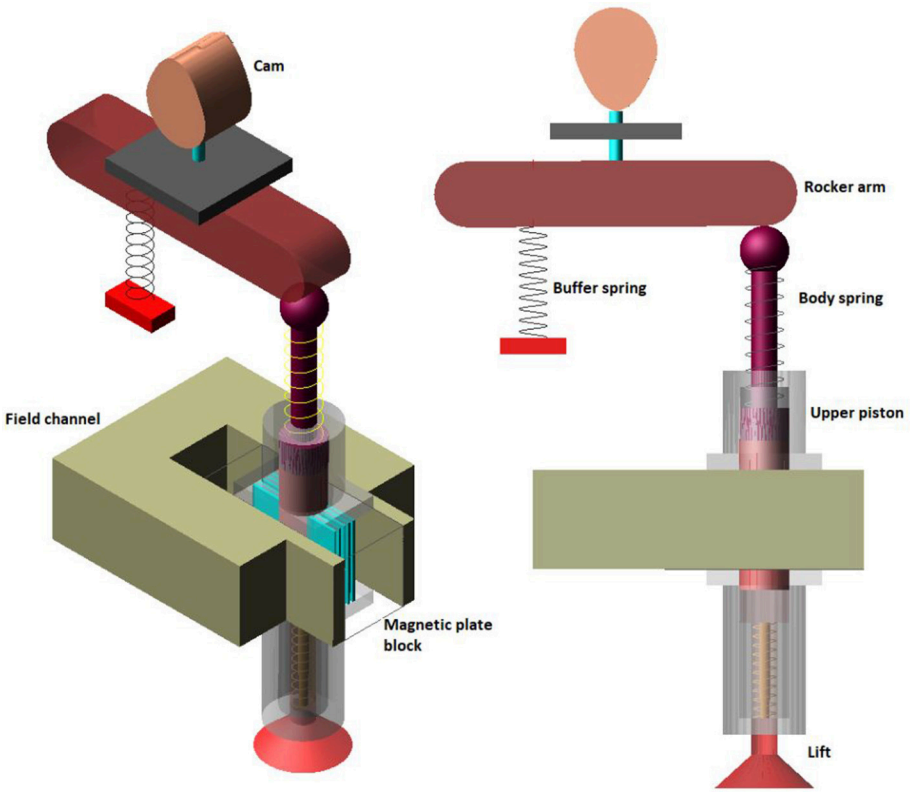

FIGURE 9 | Kinematic model of MR valve.

thickness of 1 mm (resistance at 3 mm is 97% of that at 1 mm). The resistance force was significantly reduced by 17 N when the wall thickness changed from 3 to 4 mm (resistance at 4 mm is 94.5% of that at 3 mm). Therefore, it is appropriate to select a thickness of 3 mm to obtain sufficient structural support and reduce the loss of resistance force.

Figure 5B presents an analysis of the width of the magnetic flux channel with respect to the resistance force. In the analysis, width values from 15 to 30 mm were studied and maximum resistance change was observed.

The magnetic channel cross-section area affects magnetic flux. The larger the cross-sectional area of the magnetic channel is, the higher is the magnetic flux. However, because the total volume was limited by the engine cylinder head, the area was set to 900 mm^2. As shown in **Figure 5B**, the smaller the width of the magnetic channel is, the smaller is the resistance force. However, the maximum resistance force was saturated when the magnetic path width was higher than 25 mm. This saturation occurred because the width of 25 mm was sufficiently large to allow most of the magnetic flux to pass through. Thus, the resistance force increased by only 2.269 N (about 0.72%) when the thickness value increased from 25 to 30 mm. For material mitigation, a thickness of 25 mm is the most suitable. As shown in **Figure 5C** the relation between resistance force and channel height is linearly proportional. Therefore maximum allowable height is considered for this design.

Next is the selection of end wall for the prevention of MR fluid leakage. At the beginning of valve design, two options for the end wall were considered: non-magnetic material end wall and magnetic end wall. There are advantages and disadvantages for both designs. Non-magnetic end wall gives larger MR resistance force (because of more magnetic field in MR layers as shown in **Figure 6B**, but it increases valve volume because of the anti-leakage mechanisms, like O-ring etc. It also increases the manufacturing complexity that is not good for mass production conditions. On the other hand, if magnetic material is used for end wall, the MR resistance force is reduced, but the valve has simple structure. Therefore, the end wall was designed as thin as possible to get magnetic saturation in the path of end wall on purpose. Because of the magnetic saturation at the end wall, magnetic flux going through this short path is limited, and then most of magnetic flux will flow to the MRF layers. That is why the magnetic flux density in end wall at **(Figures 3, 6A)** are so high, and this is the expected effect in design.

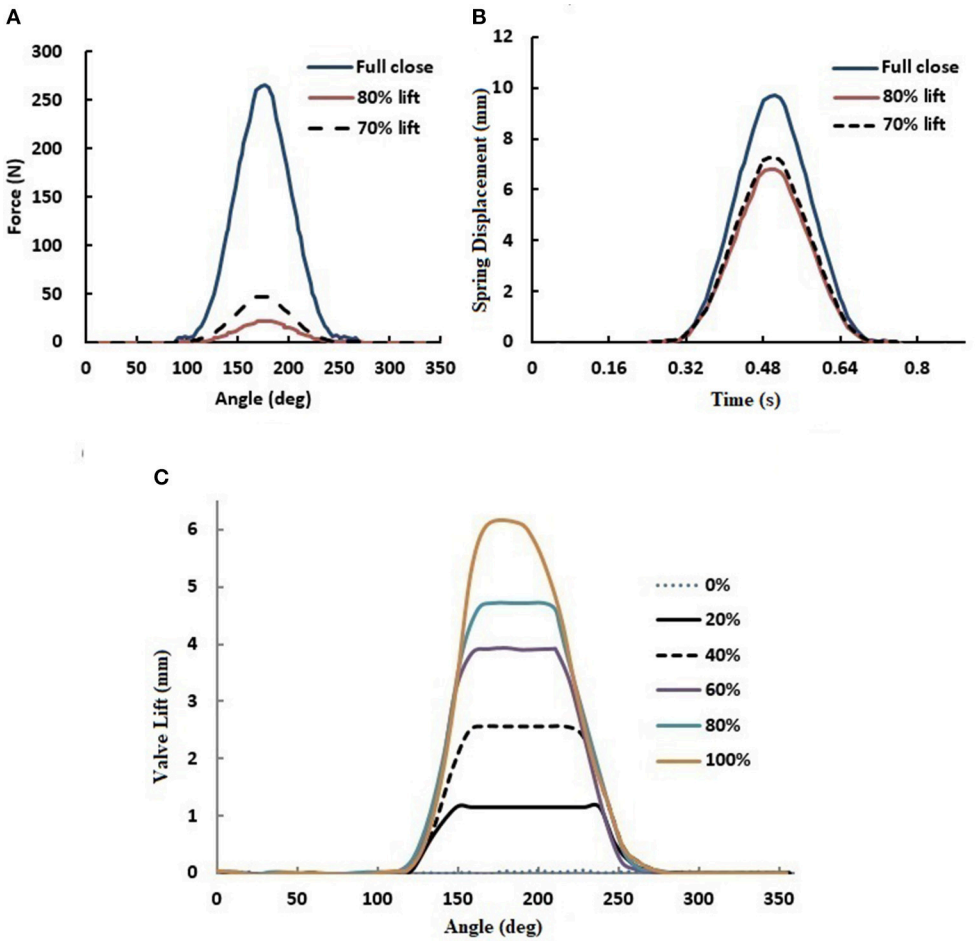

FIGURE 11 | Computer simulation results of **(A)** resistance force at different lifts, **(B)** compression of buffer spring lift at different lifts, and **(C)** different valve lifts.

Computer simulations of these two optional designs were performed. According to those simulation results, the resistance force of the design with magnetic-material end wall is 303 N, whereas the force of the design of non-magnetic (aluminum) end wall produces 365 N. Thus only 16% force reduction in the magnetic end wall case. It proves that the magnetic-end-wall design can obtain simple system mechanisms without much performance reduction. It is a compromise between the force performance and mass-production manufacturing cost. Finally, it was decided that little force performance was sacrificed to get benefits of manufacturing simplicity and cost. Therefore, single component structure (magnetic end wall) was considered for the MR valve as shown in **Figure 4C**.

The magnetic induction for this final design is presented in **Figure 6A**. The magnetic induction intensity using the final parameters was almost saturated in the magnetic channel, which implies that the parameters were close to the limit of lightweight materials.

The AT number has a considerable influence on the resistance force of the plate block. A high AT number can result in a strong magnetic field and thus a large resistance force. However, the magnetic induction intensity can increase only when the magnetic channel is not saturated. The maximum electrical current provided by the power supply in this study was 2 A. A large resistance force can be generated in the plate block if the number of coil turns increases. The maximum force can be reached when the magnetic flux channel is magnetically saturated.

After applying a current of 2 A, 4361 AT can be achieved. However, because of the difficulty in winding, the number of windings is reduced. Finally, the total available number of ATs was 2500 AT in simulation, and only 1500 AT was used in practical applications. Moreover, the thickness of the end wall is also mentioned together, as shown in **Figure 7**. The maximum resistance force in the plate block can be observed under various conditions.

Figure 7 shows that the force increase rate begins to slow down at ∼1200 AT. When the ATs are ∼1500 AT, the force still increases as the electric current increases, but the force is almost saturated. Moreover, the difference in force value for an end wall thickness of 3 mm and 1 mm is only 10 N. Even for a thickness of 3 mm from 1500 to 2000 AT, only an increase of 10 N was observed. Considering the difficulty and manufacturing processes involved in winding technology, an end wall thickness of ∼3 mm should be reserved to successfully achieve the coil winding. The final AT setting was 1500 AT, and a wall thickness of 3 mm was the most suitable. From these magnetic simulations, the design of magnetic plate block was optimized. Moreover, the different resistance forces were calculated for the various valve

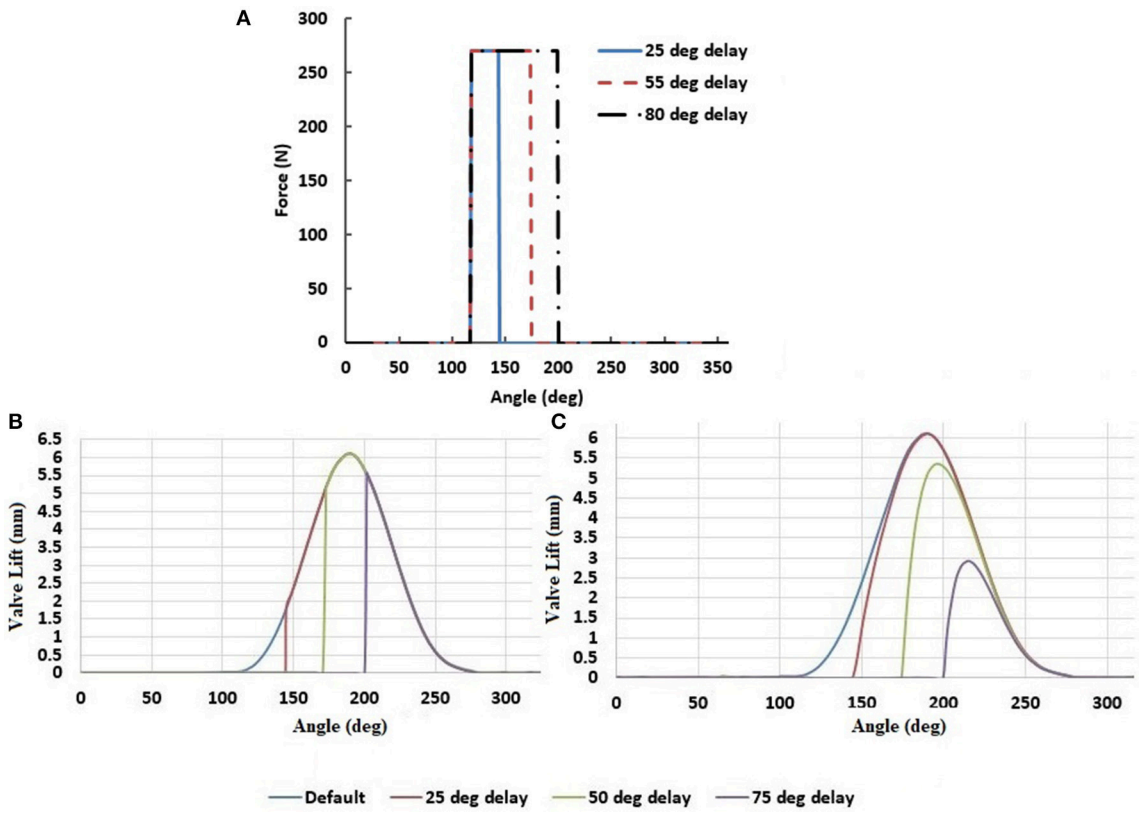

FIGURE 12 | (A) Schematic diagram of simulated force application **(B)** variable timing expected profiles **(C)** dynamic simulation of variable timing of the valve with full lift.

actuation conditions. **Table 1** presents the final parameters and maximum resistance. The final step in size reduction is cutting out the corners by 8 mm as shown in **Figure 4C**, which has a negligible negative effect on magnetic intensity.

DYNAMIC SIMULATIONS

Several mechanical and electrical valve trains have been used in present engines, which have limited sets of valve profiles. The proposed valve train is more flexible and was designed to enable more variations in valve opening. Therefore, the purpose of this simulation is to identify whether the proposed valve train can achieve more opening variations.

To understand the working operational characteristics of the valve, an MR valve model was developed in the Adams simulation software program. The input of the model is the plate block's resistance force that is generated from magnetic simulations, and the cam speed is 30 rpm. Because of the limited equipment available in the laboratory, the experimental cam of a 125-cc single-cylinder engine was used, as shown in **Figure 8**.

The resistance force of the magnetic plate block was obtained from the magnetic field simulation program. Based on that resistance, the elastic coefficient of the buffer spring and the upper and lower springs of the body were obtained. After all power parameters and size settings were completed, the kinematic model of the MR valve was achieved, as presented in **Figure 9**.

Cam Analysis

After the kinematic models were developed, the dynamic performance of the valve was simulated. The cam was the active component in this study that pushes the entire valve. Therefore, the cam had considerable importance. **Figure 10** presents a comparison between the modeled cam profile of the simulation and the contour of the real cam. The results reveal that the simulated cam profile is markedly similar to the contour of the real cam. Because of the friction of the mechanical components and errors due to the spring stiffness, only minimal difference were observed in valve closing time. Thus, this cam model can be used as the primary active component in the valve train model for conducting dynamic analysis to operate the valve.

Dynamic Lift Simulation

The purpose of this simulation was to study the different lift options of the proposed valve train. By changing the magnitude of resistance force in the magnetic plate block (which acts as a reverse acting force to the piston motion), the respective lifts can be achieved. For example, a 0-N resistance force is required to activate full lift mode, a 25-N resistance force is required to lift the valve by 85%, and a 45-N force is required to lift the valve by 75%. Lifts of 0, 20, 40, 60, 80, and 100% were tested.

When the valve was fully closed, the resistance force of the magnetic plate block was at its maximum, that is, at approximately 270 N, as shown in **Figure 11A**. Therefore, the valve does not open, and the entire compression force is on the buffer spring. This force compresses the buffer spring to its maximum lift. The displacement of the buffer spring for different lift values is displayed in **Figure 11B**. Similarly, during the partial valve lift conditions, part of the compression force of the rocker arm is transferred to the buffer spring.

From the dynamic simulation results of the variable lift of this model, as shown in **Figure 11C**, it is clear that the new MR valve has a favorable effect on the variable lifts. Within the allowable compression amount of the buffer spring and by regulating various types of compression, the function of various valve lifts can be attained.

Dynamic Valve Timing Simulation

Next, the possibilities of VVTs were analyzed. To understand the default timing, 25° delay, 50° delay, and 75° delay conditions were simulated. **Figure 12A** presents a schematic of the force applied during the simulation. When the valve was about to open,

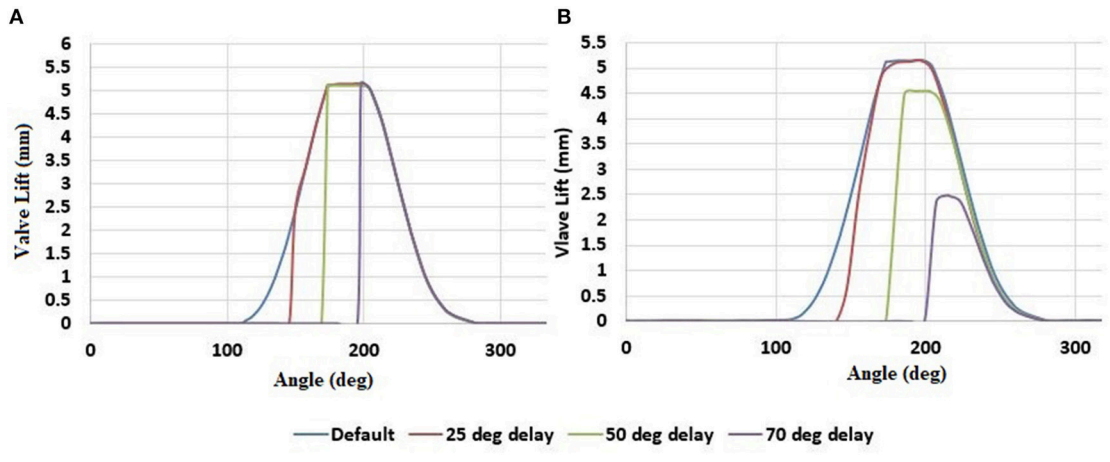

FIGURE 13 | Different timings with 85% valve lift **(A)** expected profiles **(B)** MR valve-train simulation results.

that is, at approximately 117°, a maximum force of 270 N was applied. When the required timing angle was attained, the force was reduced to zero immediately.

Figure 12C shows the dynamic simulation of the various timings of the valve in the full lift condition. Although the cam began to push the rocker at its default timing, that is, at 117°, the valve did not open until the set time was reached because of the resistance force, as shown in **Figure 12A.**

As shown in **Figure 12B**, after the required time was reached, the expected valve profile for a full lift could be observed. However, this behavior cannot be attained in a real-world scenario because of magnetic hysteresis. The resistance force in the magnetic plate block was gradually reduced to zero. By that time, the cam profile began a downward trend, as shown in **Figure 12C**. Thus, the obtained profile was slightly different from the expected profile. However, these profiles are useful for enhancing the engine performance. In the future, by performing engine simulation studies, optimal profiles can be determined for given speed and load conditions.

Dynamic Valve Lift and Timing Simulation Results

Finally, the proposed valve train was tested in terms of obtaining various valve lifts and timing flexibility simultaneously. **Figure 13** presents the simulation results of the variable timings of the valve at an 85% lift. Because of the resistance force throughout the valve lifts, as shown in **Figure 11A**, a maximum lift of only 85% was attained for all the timing conditions. As such, both VVT and VVLs were achieved simultaneously. Similarly, **Figure 14** displays the simulation results of various timings of the valve at a 70% lift. The new MR valve controls both various lifts and various valve opening times.

Figure 12B shows the dynamic simulation of the variable timing of the valve in the full lift condition. Although the cam began pushing the rocker at its default timing, that is, at 117°, the valve did not start opening until the set timing—120°, 145°, 175°, and 200°–is reached because of the resistance force that is shown in **Figure 12A**. The maximum lifts were attained as each cam lifts were available at that angle.

However, at lower lift modes, some lift fluctuations were evident when the time for the maximum lift was reached because of a high degree of tension in the springs. Moreover, during late opening times, the valve profiles could not reach the highest point of the expected profiles. As discussed, this is due to magnetic hysteresis. This valve train was developed to attain variable profiles and not to achieve particular profiles. All the aforementioned simulations reveal that the proposed valve train can provide valve profiles, that is, VVT, VVL, and VVT&L. Therefore, the proposed MR valve train is valid and useful.

The introduced device is a novel IC engine valve train. Therefore, this paper discusses the conceptual model and valve working validation only. In the future, an experimental study will be conducted on the prototype to elucidate its operational modes at different speeds. Magnetic hysteresis is one of the major problems in such components that affects the valve response. However, in the proposed device, magnetic hysteresis can be avoided by using a control strategy—input current timing. After experimental study is conducted, this control strategy can be established. Moreover, considering manufacturing aspects end wall of magnetic plate block was designed with magnetic material, which has little performance reduction. In the future, this device will try to use non-magnetic end walls to enhance the force performance of the MR valve while balancing its manufacturing cost, design complexity, and device weight. Thus, this device will be more attractive to the users especially in long run.

CONCLUSIONS

This study introduced a novel MR valve train that is lightweight and consumes less energy than other related devices. Because of the volume restrictions on the engine, the maximum possible resistance force from the plate block should be achieved at

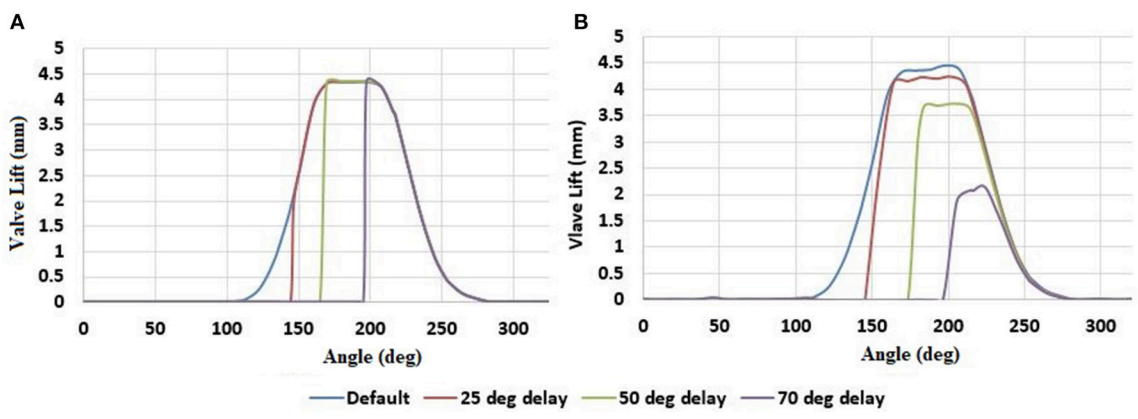

FIGURE 14 | Different timings with 70% valve lift **(A)** expected profiles **(B)** MR valve-train simulation results.

the smallest plate block. This task was achieved by using an optimized design for a magnetic plate block and was explained using magnetic simulation. The possibilities of valve actuation with different opening variations and the force distribution from the cam to the magnetic plate block, to the springs, and the valve were simulated. Based on those simulations, the designed MR valve train was proven to be flexible in producing various valve profiles with different valve times and lift combinations. Therefore, this valve, with an appropriate valve opening strategy, could be used in an IC engine to improve the engine's efficiency and reduce exhaust gas emissions.

AUTHOR CONTRIBUTIONS

Idea, conceptual study, theory, literature study, and manuscript quality enhancement done by YS. Magnetic and dynamic simulation, manuscript writing done by MK. Structural design and modeling work done by J-WJ.

ACKNOWLEDGMENTS

This research is financially supported by Ministry of Science and Technology, Taiwan (project number: MOST 105-2221-E-027-091).

REFERENCES

Bernard, L., Ferrari, A., Micelli, D., Perpttp, A., Rinolfi, R., and Vattaneo, F. (2009). Electro-hydraulic valve control with multiair technology. *MTZ Worldwide* 70, 4–10. doi: 10.1007/BF03226988

Dyke, S. J., Spencer, B. F., Sain, M. K., and Carlson, J. D. (1996a). Modeling and control of magneto-rheological dampers for seismic response reduction. *Smart Mater. Struct.* 5, 565–575. doi: 10.1088/0964-1726/5/5/006

Dyke, S. J., Spencer, B. F., Sain, M. K., and Carlson, J. D. (1996b). Phenomenological model of a magneto-rheological damper. *J. Eng. Mech-ASCE.* 123, 230–238.

Dyke, S. J., Spencer, B. F., Sain, M. K., and Carlson, J. D. (1998). An experimental study of MR damper for seismic protection. *Smart Mater. Struct.* 7, 693–703.

Flierl, R., and Klüting, M. (2000). The third generation of valvetrains-new fully variable valvetrains for throttle-free load control. *SAE Technical Paper* (Detroit, MI), 0148–7191.

Ichwan, B., Mazlan, S. A., Imaduddin, F., Koga, T., and Idris, M. H. (2016). Development of a modular MR valve using meandering flow path structure. *Smart Mater. Struct.* 25:037001. doi: 10.1088/0964-1726/25/3/037001

Lee, H. B., Kwon, H., and Min, K. (2007). Effects of various VVA systems on the engine fuel economy and optimization of a CVVT-VVL SI engine using 1D simulation. *Int. J. Automot. Technol.* 8, 675–685.

Lee, J. H., Han, C., Ahn, D., Lee, J. K., Park, S. H., and Park, S. (2013). Design and performance evaluation of a rotary magneto-rheological damper for unmanned vehicle suspension systems. *Sci. World J.* 2013:894016. doi: 10.1155/2013/894016

Lord-corporation (2012). *Magneto-Rheological Fluid MRF-140CG*. Available online at: http://www.lordfulfillment.com/upload/DS7012.pdf

Phu, D. X., and Choi, S. B. (2019). Magnetorheological fluid based devices reported in 2013–2018: mini-review and comment on structural configurations. *Front. Mater.* 6:19. doi: 10.3389/fmats.2019.00019

Pierik, R. J., and Burkhard, J. F. (2000). Design and development of a mechanical variable valve actuation system. *SAE Technical Paper* (Detroit, MI), 0148–7191.

Sawant, P., and Bari, S. (2018). Effects of variable intake valve timings and valve lift on the performance and fuel efficiency of an internal combustion engine. *SAE Technical Paper,* 2018-01-0376. doi: 10.4271/2018-01-0376

Shiao, Y., and Cheng, W. H. (2016). Performance investigation of an SI engine with VVT and VVL based on magneto-rheological valve. *T. Can. Soc. Mech. Eng.* 40, 749–760. doi: 10.1139/tcsme-2016-0061

Shiao, Y., and Dat, L. V. (2013). A new electromagnetic valve train with PM/EM actuator in SI engines. *T. Can. Soc. Mech. Eng.* 37, 787–796. doi: 10.1139/tcsme-2013-0066

Smith, C. (2018). *Electro-Mechanical Hydraulic Valve Lifter for Precise Control of Fuel Consumption*. US. Patent No. US20180187577A1. Washington, DC: U.S. Patent and Trademark Office.

Sun, Z., and He, X. (2007). Development and control of electro-hydraulic fully flexible valve actuation system for diesel combustion research. *SAE Technical Paper* (Rosemont, IL), 0148−7191.

Yao, Z., Yap, G., Fook, F., Chen, G. (2002). MR Damper and its application for semi-active control of vehicle suspension system. *Mechatronics* 12, 963–973. doi: 10.1016/S0957-4158(01)00032-0

Yoo, J. H., and Wereley, N. M. (2002). Design of a high-efficiency magneto rheological valve. *J. Intell. Mat. Syst. Struct.* 13, 679–685. doi: 10.1177/1045389X02013010012

Conflict of Interest Statement: The authors declare that the research was conducted in the absence of any commercial or financial relationships that could be construed as a potential conflict of interest.

frontiers in Materials

ORIGINAL RESEARCH
published: 24 April 2019
doi: 10.3389/fmats.2019.00068

Parametric Modeling of a Magnetorheological Engine Mount Based on a Modified Polynomial Bingham Model

Shiwei Chen[1], *Rui Li*[2]*, *Pengfei Du*[1], *Hengwei Zheng*[1] *and Dingyu Li*[1]

[1] *Chongqing University of Science and Technology, Academe of Mathematics and Physics, Chongqing, China,* [2] *Department of Automation, Chongqing University of Posts and Telecommunications, Chongqing, China*

This work mainly addresses the establishment of a phenomenological mechanical model for magnetorheological (MR) engine mounts under frequency variation and magnetic variation effects. First, the mounts' reaction force is divided into three parts: a Coulomb damping force, an elastic reaction force, and a viscous damping force. Then, by using correlation analysis on these forces with the frequency and magnetic field, a modified polynomial Bingham parameterized model is proposed. This model takes external current and external loading frequency as the variables. As a result of analyzing the relationship between energy dissipation and storage caused by the external displacement excitation, an identifying method is proposed to identify the nine parameters in the model. Based on this model, an experimental scheme was designed, and the force–displacement relationship of a typical MR mount under different working conditions was tested through an experiment. By using the proposed method, the relationship of the reaction force of an MR mount with current and external loading frequency was obtained. The experimental results show that the proposed model can correctly reflect the wide-frequency dynamic characteristics of the mounts in dynamic stiffness, lagging angle, and hysteretic curve.

Keywords: engine isolation, MRF mounts, laboratory experiment, Bingham model, vibration control

OPEN ACCESS

Edited by:
Weihua Li,
University of Wollongong, Australia

Reviewed by:
Yancheng Li,
University of Technology Sydney, Australia
Tianhong Yan,
China Jiliang University, China

****Correspondence:***
Rui Li
lirui_cqu@163.com

Specialty section:
This article was submitted to Smart Materials, a section of the journal Frontiers in Materials

Received: *17 September 2018*
Accepted: *01 April 2019*
Published: *24 April 2019*

Citation:
Chen S, Li R, Du P, Zheng H and Li D (2019) Parametric Modeling of a Magnetorheological Engine Mount Based on a Modified Polynomial Bingham Model. Front. Mater. 6:68. doi: 10.3389/fmats.2019.00068

INTRODUCTION

Engine mounts are usually installed between the engine and vehicle frame. They are used for isolating the engine's vibration, which would spread to the vehicle body, and reducing the vibration amplitude of the engine itself (Shangguan, 2009; Tikani et al., 2015). An ideal engine mount should exhibit a low damping property when the engine is at high revolution speed, and it should be quickly changed to a high damping state when the engine revolution speed is low(Barber and Carlson, 2010). As a new member of the novel smart mount, magnetorheological (MR) fluid mounts boast a series of advantages, such as controllable damping force, simple structure, quick response, low energy consumption, and low cost. Hence, these advantages provide broad application prospects and important research significance for motor vibrating control (Behrooz et al., 2011; Wang and Chen, 2017).

On account of the complex internal structure of MR mounts, the rubber structure features a hyper-visco-elastic-plastic mechanical property. Its elastic modulus has a strong correlation to amplitude (Delattre et al., 2016) and external loading frequency (Lin and Lee, 1998). However, MR fluid, as a non-Newtonian liquid, has the mechanical property that its yield stress varies with the change of external applied magnetic field, and it has the frequency correlation that its apparent viscosity mainly varies with the external loading frequency (Wang and Faramarz, 2009; Zhu et al., 2011). These characteristics endow the mechanical feature of MR fluid with strong non-linearity (Sado, 2013). Therefore, how to establish the mechanical model accurately and succinctly is continually attracting research in the engineering field (Hoang et al., 2011). The existing studies mainly describe the dynamic characteristics of mounts' components using the following three methods.

First, the lumped parameter method generally adopts bond group theory to describe the relationship of the system's dynamic stiffness and lagging angle with the internal structural parameters of mounts (Farjoud et al., 2014; Tikani et al., 2015). Because the lumped parameter method is based on a linear viscoelastic system, there is great difference between the calculation model and the final testing results.

Second, the finite-element method (FEM) involves the simulation of dynamic characteristics of mounts through the secondary development of commercial finite-element software (Shangguan and Lu, 2003; Wang and Lu, 2003). Nguyen (Nguyen et al., 2013) investigated the optimal design of an engine mount based on the FEM. However, because of the fluid–solid coupling characteristics of MR mounts and the fact that numerous experiments (Li et al., 2013) are required to obtain the parameters of the viscoelasticity, elastoplasticity, and superelasticity of structural materials, it is difficult to predict the reaction force of MR mounts.

Third, the phenomenological model describes the mechanical property of mounts by establishing a presupposed skeleton model and combining experiments with matching the undetermined parameters, which sometimes has no physical meaning, in the skeleton model. Because of the advantages of the simple model and high accuracy, using the Bingham model, Bouc–Wen model, and other improved models based on Bouc–Wen, researchers have applied the phenomenological model method to describe the dynamic characteristics of an MR damper (Razman et al., 2014). For example, Spaggiari and Dragoni (2012) used an improved Bouc–Wen model to perform parameterized modeling for an MR damper at the low-frequency stages. Liao (Chang-rong et al., 2013) conducted magnetic circuit analysis for MR fluid mounts of engines and carried out mechanical-characteristic research on the extrusion model of MR fluid. Finally, that work reveals the relationship between the applied current and extrusion force. Choi et al. (2001) performed fitting calculation on the experimental results of MR fluid mounts through a polynomial model. This model boasts the advantages of high control accuracy and quick reverse current of the reacting force.

Recently, research on applying MR dampers for vibration control of mechanical system has made great progress. Many models that possess the merits of high accuracy in the prediction of MR dampers with low-frequency behavior have been widely investigated. For examples, Xu et al. (2014) utilized the Bouc–Wen model to model a vehicle MR suspension, and Bai et al. (2015) studied a new MR damper with an inner bypass configuration.

There already have been many studies for system modeling with the characteristics of hysteresis (Swevers et al., 2000). However, unlike the vehicle suspension system, the engine isolation system has its unique properties. It operates under a lower vibration amplitude and a broad band of frequency (0–100 Hz). Moreover, the vibration of the engine system is mainly caused by the engine's unbalance force. Hence, the vibration source frequency is deeply related to the engine revolution speed, which could be tested easily. Although Chen et al. (2016) proposed a new model to describe mechanical behaviors of MR dampers working at the medium-frequency range, current studies have not considered the modeling of MR dampers for a broadband dynamic range. Therefore, a control method based on existing models would be ineffective or even counterproductive when the engine is vibrating at high frequency. In addition, because the excitation frequency of the engine vibration system varies in a wide range, the MR fluid and rubber in the MR mount face the displacement excitations with a great difference in rate. Therefore, this creates higher requirements for broadband mechanical properties characterization of MR mounts.

To address the above-mentioned problem, by considering the broadband characteristics of an engine vibration system and ignoring the amplitude effect on the mechanical behaviors of the MR mounts, this study takes an MR mount as the example, proposes a polynomial Bingham phenomenological model through the component analysis of the mounts' reaction force, and comes up with a parameter-identifying method for the polynomial model by analyzing the energy dissipation and storing relationship of external excitation. Through testing experiments, the relationship that the reaction force of MR mounts varies with the current and excitation frequency was obtained. The comparison results show that this improved model can correctly reflect the dynamic characteristics of wideband MR mounts.

PHENOMENOLOGICAL MECHANICAL MODEL

The present work adopts MR fluid mounts as the study object, as shown in **Figure 1**. The piston rod of the MR fluid mounts uses a rigid connection with a vibration separating system. The vibration excited by the vibrating source causes an up–down movement of the piston rod so as to drive the up–down movement of the extrusion disc. Then, the MR fluid of the working cylinder spreads toward the two sides under the extrusion of the disc, forming a flow. A magnetic field is produced from the magnetic exciting coil, vertical to the extrusion disc. The flowing direction of the MR fluid is parallel to the extrusion disc; thus, the flowing direction of the MR fluid is vertical to the magnetic field, obstructing the flow. By this means, the damping force can be changed.

Furthermore, **Figure 2** gives the structure parameter of the MR mounts work area, and the parameter value is given in **Table 1**.

To show that the working area of the MR mount is in the path of the magnetic circuit, **Figure 3** gives the magnetic circuit of the MR damper analyzed by the FEM software COMSOL 5.0. As **Figure 3** shows, the magnetic field in the working area is close to 0.8 T when the coil current is 1 A.

According to the traditional Bingham model, as shown in **Figure 4**, when the engine vibrates, the extrusion disc moves a displacement **X**, and the reaction force to the engine (Hong et al., 2008) from mounts can be expressed as:

$$\mathbf{F}_{MR} = \mathbf{F}_1 + \mathbf{F}_2 + \mathbf{F}_3 \quad (1)$$

According to the traditional Bingham model, the reaction force of MR mounts can be divided into three parts. The first part $\mathbf{F}_1$ represents the viscous damping force produced from the rubber gasket and MR fluid, and that can be regarded as the function of the displacements-velocity in the Bingham model.

The second part of the reaction force $\mathbf{F}_2$ is the Coulomb damping force produced by the magnetic effect of the MR fluid. Yield stress is mainly controlled by the magnetic-field strength.

TABLE 1 | Structure parameters value of the MR mounts.

Parameter	Value
MR fluent chamber height H1	15 (mm)
Rubber gasket thickness H2	50 (mm)
Extrusion round disc thickness H3	3 (mm)
Extrusion round disc radius R1	27 (mm)
Connect rod radius R2	6 (mm)
Extrusion round disc radius R3	30 (mm)
Extrusion round disc radius R4	39 (mm)
Number of coil's turn	800

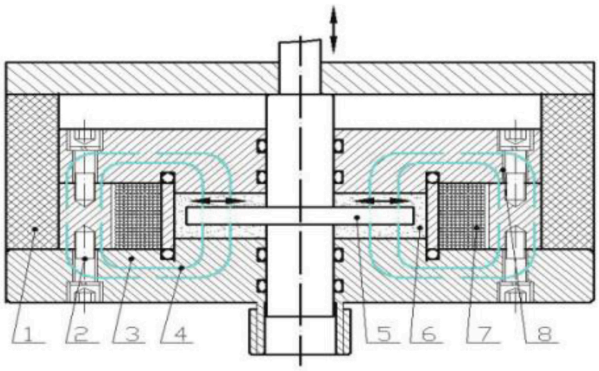

FIGURE 1 | Structural diagram of MR mounts based on extrusion working mode (1)Rubber gasket (2) Connecting bolt (3)Connecting base (4) Exciting flux (5) Extrusion round disc (6) MR fluid (7) Magnet exciting coil (8) Seal covered plate.

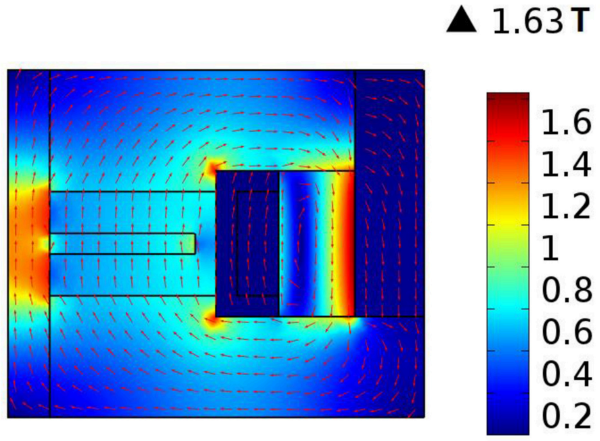

FIGURE 3 | Result of the magnetic circuit analysis.

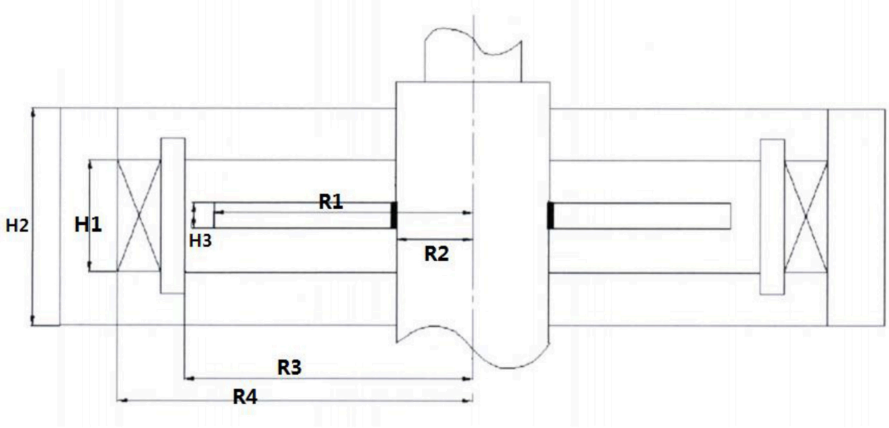

FIGURE 2 | Structure parameters diagram of the MR mounts.

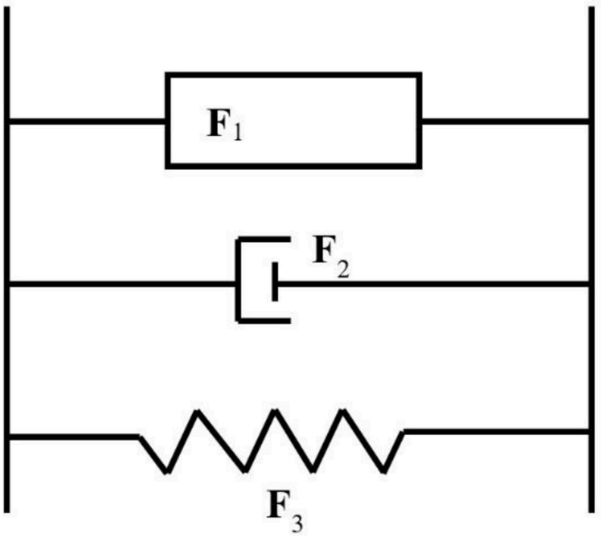

FIGURE 4 | The Bingham phenomenological model.

Therefore, $\mathbf{F}_2$ is related to the current applied to the mounts. It is a kind of adjustable damping force, with the damping force characteristics of a friction damper.

The elastic force $\mathbf{F}_3$ represents the equivalent stiffness of the rubber gasket mounted on the external package. It changes with the frequency because of the viscoelasticity of rubber as a polymer material.

Because of the small amplitude of engine vibration, it can be simplified as follows. According to the correlation analysis above, the reaction force expression equation is built by a binomial fitting according to current I and external-loading frequency ω to obtain the improved Bingham model.

$$\mathbf{F}_{MR} = \text{sign}\left(\dot{\mathbf{X}}\right)\mathbf{F}_I(I) + k(\omega)\mathbf{X} + \text{c}(\omega)\dot{\mathbf{X}} \tag{2}$$

$$\mathbf{F}_I\,(I) \;=\; A_I I^2 + B_I I + C_I \tag{2a}$$

$$k\,(\omega) \;=\; A_k\omega^2 + B_k\omega + C_k \tag{2b}$$

$$c\,(\omega) \;=\; A_c\omega^2 + B_c\omega + C_c \tag{2c}$$

Where $c(\omega)$ is the equivalent viscous damping of the MR mounts; $k(\omega)$ represents the equivalent stiffness of the MR mounts; $\mathbf{F}_I$ is the coefficient of Coulomb damping of the MR mounts; and the parameters A_I, B_I, C_I, A_k, B_k, C_k, A_c, B_c, and $C_c$are the fitting parameters used to describe the dynamic mechanical properties of MR mounts.

PARAMETER IDENTIFICATION

If the mounts are subjected to a forced vibration under a single-frequency sinusoidal vertical displacement excitation with the amplitude of X_0, the mounts' movement can be expressed as follows.

$$\mathbf{F}_{MR} = \text{sign}\left(\dot{\mathbf{X}}\right)\mathbf{F}_I(I) + k(\omega)\mathbf{X} + \text{c}(\omega)\dot{\mathbf{X}} \tag{3}$$

$$\mathbf{X} \;=\; X_0\sin(\omega t + \varphi) \tag{3a}$$

$$\dot{\mathbf{X}} \;=\; \omega X_0\cos(\omega t + \varphi) \tag{3b}$$

Within a complete period, according to Equation (3), the external work P_{op}made by the displacement exciter to mounts can be expressed as:

$$\mathbf{P_{op}} = \oint F_{MR}d\mathbf{X} = \oint F_{MR}\dot{\mathbf{X}}d\mathbf{t} = \oint F_{MR}\omega\sqrt{X_0^2 - \mathbf{X}^2}\,\text{sign}(\dot{\mathbf{X}})dt \tag{4}$$

According to energy equivalence, within a complete period, the external work equals the energy internally consumed within the mounts.

$$P_{op}\,(I,\omega) = P_I\,(I) + P_c(\omega) \tag{5}$$

$$P_I\,(I) \;=\; \oint \text{sign}(\dot{\mathbf{X}})\mathbf{F}_I d\mathbf{X} = 4X_0\mathbf{F}_I \tag{5a}$$

$$P_c\,(\omega) \;=\; \oint c_\omega\dot{\mathbf{X}}d\mathbf{X} = \pi\, c_\omega\omega^2 X_0 \tag{5b}$$

where P_I represents Coulomb damping force work and $P_c$represents damping force work.

The physical significance of Equation (5) demonstrates that the work done by the displacement exciter within a complete period is consumed by mounts. The consumed work can be expressed in two parts: one is the energy related to the externally added current intensityP_I; and the other is the energy P_c related to the externally applied load.

According to this characteristic, if keeping the amplitude of displacement excitation X_0 and the externally applied current I invariable, by measuring the external work under different excitation frequencies and subtracting the test data, the difference between two external works can be derived as

$$P_{op}\,(I,\omega_k) - P_{op}\left(I,\omega_{k+1}\right) = P_c\,(\omega_k) - P_c\left(\omega_{k+1}\right) \tag{6}$$

where ωk is the external frequency in the k-th time testing. Concerning Equations (2) and (5), this equation can be derived as follows:

$$\begin{aligned}&\left(\omega_k^4 - \omega_{k+1}^4\right)A_c + \left(\omega_k^3 - \omega_{k+1}^3\right)B_c + \left(\omega_k^2 - \omega_{k+1}^2\right)C_c \\ &\quad= \frac{P_c\,(\omega_k) - P_c\left(\omega_{k+1}\right)}{\pi X_0^2}\end{aligned} \tag{7}$$

By testing the reacting force of the MR mounts in ω_k, $\omega_{k+1,}$ and ω_{k+2}, three different excitation frequencies, the expression of the fitting parameters of viscous damping A_c, B_c, and C_c can be obtained as follows.

$$\begin{aligned}&\pi X_0^2\begin{bmatrix}\omega_k^4 - \omega_{k+1}^4 & \omega_k^3 - \omega_{k+1}^3 & \omega_k^2 - \omega_{k+1}^2\\ \omega_{k+1}^4 - \omega_{k+2}^4 & \omega_{k+1}^3 - \omega_{k+2}^3 & \omega_{k+1}^2 - \omega_{k+2}^2\\ \omega_{k+2}^4 - \omega_k^4 & \omega_{k+2}^3 - \omega_k^3 & \omega_{k+2}^2 - \omega_k^2\end{bmatrix}\begin{bmatrix}A_c\\B_c\\C_c\end{bmatrix} \\ &\quad= \begin{bmatrix}P_{op}\,(I,\omega_k) - P_{op}\left(I,\omega_{k+1}\right)\\ P_{op}\left(I,\omega_{k+1}\right) - P_{op}\left(I,\omega_{k+2}\right)\\ P_{op}\left(I,\omega_{k+2}\right) - P_{op}\,(I,\omega_k)\end{bmatrix}\end{aligned} \tag{8}$$

From Equation (8), it can be shown that the relationship that the equivalent viscous damping of MR mounts changes with

excitation frequency can be worked out by an inverse solution of external work under different excitation frequencies through the testing system.

Similarly, if the amplitude of displacement excitation and externally applied frequencies are kept invariable, the external work can be measured under different excitation currents and subtracting the test data.

$$P_{op}\left(I_k,\omega\right)-P_{op}\left(I_{k+1},\omega\right)=P_I\left(I_k\right)-P_I\left(I_{k+1}\right) \tag{9}$$

where I_k is the externally applied current load in the k-th time testing; concerning Equation (5a), this equation can be derived as follows when the k-th and $k+1$-th time tests are finished.

$$\left(I_k^2-I_{k+1}^2\right)A_I+\left(I_k-I_{k+1}\right)B_I=\frac{P_I\left(I_k\right)-P_I\left(I_{k+1}\right)}{4X_0} \tag{10}$$

The two fitting parameters of the Coulomb damping coefficient A_I and B_I can be obtained as follows.

$$\begin{aligned}4X_0\begin{bmatrix}I_k^2-I_{k+1}^2 & I_k-I_{k+1}\\ I_{k+1}^2-I_{k+2}^2 & I_{k+1}-I_{k+2}\end{bmatrix}\begin{bmatrix}A_I\\ B_I\end{bmatrix}\\ =\begin{bmatrix}P_{op}\left(I_k,\omega\right)-P_{op}\left(I_{k+1},\omega\right)\\ P_{op}\left(I_{k+1},\omega\right)-P_{op}\left(I_{k+2},\omega\right)\end{bmatrix}\end{aligned} \tag{11}$$

Additionally, the fitting parameter C_I can be obtained as follows when the applied current is zero.

$$C_I=\left(P_{op}\left(I=0,\omega\right)-\pi c_\omega\omega^2X_0\right)/4X_0 \tag{12}$$

Concerning Equations (11, 12), the three fitting parameters of the Coulomb damping coefficient can be obtained as follows.

$$\begin{aligned}\pi X_0^2\begin{bmatrix}I_k^2-I_{k+1}^2 & I_k-I_{k+1} & 0\\ I_{k+1}^2-I_{k+2}^2 & I_{k+1}-I_{k+2} & 0\\ 0 & 0 & 4X_0\end{bmatrix}\begin{bmatrix}A_I\\ B_I\\ C_I\end{bmatrix}\\ =\begin{bmatrix}P_{op}\left(I_k,\omega\right)-P_{op}\left(I_{k+1},\omega\right)\\ P_{op}\left(I_{k+1},\omega\right)-P_{op}\left(I_{k+2},\omega\right)\\ P_{op}\left(I=0,\omega\right)-\pi c_\omega\omega^2X_0\end{bmatrix}\end{aligned} \tag{13}$$

Equation (13) is the parameter identifying equation of Coulomb damping. The equation shows that, under the circumstance of presupposing the system equivalent viscous damping, the Coulomb damping coefficient F_I can be obtained through the external work under different externally applied current conditions.

After identifying the equivalent viscous damping and coulomb damping force coefficient and solving Equation (4), one obtains

$$k(\omega)=\frac{F_{MR}-c_\omega\omega\sqrt{X_0^2-\mathbf{X}^2}sign\left(\dot{\mathbf{X}}\right)-sign\left(\dot{\mathbf{X}}\right)\left(A_II^2+B_II+C_I\right)}{\mathbf{X}} \tag{14}$$

The equivalent stiffness k_ω in the above equation is the function of frequency, which can be identified by least-squares fitting.

$$\min\left(\sum\left(A_k\omega^2+B_k\omega+C_k-k_\omega(\omega)\right)^2\right) \tag{15}$$

Optimizing A_k, B_k, and $C_k$can minimize Equation (15). The optimized solution is the fitting parameter that MR damper stiffness varies with the frequency.

EXPERIMENTAL TESTING PROCEDURE

In conclusion, the parameter identification flow of the improved Bingham fitting model proposed is shown in **Figure 5** as follows.

(a) Apply a current to the MR mounts; do not change the externally applied load amplitude; measure the displacement–force curve under different external load frequencies; calculate the external work through Equation (4); identify the equivalent viscous damping of the mounts through Equation (6).
(b) Similar to the first step, apply a sine exciting force with the same amplitude and excitation frequency to the MR mounts by different currents to calculate the external work made by different exciting forces; substitute different values of external work into Equation (7) to calculate the Coulomb damping force coefficient of the mount system.
(c) Obtain the inverse solution of the rule that mount stiffness changes with frequency by identifying the obtained viscous damping force and Coulomb damping force.

EXPERIMENTAL RESULTS AND DISCUSSION

The proposed method was applied to MR mounts and an experimental platform, as shown in **Figures 6**, **7**. The MR mounts are installed under the vibration exciting platform composed of the electrohydraulic excitation control system, force sensor, computer, fixture, current source, data collection and control software, and hardware system. The electrohydraulic servo excitation control system includes an MTS 242.01 actuator and a built-in high-accuracy displacement sensor. The force sensor is a BK-1 strain sensor produced by The Aerospace Aerodynamic Research Institute, China.

The main technological parameters of the excitation platform are defined as follows: the maximum vibration excitation amplitude is 5 mm, and the excitation frequency range is 0–150 Hz. In addition, the measurement range of the force sensor is from −6000 to 6000 N, and its accuracy grade is 0.6 N. The measurement range of the displacement sensor is from −10 to 10 mm, and the accuracy grade of the two sensors is 0.005 mm.

Five groups of dynamic characteristic tests under different external loading frequencies were performed on the MR fluid mounts, with the condition not changing the current according to the testing theory. **Figure 8** indicates that the mounts' reaction force changes with the time and displacement under the conditions of 600 N preloading force, and **Figure 8A** shows the reaction force–displacement relationship of the MR mounts in a 0.4 A externally applied current. **Figure 8B**

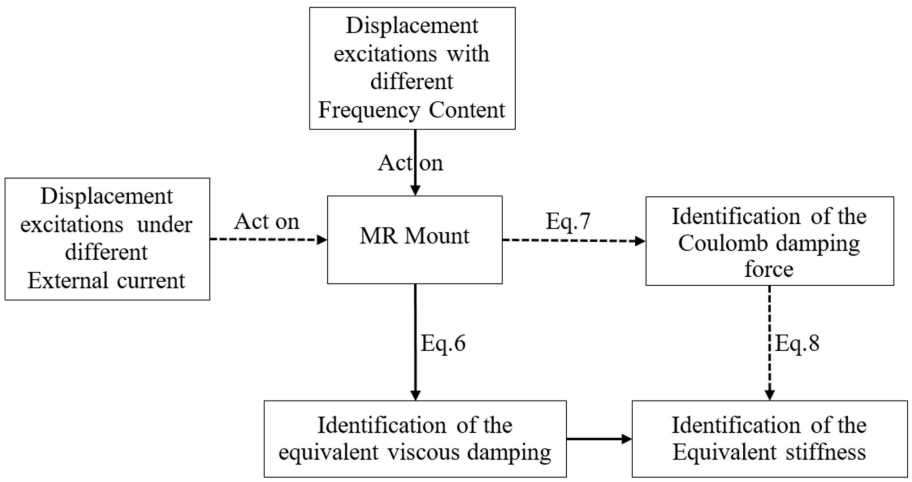

FIGURE 5 | Parameter experimented fitting flow figure to be identified in parameterized model.

FIGURE 6 | MR mounts adopt in this paper.

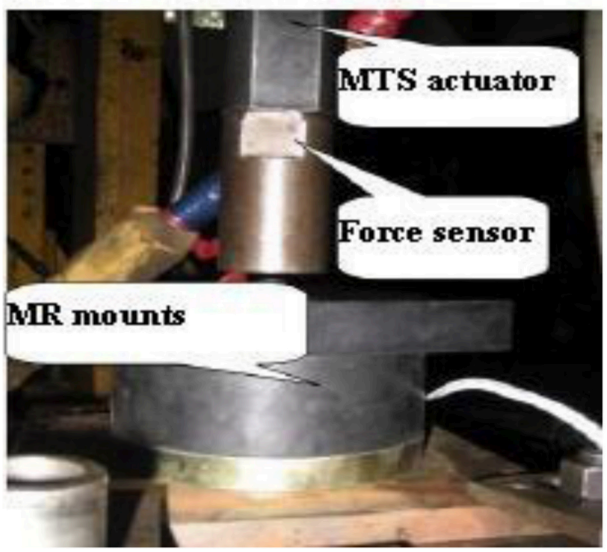

FIGURE 7 | Testing platform of MR mounts.

gives the reaction force–displacement relationship at a 0.5-mm excitation amplitude.

According to the theory proposed here, the fitting parameters of dynamic characteristics of MR fluid mounts are calculated, as shown in **Table 2**.

Figures 9–11 illustrate the identification curves, which shows that the dynamic characteristic parameters of MR mounts vary with the current.

The following can be concluded from **Figure 9**. (a) The Coulomb damping force of the MR mounts increases with the current; when the current exceeds 0.7 A, the Coulomb force rises with the current, but not evidently. This shows that the MR effect of MR fluid tends to a saturation state. (b) When the externally applied current is 0 A, the MR mounts still have some friction damping force of ∼22.4 N; when the current reaches 1.0 A, tending to saturation, the largest damping force reaches 225.2 N, and the adjustable multiple is ∼10. This demonstrates that the designed MR damper structure can change the damping force within a wide range, with a fine adjustable characteristic of damping force.

It can be concluded from **Figure 10** that: (a) the equivalent stiffness of the MR mounts rises with the frequency, and the rising speed goes faster and faster, which is caused by the dynamic effect of rubber, and (b) when the engine is working at a high frequency, the stiffness of the MR mounts is improved up to 821 N/mm—approximately twice 401.5 N/mm, the static value of stiffness. With the rise of the stiffness, the transmissibility of the engine goes faster and faster, which makes it necessary to apply a larger

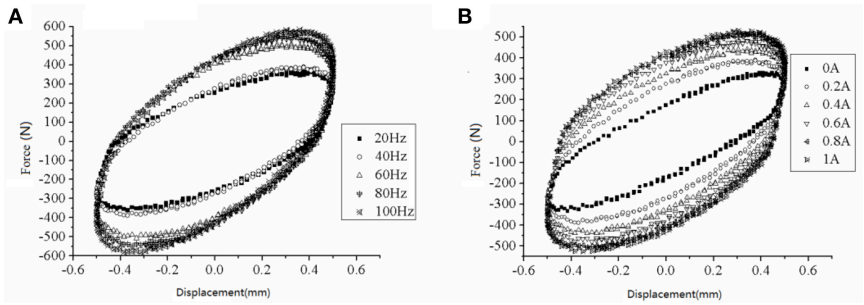

FIGURE 8 | The force-displacement relationship of MR fluid mounts **(A)** in different excitation frequency **(B)** in different currents.

TABLE 2 | Identifying parameter results of MR fluid.

Parameter	A_k(N*m-1 Hz-2)	B_k(N*m-1 Hz-1)	C_k(N*m-1 Hz)	A_I	B_I
value	0.045	−0.5	401.5	−175.4	378.2
parameter	C_I	Ac	Bc	Cc	—
value	22.4	−0.138	10.46	1024.4	—

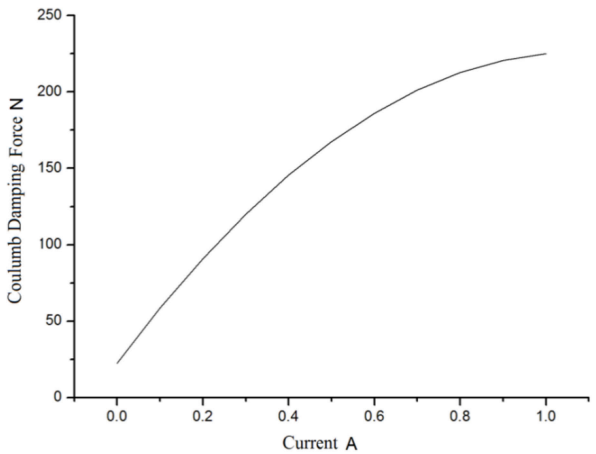

FIGURE 9 | Fitting results of MR mounts coulomb damping force.

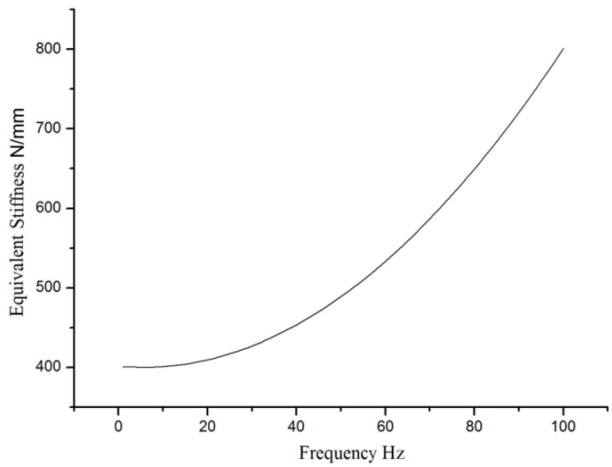

FIGURE 10 | Fitting results of equivalent stiffness of MR mounts.

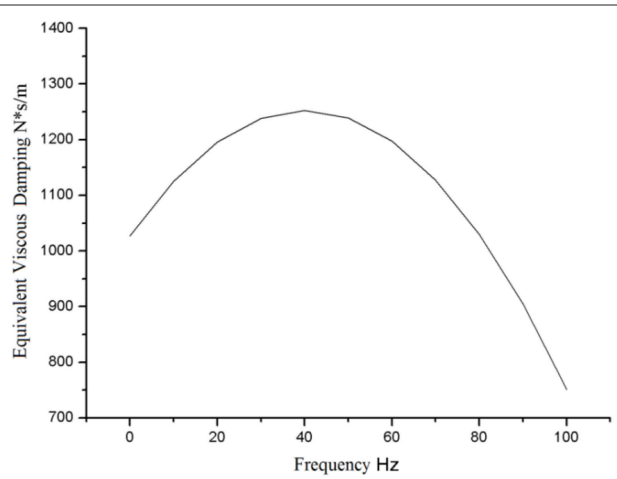

FIGURE 11 | Fitting results of equivalent viscous damping of MR mounts.

current to improve the Coulomb damping force and achieve vibrating control.

Figure 11 provides the viscous damping identifying results of the MR mounts. **Figure 11** shows that the viscous damping of the MR mounts goes up with the rise of working frequency when the engine is working at a low frequency (lower than 40 Hz), but lowers with the rise of working frequency when the engine is working at a high frequency (higher than 40 Hz), With a view to further verifying the reliability of the fitting results, **Figures 12**, **13** give the MR mounts' fitting results of dynamic stiffness and lagging angle under different excitation frequencies and external currents. Moreover, **Figure 12** provides the fitted and experimental result of the force–displacement relationship.

By comparing **Figures 12**, **13**, one can find that, because of the inherent defect of the Bingham model at low speeds in describing the mounts' dynamic characteristics, the fitting result has errors at the maximum mount displacement (low-speed

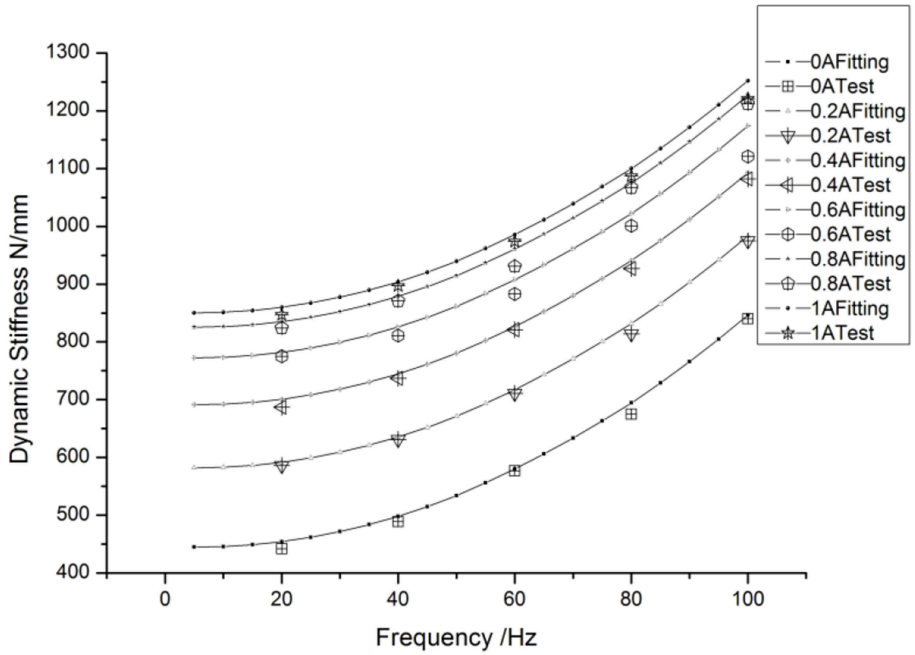

FIGURE 12 | Fitting experiment contrast figure of dynamic stiffness of MR mounts.

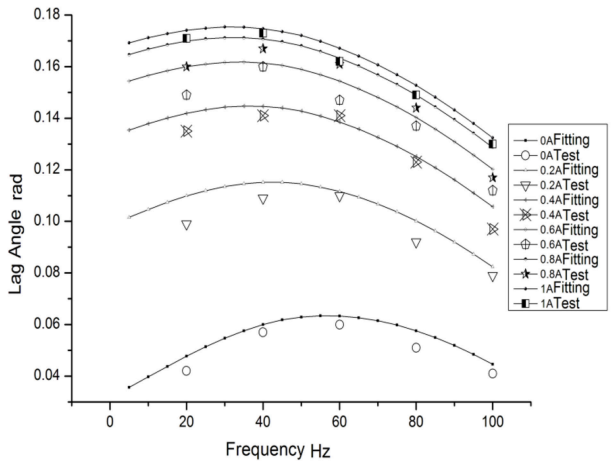

FIGURE 13 | Fitting experiment contrast figure of lagging angle of MR mounts.

range), leading to an obvious difference in the fitting results of dynamic stiffness and lagging angle from the true ones. **Figure 14** shows that, in general, the fitted hysteretic curve of the mounts is in accordance with the experimental curve, which demonstrates that the improved polynomial Bingham model proposed can properly describe the dynamic characteristics of the MR fluid mounts in a wide frequency band and lay a rational foundation for the active vibration control and optimal design of engine mounts.

CONCLUSIONS

For the purpose of describing the dynamic characteristic behavior of MR fluid mounts in a wide frequency band, an improved polynomial Bingham model based on experiments was proposed. The fitted result based on the model shows that the viscous damping of MR mounts goes up with the rise of frequency when working at low frequencies or lowers with the rise of frequency when working at high frequencies. The equivalent stiffness produces a dynamic stiffness effect—that is, the mounts' stiffness rises with the frequency, and the rising speed goes faster and faster, which is caused by the dynamic effect of rubber. It is approximately twice the rubber stiffness in a static status when working at high frequencies. The mounts' Coulomb damping force rises with the increase in current; however, when the current exceeds 0.7 A, the rise is not obvious, which demonstrates that the MR effect tends to a saturation state.

In addition, comparison of the experimental result shows a poor performance in describing the mounts' dynamic effect when the displacement of the mount reaches its maximum. However, the improved polynomial Bingham model can properly describe the dynamic characteristics of the MR mounts in a wide frequency band.

Finally, compared with other parameterized models, this model features simple calculation, fewer variables, and explicit expressions, which provides a basis for applying the mounts to vibration control research on engines and the optimal design of mount components.

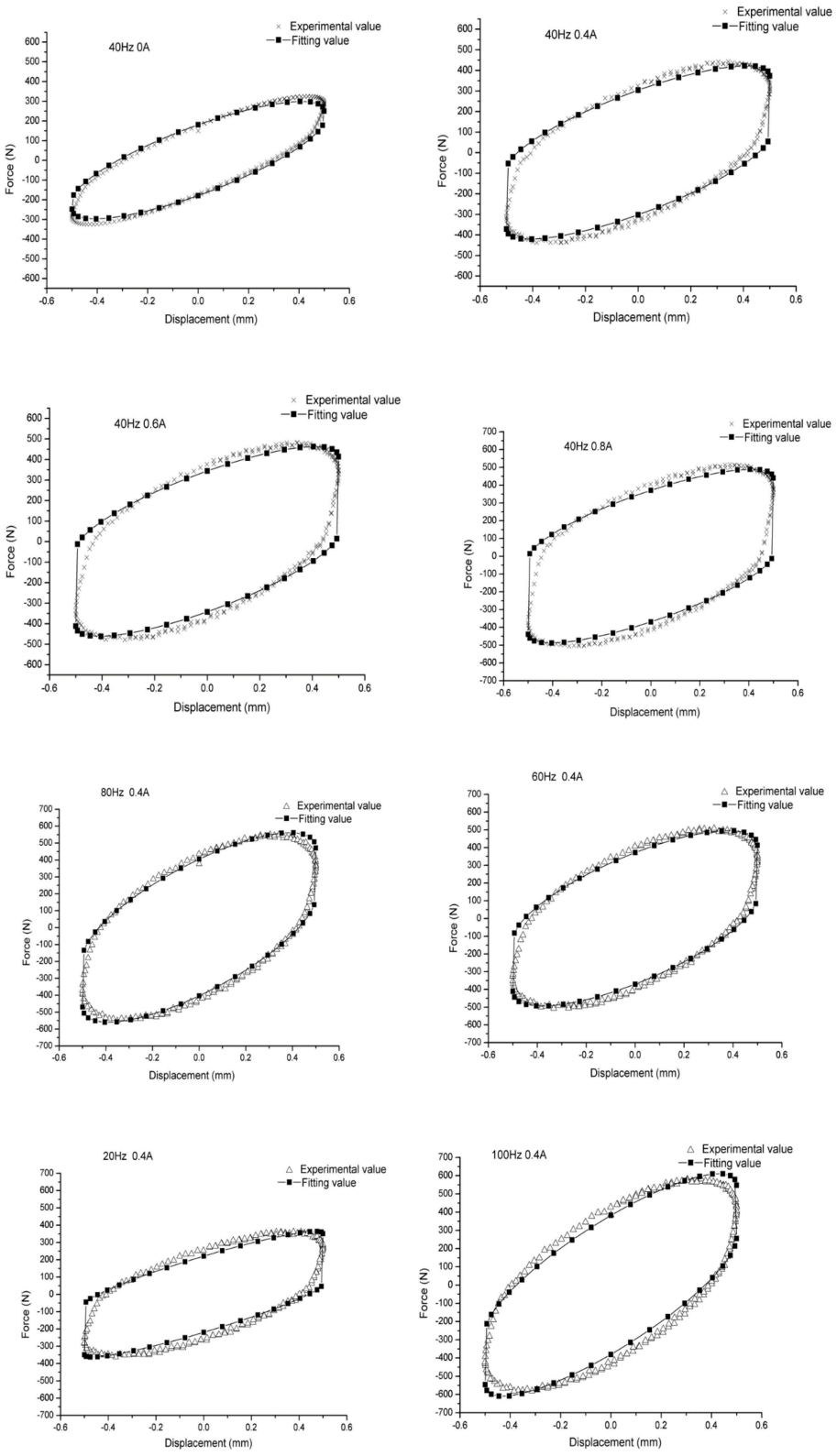

FIGURE 14 | Contrast fitting value figure of the experimental value of hysteretic curve under all working conditions.

AUTHOR CONTRIBUTIONS

SC writes the paper and contributes to the model's establishment. RL design the MR mounts, and PD contributes to the experimental validation. HZ and DL analyzed magnetic circuit of the mount by using FEM.

FUNDING

Financial support was received from the National Natural Science Foundation of China (Grant NO. 11602043) and from the China Postdoctoral Science Foundation (NO. 2017M610386).

REFERENCES

Bai, X., Wereley, N. M., and Hu, W. (2015). Maximizing semi-active vibration isolation utilizing a magnetorheological damper with an inner bypass configuration. *J. Appl. Phys.* 117:288. doi: 10.1063/1.4908302

Barber, D. E., and Carlson, J. D. (2010). Performance Characteristics of Prototype MR Engine Mounts Containing Glycol MR Fluids. *J. Intell. Mater. Syst. Struct.* 21, 1509–1516. doi: 10.1177/1045389X09351957

Behrooz, M., Sutrisno, J., Wang, X., Fyda, R., Fuchs, A., Gordaninejad, F. (2011). A new isolator for vibration control. *Proc. SPIE Int. Soc. Opt. Eng.* 79770Z. doi: 10.1117/12.881871

Chang-rong, L., Lei, X., Dan-xia, Z., Qiong, L. (2013). Quasi-steady modelling for magneto-rheological fluid mount based on squeeze mode and experimental testing. *Int. J. Veh. Des.* 63, 275–290. doi: 10.1504/IJVD.2013.056156

Chen, P., Bai, X. X., and Qian, L. J. (2016). Magnetorheological fluid behavior in high-frequency oscillatory squeeze mode: experimental tests and modelling. *J. Appl. Phys.* 119:105101. doi: 10.1063/1.4943168

Choi, S. B., Lee, S. K., and Park, Y. P. (2001). A hysteresis model for the field-dependent damping force of a magnetorheological damper. *J. Sound Vib.* 245, 375–383. doi: 10.1006/jsvi.2000.3539

Delattre, A., Lejeunes, S., Lacroix, F., Méo, S. (2016). On the dynamical behavior of filled rubbers at different temperatures: experimental characterization and constitutive modeling. *Int. J. Solids Struct.* 90, 178–193. doi: 10.1016/j.ijsolstr.2016.03.010

Farjoud, A., Taylor, R., Schumann, E., Schlangan, T. (2014). Advanced semi-active engine and transmission mounts: tools for modelling, analysis, design, and tuning. *Veh. Syst. Dyn.* 52, 218–243. doi: 10.1080/00423114.2013.870345

Hoang, N., Zhang, N., and Du, H. (2011). An adaptive tunable vibration absorber using a new magnetorheological elastomer for vehicular powertrain transient vibration reduction. *Smart Mater. Struct.* 20:015019. doi: 10.1088/0964-1726/20/1/015019

Hong, S. R., Wereley, N. M., Choi, Y. T., Choi, S. B. (2008). Analytical and experimental validation of a nondimensional Bingham model for mixed-mode magnetorheological dampers. *J. Sound Vib.* 312, 399–417. doi: 10.1016/j.jsv.2007.07.087

Li, Z. J., Ni, Y. Q., Dai, H. Y., Ye, S. Q. (2013). Viscoelastic plastic continuous physical model of a magnetorheological damper applied in the high speed train. *Sci. China* 56, 2433–2446. doi: 10.1007/s11431-013-5342-y

Lin, C. R., and Lee, Y. D. (1998). Effects of viscoelasticity on rubber vibration isolator design. *J. Appl. Phys.* 83, 8027–8035. doi: 10.1063/1.367895

Nguyen, Q. H., Choi, S. B., Lee, Y. S., Han, M. S. (2013). Optimal design of high damping force engine mount featuring MR valve structure with both annular and radial flow paths. *Smart Mater. Struct.* 22:115024. doi: 10.1088/0964-1726/22/11/115024

Razman, M. A., Priyandoko, G., and Yusoff, A. R. (2014). Bouc-Wen model parameter identification for a MR fluid damper using particle swarm optimization. *Adv. Mat. Res.* 903, 279–284. doi: 10.4028/www.scientific.net/AMR.903.279

Sado, D. (2013). Nonlinear dynamics of a non-ideal autoparametric system with MR damper. *Shock Vib.* 20, 1065–1072. doi: 10.1155/2013/605725

Shangguan, W. B. (2009). Engine mounts and powertrain mounting systems: a review. *Int. J. Veh. Des.* 49, 237–258. doi: 10.1504/IJVD.2009.024956

Shangguan, W. B., and Lu, Z.-H. (2003). Finite element analysis of elastic characteristics of rubber isolator for automotive powertrain systems. *Chin. Intern. Combust. Eng. Eng.* 24, 50–55. doi: 10.1007/BF02974893

Spaggiari, A., and Dragoni, E. (2012). Efficient dynamic modelling and characterization of a magnetorheological damper. *Meccanica* 47, 2041–2054. doi: 10.1007/s11012-012-9573-y

Swevers, J., Al-Bender, F., Ganseman, C. G., and Projogo, T. (2000). An integrated friction model structure with improved presliding behavior for accurate friction compensation. *IEEE Trans. Automat. Contr.* 45, 675–686. doi: 10.1109/9.847103

Tikani, R., Vahdati, N., and Ziaeirad, S. (2015). Two-mode operation engine mount design for automotive applications. *Shock Vib.* 19, 1267–1280. doi: 10.1155/2012/651591

Wang, L. R., and Lu, Z. H. (2003). Modeling method of constitutive law of rubber hyperelasticity based on finite element simulations. *Rubber Chem. Technol.* 76, 271–285. doi: 10.5254/1.3547739

Wang, X., and Faramarz, G. (2009). A new magnetorheological fluid–elastomer mount: phenomenological modeling and experimental study. *Smart Mater. Struct.* 18:095045. doi: 10.1088/0964-1726/18/9/095045

Wang, X. E., and Chen, Z. Y. (2017). Vibration control and design of vehicle engine mount activated by magneto-rheological fluid. *Tech. Autom. Appl.* 2–3:1077–1081. doi: 10.4028/www.scientific.net/AEF.2-3.1077

Xu, Y., Ahmadian, M., and Sun, R. (2014). Improving vehicle lateral stability based on variable stiffness and damping suspension system via MR damper. *IEEE Trans. Veh. Technol.* 63, 1071–1078. doi: 10.1109/TVT.2013.2282824

Zhu, X., Jing, X., and Cheng, L. (2011). A magnetorheological fluid embedded pneumatic vibration isolator allowing independently adjustable stiffness and damping. *Smart Mater. Struct.* 20, 85025–85042. doi: 10.1088/0964-1726/20/8/085025

Conflict of Interest Statement: The authors declare that the research was conducted in the absence of any commercial or financial relationships that could be construed as a potential conflict of interest.

frontiers in Materials

ORIGINAL RESEARCH
published: 22 March 2019
doi: 10.3389/fmats.2019.00045

Application of Magneto-Rheological Fluids for Investigating the Effect of Skin Properties on Arterial Tonometry Measurements

Adam Coon[1], *Tae-Heon Yang*[2], *Young-Min Kim*[3], *Heeshin Kang*[4] *and Jeong-Hoi Koo*[1]*

[1] Department of Mechanical and Manufacturing Engineering, Miami University, Oxford, OH, United States, [2] Department of Electronic Engineering, Korea National University of Transportation, Chungju-si, South Korea, [3] Future Medicine Division, Korea Institute of Oriental Medicine, Daejeon, South Korea, [4] Department of Laser and Electron-Beam Application, Korea Institute of Machinery and Materials, Daejeon, South Korea

OPEN ACCESS

Edited by:
Seung-Bok Choi,
Inha University, South Korea

Reviewed by:
Young Choi,
University of Maryland, United States
Woon-Hong Yeo,
George W. Woodruff School of Mechanical Engineering, Georgia Institute of Technology, United States
Ali El Wahed,
University of Dundee, United Kingdom

***Correspondence:**
Jeong-Hoi Koo
koo@miamioh.edu

Specialty section:
This article was submitted to Smart Materials, a section of the journal Frontiers in Materials

Received: 01 December 2018
Accepted: 25 February 2019
Published: 22 March 2019

Citation:
Coon A, Yang T-H, Kim Y-M, Kang H and Koo J-H (2019) Application of Magneto-Rheological Fluids for Investigating the Effect of Skin Properties on Arterial Tonometry Measurements. Front. Mater. 6:45. doi: 10.3389/fmats.2019.00045

Accurate, non-invasive measurements of blood pressure and its continuous monitoring are extremely important for personal health care. Arterial tonometry, a method that is used to provide a detailed image of a patient's cardiovascular health, shows promise for being a non-invasive alternative to current blood pressure measurement methods. However, its measurement accuracy is sensitive to patient variations such as the stiffness of the skin. Thus, this project intends to investigate the effect of skin properties (i.e., stiffness) on the accuracy of tonometric blood pressure measurements. To this end, a test platform, consisting of a pulsatile system and a tunable skin stiffness apparatus (or MR apparatus), is constructed. The cam-follower pulsatile system built based on *in vivo* testing of human pulses is used to generate realistic pulse waveforms. The MR apparatus is able to adjust its stiffness using Magneto-Rheological (MR) fluid whose apparent viscosity changes with applied magnetic fields. Placed at the surface of the MR apparatus, a cylinder with a frictionless plunger simulates a variable applanation force or "hold-down pressure" of tonometry by adjusting the added weights atop the cylinder. Using this test setup, a series of tests were performed by varying the input magnetic field and the weights, which effectively adjusts the skin stiffness and the hold-down pressure, respectively. The vertical displacement of the plunger caused by the internal pulse pressure was measured using a laser displacement sensor. The output displacement waveforms were analyzed with the focus on the peak amplitude difference of the waveforms, which is related to the augmentation index (a surrogate measure of arterial stiffness). The results show that there exists an "optimal" plunger weight or "hold-down pressure" that provides the most distinct output pulse waveforms. The results further show that the difference in the first two peak values decreases as the skin stiffness increases, indicating that the stiffer the skin property, the less the "hold-down pressure" effects on the accuracy of the tonometry measurements.

Keywords: magneto-rheological fluid, skin properties, blood pressure, sub-cutaneous tissue, pulse waveforms, tonometry

INTRODUCTION

Human skin is a very complex organ that can be separated into three different layers; the epidermis, the dermis, and the hypodermis or subcutaneous tissue (Geerligs, 2006). All of these layers work to define the mechanical properties and characteristics of the skin. Due to the human skin being the main barrier in determining a patient's vitals, it is imperative that we understand its mechanical properties and how it affects the measurements of vital signals. Research into the human skin's mechanical properties will help in the creation of accurate, continuous, and non-invasive vital monitoring systems. Internal vital measurements, such as blood pressure, are extremely important in determining the health of a patient's cardiovascular system. In the United States, cardiovascular diseases have long been the leading cause of death. Hypertension is one of the most prevalent contributors to these diseases and has been known to increase the risk for all atherosclerotic cardiovascular diseases an average of 2 to 3-fold (Kannel, 1996). Currently, the "gold standard" for non-invasive blood pressure measurement is blood pressure "cuffs" (Chung et al., 2013). However, the need to constrict the arm with the inflated cuff can cause discomfort for the patient and make it less desirable for continuous monitoring. More importantly, cuffs only measure the systolic and diastolic values and brachial artery pressure, which do not provide a complete picture of a patient's internals (Smulyan et al., 2003; Singh et al., 2017). Furthermore, "white coat" hypertension, where a patient has high blood pressure due to anxiety during the measurement, has been known to increase a patient's blood pressure as much as 30 mmHg (Beevers et al., 2001). Due to these downsides of measuring blood pressure using cuffs, other ways of non-invasive measurement should be investigated.

Recently, the arterial tonometry method is being used widely as it overcomes limitations of the conventional cuff-based blood pressure measurements. The tonometry method places a pressure sensor on the surface of the skin where the radial artery is located to measure blood pressure. Unlike the cuff devices, which require pressurizations, the tonometry method applies a minimal pressure on the skin. Moreover, with tonometry, the actual arterial pulse waveform, augmentation index, and systolic and diastolic pressures can be continuously monitored which can provide better diagnoses of heart-related diseases (Smulyan et al., 2003; Tomiyama et al., 2014; Langwieser et al., 2015). Tonometry and its applications have shown great promise in the field of non-invasive continuous blood pressure monitoring. Langwieser et al. studied arterial blood pressure tonometry's use in cardiac intensive care. Usually, an invasive catheter is used to continuously measure arterial blood pressure. However, it was shown that arterial tonometry for intensive care patients is feasible and provided reasonable results when compared to the catheter method (Langwieser et al., 2015). Additionally, Digiglio et al. developed a method that uses a "microflotronic" arterial tonometry system. By utilizing a combination of microfluid and electronic devices, they successfully developed a completely non-invasive, nearly imperceptible device that is able to be worn on the wrist and provide continuous blood pressure monitoring (Digiglio et al., 2014).

While it has been proven that arterial tonometry is a viable replacement for current, invasive blood pressure monitoring techniques, there are some issues that need to be addressed. Arterial tonometry has been shown to be a very sensitive process that is accurate but can be unreliable (Weiss et al., 1996). If the device's contact with the skin over the artery is misaligned or even tilted slightly, the results can be affected. Furthermore, the precise measurement of blood pressure can be affected if the device places insufficient pressure on the artery (Shioya and Dohi, 2013). The mechanical properties of the skin will also affect the measurements read by the tonometer. Using an indentation test, which uses a method similar to a tonometer, it was shown that the skin responded differently for different age groups. For the same indentation force and speed, the response for the young people's skin was much more elastic than the response of the older people's skin (Zahouani et al., 2009). Since both the indentation test and arterial tonometry require a small external force application, the effect of a patient's age on indentation response may hold for the arterial tonometry as it did for the indentation test. This correlation is corroborated by Boyer et al. whose study showed, through *in vivo* indentation testing, that the stiffness and damping of the human skin decreased with increasing age (Boyer et al., 2009). In their computational work, Singh et al. studied the accuracy of tonometers and the problem of patient variability, specifically age, on radial artery tonometry to design new tonometers. It was found that the skin stiffness for age groups from 35–45 to 55–65 and the shape of the tonometer plunger were significant and must be accounted for in device calibration for tonometers (Singh et al., 2017). These studies suggest that the age-related change in skin properties may affect the results of arterial tonometry. Furthermore, accounting for the variability of the human body, specifically, the age-dependency of skin stiffness is critical to developing blood pressure monitoring devices.

Besides conventional arterial tonometer measurements, it is imperative to understand the role of skin property on wearable, non-invasive blood pressure monitoring devices. The wearable devices make constant contact with the skin during the measurement process, so the skin's properties play an important role in their measurement accuracy. When under stress, skin shows anisotropic and viscoelastic properties which would unusually distort the expansion of the artery and therefore external pressure measurements (Khatyr et al., 2004). Woo et al. studied a tissue-informative mechanism to obtain blood pressure measurements non-invasively using a wearable pressure sensor module. By modeling the subcutaneous tissue using a spring and damping constant, they found that the stiffness of the subcutaneous tissue changes with respect to average blood pressure. Using this relationship, they were then able to measure radial blood pressure without any additional pressure from the measurement device (Woo et al., 2014).

Despite the significance of skin property on blood pressure measurements, limited studies investigated the skin stiffness effect on arterial tonometry measurements. Furthermore, there exists a growing need for establishing a more holistic view of the skin stiffness effect on wearable, non-invasive blood pressure monitoring systems in order to develop such devices. Using human subjects for skin effect studies would be resource

intensive and time-consuming. Therefore, this study intends to investigate the effect of skin stiffness on the arterial tonometry measurements. To this end, a test setup that is able to simulate the blood pulsations and variations of skin stiffness is created. To obtain meaningful results without involving human subjects, it is critical to have a component that can generate realistic human pulse waveforms and provide them consistently. In this study, a cam system is employed, which was created based on *in vivo* testing in a separate study, to provide "standard" pulse waveforms. With its mechanical simplicity and consistent motions, a cam system can provide the reference pulse waveforms required in this study. Another critical component is a tunable stiffness element. For the current study, a tunable stiffness apparatus was constructed based on Magneto-Rheological (MR) fluid. MR fluid is a controllable fluid, comprised of micron-sized iron particles suspended in a binding agent, often a type of oil. The apparent viscosity of MR fluids can be controlled by applying external magnetic fields. The ability to change the state of MR fluids, by the applied magnetic field, from liquid to semi-solid is fast (in milliseconds) and reversible. In the current study, the MR fluid is placed into a fluid container to create an artificially tunable skin stiffness apparatus. The pulses generated by the cam system are sent through a silicone tube that is submerged in MR fluid. Using an electromagnet, the stiffness of the MR fluid is varied. To simulate varying hold-down pressures of a tonometer, a cylinder with a frictionless plunger and a stack of weights is placed on top of the MR apparatus with the plunger resting on the tube surface. A precision laser sensor is used to measure the displacement of the plunger while varying the magnetic fields and weights. These "output pulse" data is compared with the actual pressure waveform in the tube to assess the effect of the skin stiffness effect of the tonometry measurements.

DESIGN AND CONSTRUCTION OF THE TEST PLATFORM

This section presents the design and fabrication of the test platform used in this study and the working principles of each element. The test platform has two main components: (1) the cam system and (2) the artificially tunable skin stiffness apparatus. The cam system was used to generate uniform, continuous reference waveforms and the tunable skin stiffness apparatus was used to adjust its stiffness.

Cam Pulsation System

In order to conduct this study, a device that is able to consistently and continuously reproduce a human pulse waveform was needed. To this end, a cam pulsation system is selected as a cost-effective way of generating a reference human pulse waveform. The cam system was designed and constructed in a separate study conducted by Yang et al. While details of the design and the performance validation of the cam system can be found in the reference (Yang et al., 2019), this section briefly explains how the system was created. **Figure 1** shows the design process for developing a disk cam, the key element of the cam pulsation system. The shape of this cam was designed by collecting *in vivo* data of the pulse waveform and mapping the results to a circular pattern. The *in vivo* data was taken from the arterial pulse of a young, male subject using the radial pulse measurement system shown in **Figure 1A**. The pulse data taken was then averaged into the pulse waveform, which shows three distinct peaks as shown in **Figure 1B**, which shows the normalized blood pressure over a period of time. This pulse waveform was then converted to radial coordinates (see **Figure 1C**). **Figure 1D** shows the machined final cam based on the shape in radial coordinates.

Figure 2 shows the full assembly of the cam pulsation system, consisting of a cam, an electric motor, and a piston unit that includes a spring and bellows. When the cam rotates, it presses the bellows in such a way that a human pulse waveform is output to a silicone tube. The piston is kept in contact with the cam by a return spring. By moving this spring closer to the cam system, the pressure in the system can be shifted up and down. The cam system also includes a pressure sensor that collects the internal pressure of the system, which can be monitored on an oscilloscope. By varying the voltage supplied to the motor, the speed of the rotating cam is increased and the "heart rate" of the simulated pulse can be adjusted.

Artificially Tunable Skin Stiffness Apparatus

Another key component to conduct this study is a tunable stiffness apparatus. It will enable us to test the effect of skin stiffness on perceived blood pressure at the surface of the artificial

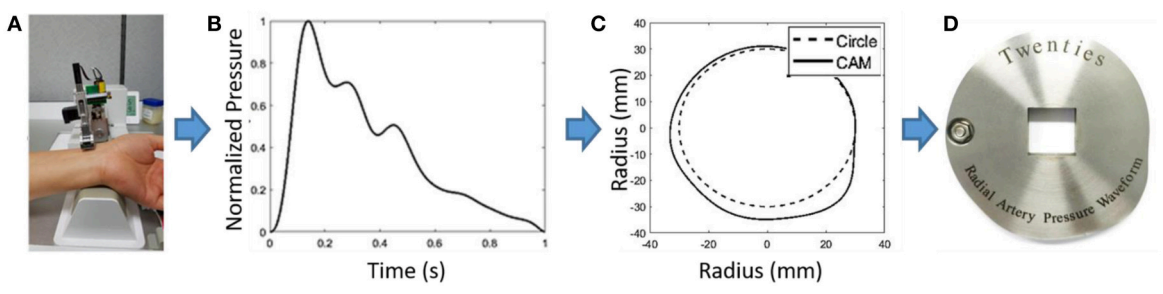

FIGURE 1 | (A) *In vivo* data collection using robotic tonometry system to get an example pulse waveform, **(B)** Normalized blood pressure of waveform vs. time, **(C)** Conversion of waveform into a radial geometry, **(D)** Manufactured cam disk from radial waveform (Yang et al., 2019).

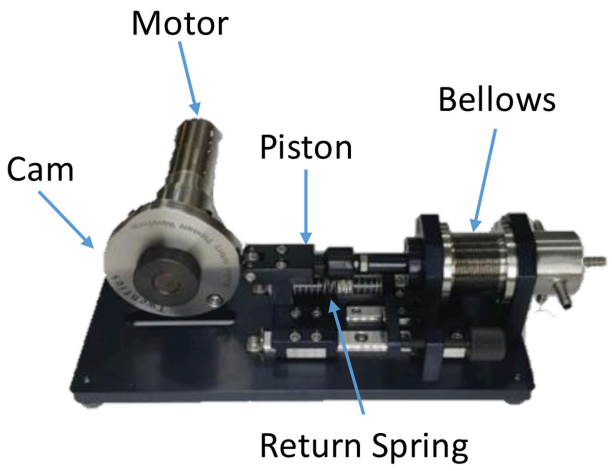

FIGURE 2 | Photo of the cam system used to generate human pulse waveforms.

skin. In this study, the tunable skin stiffness apparatus was designed based on MR fluid whose apparent properties can be controlled by external magnetic fields. The apparatus, shown in **Figure 3A**, has a container with a cavity in the center and a tube, which represents a radial artery, running across the middle. The tube is connected to the inlet shown on the outside of the container, stretched over the cavity, and connected to a plug on the right side. The inlet of the container is then connected to the cam system. The apparatus has a flexible membrane made of 3M VHB^{TM} Tape stretched over the MR fluid-filled cavity, depicted in the top of **Figure 3A**. The apparatus was designed to be placed on an electromagnet. A power supply is connected to the electromagnet in order to supply up to 24 V to it. As the electromagnet is turned on, the fluid in the container becomes stiffer which uniformly constricts the tube, which is illustrated in **Figure 3B**. By increasing the magnetic field, one should be able to suppress the pulsation felt in the tubing that is submerged in the MR fluid.

To study the magnetic field distribution in the MR apparatus, a simulation was conducted using the Finite Element Method Magnetics (FEMM) software. It is important to ensure that the electromagnet can activate the MR fluids with sufficiently strong and reasonably uniform magnetic fields. **Figure 4A** shows the simulation setup and results of the simulation in a cross section of the experimental setup shown in **Figure 3A**. The electromagnet was modeled using copper solenoid coils and an iron core. The MR apparatus is shown in the figure as the aluminum housing with iron at the center. Note that, in fabricating the MR apparatus, an iron core (or iron extension in **Figure 4A**) is used at its bottom portion that directly contacts with the electromagnet in order to direct maximum magnetic fields through the MR fluid. In order to increase the accuracy of the simulation, note also that the B-H curve of the MR fluid (MRF-140CG) was assigned in the cavity of the MR apparatus, where the MR fluid is. To further analyze the result, the magnetic flux density was taken across the black dashed line shown in **Figure 4A**. As shown in **Figure 4B**, the magnetic flux density values are ∼40 ± 5 mT, having the maximum near the edge of the MR housing. The flux density drops drastically in the middle of the graph (between the distance 8 and 12 mm) because this is the place where the air filled tube is located. From the graph, the magnetic field was ∼36 mT at the center of the magnet. These results corroborate the experimental measurements used in this study.

Figure 5 shows the plunger-cylinder system with a stack of weights. While the MR apparatus adjusts the stiffness level of the skin, the plunger-cylinder system is designed to vary the "hold-down pressure" by adding or removing the weights atop the plunger. As shown in **Figure 5**, the plunger-cylinder system is fixed to the top cover of the MR apparatus. The bottom of the frictionless plunger is placed on top of the apparatus (on top of the submerged tube). As the tube expands due to the pulse pressure, the plunger moves up and down. Thus, this displacement of the plunger is directly related to the perceived pressure at the surface measured by a tonometer. In other words, the tunable stiffness apparatus along with the plunger-cylinder setup can be used to control and test the effect of skin/tissue stiffness and hold down pressure on perceived pressure at the surface of the skin.

In the current study, the MR apparatus is intended to vary a range of its stiffness similar to the age-dependent human skin stiffness variation. According to a study by Boyer et al. human skin stiffness values could range between ∼20 N/m at the oldest to ∼70 N/m at the youngest, about a 350% difference (Boyer et al., 2009). Thus, to justify the efficacy of the MR apparatus for the age-dependent stiffness study, the target stiffness range should be close to 350%. To evaluate the stiffness range of MR apparatus, a series of indentation testing was conducted on the MR device using a Dynamic Mechanical Analyzer (DMA). During the test, the force vs. indentation depth was measured while varying the magnetic field from 0 to 36 mT. The results show that the stiffness value produced by the MR device ranges between ∼300 and ∼900 N/m for the magnetic field range considered in this study. Although the actual stiffness values between human skin and "MR skin" are different, the percent range of stiffness of the MR device is 300%. The results show that the MR system is capable of producing a range of stiffness in proportion to the age-dependent skin stiffness variation. Thus, the MR apparatus is suitable to investigate the effect of skin stiffness on arterial tonometry measurements, considering the skin stiffness variation over time. Please note that mimicking the exact *in vivo* human skin properties is out of the scope of the current study.

Experimental Setup

The primary purpose of this experiment was to study the effect of stiffness of the skin by evaluating the difference between the perceived pressure at the surface of the submerged tube and the actual pressure being supplied by the cam system. While the pulse was being supplied by the cam system, the pressure inside of the tube was measured using two methods. One was using a pressure sensor connected directly to the cam system to measure the actual pressure. The second method was a plunger with adjustable weight fixed to the MR apparatus with the plunger head resting on the flexible membrane (silicone skin) and tube, similar to

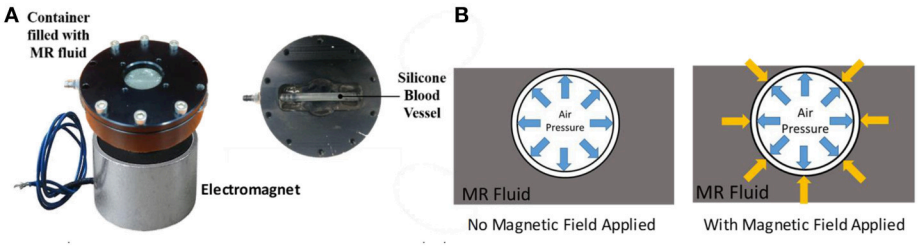

FIGURE 3 | Variable skin stiffness apparatus: **(A)** overhead view showing the apparatus assembled and disassembled, **(B)** Reaction in apparatus with and without magnetic field.

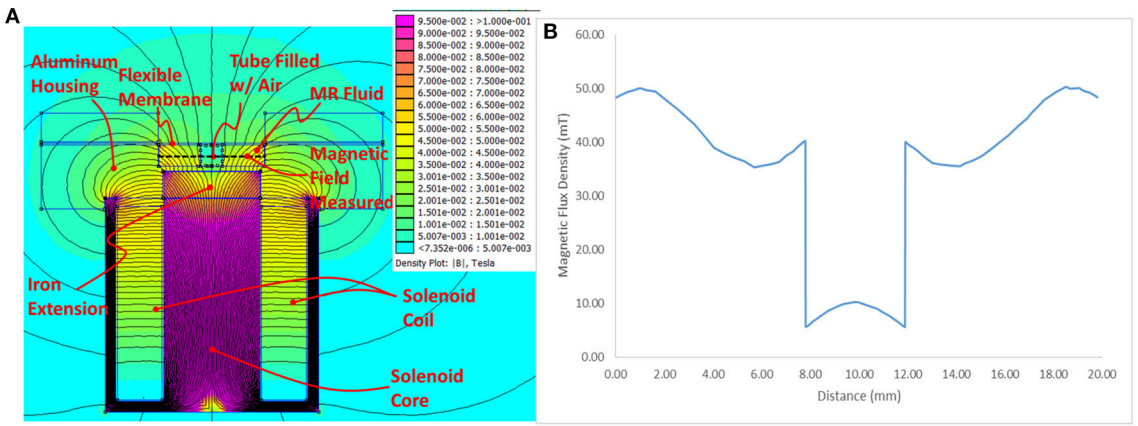

FIGURE 4 | FEMM simulation results: **(A)** Contour plot depicting the simulated magnetic field, **(B)** Magnetic field strength along the sample line.

the method utilized by tonometers. A laser displacement sensor was used to measure the vertical displacement of the plunger, which will be used to indirectly determine the pressure in the submerged tube. By adding weights to the plunger, the "hold-down pressure" is effectively being increased. The actual pressure measured by the pressure sensor and the displacement measured by the laser were measured for analysis. Power was supplied to the laser, electromagnet, and cam system using a 30 V DC lab power supply.

The full experimental setup is depicted in **Figure 6**. The cam system (left) sends a simulated pulse to the tunable skin stiffness apparatus (the black cylinder on the right). The apparatus is placed on top of an electromagnet and the plunger is fastened on top. Finally, a laser sensor is placed above the piston to accurately measure its vertical displacement. Two variables were adjusted to determine their effect. The magnetic field applied to the electromagnet and the weight on top of the plunger were varied to determine the effect of skin stiffness and hold down pressure on the system.

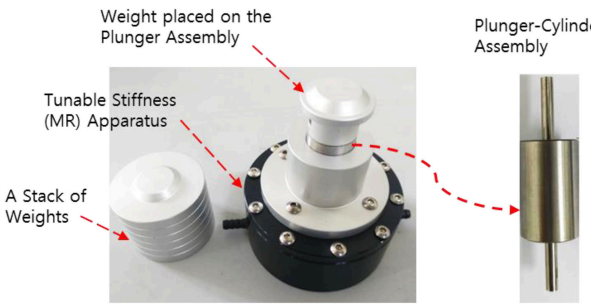

FIGURE 5 | Frictionless plunger used in the experimental setup. Applanation force or "hold-down pressure" is varied by adjusting the weights atop the cylinder with a frictionless plunger.

EXPERIMENTAL RESULTS

This section presents the experimental results obtained by varying the magnetic fields and the weights. By changing the weights, the effect of "hold-down" pressure was studied. To examine the effect of skin stiffness, the magnetic field was varied from 0 to 36 mT as measured using an axial gauss meter directly above the center of the electromagnet. The displacement of the plunger was measured and plotted for combinations of these changes. The displacement waveform results are compared with the reference pulse waveform. In particular, the distance between the first and second peak of the displacement response was

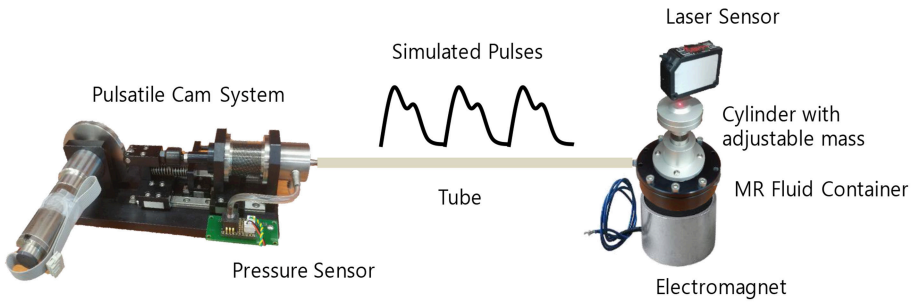

FIGURE 6 | Experimental test setup including a cam system, a silicon tube, a laser sensor, and the adjustable skin stiffness apparatus.

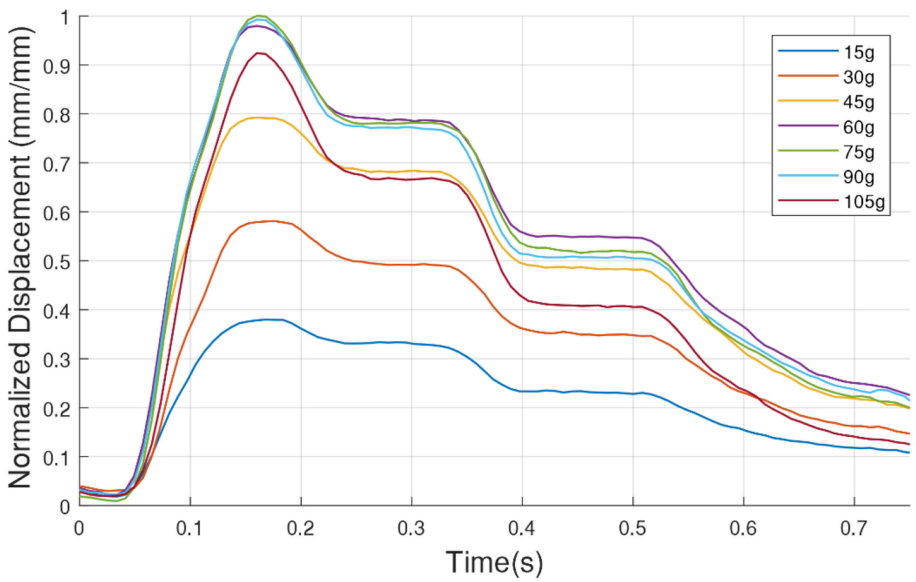

FIGURE 7 | Variations of the normalized displacement (pulse waveform) over time while changing the "hold-down" pressure by varying the mass from 15 to 105 g with an increment of 15 g.

analyzed for different weights and magnetic fields to assess the effect of stiffness.

Effect of Tonometry "Hold-Down Pressure"

In this section, the effect of "hold-down pressure" is studied to evaluate how the applied pressure affects the tonometry measurements. For this study, the mass load on the plunger is varied from 15 to 105 g in 15 g increments. No magnetic field was applied for these tests in order to establish a baseline understanding of the effect of hold down pressure. Each data point for all masses was normalized by dividing by the maximum displacement found across all tests. **Figure 7** shows the normalized displacement waveforms of the system with varying mass loading. As shown in the figure, the waveforms increase as the mass increases from 15 to 75 g, and they decrease as the mass further increases. This pattern is attributed to the fact that as the mass on the plunger is increased, the silicone tube increasingly deforms. Therefore, when the tube expands to its original dimensions from the pressure supplied by the cam system, the displacement is larger with increased initial deformation of the tube. In this case, the 75 g load provided the largest displacement. When the mass is increased past 75 g and the pressure supplied by the cam system is insufficient to expand the tube and lift the plunger, the displacement decreases again. The results indicate that the measured blood pressure using a tonometer would change depending on the hold-down pressure of the tonometer. Furthermore, the results show that there exists an optimum hold pressure when measuring blood pressure using tonometric methods. These results are consistent with the computational work performed by Singh et al. who determined that there was an optimum hold-down level for the plunger when using radial artery tonometry (Singh et al., 2017). For the range of mass used in this study, the mass load of 75 g applies an "optimal" hold-down pressure on the artificial artery that enables most distinct pulse readings. This study suggests the patient-to-patient accuracy may be affected depending on the

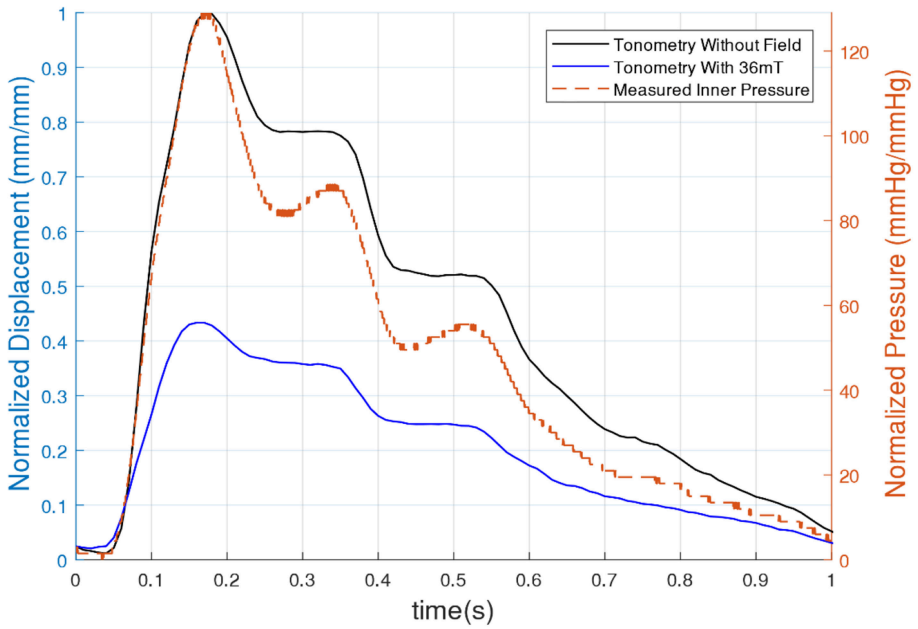

FIGURE 8 | Pressure and normalized displacement vs. time for a 75 g load with and without an applied magnetic field.

hold-down pressure used by the machine. For such a system to be used for blood pressure monitoring, the hold-down pressure must be calibrated for the patient's specific skin properties for truly accurate results.

Effect of MR Stiffness

This section evaluates the effect of tunable stiffness on pulse waveform measurements. For this part of the study, the cam system is supplied with 10 V to set the cycle time of each pulse at around 950 ms, which is about 60 beats per minute (bpm). This is because the average human heartbeat (or pulse) ranges from 60 to 80 bpm. Moreover, this study was performed at a fixed load of 75 g because it was found in **Figure 7** that a 75 g load created the most pronounced displacement values.

Figure 8 shows the plunger displacement waveform results for a 75 g load with no magnetic field and with the maximum magnetic field of 36 mT. For comparison, these were plotted against the pressure measurements taken from the cam system's pressure sensor. The results show that the displacement waveform does not perfectly match the inner pressure due to the "skin effect." The skin (the silicone membrane and MR fluid around the tube) filters the inner pressure signals (pulse waveform traveling in the tube). As shown in **Figure 8**, the inner pressure displays valleys after each peak, but the displacement response plateaus until it decreases to the next peak. This is attributed to the dampening of the MR skin. Furthermore, the figure shows that the displacement waveform decreased drastically with the maximum magnetic field (36 mT) as compared to that of the zero magnetic field case. The results indicate that the change in viscosity of the MR fluid successfully affected the displacement waveform and therefore is able to simulate the skin stiffness effect.

It is clear to see that the application of the magnetic field had a large impact on the displacement of the plunger as well as the distance between peaks. Therefore, to study this effect further, more tests were run by incrementing the magnetic field from 0 to 36 mT by 6 mT steps. The results for a 75 g load with varying magnetic fields are shown in **Figure 9**. As shown in the figure, the displacement waveform decreases as the applied magnetic field increases, indicating that the stiffness of the MR skin surrounding the tube clearly affected the external displacement of the plunger at the surface. The figure further shows that the rate of decrease of the waveform magnitudes is larger at lower magnetic fields. At higher magnetic fields, the displacement response seems to approach a saturation point. Furthermore, the results show a more sluggish response, represented by the decrease in the slope of the initial rise as well as the decrease in the distance between the first and second peaks, or ΔP, with increasing magnetic field. Overall, the results indicate the displacement of the plunger (i.e., perceived pressure) was lower when the MR fluid around the tube was stiffer. These results can be related to several studies that report on the age-dependent human skin stiffness variation (i.e., the elastic modulus of skin decreases as the age increases). Thus, the accuracy of a tonometer will be affected by the stiffness of the patient's skin and therefore the age of the patient.

Peak Displacement Change

The most holistic view of this study was examined by finding the magnitude differences between the first and second peak (ΔP) of each waveform for 75, 90, and 105 g loads with increasing magnetic flux density. The ΔP-values can be related to the

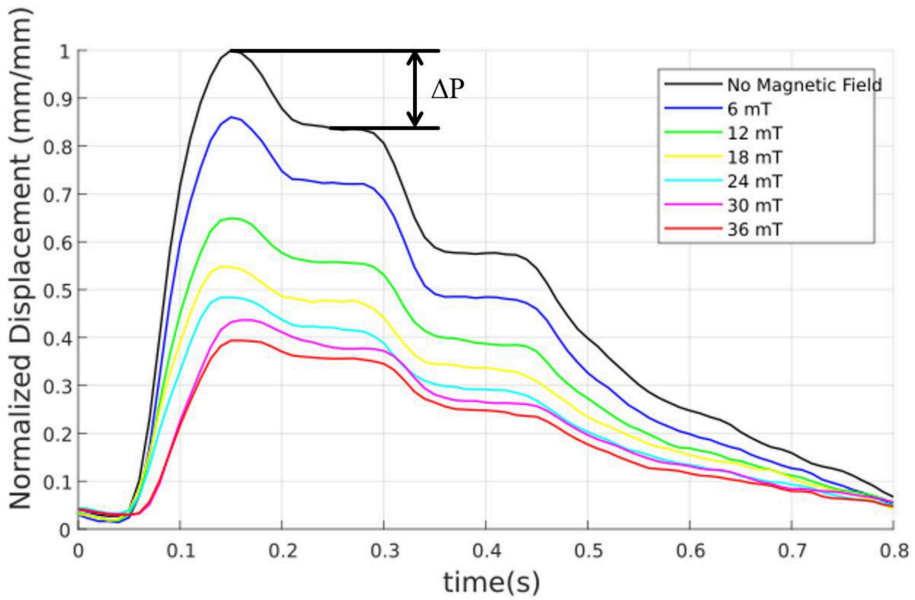

FIGURE 9 | Variation of normalized displacement curves for a 75 g load with a varying magnetic field from 0 to 36 mT.

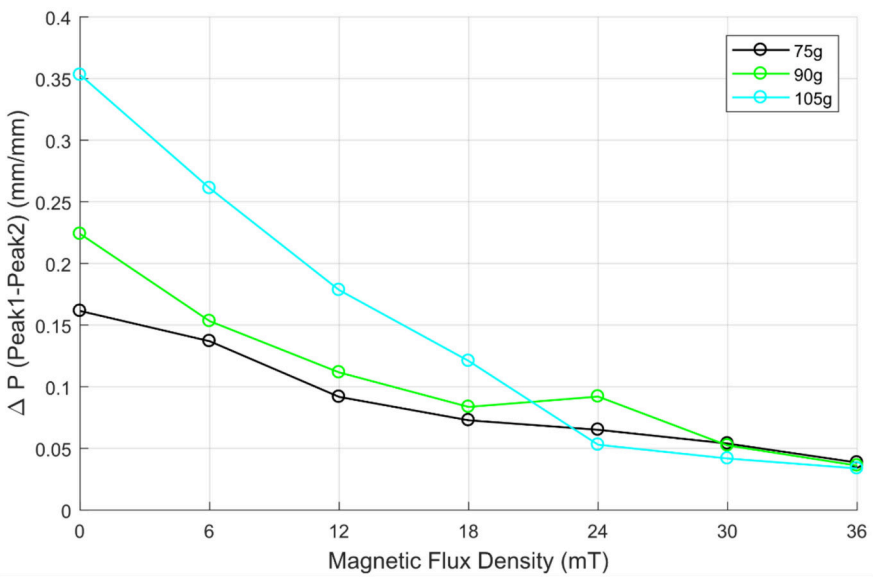

FIGURE 10 | Variation of the first two peak differences as a function of magnetic flux density for the mass of 75, 90, and 105 g.

augmentation index (AI), which is a ratio of the first two peak magnitudes of pulse waveforms. Clinically, the AI is widely used as a surrogate marker for cardiovascular diseases. **Figure 10** shows a variation of ΔP as the mass on the plunger (the hold down pressure) and the magnetic flux density (skin stiffness) vary. It is important to note that only masses above 75 g were considered for this analysis. This is due to the trend found in **Figure 7**. It was found that the displacement waveforms for masses above 75 g would mirror those for masses below 75 g. As shown in **Figure 10**, the differences in the peak displacement values (ΔP) were mostly proportional to increasing hold down pressure while being inversely proportional to the increasing magnetic field. The results further show that, as the magnetic field increases, the changes in ΔP for different hold down pressures became insignificant, with the peak displacements being almost identical at the maximum magnetic field of 36 mT. This would suggest that the hold-down pressure plays a higher role in accuracy when examining older patients with skin that is less

stiff (lower magnetic fields cases for this study). On the same note, it suggests that for younger patients with stiffer skin (higher magnetic field cases), the hold-down pressures may not be an issue when using tonometers. With the older patients being at a higher risk of cardiac events, it is important to note that their results are affected most. Furthermore, while the trends are fairly consistent for each mass load, the curve of the 105 g load crosses over the 75 and 90 g curves after the 18 mT results. This is most likely attributed to experimental error and the post-processing of data. The experimental set up used may not have been accurate enough once the results began to converge toward one another. Also, as one can see in **Figure 9**, the second peak becomes more and more indeterminate as the magnetic field increases. Therefore, to combat this, an average of several points along the second peak was used to get an average of the second peak value. This may have caused the results to skew the trends after the 18 mT mark when greater precision was needed to accurately show the differences between the curves.

CONCLUSION

This study has investigated the effect of skin stiffness on arterial tonometry. To adjust the skin stiffness, a tunable skin stiffness apparatus was successfully created using Magneto-Rheological (MR) fluid and an electromagnet. This apparatus was implemented along with a cam system that was able to continuously provide a human radial pulse waveform obtained by *in vivo* testing. To simulate the hold down pressure of tonometers, a frictionless plunger was employed in the test setup. By varying the weight atop the plunger, the effective "hold-down pressure" of the system was able to be adjusted. The displacement of the plunger was monitored for changing both the magnetic field applied as well as the weight atop the plunger head. The results show that the accuracy of measurements taken by a tonometer can be affected by both skin stiffness as well as hold-down pressure. The results of this study indicate that the hold-down pressure of the machine, as well as the stiffness of the patient's skin, can skew the results of a tonometer. The results further showed that as the stiffness of the MR fluid decreased, the difference in the magnitude of the first and second peaks in the pulse waveform increased. These results imply that, as age increased and stiffness of the skin decreased, the accuracy of the arterial tonometry measurements would be affected more heavily by the "hold-down pressure."

Beyond the arterial tonometry methods for blood pressure measurements, the study on the skin effect may have implications regarding Oriental Medicine (OM) or traditional Chinese Medicine. Pulse diagnosis in OM, which examines radial blood pulsations on the wrist using a "three finger" method, is used to predict internal problems in a patient and is thought to even be able to narrow down which organ is having an issue. This method is completely non-invasive and is believed by many to be very effective (Dharmananda, 2000). Arterial tonometry is very similar to the traditional Chinese "three finger" method in a sense that both methods use a small exterior pressure in order to measure and analyze the interior pressure of the artery. Consequently, the skin effect can play an important role in pulse diagnoses in OM as well.

AUTHOR CONTRIBUTIONS

All authors listed have made a substantial, direct and intellectual contribution to the work, and approved it for publication.

FUNDING

This work was supported by the Korea Institute of Oriental Medicine (grant no. K18022) funded by the Korean government. The financial support is greatly appreciated.

REFERENCES

Beevers, G., Lip, G., and O'Brien, E. (2001). Blood pressure measurement. *BMJ* 323, 981–985. doi: 10.1136/bmj.322.7292.981

Boyer, G., Laquièze, L., Le Bot, A., Laquièze, S., and Zahouani, H. (2009). Dynamic indentation on human skin *in vivo*: ageing effects. *Skin Res Technol.* 15, 55–67. doi: 10.1111/j.1600-0846.2008.00324.x

Chung, E., Chen, G., Alexander, B., and Cannesson, M. (2013). Non-invasive continuous blood pressure monitoring: a review of current applications. *Front. Med.* 7, 91–101. doi: 10.1007/s11684-013-0239-5

Dharmananda, S. (2000). *The Significance of Traditional Pulse Diagnosis in The Modern Practice of Chinese Medicine*. Portland, OR: Institute for Traditional Medicine. Available online at: http://www.itmonline.org/arts/pulse.htm

Digiglio, P., Li, R., Wang, W., and Pan, T. (2014). Microflotronic arterial tonometry for continuous wearble non-invasive hemodynamic monitoring. *Ann. Biomed. Eng.* 42, 2278–2288. doi: 10.1007/s10439-014-1037-1

Geerligs, M. (2006). A literature review of the mechanical behavior of the stratum corneum, living epidermis and the subcutaneous fat tissue. *Phillips Res.* Technical Note: PR-TN 2006/00450.

Kannel, W. B. (1996). Blood pressure as a cardiovascular risk factor prevention and treatment. *J. Am. Med. Assoc.* 275, 1571–1576.

Khatyr, F., Imberdis, C., Vescovo, P., Varchon, D., and Lagarde, J. M. (2004). Model of the viscoelastic behaviour of skin *in vivo* and study of anisotropy. *Skin Res. Technol.* 10, 96–103. doi: 10.1111/j.1600-0846.2004.00057.x

Langwieser, N., Prechtl, L., Meidert, A. S., Hapfelmeier, A., Bradaric, C., Ibrahim, T., et al. (2015). Radial artery applanation tonometry for continuous noninvasive arterial blood pressure monitoring in the cardiac intensive care unit. *Clin. Res. Cardiol.* 104, 518–524. doi: 10.1007/s00392-015-0816-5

Shioya, K., and Dohi, T. (2013). "Blood pressure measurement device based on the arterial tonometry method with micro triaxial force sensor," in *2389–92. United States: Transducers & Eurosensors XXVII* (Barcelona). doi: 10.1109/Transducers.2013.6627287

Singh, P., Choudhury, M. I., Roy, S., and Prasad, A. (2017). Computational study to investigate effect of tonometer geometry and patient-specific variability on radial artery tonometry. *J. Biomech.* 58, 105–112. doi: 10.1016/j.jbiomech.2017.04.023

Smulyan, H., Siddiqui, D. S., Carlson, R. J., London, G. M., and Safar, M. E. (2003). Clinical utility of aortic pulses and pressures calculated from applanated radial-artery pulses. *Hypertension* 42, 150–155 doi: 10.1161/01.HYP.0000084051.34269.A9

Tomiyama, H., Odaira, M., Kimura, K., Matsumoto, C., Shiina, K., Eguchi, K., et al. (2014). Differences in effects of age and blood pressure on augmentation index. *Am. J. Hypertens.* 27:12. doi: 10.1093/ajh/hpu082

Weiss, B. M., Spahn, D. R., Rahmig, H., Rohling, R., and Pasch, T. (1996). Radial artery tonometry: moderately accurate but unpredictable technique of continuous non-invasive arterial pressure measurement. *Br. J. Anaesth.* 76, 405–411.

Woo, S. H., Choi, Y. Y., Kim, D. J., Bien, F., and Kim, J. J. (2014). Tissue-informative mechanism for wearable non-invasive continuous blood pressure monitoring. *Sci. Rep.* 4:6618. doi: 10.1038/srep 06618

Yang, T. H., Jo, G., Koo, J. H., Woo, S. Y., Kim, J. U., and Kim, Y. M. (2019). A compact pulsatile simulator based on cam-follower mechanism for generating radial pulse waveforms. *Biomed. Eng. Online* 18:1. doi: 10.1186/s12938-018-0620-3

Zahouani, H., Pailler-Mattei, C., Sohm, B., Vargiolu, R., Cenizo, V., and Debret, R. (2009). Characterization of the mechanical properties of a dermal equivalent compared with human skin *in vivo* by indentation and static friction tests. *Skin Res. Technol.* 15, 68–76. doi: 10.1111/j.1600-0846.2008.00329.x

Conflict of Interest Statement: The authors declare that the research was conducted in the absence of any commercial or financial relationships that could be construed as a potential conflict of interest.

frontiers in Materials

ORIGINAL RESEARCH
published: 08 March 2019
doi: 10.3389/fmats.2019.00032

Tribological Behavior of Glycerol/Water-Based Magnetorheological Fluids in PMMA Point Contacts

*Wagner O. Rosa, Fernando Vereda and Juan de Vicente**

Biocolloid and Fluid Physics Group, Department of Applied Physics and Excellence Research Unit "Modeling Nature" (MNat), Faculty of Sciences, University of Granada, Granada, Spain

Comprehension of the tribological behavior of magnetorheological fluids is crucial for many applications, in particular for those related with high quality surface finishing. In this contribution, we describe a thorough experimental investigation on the tribological properties of magnetorheological (MR) fluids in poly(methyl methacrylate) (PMMA) point contacts. First, magnetic iron oxide particles with diameters of ∼0.4, 1,3, and 2.0 μm were prepared using wet chemistry procedures. Then, MR fluids were formulated by dispersion of the magnetic particles in glycerol/water mixtures. The tribological experiments were run in a PMMA ball-on-three plates tribometer and Stribeck regions were identified for a wide range of sliding speeds. The wear tracks were also visualized in a confocal microscope to correlate them with friction coefficient data. The results show the effect of both particle size and applied magnetic field in the friction coefficient and wear scar volume, suggesting a slight decrease on the wear process when the magnetic field is present.

Keywords: PMMA, boundary lubrication, particle size, abrasion, sliding friction

OPEN ACCESS

Edited by:
Seung-Bok Choi,
Inha University, South Korea

Reviewed by:
Wanli Song,
Northeastern University, China
Yu Tian,
Tsinghua University, China
Chul-Hee Lee,
Inha University, South Korea

****Correspondence:***
Juan de Vicente
jvicente@ugr.es

Specialty section:
This article was submitted to Smart Materials, a section of the journal Frontiers in Materials

Received: *03 December 2018*
Accepted: *14 February 2019*
Published: *08 March 2019*

Citation:
Rosa WO, Vereda F and de Vicente J (2019) Tribological Behavior of Glycerol/Water-Based Magnetorheological Fluids in PMMA Point Contacts. Front. Mater. 6:32. doi: 10.3389/fmats.2019.00032

INTRODUCTION

Magnetic suspensions and colloids are defined as dispersions of relatively small magnetic particles in non-magnetic liquid carriers. If we take into account the magnetic particles' dimensions, two main types can be distinguished: 1- ferrofluids (FF) and, 2- magnetorheological (MR) fluids. The former (FF) are, by definition, made of monodomain magnetic particles in the range of few nanometers (from 1 up to 20 nm diameter, approximately), whereas the later are prepared with multidomain magnetic particles (from 1 μm diameter and above). In this regard, magnetic particles with different sizes result in massive differences in the mechanical properties of the suspensions; while FF remain as a liquid when magnetic fields are applied (or absent), MR fluids show a clear "liquid-to-solid" transition when they are magnetized (Odenbach and Thurm, 2002; Park et al., 2010; de Vicente et al., 2011). Colloidal particles are very attractive since we have the possibility to create ordered and complex materials with technological applications (Kaewsaneha et al., 2013; Sahiner and Yasar, 2016). In that sense, magnetite particles represent an interesting material since they can be produced, with high reproducibility, in a wide range of sizes and shapes (Itoh and Sugimoto, 2003; Vereda et al., 2007; Lei et al., 2017). Controlled abrasion using magnetorheological fluids has been previously studied. Duradji et al. (2016) have shown, for instance, that magnetite particles dispersed

in oil (1–2 vol%) can be used as antiwear and antifriction catalysts due to their magnetic properties. Xiang et al. (2014) have also discussed the properties of magnetite nanoflakes as additives in #40 base oil (Sinopec Co., Ltd., China), showing that the friction coefficient decreased by 18% when the particles are dispersed at 1.5 wt%.

Polymers are taking the place of metals in many applications as a result of their very interesting properties, such as high specific strength and low specific density. Previous works have studied the low friction and wear resistance of polymers and polymeric composites in order to enhance their performance, particularly in the context of tribological applications such as gears, bearings, seals, and artificial joints (Nuño et al., 2002; Byun et al., 2017; Zhou and Wang, 2017; Gu et al., 2018). For this purpose, polymethyl methacrylate (PMMA) is a vastly used material because of its properties, which include transparency, low water absorption, and compliance with food regulations. Furthermore, it can be fabricated with a wide range of mechanical and optical properties Among the many applications, PMMA has been used in protective spectacle lenses, car headlights, ornaments, and even in medicine for strengthening of biocompatible bone cement (Thomson et al., 1992). PMMA is relatively hard, its Brinell hardness being 20.6 (Akkus and Gorgun, 2015).

In this study, we conducted tribological tests on PMMA-PMMA tribopairs at various sliding speeds for a fixed load with glycerol-based suspensions of magnetite particles, exploring the effect of the particle size across different lubrication regimes, both in the presence and in the absence of a magnetic field. It was found that due to the glycerol viscosity we had an effective elastohydrodynamic lubrication regime over a wide range of speeds. Afterwards, the lubricating film thickness at the contact interface was estimated, following the determination of the working lubrication regime for our specific conditions. Finally, we analyzed the resultant wear scars from PMMA plates, in order to analyze and quantify the amount of abrasion work done by the magnetite particles, and the effect of the applied magnetic field in such measurements as well.

EXPERIMENTAL METHODS

Synthesis and Characterization of Magnetite Particles

Magnetite particles were synthesized by means of the partial oxidation of ferrous hydroxide with nitrate. The particular procedure was based on that described by Sugimoto and Matijevic (1980), and particle size was controlled by adjusting the concentration of Fe^{2+} in the reactant mixture, as has been described by our group in detail in the past (Vereda et al., 2013). We fabricated particles in excess concentrations of Fe^{2+} ($[Fe^{2+}]_{Exc}$) that ranged from 0.004 to 0.010 M. The excess concentration of Fe^{2+} is calculated as $[Fe^{2+}]_{Exc} = [Fe^{2+}]_{Total} - [Fe(OH)_2]$, where $[Fe(OH)_2]$ was always 0.025 M.

All the reactants' concentrations, the particular excesses of Fe^{2+} and the resulting particle sizes are summarized in **Table 1**, in the Results section. After the synthesis the particles were stored in ethanol and dried at 40°C whenever a dry powder sample was needed.

Scanning electron microscopy (SEM) was the main tool used for determining particle size. To prepare the samples for microscopy analysis, the magnetic powders were redispersed in the ethanol in which they were stored, and a small aliquot was dried and then coated with a thin (ca. 10 nm) layer of carbon.

MR Fluid Preparation

The MR fluids were prepared by dispersing the proper amount of dry magnetite powder in a mixture of glycerol and water with a mass concentration of 88% glycerol. Glycerol was chosen as a liquid carrier due to its properties as polar, biocompatible, and highly viscous liquid, which readily dissolves in water. Regarding all these properties, our expectation was to achieve an extension of the hydrodynamic regime to lower sliding speeds, due to the high viscosity. Moreover, in a recent work by Shahrivar et al. (2017), it was demonstrated that the viscosity of the carrier fluid plays an important role when it comes to particle aggregation. Being the glycerol a high viscosity carrier, the magnetite particles should be better dispersed, minimizing particle aggregation during the experiments. The particle concentration for all the MR fluids was chosen properly and set to be 1 vol%. A density of 5.17 g cm^{-3} was assumed to calculate the mass of the solid phase. Dispersion of the particles was achieved by means of mechanical stirring followed by sonication.

Friction Measurement Method

To perform the friction measurements we used a contact geometry of non-conforming ball-on-three-plates, based on a modified form of the MCR302 rheometer (Anton Paar). In this particular experimental set-up, a PMMA ball of radius R (R = 0.25 inch = 6.35 mm) is mounted into a stem and then loaded at a determined normal force F_N against three plates, which are mounted over a special movable holder with their surfaces arranged in tetrahedral geometry relative to the ball's rotation axis, ensuring equal applied load distribution on the three frictional pairs. Afterwards, the ball starts to rotate at a given sliding speed V while the plates remain stationary, hence producing three stationary sliding point contacts. In this device (see **Figure 1**), the sliding speed V is related to the angular velocity (ω, rad/s) through $V = \frac{R\omega}{\sqrt{2}}$. The total normal load F_L applied acting on the plates, due to this configuration (plates at 45°), is related to the normal force F_N as follows (Shahrivar and de Vicente, 2014):

$$F_L = \sqrt{2}F_{\mathbf{N}} \tag{1}$$

In this study, the applied normal force F_N is equal to 0.5 N, in order to minimize the ball-plate contact as much as possible. Furthermore, the torque sensed by the ball, T, is related to the total frictional force, F_F, in this fashion:

$$F_F = \frac{\sqrt{2}T}{R} \tag{2}$$

TABLE 1 | Information regarding the synthesis process and the size of the magnetite particles of the three samples.

Sample	[KOH] (M)	[KNO_3] (M)	[$FeSO_4 \cdot 7H_2O$] (M)	[$Fe(OH)_2$] (M)	$[Fe^{2+}]_{Exc}$ (M)	Particle diameter (nm)	Standard deviation (nm)
M1	0.055	0.20	0.029	0.025	0.004	400	70
M2	0.055	0.20	0.030	0.025	0.005	1,300	220
M3	0.055	0.20	0.035	0.025	0.010	2,000	400

The concentrations in the table refer to the final reactant mixture, which always had a total volume of 200 mL. The solutions of $FeSO_4 \cdot 7H_2O$ were prepared in H_2SO_4 0.01 M (vol. = 50 mL). The concentration $Fe(OH)_2$ was always 0.025 M, and an small excess of KOH was introduced in the system to compensate for the presence of acid.

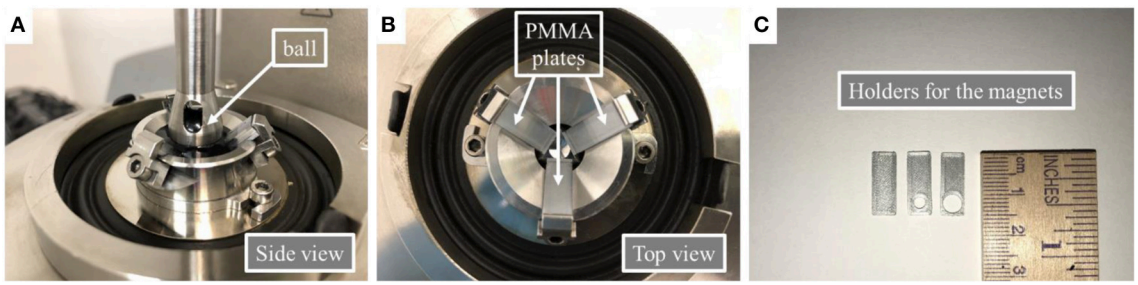

FIGURE 1 | Experimental set-up of the ball on-three-plates contact for tribology tests in the absence or the presence of magnetic fields: **(A,B)** Schematics of the ball-on-three-plates contacts without magnetic fields applied; **(C)** Detail of the 3D printed holder employed to superimpose non-homogeneous magnetic fields.

Eventually, the friction coefficient can be obtained from:

$$\mu = \frac{F_F}{F_L} = \frac{T}{F_N R} \tag{3}$$

where F_F is the frictional force and T is the torque sensed by the ball.

All the tests were carried out at a temperature of 25°C and at a constant slide-to-roll ratio of SRR = 2 (i.e., pure-sliding conditions). All PMMA plates used had a thickness of 2 mm and they were placed over 1 mm thick spacers. In order to apply magnetic fields, a special set of spacers with cylindrical holes has been fabricated, which were used to hold cylindrical neodymium–iron–boron (NdFeB) permanent magnets (one for each spacer) in contact with the polymer plates (PMMA) at the required position. Those cylindrical NdFeB magnets (with 1 mm height) have 3 and 5 mm diameters and they generate a maximum magnetic field on their surface of 250 and 170 mT, respectively. However, due to the thickness of the PMMA plates (2 mm), at the contact point the measured magnetic fields are reduced to 22 and 14 mT for the 3 and 5 mm magnets, respectively. The materials used in the experimental set-up were non-magnetic and therefore no conduction of the magnetic flux density is expected.

Confocal Microscopy

Topography measurements of the PMMA plates were performed using a confocal microscope Sensorfar PLμ 2300 Optical Imaging Profiler. This equipment enabled us to measure the 3D topography of all PMMA plates used in the tribology experiments. Therefore, we performed measurements of wear scar diameter, surface roughness, and mean wear volume using 10× magnification, which covers an area of $1.39 \times 1.02\ mm^2$.

RESULTS

Magnetite Particles

In order to obtain the size histogram of the magnetic particles, a set of samples were prepared to be analyzed using Scanning Electronic Microscopy (SEM). **Figure 2** shows representative SEM micrographs, obtained under the same magnification, of the three samples synthesized at different excess of Fe^{2+}, together with the size distribution of each sample.

Visual inspection of the micrographs suggests that, for each sample, the particle size is relatively uniform. The actual particle size distributions were calculated using ImageJ software (Rueden et al., 2017). The diameter of, at least, 225 particles was measured for each sample. The results of these measurements for the different $[Fe^{2+}]_{Exc}$ are summarized in **Table 1**.

As can be observed, the particle size varies in a range from 400 to 2,000 nm and the standard deviations are close to 18% of the average diameters, for samples M1 and M2, and goes up to 20% for sample M3. Moreover, for the larger particles, the kinetics of particle growth (Vereda et al., 2013) results in a rough surface morphology, as opposed to the smoother surfaces observed for the smaller particles.

We knew, from previous studies (Vereda et al., 2013), that all these particles exhibit very similar magnetic properties. Concretely, they have a saturation magnetization close to the bulk value frequently reported for magnetite (92 $A \cdot m^2 \cdot kg^{-1}$) at room temperature, and they exhibit soft hysteresis loops, with low values of both the remanence and the coercivity. The latter agrees with the fact that these particles are big enough

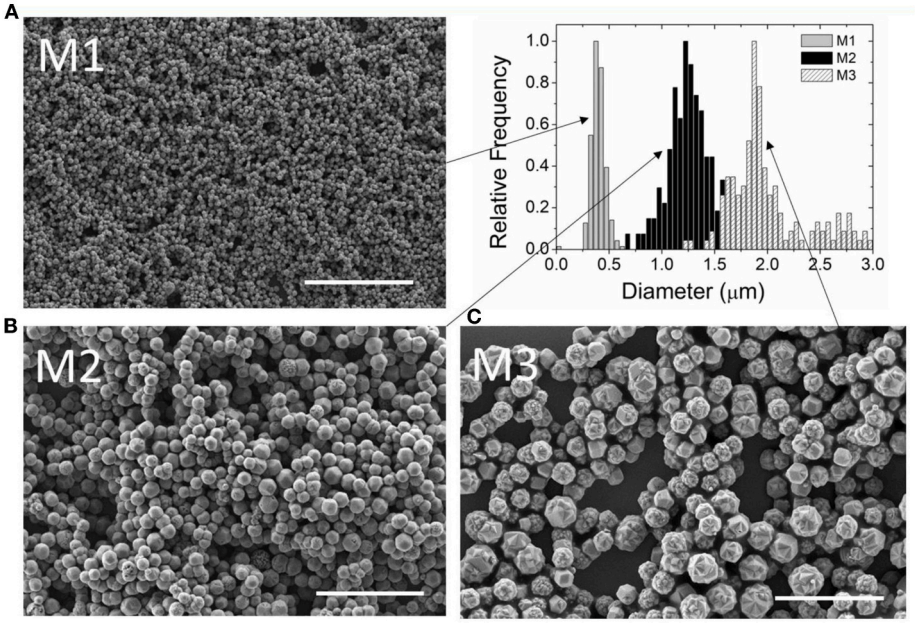

FIGURE 2 | SEM micrographs of magnetite particles obtained for different $[Fe^{2+}]_{Exc}$ concentrations: **(A)** M1; 0.004 M; **(B)** M2; 0.005 M; and **(C)** M3; 0.01 M. Scale bar is 10 μm.

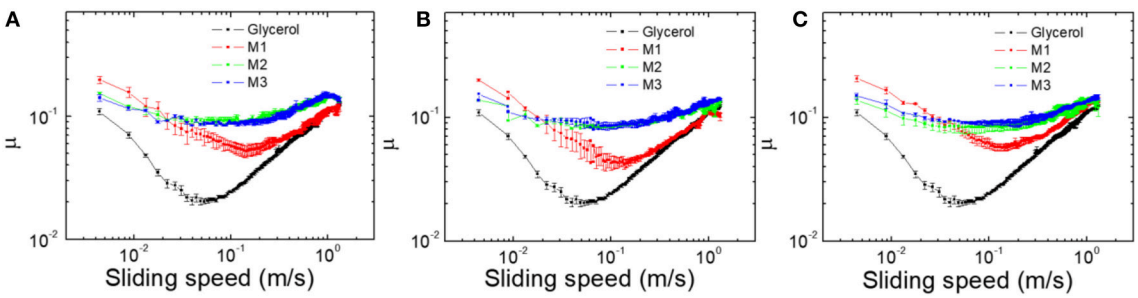

FIGURE 3 | Variation of the friction coefficient with the sliding speed for: **(A)** 0 mT, **(B)** 14 mT; and **(C)** 22 mT.

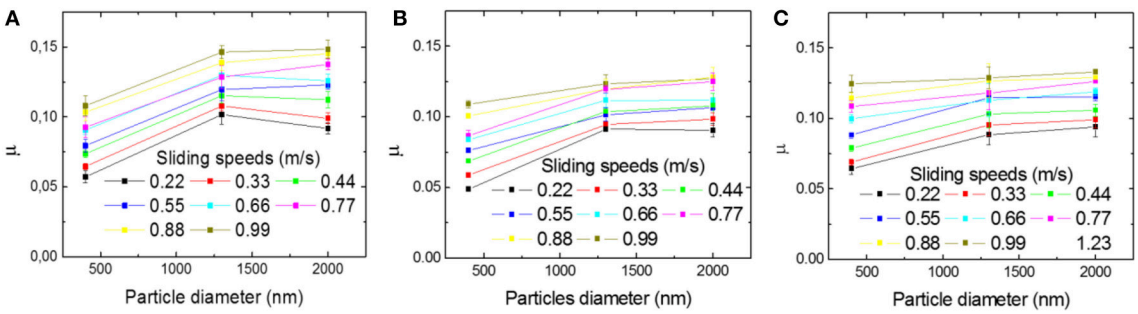

FIGURE 4 | Variation of friction coefficient as a function of particle diameter for: **(A)** 0 mT, **(B)** 14 mT; and **(C)** 22 mT.

to contain multiple magnetic domains, so that magnetization reversal occurs by motion of domain walls.

Friction Experiments and Stribeck Curve

The measured friction coefficients are displayed in **Figure 3**. The resultant plotted curves are composed from an average of three measurements using the same conditions (ramping down from 2,800 rpm to 0, or 1.3 m/s to 0). Firstly, we analyze the effect of the different particle addition to the glycerol/water mixture (88%). Comparing the friction coefficients for each of the suspensions, we can note that the friction coefficient changes drastically from pure glycerol/water mixture to MR fluids (see **Figure 3A**). The

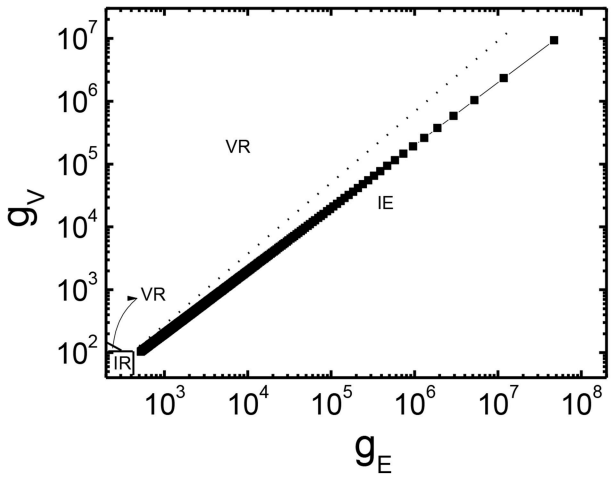

FIGURE 5 | Dimensionless viscosity as a function of the dimensionless elasticity.

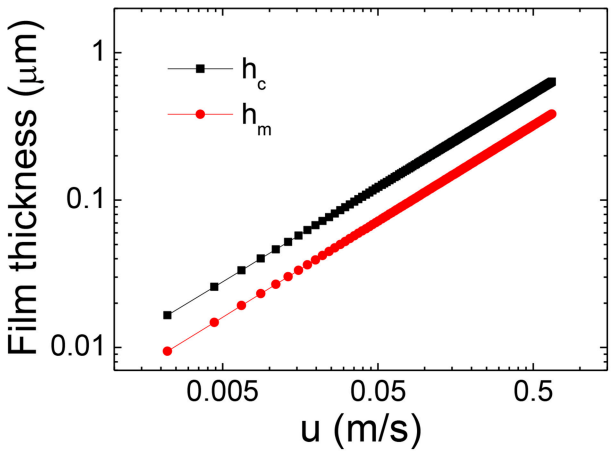

FIGURE 6 | Thin film thickness as a function of entrainment speed (u = V/2).

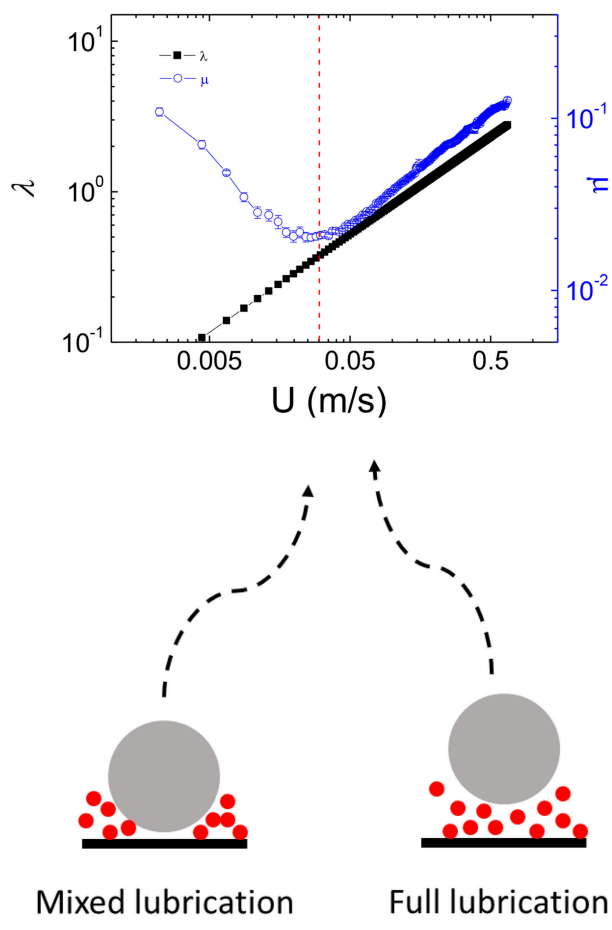

FIGURE 7 | Lambda ratio (λ–black symbols) and glycerol friction coefficient (μ–blue symbols) as a function of the entrainment speed. Dashed line indicates the transition from mixed state to full lubrication regime.

classical Stribeck curve is observed for the carrier (without particles); boundary regime at small speeds, mixed regime at intermediate speeds and full film isoviscous-elastohydrodynamic lubrication regime for large speeds (Stribeck, 1902; Bombard and de Vicente, 2012; Wäsche and Woydt, 2014). In MR fluids, particles with larger diameters (M2 and M3) present larger friction coefficients, although the particle concentration is kept constant through the experiments (1 vol%). Moreover, the friction coefficient is nearly constant through the whole sliding speed range for those MR fluids (M2 and M3).

The presence of a non-homogeneous magnetic field (see **Figures 3B,C**) produces a slight decrease on the friction coefficients, although the change is not dramatic. **Figure 4** displays the variation of the friction coefficient as a function of the particle size in a range of sliding speeds (from 0.22 to 0.99 m/s). The effect of the applied magnetic field is also plotted in this figure (see **Figures 4B,C**). As one can observe, the presence of the magnetic field tends to slightly reduce the friction coefficients. Compared to the values obtained without any magnetic field applied, the decreasing of the friction coefficient is around 11% for both 14 and 22 mT, corresponding to 5 and 3 mm magnets diameter, respectively. This reduction can be explained as the magnetite particles have the tendency to be concentrated around the area where the magnetic field is acting and, then, this leads to the formation a thin film of magnetic particles around the contact area, preventing the ball-plate contact as much as possible. Such a reduction in friction upon the application of a magnetic field was also observed by Shahrivar et al. for the lubrication with a comercial iron-based MR fluid (Sharivar et al., 2014).

Lubrication Regime and Film Thickness Calculations

In order to determine the lubrication regime for these MR fluids, we estimated the values for hard contacts in glycerol/water mixtures (88% glycerol). In addition to their inherently high viscosities at normal conditions of ambient pressure and temperature, the pressure-viscosity coefficients (α) of aqueous glycerol mixtures can be used also to improve the load-bearing capacity of hard contacts, therefore opening the

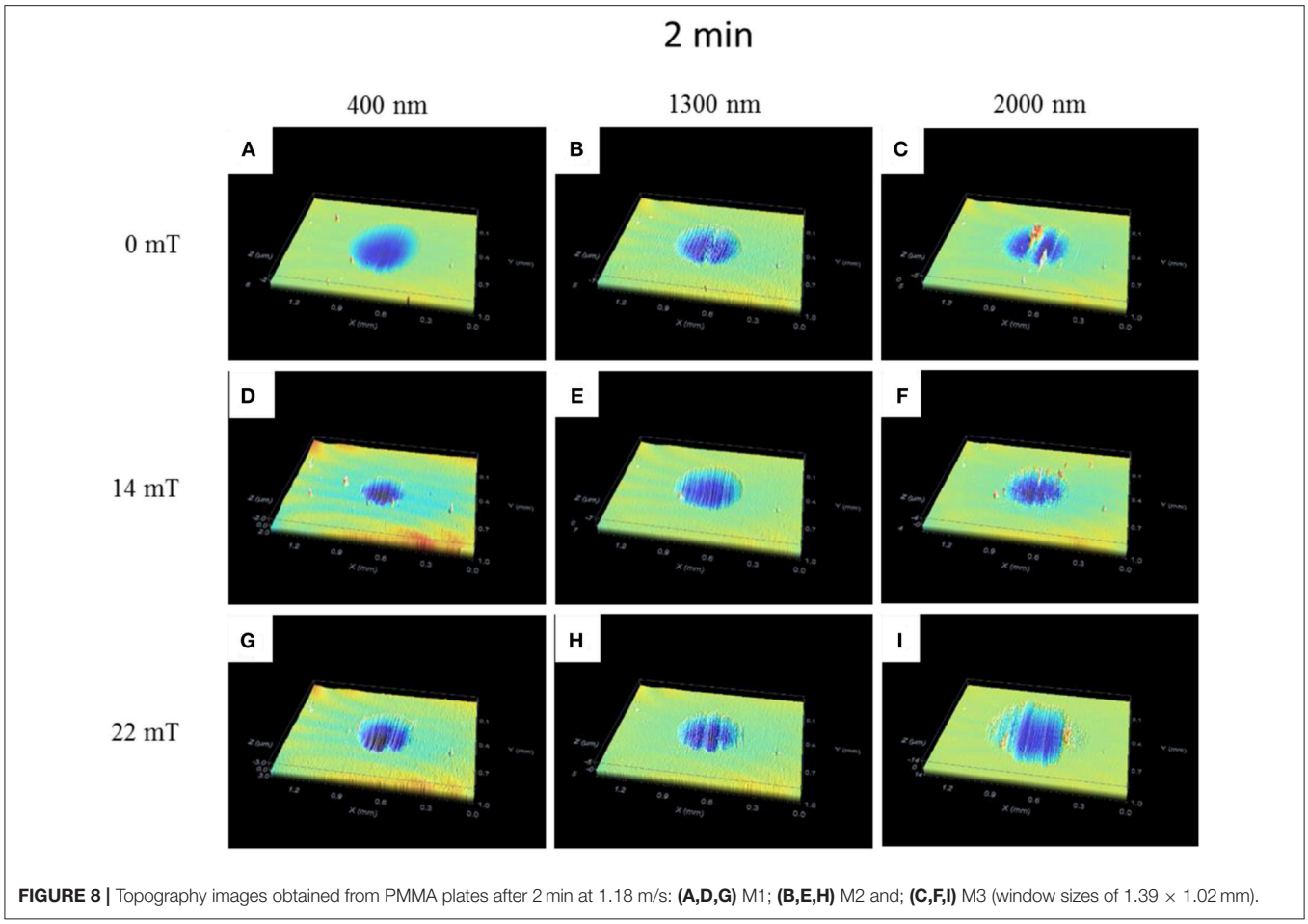

FIGURE 8 | Topography images obtained from PMMA plates after 2 min at 1.18 m/s: **(A,D,G)** M1; **(B,E,H)** M2 and; **(C,F,I)** M3 (window sizes of 1.39 × 1.02 mm).

possibility to manipulate, and modify the working lubrication regime. Former theoretical models have explicitly demonstrated that, basically, the two main parameters responsible for determining the nature of the fluid film formed between the contacting surfaces are both the elasticity of the contact material and the viscosity of the lubricant (Hamrock and Dowson, 1978). In that regard, the relative magnitudes of these quantities are key to determine in which type of fluid-film lubrication regime we are working. Mainly, we can divide these regimes into four specific types: iso-viscous rigid (IR), piezo-viscous rigid (VR), iso-viscous elastic (IE), and piezo-viscous elastic (VE). All the equations used in the calculation of the dimensionless viscosity and elasticity parameters, for the contacts, are given by Hamrock and Dowson (1978) and Esfahanian and Hamrock (1991).

$$\textit{Dimensionless viscosity parameter};\ g_V = \frac{GW^3}{U^2} \tag{4}$$

$$\textit{Dimensionless elasticity parameter};\ g_E = \frac{W^{\frac{8}{3}}}{U^2} \tag{5}$$

where G, W, and U are the dimensionless material parameter, dimensionless load parameter, and dimensionless speed parameter, respectively. These dimensionless parameters are normally used in elastohydrodynamical lubrication and are defined as follow:

$$\textit{Dimensionless material parameter};\ G = \alpha E' \tag{6}$$

$$\textit{Dimensionless load parameter};\ W = \frac{Q}{E' R_x^2} \tag{7}$$

$$\textit{Dimensionless speed parameter};\ U = \frac{\eta_0 u}{E' R_x} \tag{8}$$

where α is the pressure-viscosity coefficient of the lubricant, E' is the effective elastic modulus, Q is the applied load, η_0 is the viscosity of the lubricant in the contact, u is the entrainment speed of the contact, which in our case is the sliding speed divided by two, and R_x is the effective radius of the contact in the sliding direction. The pressure-viscosity coefficients for glycerol-water mixtures have been taken from the literature (Totten, 2000; Shahrivar et al., 2017) and the resulting value for the intermediate aqueous glycerol mixture used in this work was obtained by interpolation. For 88% glycerol-water, the dynamic shear viscosity is estimated to be $\eta = 0.0404$ Pa·s. In our experimental set-up, we can consider that the ellipticity parameter (k) is equal to one for the PMMA ball in contact with the PMMA plates, since the contact area is considered to be circular ($E' = 5$

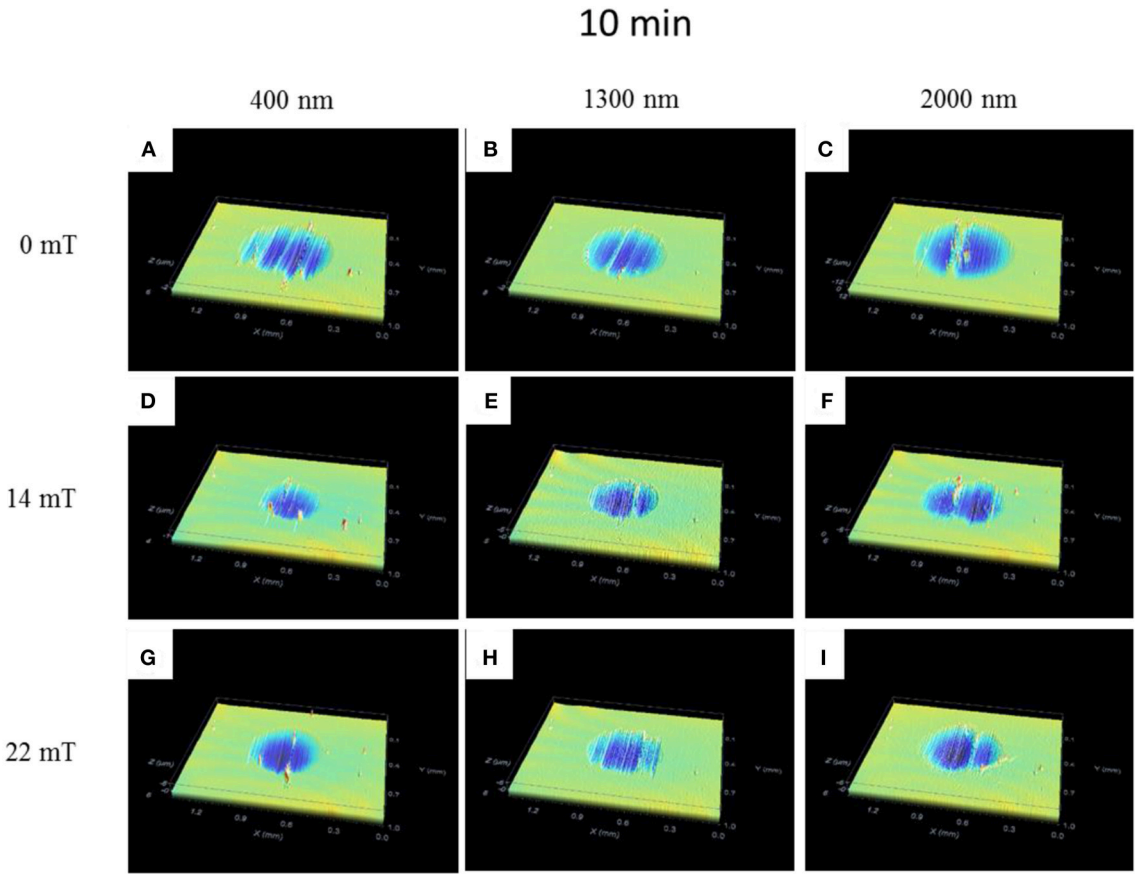

FIGURE 9 | Topography images obtained from PMMA plates after 10 min at 1.18 m/s: **(A,D,G)** M1; **(B,E,H)** M2 and; **(C,F,I)** M3 (window sizes of 1.39 × 1.02 mm).

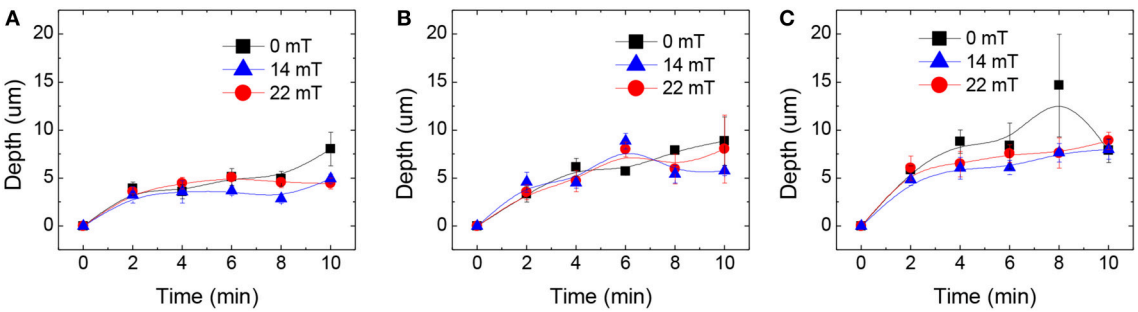

FIGURE 10 | Maximum removal depth as a function of time for **(A)** M1, **(B)** M2, and **(C)** M3 MR fluids. Lines are shown as a guide to the eye.

GPa, $R_x = 6.35\ 10^{-3}$ m). Operating conditions of the experiments are then used as input parameters to calculate the non-dimensional elastic (g_E) and viscosity (g_V) parameters according to Equations 4, 5. The calculated values are plotted in **Figure 5**. As observed, the contact operates in the isoviscous-elastic regime.

Therefore, the estimated lubrication film thickness is calculated from the dimensionless parameters which correspond to those of the isoviscous-elastic regime. For spheres onto flat plates, we can assume that the film thickness in the isoviscous-elastic regime is (de Vicente et al., 2005; Shahrivar and de Vicente, 2014):

$$h_c = 3.3 \cdot R_x \cdot U^{0.64} \cdot W^{-0.22} \quad (9)$$

$$h_m = 2.8 \cdot R_x \cdot U^{0.65} \cdot W^{-0.21} \quad (10)$$

where h_c is the central film thickness and h_m is the minimum film thickness. **Figure 6** exhibits the variation of the formed thin film

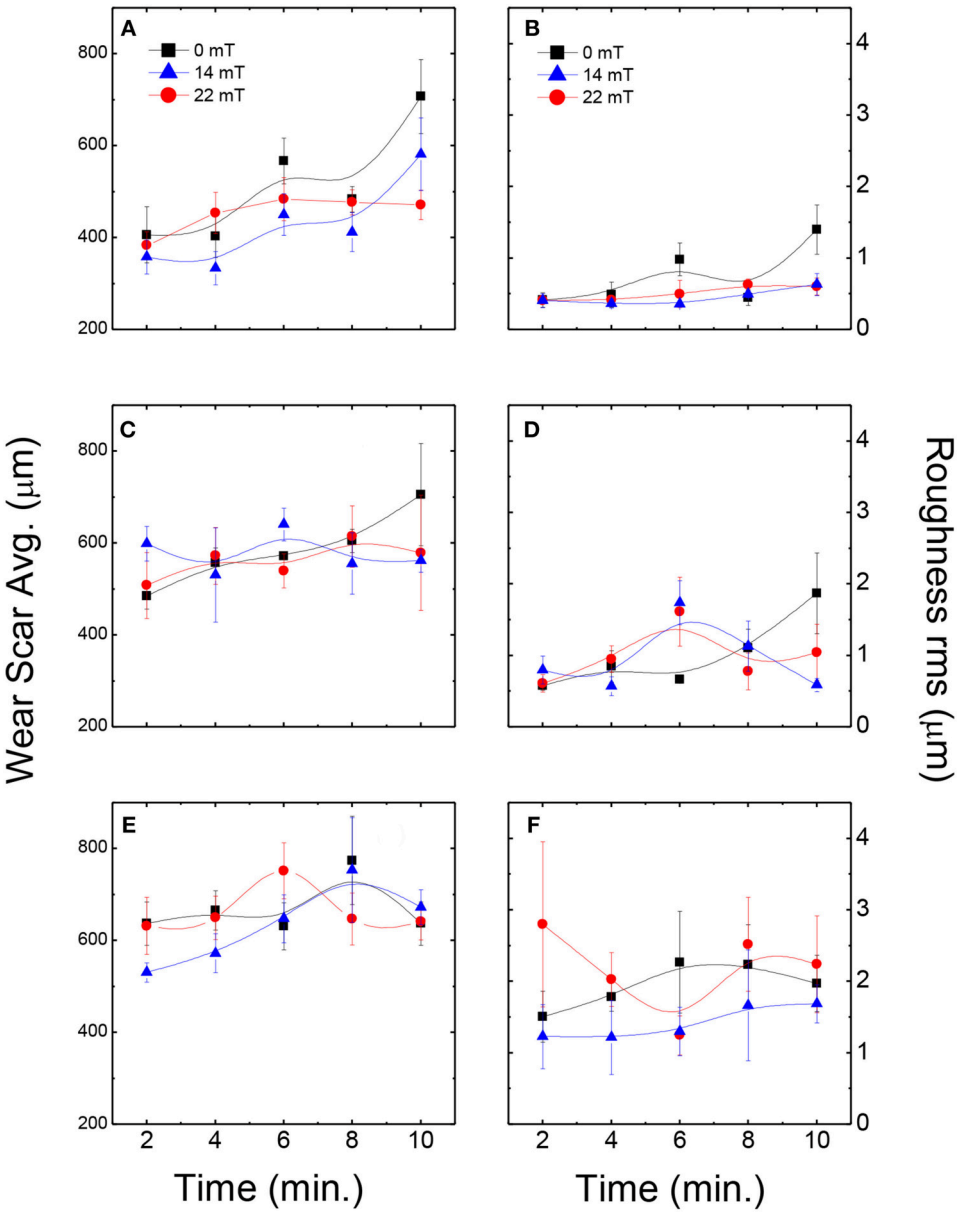

FIGURE 11 | Average wear scar diameter (**A** M1, **C** M2, **E** M3) and rms surface roughness (**B** M1, **D** M2, **F** M3) for different magnetite particles. Lines are shown as a guide to the eye.

thickness with the entrainment velocity. In our experiments, the maximum values estimated for such thin film thickness is $h_c = 0.636$ and $h_m = 0.383\,\mu$m for an entrainment speed of 0.66 m/s (2,800 rpm), which is the highest possible rotational speed in our measurement system. This means that only the smallest particles could be entrained in the contact during a test.

In physical tribological contacts, we have to take into account that the contact surfaces have a non-negligible roughness, which can lead to asperities and hard contact friction in comparison to the lubricating film thickness formed at the interface. The so-called λ ratio is a direct comparison between the estimated film thickness and the surface roughness. The λ ratio is given by the following expression (Stachowiak and Batchelor, 1993; Nalam et al., 2010).

$$\lambda = \frac{h_m}{\sqrt{\left(r_{ball}^2 + r_{plate}^2\right)}} \tag{11}$$

where r_{ball} is the rms surface roughness of the PMMA ball, r_{plate} is the rms surface roughness of the plate and h_m is the minimum film thickness. The λ ratio estimates the lubrication regime for rough surfaces; the λ values indicate a

high probability for asperity contact at low speeds ($\lambda < 1$) and lubrication regime for high speeds ($\lambda > 1$). In this work, the rms roughness values for PMMA ball and PMMA disk used are 126 and 34 nm, respectively (obtained from confocal microscopy images). In **Figure 7** we plot the λ values against the entrainment speed for all of the experiments. The curve shows that all the contacts during tribological measurements were in the boundary-lubrication regime. A good correspondence is observed with the minimum in the friction coefficient also shown in **Figure 7**. The transition from the mixed to the hydrodynamic regime occurs for value of λ in the vicinity of 0.4, which is much lower than the values reported by other authors (Hamrock and Dowson, 1978; de Vicente et al., 2005) maybe due to the different elastic modulus of the compliant surfaces.

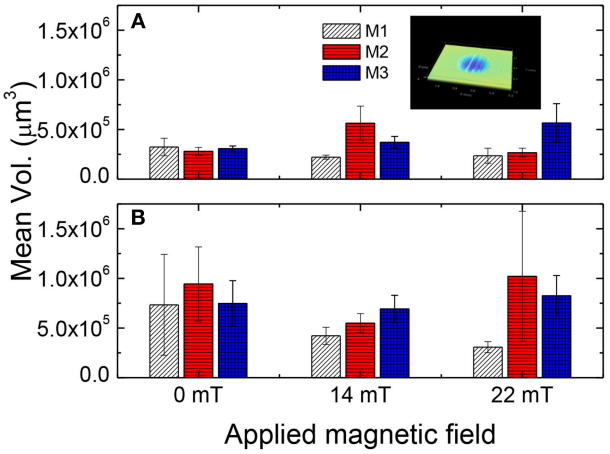

FIGURE 12 | Mean volume of the wear scars after **(A)** 2 min and **(B)** 10 min.

Wear Scar and Roughness Analysis: Fixed Sliding Speed

To investigate the role of the particle size, we performed a series of measurements fixing the normal force at $F_N = 0.5N$ and sliding speed at 2,500 rpm (1.18 m/s) to promote the formation of a thin film in the contact. Tests are then conducted for different time intervals from 2 up to 10 min. In particular, for that sliding speed, a thin film thickness around 0.5 microns is expected, following the assumptions and the data plotted in **Figure 6** (h_c thin film value). In **Figures 8**, **9**, we can observe the wear scars produced by the magnetite particles after acting by 2 and 10 min, respectively. From these topography images, we were able to determine and measure the maximum depth removal, volume eroded, and the rms surface roughness of the wear scars. The maximum material removal depth for the different samples can be visualized in **Figure 10**. The MR fluids prepared with particles of larger diameters (M3) display a higher abrasion, having a maximum removal depth of 14.7 microns. As seen on this figure, the action of the applied magnetic field is minimum in the field range investigated (14 or 22 mT). In conjunction of the maximum removal depth analysis, we have compared the evolution of the wear scar diameter and rms surface roughness after the abrasion performed by the magnetite particles. **Figure 11** shows a comparison between the measurements of average wear scar diameter and rms surface roughness with and without applied magnetic field. As we can appreciate, the effect of the applied magnetic field is more relevant for the smaller particles (M1), in which case the size of wear scar diameter and rms roughness is reduced when compared to the values of those without the magnetic field. The minimum rms roughness are achieved when the 14 mT magnetic field is applied (355 ± 18 nm). The 5 mm magnet, at the contact point, produces a more homogeneous magnetic field, in comparison to the 3 mm magnet, leading to a larger area of particle concentration. In that sense, we understand that the fact that triggers the decrease of the wear scar dimensions, in the case of MR fluid lubrication in the presence of magnetic fields, is the magnetic field gradient, which promotes particle agglomeration in a given region of the space around the magnets. This produces a confinement of the abrasion region to a small zone, which is in agreement with previous reports (Song et al., 2011; Hu et al., 2012).

Furthermore, the negligible magnetic field effect for the larger particles can be associated to the resultant film thickness formed for glycerol 88% that, in our predictions, is lower than those particle sizes.

Figure 12 summarizes the mean wear volume produced by the different magnetite particles over the PMMA plates. It is worth noting the effect of the applied magnetic field, which displays the tendency to increase the wear volume for short periods (up to 4 min) and, conversely, to decrease the wear volume after more than 8 min. At this stage, the non-homogeneous magnetic field generates a film of magnetite particles that prevent further abrasions at surface level. This protection against abrasion over time makes these MR fluids to act like antiwear and antifriction catalysts, which was previously described by Duradji et al. (2016).

CONCLUSIONS

We studied the effect of particle size on the tribological behavior of model MR fluids. Magnetite particles with a broad range of sizes (from 400 to 2,000 nm) were synthesized with high reproducibility by chemical methods. The tribological behavior of MR-fluid-lubricated PMMA–PMMA point contacts was compared in a custom-built experimental set-up, both in the absence and in presence of magnetic fields. Relevant differences between the MR fluids were observed after measuring their friction coefficients. In all cases, an elastohydrodynamic regime was achieved at relatively slow sliding speeds (from 0.1 m/s and beyond) and, therefore, a lubricating thin-film whose thickness we could estimate was formed. The effect of a magnetic field in the frictional properties of the lubricated contacts was more noticeable for the larger magnetite particles (M2 and M3). Those MR fluids experienced a decrease in the friction coefficient. From lamba ratio calculations we can

assure that, for entrainment speeds over 0.05 m/s, we had a full lubrication regime, with very low probability of asperity contact. The application of a magnetic field during the fixed sliding speed tests shows a slight friction reduction for the MR fluids, as a result of the concentration of the iron particles within a confined region, determined by the area of each magnet used and their generated magnetic field. With the increase of the sliding distance (i.e., time × sliding speed), the effect of magnetic field in the frictional properties is more noticeable. However, after a certain time/sliding distance, the maximum removal depth does not increase, with the MR fluids acting like a protective layer preventing further abrasions. The wear scars and rms surface roughness produced by the MR fluids abrasion, over time, shows that the smaller particles (M1) have the tendency to generate smoother wear scars than the other studied MR fluids.

AUTHOR CONTRIBUTIONS

WR performed the experiments and data analysis. FV synthetized the magnetite particles. JdV designed this research work. WR, FV, and JdV wrote the manuscript.

FUNDING

This work was supported by PCIN-2015-051 and MINECO MAT 2016-78778-R projects (Spain), and European Regional Development Fund (ERDF).

REFERENCES

Akkus, A., and Gorgun, E. (2015). The investigation of mechanical behaviors of poly methyl methacrylate (PMMA) with the addition of bone ash, hydroxyapatite and keratin. *Adv. Mater.* 4, 16–19. doi: 10.11648/j.am.20150401.14

Bombard, A. J. F., and de Vicente, J. (2012). Thin-film rheology and tribology of magnetorheological fluids in isoviscous-EHL contacts. *Tribol. Lett.* 47, 149–162. doi: 10.1007/s11249-012-9971-2

Byun, J. Y., Pratama, P., Kim, J. H., Park, I. S., Choi, S. M., Kwon, S. H., et al. (2017). The friction and wear characteristic comparison of PMMA and MC nylon as spreading device pad material in copper coil forming. *Key Eng. Mater.* 723, 220–223. doi: 10.4028/www.scientific.net/KEM.723.220

de Vicente, J., Klingenberg, D. J., and Hidalgo-Álvarez, R. (2011). Magnetorheological fluids: a review. *Soft Matter.* 7, 3701–3710. doi: 10.1039/c0sm01221a

de Vicente, J., Stokes, J. R., and Spikes, H. A. (2005). The frictional properties of Newtonian fluids in rolling–sliding soft-EHL contact. *Tribol. Lett.* 20, 273–286. doi: 10.1007/s11249-005-9067-3

Duradji, V. N., Kaputkina, D. E., and Duradji, A. (2016). Tribological studies of antiwear antifriction composition and its application. *Tribology in Industry* 38, 496–507.

Esfahanian, M., and Hamrock, B. J. (1991). Fluid-film lubrication regimes revisited. *Tribol. Trans.* 34, 628–632. doi: 10.1080/10402009108982081

Gu, D., Zhang, L., Chen, S., Song, K., and, Liu, S. (2018). Significant reduction of the friction and wear of PMMA based composite by filling with PTFE. *Polymers* 10:996. doi: 10.3390/polym10090966

Hamrock, B. J., and Dowson, D. (1978). "Minimum film thickness in elliptical contacts for different regimes of fluid-film lubrication," in *Proceedings-Society of Photo-Optical Instrumentation Engineers, NASA-TP-1342* (Cleveland, OH).

Hu, Z. D., Yan, H., Qiu, H. Z., Zhang, P., and Liu, Q. (2012). Friction and wear of magnetorheological fluid under magnetic field. *Wear* 278–279, 48–52. doi: 10.1016/j.wear.2012.01.006

Itoh, H., and Sugimoto, T. (2003). Systematic control of size, shape, structure, and magnetic properties of uniform magnetite and maghemite particles. *J. Coll. Int. Sci.* 265 283–295. doi: 10.1016/S0021-9797(03)00511-3

Kaewsaneha, C., Tangboriboonrat, P., Polpanich, D., Eissa, M., and Elaissari, A. (2013). Janus colloidal particles: preparation, properties, and biomedical applications. *ACS Appl. Mater. Interfaces* 5, 1857–1869. doi: 10.1021/am302528g

Lei, W., Liu, Y., Si, X., Xu, J., Du, W., Yang, J., et al. (2017). Synthesis and magnetic properties of octahedral Fe3O4 via a one-pot hydrothermal route. *Phys. Lett. A* 38, 314–318. doi: 10.1016/j.physleta.2016.09.018

Nalam, P. C., Clasohm, J. N., Mashaghi, A., and Spencer, N. D. (2010). Macrotribological studies of Poly(L-lysine)-graft-Poly(ethylene glycol) in aqueous glycerol mixtures. *Tribol. Lett.* 37, 541–552. doi: 10.1007/s11249-009-9549-9

Nuño, N., Amabili, M., Groppetti, R., and Rossi, A. (2002). Static coefficient of friction between Ti-6Al-4V and PMMA for cemented hip and knee implants. *J. Biomed. Mater. Res.* 59, 191–200. doi: 10.1002/jbm.1233

Odenbach, S., and Thurm, S. (2002). *Magnetoviscous Effects in Ferrofluids*. Berlin; Heidelberg: Springer-Verlag.

Park, B. J., Fang, F. F., and Choi, H. J. (2010). Magnetorheology: materials and application. *Soft Matter.* 6, 5246–5253. doi: 10.1039/c0sm00014k

Rueden, C. T., Schindelin, J., Hiner, M. C., De Zonia, B. E., Walter, A. E., Arena, E. T., et al. (2017). ImageJ2: ImageJ for the next generation of scientific image data. *BMC Bioinformatics* 18:529. doi: 10.1186/s12859-017-1934-z

Sahiner, N., and Yasar, A. O. (2016). A new application for colloidal silica particles: natural, environmentally friendly, low-cost, and reusable catalyst material for H_2 production from $NaBH_4$ methanolysis. *Ind. Eng. Chem. Res.* 55, 11245–11252. doi: 10.1021/acs.iecr.6b03089

Shahrivar, K., Carreón-González, E., and de Vicente, J. (2017). On the importance of carrier fluid viscosity and particle-wall interactions in magnetic guided assembly of quasi-2D systems. *Microfluid Nanofluid* 21:120. doi: 10.1007/s10404-017-1955-y

Shahrivar, K., and de Vicente, J. (2014). Ferrofluid lubrication of compliant polymeric contacts: effect of non-homogeneous magnetic fields. *Tribol. Lett.* 56, 281–292. doi: 10.1007/s11249-014-0408-y

Sharivar, K., Ortiz, A. L., and de Vicente, J. (2014). A comparative study of the tribological performance of ferrofluids and magnetorheological fluids within Steel-plate point contacts. *Tribol. Int.* 78, 125–133. doi: 10.1016/j.triboint.2014.05.008

Song, W.-L., Choi, S.-B., Choi, J.-Y., and Lee, C.-H. (2011). Wear and friction characteristics of magnetorheological fluid under magnetic field activation. *Tribol. Trans.* 54, 616–624. doi: 10.1080/10402004.2011.584365

Stachowiak, G. W., and Batchelor, A. W. (1993). *Engineering Tribology*. Amsterdam: Elsevier.

Stribeck, R. (1902). Die wesentlichen Eigenschaften der Gleit- und Rollenlager. *Zeitschrift des Vereins Deutscher Ingenieure* 36, 1463–1470.

Sugimoto, T., and Matijevic, E. (1980). Formation of uniform spherical magnetite particles by crystallization from ferrous hydroxide gels. *J. Coll. Int. Sci.* 74, 227–283. doi: 10.1016/0021-9797(80)90187-3

Thomson, L. A., Law, F. C., James, K. H., Matthew, C. A., and Rushton, N. (1992). Biocompatibility of particulate polymethylmethacrylate bone cements: a comparative study *in vitro* and *in vivo*. *Biomaterials* 13, 811–818. doi: 10.1016/0142-9612(92)90173-L

Totten, G. E. (2000). *Handbook of Hydraulic Fluid Technology*. New York, NY: Marcel Dekker, Inc.

Vereda, F., de Vicente, J., and Hidalgo-Álvarez, R. (2007). Influence of a magnetic field on the formation of magnetite particles via two precipitation methods. *Langmuir* 23, 3581–3589. doi: 10.1021/la0633583

Vereda, F., Morales, M. P., Rodríguez-González, B., de Vicente, J., and Hidalgo, R. (2013). Control of surface morphology and internal structure in magnetite microparticles: from smooth single crystals to rough polycrystals. *Cryst. Eng. Commun*. 15, 5236–5244. doi: 10.1039/c3ce40424b

Wäsche, R., and Woydt, M. (2014). "Stribeck curve," in *Encyclopedia of Lubricants and Lubrication*, eds T. Mang (Berlin; Heidelberg: Springer), 1998–2005 doi: 10.1007/978-3-642-22647-2_274

Xiang, L., Gao, C., Wang, Y., Pan, Z., and Hu, D. (2014). Tribological and tribochemical properties of magnetite nanoflakes as additives in oil lubricants. *Particuology* 17, 136–144. doi: 10.1016/j.partic.2013.09.004

Zhou, Y.-J., Wang, D.-G, and Guo, Y. (2017). The reduction of static friction of rubber contact under sea water droplet lubrication. *Lubricants* 5:12. doi: 10.3390/lubricants5020012

Conflict of Interest Statement: The authors declare that the research was conducted in the absence of any commercial or financial relationships that could be construed as a potential conflict of interest.

frontiers in Materials

ORIGINAL RESEARCH
published: 05 March 2019
doi: 10.3389/fmats.2019.00028

Design and Modeling for 2D Plate Type MR Damper

Bingsan Chen[1,2]*, *Dicheng Huang*[1], *Chunyu Li*[1,3] *and Changrong Chen*[1]

[1] Department of Mechanical and Automotive Engineering, Fujian University of Technology, Fuzhou, China, [2] Fujian Province Machine Tool Industry Technology Innovation Public Service Platform, Fuzhou, China, [3] Digital Fujian Industrial Manufacturing IoT Lab, Fuzhou, China

A two-dimensional magnetorheological damper is developed for the engineering two-dimensional damping need. The velocity and pressure distribution model of the two-dimensional plate-type damper, and the damping force calculation model are established based on the Navier-Stokes equation. Several structural and physical parameters, including the working gap δ, the length *a,* and the width *a* of the middle slide plate, are analyzed theoretically. The damping performance of the two-dimensional plate-type magnetorheological damper was evaluated using a two-dimensional vibration test-bed, with the effect of the excitation current analyzed. The experimental results suggest a significant influence of Coulomb damping force on the damping force of magnetorheological damper when using appropriate magnetorheological fluid. As the excitation current increases, the damping force of magnetorheological damper becomes larger while the system amplitude decreases gradually in both directions, a maximum reduction of 2.5956 times. It's confirmed that the design of the two-dimensional plate-type magnetorheological damper is reasonable.

Keywords: magnetorheological fluids, two-dimensional plate-type magnetorheological damper, mechanical modeling, damping experiments, plate-type

OPEN ACCESS

Edited by:
Seung-Bok Choi,
Inha University, South Korea

Reviewed by:
Taihong Cheng,
Wenzhou University, China
Jung Woo Sohn,
Kumoh National Institute of Technology, South Korea

***Correspondence:**
Bingsan Chen
bschen126@163.com

Specialty section:
This article was submitted to Smart Materials, a section of the journal Frontiers in Materials

Received: *03 December 2018*
Accepted: *11 February 2019*
Published: *05 March 2019*

Citation:
Chen B, Huang D, Li C and Chen C (2019) Design and Modeling for 2D Plate Type MR Damper. Front. Mater. 6:28. doi: 10.3389/fmats.2019.00028

INTRODUCTION

Magneterorheological Fluids (MRFs) are one kind of smart materials, which have good rheological property, and unique rheological effects. When the MRFs are placed under a magnetic field, the apparent viscosity of the MRFs can be adjusted by changing the magnetic field intensity, even to the solid state. When the magnetic field is absent, MRFs will return from the solid state to their original liquid state, i.e., non-Newtonian fluid. This "liquid-solid" conversion is continuously and reversibly controllable. It is also safe and reliable with low energy consumption and stable temperature (Liao et al., 2002). The unique rheological properties of MRF have attracted wide research interests in various applications, such as in the automotive industry (Edward et al., 2008; Shiao and Nguyen, 2014; Hema et al., 2017), precision polishing (Jang et al., 2010; Anwesa and Manas, 2018; Luo et al., 2018) and buildings (Luu et al., 2014; Ha et al., 2018; Christie et al., 2019). One of the most popular applications is the MR damper which replaced the hydraulic oil with the MRFs in the cylinder of the conventional damper. Compared to conventional hydraulic damper, the damping stiffness of MR damper can be changed using an embedded control system, which can produce a controllable magnetic field intensity by the coil placed on the piston. The MR damper was widely used in many fields, such as vehicle suspension systems (Nguyen et al., 2014; Yu et al., 2017; Anwesa and Manas, 2018), clutches (Hema et al., 2017; Topcu et al., 2018), bridges and buildings (Mohammad and Amir, 2018) and the control systems for MR damper have been researched (Kang et al., 2018; Pang et al., 2018), by using control system, the damper can be easily controlled.

Many scholars are devoted to the structural development and mechanical modeling of dampers. Shaju designed a MR damper with a two-cylinder structure, conducted experiments, and test analysis (Shaju et al., 2008); Yang et al. proposed a large-scale MR damper with 200 KN damping force for vibration mitigation and seismic protection of the buildings, and established the phenomenological mechanical model on the symmetrical structure. Simultaneously, some academia used genetic algorithm to find the optimal placement positions and the control effect for MR dampers in the 9-story seismic frame structure (Yang et al., 2002; Cha et al., 2014). David designed a small-scale MR damper for a tremor attenuation orthosis, and applied a finite-element approach to resolve the inherent static and dynamic modeling problems (David et al., 2014). Wang et al. developed a blade type and slit-opened type MR damper, established the damping torque calculation model and analyzed the influencing factors of the adjustable coefficients, with experimental verification (Wang, 2010; Zhang et al., 2013). Zheng presented a double-loop structure MR damper applied to the traction of the elevator, to overcome the shortcomings of mechanical brakes with large impact and large noise (Zheng et al., 2016). Chen et al designed a MR rubber-coupled damper, and analyzed the non-linearity of the damping system using fractional order theory and damping characteristics Chen and Huang, 2009).

Based on the rheological effect of MRFs, this paper attempts to develop a planar plate type of MR damper with two controllable magnetic fields to realize two-dimensional (2D) vibration reduction in engineering. For example, a vibratory roller needs to use vibration energy to compact the road surface while it is working, and at the same time, it is necessary to suppress the impact of the vibration rebound on the frame. And the dampers used on the vibratory roller need to reduce vibration in two dimensions.

DESIGN FOR 2D PLATE TYPE MR DAMPER

Structural Design for 2D Plate Type MR Damper

The three-dimensional model of planar MR damper with bipolar coil is shown in **Figure 1** and the main sizes of the MR damper are listed in **Table 1**. The damper is comprised of two parts: inner frame and outer frame. The outer frame can move in any direction relative to the inner frame in the plane. The inner frame and the outer frame are dynamically connected through eight guide pillars. The MRFs and the slide plate are placed in a

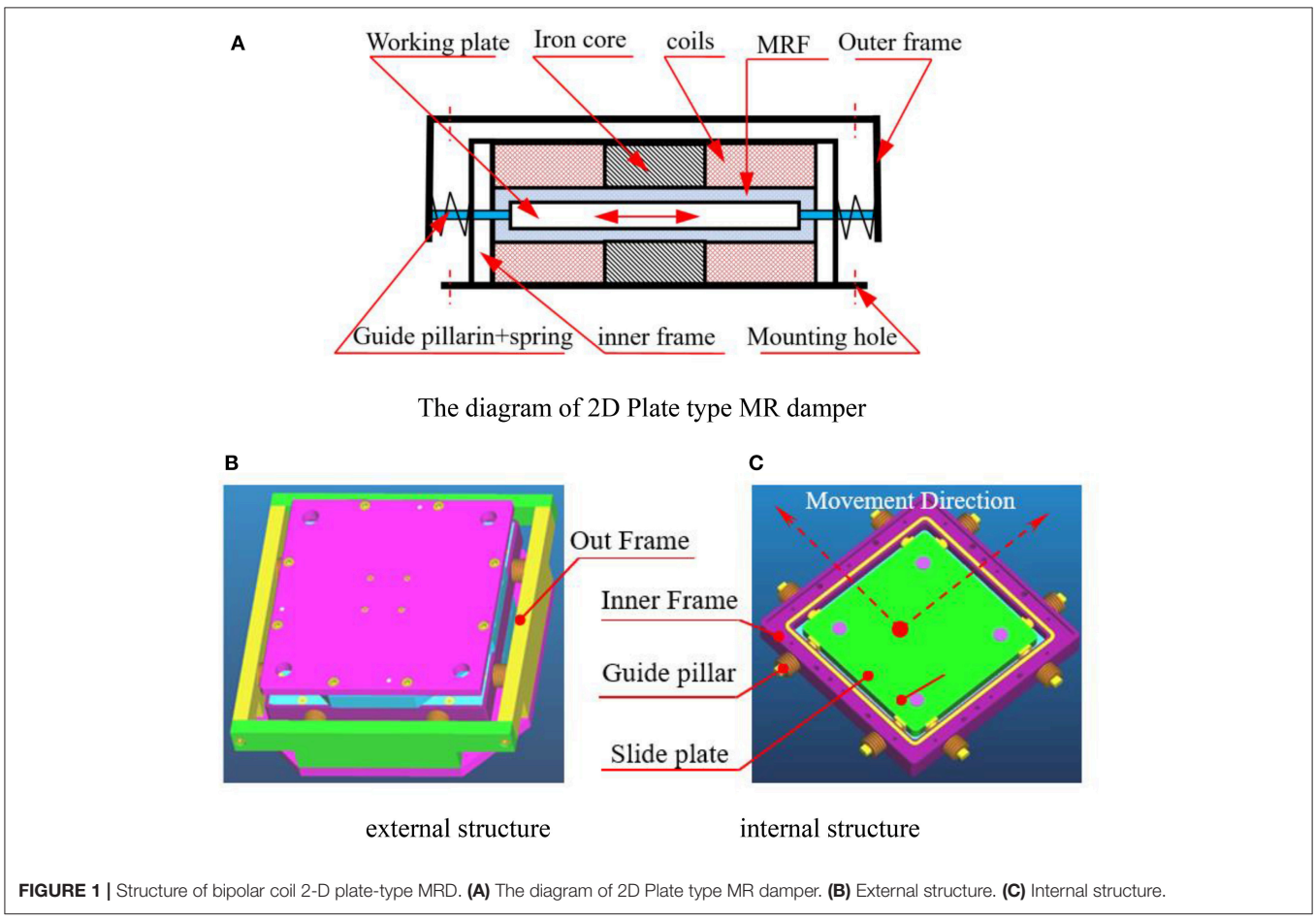

FIGURE 1 | Structure of bipolar coil 2-D plate-type MRD. **(A)** The diagram of 2D Plate type MR damper. **(B)** External structure. **(C)** Internal structure.

TABLE 1 | The main size of the damper.

Name	Size
The length, width and height of the MR damper/mm	230 × 230 × 76 mm
The length and width of the slide plate ($a \times a$)/mm	130 × 130 mm
Thickness of the slide plate/mm	12 mm
Inner frame	150 × 150 mm
Working gap	1 mm
Number of coils	300 × 2

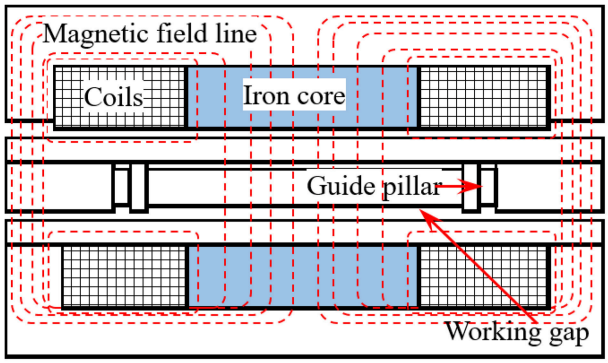

FIGURE 2 | Diagram of bipolar magnetic circuit structure.

cavity of the inner frame. The slide plate can move relatively to the inner frame because of the gap and return back by the disc type spring set up outside the guide pillars. The guide pillars are located in two directions, longitudinal, and horizontal. The force and displacement due to relative motion between outer and inner frame can be decomposed into two components and realized by the two subgroups of guide pillars. The slide plate drives the MRFs to shear movement and pressure-gradient flow. The force of MRFs act on the slide plate is the controllable damping force of the MR damper.

The relative motion among the components of the 2D plate type MR damper is complicated. When the outer frame drives the guide pillars, the outer frame slides perpendicular to the axis, relatively to pillars at the same time. In the same way, the pillars drive the slider to move, and the slider slides relatively to the pillars. The wide of interval between the slider and the surface of the cavity depends on the height of the copper pillar embedded in the slider.

Structural Design for Magnetic Circuit

The structure of the magnetic circuit of the 2D plate MR damper is shown in **Figure 2**. The magnetic circuit is composed of two coils with iron cores in the center. By means of controlling the winding direction of the coil, the superimposed magnetic field can be obtained at the working gap of the damper. The dash line in the picture is the magnetic field lines produced by the magnetic flux pass through the iron core.

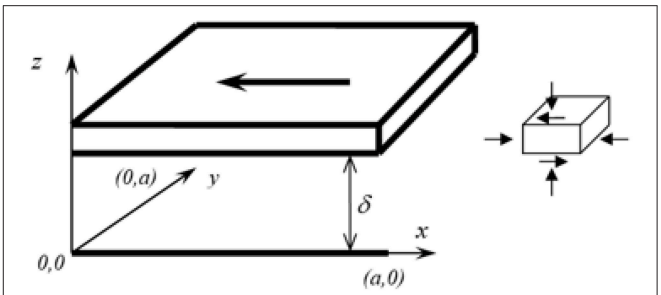

FIGURE 3 | Coordinate model of the flowing MRF between a gap.

MODELING FOR MR DAMPER

Equation of Motion

The MR effect of MRFs is a typical characteristic for the MR damper and it appears when the MRFs are exposed to an external magnetic field. Since the carbonyl iron particles inside the MRFs form chains and clusters along the direction of the external magnetic field, the relative direction of the flow and the external magnetic field would affect the MR effect largely (Gong et al., 2014). Therefore, the rheological characteristics of the MRFs depended on the direction of the flow relative to the external magnetic field. The behavior of the MRFs can be divided into three categories according to the relative direction of the flow and the external magnetic field: flow mode, shear mode, extrusion mode (Liao et al., 2002), and any combination of these three basic modes. Based on the structural characteristics of the damper in this paper, the work mode of the MRFs is the composite mode of flow and shear mode. The flow model coordinates are established as shown in **Figure 3**. The MRFs are regarded as generalized Newtonian fluids. The symbol u is the motion velocity of slide plate, the symbol δ is the working unilateral clearance of the plate, and η_α is the apparent viscosity of MRF. According to the Navier-Stokes equation, the equation of motion of MRF can be obtained, i.e.,

$$\rho \vec{f} - \nabla p + \eta_a \nabla^2 \vec{u} = \frac{d\vec{u}}{dt} \tag{1}$$

In Equation (1), ρ, $\vec{f}$, p and $\vec{u}$ mean density, mass force, pressure, and velocity of MR fluids, respectively, and then $\vec{\mathbf{u}}(x,y,z) = u_x \vec{i} + u_y \vec{j} + u_z \vec{k}$.

The following assumptions are made: The flow of MR fluids is laminar and non-slip between plates, that is, the velocity of the fluid is the same as that on the plate. Mass forces, such as gravity, are negligible and MRFs are incompressible. That is: ρ = const. The pressure is constant along the z direction, namely, $\frac{\partial p}{\partial z}=0$.

The motion is stable, namely, $\frac{\partial u_x}{\partial t}=\frac{\partial u_y}{\partial t}=\frac{\partial u_z}{\partial t}=0$.

According to the rheological effect of MRFs, the relationship between shear stress τ and shear rate $\dot{\gamma}$ is a power law, and the apparent viscosity η_α ($m^2 s^{-1}$) is only related to the magnetic field strength H and $\dot{\gamma}$ (Wang et al., 2016), i.e., $\tau = k\dot{\gamma}^n = \eta_a \dot{\gamma}$ and $\eta_a = \eta_a(H, \dot{\gamma})$.

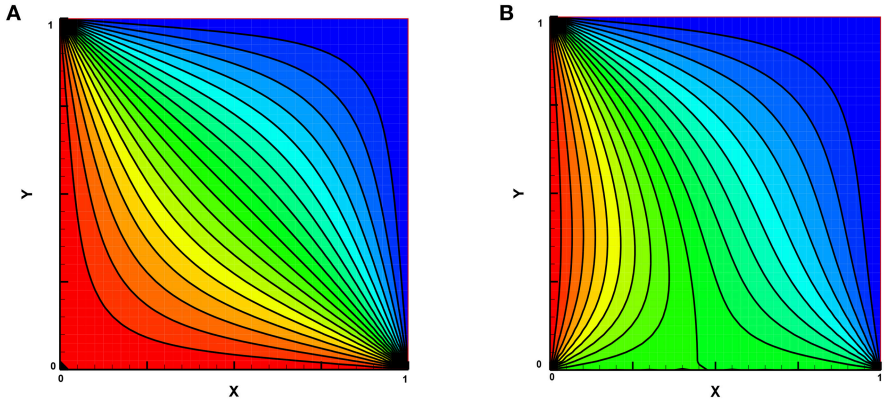

FIGURE 4 | MRF pressure distribution in two directions. **(A)** Pressure distribution line($k_p = 1$). **(B)** Pressure distribution line ($k_p = 0.5$).

Based on the structure of 2D MR plate type damper, the thickness value of slide plate (z direction) is much smaller than that of slide length (x direction) and width (y direction), so u_z can be neglected, and then:

$$\frac{\partial u_x}{\partial x} = \frac{\partial u_x}{\partial y} = \frac{\partial u_y}{\partial x} = \frac{\partial u_y}{\partial y} = 0$$

The movement of intermediate slide plate is active, according to the knowledge of fluid mechanics, and the boundary conditions of MRFs can be established for two-dimensional motion.

$$\begin{aligned} u_x(x, y, 0) &= 0, \quad u_x(x, y, \delta) = u_{x0} \\ u_y(x, y, 0) &= 0, \quad u_y(x, y, \delta) = u_{y0} \end{aligned} \tag{2}$$

where u_{x0} and u_{y0} are the initial velocities in x and y directions. The two-dimensional components of velocity can then be obtained.

$$\begin{aligned} u_x &= \frac{z}{\delta} u_{x0} - \frac{\delta^2}{2\eta_a} \frac{\partial p}{\partial x} \frac{z}{\delta} \left(1 - \frac{z}{\delta}\right) \\ u_y &= \frac{z}{\delta} u_{y0} - \frac{\delta^2}{2\eta_a} \frac{\partial p}{\partial y} \frac{z}{\delta} \left(1 - \frac{z}{\delta}\right) \end{aligned} \tag{3}$$

Pressure Components Under Two-Dimensional Vibration

Because the motion equation is linear, the pressure $p(x, y)$ can be regarded as a linear combination in two directions:

$$p(x, y) = p^1(x, y) + p^2(x, y) \tag{4}$$

When vibration is produced in the x and y directions, the following boundary conditions are discussed:

$$\begin{aligned} p(0, y) &= p, \quad p(a, y) = 0 \\ p(x, 0) &= k_p p, \quad p(x, a) = 0 \end{aligned} \tag{5}$$

In Equation (5), the dimensionless quantity k_p represents the upstream pressure ratio of y direction and x direction. Boundary conditions for two components of pressure can be written as follows:

$$\begin{aligned} &p^1(0, y) = p,\ p^1(a, y) = 0,\ p^1(x, 0) = 0,\ p^1(x, a) = 0 \\ &p^2(0, y) = 0,\ p^2(a, y) = 0,\ p^2(x, 0) = k_p p,\ p^2(x, a) = 0 \end{aligned} \tag{6}$$

where $\boldsymbol{a}$ is the length of the intermediate slide plate. Combining the method of separation of variables and the fluid continuity equation, the two-component equation of pressure can be obtained as follows:

$$\begin{aligned} p^1(x, y) = \sum_{n=1}^{\infty} [&\frac{2p}{n\pi} \frac{(1 - cosn\pi)}{e^{n\pi} - e^{-n\pi}} (e^{n\pi(1-\frac{x}{a})} \\ &- e^{-n\pi(1-\frac{x}{a})}) \sin(\frac{n\pi}{a} y)] \end{aligned} \tag{7}$$

$$\begin{aligned} p^2(x, y) = \sum_{n=1}^{\infty} [&\frac{2p}{n\pi} \frac{(1 - cosn\pi)}{e^{n\pi} - e^{-n\pi}} (e^{n\pi(1-\frac{y}{a})} \\ &- e^{-n\pi(1-\frac{y}{a})}) \sin(\frac{n\pi}{a} x)] \end{aligned} \tag{8}$$

Therefore, the pressure distribution model under two-dimensional vibration can be expressed as:

$$\begin{aligned} p(x, y) &= p^1(x, y) + p^2(x, y) \\ &= \sum_{n=1}^{\infty} \frac{2p}{n\pi} \frac{(1 - cosn\pi)}{e^{n\pi} - e^{-n\pi}} \left[\left(e^{n\pi(1-\frac{x}{a})} - e^{-n\pi(1-\frac{x}{a})}\right) \sin\left(\frac{n\pi}{a} y\right) \right. \\ &\quad \left. + k_p (e^{n\pi(1-\frac{x}{a})} - e^{-n\pi(1-\frac{x}{a})}) \sin(\frac{n\pi}{a} x) \right] \end{aligned} \tag{9}$$

The MRF pressure distribution of the vibration in two directions is simulated and shown in **Figure 4**. It can be found that when $k_p = 1$, the value of $p(x, y)$ is coordinate symmetric, and obtains the largest at the initial position, while the distribution of $p(x, y)$ shows inhomogeneity when $k_p = 0.5$.

Velocity and Flow Distribution

Combined with the structural characteristics of the damper, the two-dimensional velocity component Equation (3), and the

damper pressure distribution Equation (9), we can establish the velocity distribution model of the absorber in the x, y directions:

$$\begin{aligned} u_x &= \frac{z}{\delta}u_{x0} + \frac{\delta^2 p}{a\eta_a}\sum_{n=1}^{\infty}\frac{(1-cosn\pi)}{e^{n\pi}-e^{-n\pi}}\Big[e^{n\pi(1-\frac{x}{a})} \\ &\quad -e^{-n\pi(1-\frac{x}{a})})\sin\left(\frac{n\pi}{a}y\right) - k_p(e^{n\pi(1-\frac{y}{a})} \\ &\quad -e^{-n\pi(1-\frac{y}{a})})\cos(\frac{n\pi}{a}x)\Big]\frac{z}{\delta}(1-\frac{z}{\delta}) \\ u_y &= \frac{z}{\delta}u_{y0} + \frac{\delta^2 p}{a\eta_a}\sum_{n=1}^{\infty}\frac{(1-cosn\pi)}{e^{n\pi}-e^{-n\pi}} \\ &\quad \times\Big[e^{n\pi(1-\frac{x}{a})} - e^{-n\pi(1-\frac{x}{a})})\cos\left(\frac{n\pi}{a}y\right) \\ &\quad -k_p(e^{n\pi(1-\frac{y}{a})} - e^{-n\pi(1-\frac{y}{a})})\sin\left(\frac{n\pi}{a}x\right)\Big]\frac{z}{\delta}\left(1-\frac{z}{\delta}\right) \end{aligned} \tag{10}$$

Due to the symmetry of the working clearance of the MR fluids of 2D plate type damper, only one side flow calculation model is established to calculate the flow rate. Under two dimensional vibrations, the flow rate can be expressed as the flow rate Q_{s1_x} and Q_{s2_y} at one side clearance at x_0 and y_0. The fluid motion equation can be obtained as follows:

$$\begin{aligned} Q_{s1\_x} &= \frac{\delta a}{2}u_{x0} + \frac{\delta^3 p}{6\pi\eta_a}\sum_{n=1}^{\infty}\frac{1}{n}\frac{1-\cos n\pi}{e^{n\pi}-e^{-n\pi}} \\ &\quad \times\left[\left(e^{n\pi}+e^{-n\pi}\right)(1-\cos n\pi) - k_p\left(e^{n\pi}+e^{-n\pi}-2\right)\right] \\ Q_{s1\_y} &= \frac{\delta a}{2}u_{y0} + \frac{\delta^3 p}{6\pi\eta_a}\sum_{n=1}^{\infty}\frac{1}{n}\frac{1-\cos n\pi}{e^{n\pi}-e^{-n\pi}} \\ &\quad \times\left[k_p\left(e^{n\pi}+e^{-n\pi}\right)(1-\cos n\pi) - \left(e^{n\pi}+e^{-n\pi}-2\right)\right] \end{aligned} \tag{11}$$

According to the continuity principle of hydrodynamics, the squeezed flow generated by plate movement $u_{x0}\cdot a{\cdot}h_b$ should be equal to that of MRF flow from two pairs of parallel plates. And then:

$$\begin{aligned} u_{x0}ah_b &= \delta a u_{x0} + \frac{\delta^3 p}{3\pi\eta_a}\sum_{n=1}^{\infty}\frac{1}{n}\frac{1-\cos n\pi}{e^{n\pi}-e^{-n\pi}} \\ &\quad \times\left[\left(e^{n\pi}+e^{-n\pi}\right)(1-\cos n\pi) - k_p(e^{n\pi}+e^{-n\pi}-2)\right] \\ u_{y0}ah_b &= \delta a u_{y0} + \frac{\delta^3 p}{3\pi\eta_a}\sum_{n=1}^{\infty}\frac{1}{n}\frac{1-\cos n\pi}{e^{n\pi}-e^{-n\pi}} \\ &\quad \times\left[k_p\left(e^{n\pi}+e^{-n\pi}\right)(1-\cos n\pi) - (e^{n\pi}+e^{-n\pi}-2)\right] \end{aligned} \tag{12}$$

From Equation (12), we can obtain:

$$\frac{u_{x0}}{u_{y0}} = \frac{\sum_{n=1}^{\infty}\frac{1}{n}\frac{1-\cos n\pi}{e^{n\pi}-e^{-n\pi}}\left[\left(e^{n\pi}+e^{-n\pi}\right)(1-\cos n\pi) - k_p(e^{n\pi}+e^{-n\pi}-2)\right]}{\sum_{n=1}^{\infty}\frac{1}{n}\frac{1-\cos n\pi}{e^{n\pi}-e^{-n\pi}}\left[k_p\left(e^{n\pi}+e^{-n\pi}\right)(1-\cos n\pi) - (e^{n\pi}+e^{-n\pi}-2)\right]} \tag{13}$$

Thus, according Equation (13), k_p can be calculated by the following formula:

$$k_p = \frac{\sum_{n=1}^{\infty}\frac{1}{n}\frac{1-\cos n\pi}{e^{n\pi}-e^{-n\pi}}\left[u_{y0}\left(e^{n\pi}+e^{-n\pi}\right)(1-\cos n\pi) + u_{x0}(e^{n\pi}+e^{-n\pi}-2)\right]}{\sum_{n=1}^{\infty}\frac{1}{n}\frac{1-\cos n\pi}{e^{n\pi}-e^{-n\pi}}\left[u_{x0}\left(e^{n\pi}+e^{-n\pi}\right)(1-\cos n\pi) + u_{y0}(e^{n\pi}+e^{-n\pi}-2)\right]} \tag{14}$$

By substituting Equation (12) into (10), p can be obtained.

Damping Force Calculation

According to the structural characteristics of shock absorber, the working mode of MR fluids is mixing mode of shear and flow. Therefore, in mechanical modeling, only shear force and damping force formed by differential pressure flow are considered in this paper. The shear damping force F_{xs}, F_{ys} in the direction of x, y can be obtained by combining Equations (10), (11), and (12). That is:

$$\begin{aligned} F_{xs} &= \eta_a\frac{u_{x0}}{\delta}a^2 + \delta a p\sum_{n=1}^{\infty}\frac{(1-\cos n\pi)^2}{(n\pi)^2} \\ F_{ys} &= \int_0^a\int_0^a \tau_{y0}dxdy = \eta_a\frac{u_{y0}}{\delta}a^2 + k_p\delta a p\sum_{n=1}^{\infty}\frac{(1-\cos n\pi)^2}{(n\pi)^2} \end{aligned} \tag{15}$$

The damping force produced by the pressure difference in the direction of x, y can be approximately expressed as:

$$\begin{aligned} F_{xp} &= \int_0^a\int_0^a p dxdy = pah_b \\ F_{yp} &= \int_0^a\int_0^a k_p p dxdy = k_p pah_b \end{aligned} \tag{16}$$

Therefore, the damping force F_x, F_y produced by shear and pressure can be calculated as follows:

$$\begin{aligned} F_x &= 2F_{xs} + F_{xp} = 2\eta_a\frac{u_{x0}}{\delta}a^2 + pa[2\delta\sum_{n=1}^{\infty}\frac{(1-\cos n\pi)^2}{(n\pi)^2} + h_b \\ F_y &= 2F_{ys} + F_{yp} \\ &= 2\eta_a\frac{u_{x0}}{\delta}a^2 + 2k_p p\delta a\sum_{n=1}^{\infty}\frac{(1-\cos n\pi)^2}{(n\pi)^2} + k_p pah_b \end{aligned} \tag{17}$$

The k_p and p in Equations (15) $\sim$ (17) are determined by Equation (14) and Equation (12). Regardless of the direction, we can see from Equation (17) that the damping force is correlated with the apparent viscosity η_α of MRFs, the vibration velocity u_{x0} and the area of the working surface of the 2-D plate type MR damper. The damping force increases with a decrease of the clearance δ of the damper, and/or increase in the intermediate plate's thickness h_b.

The theoretical analysis indicates that the apparent viscosity η_a is a function of zero field dynamic viscosity η_0, the applied magnetic field strength H and shear strain. It is generally considered that the apparent viscosity consists of zero field

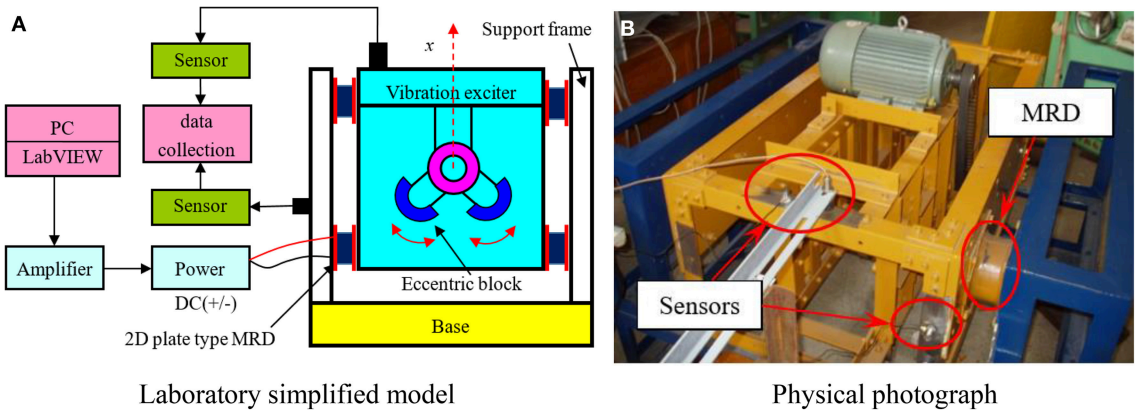

FIGURE 5 | The experimental instrument. **(A)** Laboratory simplified model. **(B)** Physical photograph.

viscosity and magnetic viscosity. The value of magnetic viscosity is several to dozens of times bigger than that of zero field viscosity under the effect of hysteresis. Therefore, two damping characteristics are presented in the damping force of MR damper i.e., viscous damping and Coulomb damping. Viscous damping is determined by the zero magnetic field dynamic viscosity of the MRFs and the structure size of MR damper, independent of the external magnetic field. However, the Coulomb damping is dependent on the external magnetic field, the material properties of MRFs, the relative motion velocity and the structure size. In general, the value of Coulomb damping force is much bigger than that of the large viscous damping force. For 2-D plate type damper, the main geometric factors affecting the damping force are the thickness h_b of the intermediate slide, the length a of the intermediate slide, and the clearance δ between the two parallel plates.

TEST BENCH AND EXPERIMENT PRINCIPLE

The basic structure of the MR vibration test system is shown in **Figure 5**. The main function of the base is to support and fix the part of the support frame. And the inner part of the frame, mainly composed of converter motor and eccentric mechanisms, is an exciting part to start or stimulate the vibration. The MR dampers are used to connect the exciting part and the support frame. Through adjusting the meshing position of the gears, the mass centers of two eccentric wheels form a certain angle with respect to their axes, as shown in **Figure 6**. When the angle is 90°, the amplitudes in both longitudinal and transverse directions are the maximum. In this paper, we only discuss the damping effect of the MR damper under the two-dimensional excited vibrations.

A photo of 2-D plate type MR damper is shown in **Figure 7**. The experiment process, as illustrated in **Figure 5A** is described as follows: the vibration bench displacement signal and acceleration signal, after denoising, are collected into the computer through the data acquisition card. It is analyzed, processed and displayed on the platform based on LabVIEW virtual instrument control, and the vibration velocity and displacement amplitude are obtained. The vibration absorption performance is further analyzed and studied by sampling data.

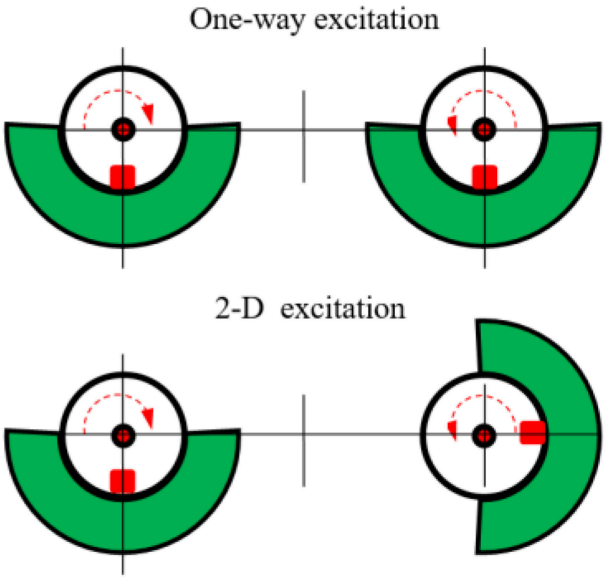

FIGURE 6 | Eccentric block position in 2-D coupled vibration.

In the experiments, the eddy current displacement sensor, combined with the high-speed data acquisition card PCI-MIO-16E-1, is used for the data acquisition. Signals gathered are sent to dynamic signal analyzer NI-4552 for processing. The whole data acquisition system is under the management of programs developed by the software platform LabVIEW. The A/D converter has 12 bits. It is written by G language given by software LabVIEW and executed with a data sampling frequency of 1,000 Hz and reading frequency of 500 Hz according to the Nyquist sampling theorem.

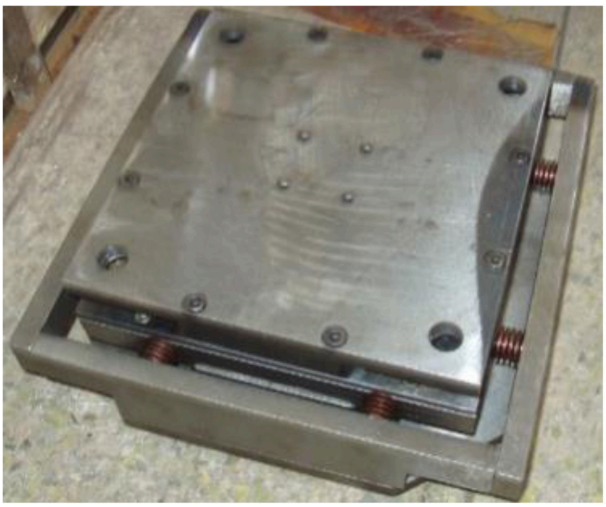

FIGURE 7 | Photo of the 2-D plate-type MRD.

FIGURE 8 | The MRF.

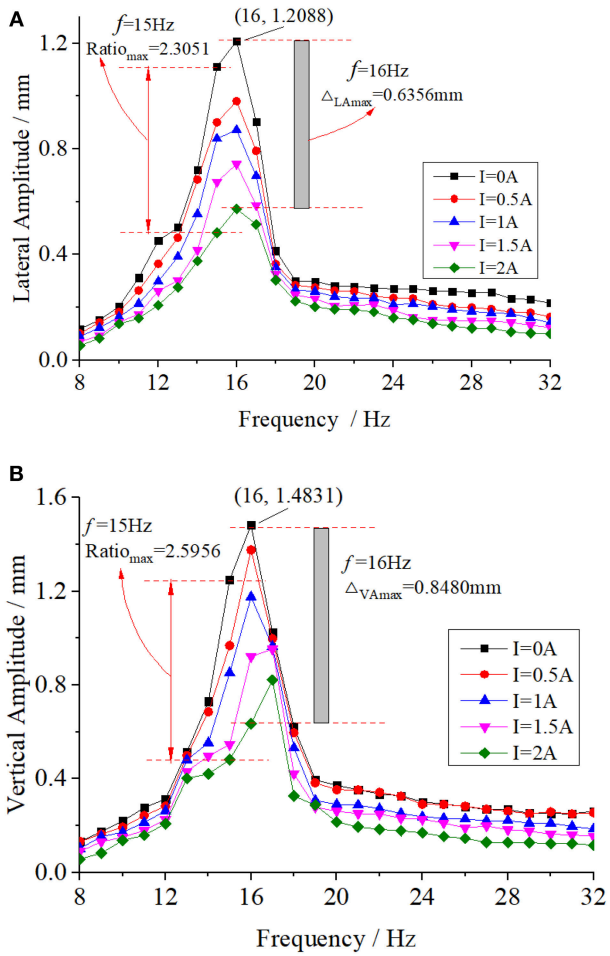

FIGURE 9 | Lateral and vertical amplitude at different excitation frequencies. **(A)** Transverse amplitude. **(B)** Longitudinal amplitude.

EXPERIMENTAL ANALYSIS OF 2-D PLATE TYPE MRD

The type of MRF we chose in the experiment is MRF2035 shown in **Figure 8**. The MRF is mainly composed of non-magnetic liquid-dimethicone and fine soft magnetic particles with high magnetic permeability and low hysteresis uniformly dispersed therein. The high yield strength of the MRF can reach 55 kPa.

A variety of testing conditions are realized by adjusting the frequency converter for different motor rotations. The range of the exciting frequency f is 8 $\sim$ 32 Hz, and the control current applied on the excitation coils of the MR damper are 0, 0.5, 1.0, 1.5, and 2.0 A. The amplitude responses of longitudinal and transverse vibrations of MR damper are obtained, as shown in **Figure 9**.

From **Figure 9**, it can be seen that when the input current I on the excitation coil is 0 A, i.e., the zero sum of the viscous damping force of the damper and the restoring force of the spring, the amplitude of the vibration system is the largest at each frequency. When the input current I of the excitation coil gradually increases to 2 A, the amplitude of the system decreases gradually. For example, when f = 14 Hz, the transverse amplitudes of the system are 0.7218, 0.6839, 0.5537, 0.168, and 0.3755mm at the excitation current I of 0, 0.5, 1, 1.5, and 2 A, respectively. The longitudinal amplitudes were 0.7305, 0.6856, 0.5532, 0.4974, and 0.4208 mm. When f = 16 Hz, the transverse and longitudinal amplitudes of the excitation system reached their maximum

TABLE 2 | Different excitation frequency *f*, lateral amplitude (LA) ratio and vertical amplitude (VA) ratio (*I* = 0 A's amplitude, *I* = 2 A's amplitude).

f/Hz	8	9	10	11	12	13	14	15	16
$Ratio_{VA}$	2.2941	2.1030	1.5983	1.7437	1.5050	1.2825	1.7360	2.5956	2.3352
$Ratio_{LA}$	2.1410	1.8388	1.4767	1.9729	2.1712	1.8247	1.9222	2.3051	2.1089
f/Hz	17	18	19	20	21	22	23	24	25
$Ratio_{VA}$	1.2463	1.9027	1.3747	1.7251	1.8147	1.8181	1.8404	1.7837	1.9031
$Ratio_{LA}$	1.7546	1.3662	1.3450	1.4802	1.4636	1.4667	1.4995	1.6827	1.7627
f/Hz	26	27	28	29	30	31	32		
$Ratio_{VA}$	1.9340	2.0900	2.0943	1.9961	2.0340	2.0366	2.2408		
$Ratio_{LA}$	1.9067	2.0162	2.1175	2.1268	2.1953	2.2468	2.1525		

values, 1.2088 and 1.4831 mm, respectively. When the frequency was higher than 16 Hz, the amplitude decreased gradually. In addition, it is found that the transverse amplitude is slightly smaller than the longitudinal, which is related to the inherent characteristics of the simulator. The resonance frequency of the system is 16 Hz, when the amplitude obtains the largest. The amplitude decreases gradually as the frequency increases with unit time. The excitation component has its own gravity, and the longitudinal amplitude is slightly larger when combined with the eccentric wheel.

In the experimental frequency range, with an increase of the current I in the excitation coil, the amplitude decreases, indicating that the damping force increases with increase of the current. When $I = 2$ A, the maximum decrease in amplitude is observed at $f = 16$ Hz. The decrease of transverse amplitude is 0.6356, and 0.8480 mm for the longitudinal. After calculation, the results show that the shear rate of shock absorber reaches the maximum when $f = 16$ Hz, suggesting that the output of damping force is greatly influenced by large shear rate.

Table 2 shows the ratios of amplitudes (transverse ratio $Ratio_{LA}$ and longitudinal ratio $Ratio_{VA}$) at different excitation frequencies f between I = 0 A and I = 2 A. Combined with **Figure 9**, it is found that the ratio of amplitude is >1 between I = 0 A and I = 2 A, meaning that the damping force plays an important role in suppressing the vibration when the excitation current is applied, and in the case of $f = 15$ Hz not at $f = 16$ Hz, the transverse and longitudinal amplitude ratio showed the maximum values of: 2.5956 and 2.3051, respectively. This is due to the smaller ratio of exciting force of exciter at $f = 15$ Hz and little difference of shear rate between two frequencies.

CONCLUSION

In this work, the structure of 2D plate type MR damper is designed. The velocity distribution, pressure distribution, flow model, and damping force have been established based on MRFs under bidirectional vibration conditions. The vibration absorption effect of dampers is tested on a two-dimensional exciting test bench. Based on the results, the following conclusions can be drawn:

(1) The damping force of 2D plate type MR damper is related to the clearance between parallel plates, the length and thickness of the intermediate slider, the zero magnetic field dynamic viscosity of MR fluid, and the working magnetic field intensity.
(2) The proposed 2-D plate type MR damper has good damping performance. The damping force increases with an increase of the control current. The larger the shear rate, the more obvious the damping effect. The maximum damping ratio of amplitude can reach up to 2.5956.

AUTHOR CONTRIBUTIONS

BC desiged the plate-type MRD, and DH and CL did the experiments. CC helped with the writing of the article.

ACKNOWLEDGMENTS

This work was supported by National Natural Science Foundation of China (No. 51305079), Natural Science Foundation of Fujian Province (No. 2015J01180), and outstanding young talent support program of Fujian Provincial Education Department (No. JA14208, JA14216). These financial supports are gratefully acknowledged.

REFERENCES

Anwesa, B., and Manas, D. (2018). Nano-finishing of bio-titanium alloy to generate different surface morphologies by changing magnetorheological polishing fluid compositions. *Prec. Eng.* 51, 145–152. doi: 10.1016/j.precisioneng.2017.08.003

Cha, Y. J., Agrawal, A. K., Phillips, B. M., and Spencer, B. F. Jr. (2014). Direct performance-based design with 200 kN MR dampers using multi-objective cost effective optimization for steel MRFs. *Eng. Struct.* 71, 60–72. doi: 10.1016/j.engstruct.2014.04.023

Chen, B. S., and Huang, Y. J. (2009). Analysis of non-linear characteristics of a magnetorheological damping system. *China Mech. Eng.* 20, 2795–2799.

Christie, M. D., Sun, S., Deng, L., Ning, D. H., Du, H., Zhang, S. W., et al. (2019). A variable resonance magnetorheological-fluid-based pendulum tuned mass damper for seismic vibration suppression. *Mech. Syst. Signal Process.* 116, 530–544. doi: 10.1016/j.ymssp.2018.07.007

David, A. C., Behzad, T., and Edmond, R. (2014). Dynamical modeling and experimental study of a small-scale magnetorheological damper. *IEEE/ASME Trans. Mechatr.* 19, 1015–1024. doi: 10.1109/TMECH.2013.2265701

Edward, J. P., Falcãoda, L., and Afzal, S. (2008). Multidisciplinary design optimization of an automotive magnetorheological brake design. *Comput. Struct.* 86, 207–216. doi: 10.1016/j.compstruc.2007.01.035

Gong, X. L., Ruan, X. H., Xuan, S. H., Yan, H., Deng, H., et al. (2014). Magnetorheological damper working in squeeze mode. *Adv. Mech. Eng.* 2014, 1–10. doi: 10.1155/2014/410158

Ha, Q., Royel, S., and Balaguer, C. (2018). Low-energy structures embedded with smart dampers. *Energy Build.* 177, 375–384. doi: 10.1016/j.enbuild.2018.08.016

Hema, L. K., Sri, U. P., and Seetharamaiah, N. (2017). Design and manufacturing aspects of magneto-rheological fluid (MRF) clutch. *Mater. Today* 4, 1525–1534. doi: 10.1016/j.matpr.2017.01.175

Jang, K. I., Jongwon, S., Min, B. K., and Lee, S. J. (2010). An electrochemomechanical polishing process using magnetorheological fluid. *Int. J. Machine Tools Manufact.* 50, 869–881. doi: 10.1016/j.ijmachtools.2010.06.004

Kang, S.-R., Cha, S.-W., Hwang, Y.-H., Lee, Y. S., Choi, S. B., et al. (2018). Controllable magnetorheological fluid based actuators for 6-degree-of-freedom haptic master applicable to robot-assisted surgery. *Sensors Actuators A* 279, 649–662. doi: 10.1016/j.sna.2018.06.057

Liao, C. R., Yu, M., Chen, W. M., Liang, X. C., and Huang, S. L. (2002). Issues in design rules of a magnetorheological fluid shock absorber for automobile. *China Mech. Eng.* 13, 723–726.

Luo, H., Guo, M. J., Yin, S. H., Chen, F., Huang, S., Lu, A., et al. (2018). An atomic-scale and high efficiency finishing method of zirconia ceramics by using magnetorheological finishing. *Appl. Surf. Sci.* 444, 569–577. doi: 10.1016/j.apsusc.2018.03.091

Luu, M., Martinez-Rodrigo, M. D., Zabel, V., and Könke, C. (2014). Semi-active magnetorheological dampers for reducing response of high-speed railway bridges. *Control Eng. Pract.* 32, 147–160. doi: 10.1016/j.conengprac.2014.08.006

Mohammad, M. Z., and Amir, M. H. (2018). Supervisory adaptive non-linear control for seismic alleviation of inelastic asymmetric buildings equipped with MR dampers. *Eng. Struct.* 176, 849–858. doi: 10.1016/j.engstruct.2018.09.045

Nguyen, P.-B., Do, X.-P., Choi, S. B., Jeon, J., Liu, Y. D., and Choi, H. J. (2014). Brake performance of core–shell structured carbonyl iron/silica based magnetorheological suspension. *J. Magn. Magn. Mater.* 367, 69–74. doi: 10.1016/j.jmmm.2014.04.061

Pang, H., Liu, F., and Xu, Z. R. (2018). Variable universe fuzzy control for vehicle semi-active suspension system with MR damper combining fuzzy neural network and particle swarm optimization. *Neurocomputing* 306, 130–140. doi: 10.1016/j.neucom.2018.04.055

Shaju, J., Anirban, C., and Norman, M. W. (2008). A magnetorheological actuation system: test and model. *Smart Mater. Struct.* 17:025023. doi: 10.1088/0964-1726/17/2/025023/meta

Shiao, Y. J., and Nguyen, Q. A. (2014). Torque enhancement for a new magnetorheological brake. *Proced. Eng.* 76, 12–23. doi: 10.1016/j.proeng.2013.10.001

Topcu, O., Yigit, T., and Konukseven, E. I. (2018). Design and multi-physics optimization of rotary MRF brakes. *Results Phys.* 8, 805–818. doi: 10.1016/j.rinp.2018.01.007

Wang, H. T. (2010). Model and analysis of damping for twin-tube magneto-rheological fluid damper based on disc type orifice. *J. Mech. Eng.* 46, 139–144.

Wang, S. Q., Li, D. C., and Ju, B. X. (2016). Preparation and properties of a magnetorheological fluid with oleic acid-coated magnetic particles. *Function Mater.*7, 7153–7156. doi: 10.3969/j.issn.1001-9731.2016.07.029

Yang, G., Spencer, B. F., Jung, H. J., and Carlson, J. D. (2002). Phenomenological model of large-scale MR damper systems. *Adv. Build. Technol.* 1, 545–552. doi: 10.1016/B978-008044100-9/50070-X

Yu, J. Q., Dong, X. M., and Zhang, Z. L. (2017). Design and control of automobile novel magnetorheological shock absorber with asymmetric mechchenics properties. *China Mech. Eng.* 28, 372–377. doi: 10.3969/j.issn.1004-132X.2017.03.020

Zhang, J. Q., Peng, Z. Z., Zhang, J., and Jie, Y. (2013). Dynamic analysis on vibration absorber of PVDF grain detecting sensor. *J. Vib. Measurement Diagn.* 33, 132–137. doi: 10.16450/j.cnki.issn.1004-6801.2013.01.013

Zheng, X. P., Chen, K. F., and Chen, S. M. (2016). Investigation on temperature properties of elevator magnetorheological brake. *China Mech. Eng.* 27, 2141–2154. doi: 10.3969/j.issn.1004-132X.2016.16.003

Conflict of Interest Statement: The authors declare that the research was conducted in the absence of any commercial or financial relationships that could be construed as a potential conflict of interest.

frontiers in Materials

ORIGINAL RESEARCH
published: 04 March 2019
doi: 10.3389/fmats.2019.00025

Experimental Performance Evaluation of a MR Brake-Based Haptic System for Teleoperation

Han Gyeol Gang[1], *Seung-Bok Choi*[2]* *and Jung Woo Sohn*[1]*

[1] Department of Mechanical Design Engineering, Kumoh National Institute of Technology, Gumi, South Korea,
[2] Department of Mechanical Engineering, Inha University, Incheon, South Korea

In this work, a new type of haptic system inspired by human wrist motion is proposed, and its performance is evaluated experimentally for teleoperation. The master device has 3-DOF rotational motion, which is the same as human wrist motion; semi-active magnetorheological brakes are installed to generate a haptic effect for the operator. To achieve a good haptic feedback effect, the master device is designed with a lightweight structure and the haptic actuator is designed with minimal size. The slave robot has 3-DOF rotational motion using servomotors, a five-bar linkage mechanism, and a pivot point. In the proposed slave robot, instead of a commercial torque sensor, a newly designed torque sensor that uses three force sensors is adopted. It is experimentally validated that the proposed haptic system has good performance in terms of the tracking control of the desired position and repulsive torque. In addition, to ensure that the human operator can actually distinguish the different magnitudes of torque, a simple recognition test is carried out. Although not continuous, it is confirmed that the torque difference can be distinguished at three levels. Finally, it is demonstrated that the proposed haptic system can be effectively applied to a real teleoperation system.

Keywords: MR fluid, MR brake, haptic actuator, haptic system, master device, slave robot

OPEN ACCESS

Edited by:
Heung Soo Kim,
Dongguk University Seoul,
South Korea

Reviewed by:
Janghyuk Moon,
Chung-Ang University, South Korea
Sungryul Yun,
Electronics and Telecommunications Research Institute, South Korea

***Correspondence:**
Seung-Bok Choi
seungbok@inha.ac.kr
Jung Woo Sohn
jwsohn@kumoh.ac.kr

Specialty section:
This article was submitted to Smart Materials, a section of the journal Frontiers in Materials

Received: *15 December 2018*
Accepted: *08 February 2019*
Published: *04 March 2019*

Citation:
Gang HG, Choi S-B and Sohn JW (2019) Experimental Performance Evaluation of a MR Brake-Based Haptic System for Teleoperation. Front. Mater. 6:25. doi: 10.3389/fmats.2019.00025

INTRODUCTION

A teleoperation control system that uses a master device to control a slave robot has several advantages, for example, the worker is not restricted to the worksite environment and can perform precise work such as robotic surgery. Many research studies have been carried out in order to utilize teleoperation in various fields, such as the space industry and nuclear energy industry. Recently, a system that can be applied to surgical operations that utilizes a master device-slave robot system has been developed, and research on a surgical robot system represented by Da Vinci has been actively conducted. Instead of conventional laparotomy, robot surgery involves insertion of a robotic arm into the body through three or four small holes in the body, and the operation then proceeds. Robotic surgery is expected to expand gradually, despite the high cost, because it has several advantages, such as a small surgical wound, low risk of infection, and quick recovery. Currently, the biggest disadvantage of a remote-control system, that uses the master-slave system, is that the operator relies solely on visual and auditory information without tactile information which decreases the worker's sense of realism and immersion. In order to compensate for this, various haptic systems that are capable of transmitting tactile information to the operator, are being studied. Many researches on haptic systems using electric motors have been proposed. When

an electric motor is used as a haptic actuator, a decelerator that uses gears and an encoder for position measurement are used together, which leads to the disadvantage of the system becoming bulky and difficult to control. In recent years, studies on haptic actuators using smart materials such as piezoelectric materials, electrorheological and magnetorheological (MR) fluids, and electro-active polymers have been actively conducted. A smart material is a material that can change its characteristics according to changes in the external environment, and a system using it can take advantage of this to generate an operating force directly without additional mechanical devices. A MR fluid, that can change its viscosity according to changes in the external magnetic field strength, is composed of a suspension of silicone oil and iron particles. The merits of MR fluid are that they have a fast response time, low energy consumption, and simple system configuration. Representative mechanical devices that apply MR fluid include automotive MR dampers, MR mounts and MR clutches/brakes. It has been confirmed that dampers and mounts that use MR fluid have better performance than the existing passive devices, and they have been commercialized and mounted on various advanced vehicles (Wang and Liao, 2011). A MR clutch/brake has the capability of reducing or stopping the rotational speed of a shaft using the MR effect, which is generated between the rotor and stator. Many studies are currently underway to improve the performance of MR brakes and to apply them to various fields. Imaduddin et al. reviewed the design of MR brakes and the characteristics of each type of MR brake, such as drum-type, disc-type, and hybrid-type, were identified and mathematical modeling techniques were discussed in detail (Imaduddin et al., 2013). Nguyen and Choi investigated the optimal design of different types of MR brake to achieve a high torque output under a constrained specific volume (Nguyen and Choi, 2012b). Sohn et al. optimized the design parameters of a disc-type MR brake for a mid-sized motorcycle, and the mechanical characteristics, such as response time and braking torque, were experimentally evaluated (Sohn et al., 2015). Wu et al. designed a new type of MR brake with a multi-pole and dual-gap configuration to increase the range of the output torque while maintaining a compact structure (Wu et al., 2016). Recently, various researches have been carried out to utilize MR brakes as haptic actuators. Liu et al. reported the design, testing, and modeling of a MR fluid brake and demonstrated example applications of a MR brake as a haptic actuator for a virtual reality hardware (Liu et al., 2006). Li et al. presented the design and development of a MR fluid-based haptic system and demonstrated the applications of a MR joystick for virtual reality by using four typical 2D and 3D interface examples (Li et al., 2007). An and Kwon proposed a five-bar linkage haptic device featuring DC motors and MR brakes, and it was demonstrated that the combination of DC motors and MR brakes has a broader *Z*-width than that of solely DC motors (An and Kwon, 2009). Senkal and Gurocak proposed a design of an MR spherical brake as a multi-DOF actuator for a joystick-type haptic application (Senkal and Gurocak, 2009). They identified virtual wall collision, damping, and Coulomb friction simulations via experiments. Nguyen and Choi proposed an optimal design of a bi-directional MR brake for a haptic system for surgical robot applications (Nguyen and Choi, 2012a). The suggested bi-directional MR brake can transmit generated active and semi-active braking torque. Nguyen and Choi also experimentally evaluated the control performance of a bi-directional MR clutch by considering hysteresis and friction effects (Nguyen and Choi, 2013). In recent years, MR brakes have been developed that can generate the sufficient required operating torque despite having a compact size. Nguyen et al. proposed a new configuration of a 3D haptic gripper for tele-manipulation and optimal design was conducted (Nguyen et al., 2013). Sohn et al. designed a new type of MR brake that increases the area where the MR effect is generated by modifying the shape of the magnetic core and experimentally validated the effectiveness of the proposed MR brake by comparing it with a conventional MR brake (Sohn et al., 2018).

The main contribution of this work is the design and experimental evaluation of a simple and low-cost haptic system that consists of a master device and slave robot. Due to considerations of real system applications, the 3-DOF master device was designed with a lightweight structure that can be driven in the same way as the motion of the human wrist. A minimized haptic actuator was also designed using a MR brake and installed to the master device. In order to obtain a large torque, a multi-disc type MR brake can be considered. However, since the size of the actuator becomes large, it cannot be applied to this work. In this study, a drum type brake was used and a dual magnetic core was applied to obtain a large torque at a small size. The motion of the master device was measured by using a chip-type MEMS gyro sensor, which is embedded in the master device. The slave robot, which can realize 3-DOF rotational motion, was designed using a five-bar linkage mechanism and servomotors. In order to measure the position of the slave robot, a gyro sensor, the same as the sensor that is installed in the master device, was used. Instead of a commercial force or torque sensor, a new type of torque sensor was fabricated and adopted for the slave robot to monitor its status. After realization of a fuzzy-PID control algorithm, the performance characteristics of the proposed haptic system were evaluated via experiments and good control performances were achieved in position tracking control of the slave robot and repulsive torque tracking control of the master device. Additionally, to ensure that the human operator can actually distinguish the different magnitudes of torque, a simple recognition test was also conducted.

COMPONENTS DESIGN

MR Brake

MR fluid is a type of smart fluid whose viscosity can be controlled by applying an external magnetic field. Typically, MR fluid is a suspension of carrier oil and micrometer-scale magnetic particles. When MR fluid is subjected to a magnetic field, the magnetic particles construct a chain structure by aligning themselves along the direction of the magnetic flux. The yield stress of the MR fluid is obtained from the breaking force of this chain structure. Since the bonding force of the chain structure depends on the strength of the applied magnetic field, the yield stress of the MR fluid can be continuously controlled

by controlling this. In this work, a commercial MR fluid, MRF-132DG of Lord Corp. is used in the proposed MR brake of the master device. The basic material properties are summarized in **Table 1** and as a magnetic property of the MR fluid, the relationship between magnetic flux density and magnetic field intensity is presented in **Figure 1A**. In addition, the relationship between the shear stress and magnetic field intensity of the MR fluid is presented in **Figure 1B**. The yield stress of the MR fluid, τ, can be expressed as follows by using the Bingham plastic model:

$$\tau = \tau_y(\mathbf{B}) + \eta\dot{\gamma} \quad (1)$$

Where $\tau_y(\mathbf{B})$ is the magnetic flux density-dependent yield stress, η is the viscosity of the MR fluid without a magnetic field, and $\dot{\gamma}$ is the shear strain rate. Then, the relationship between the shear stress and magnetic flux density of the MR fluid can be determined by the following equation.

$$\tau_y(B) = a_0 + a_1 B + a_2 B^2 + a_3 B^3 + a_4 B^4, \quad (2)$$

$$a_0 = -1.18,\ a_1 = 65.894,\ a_2 = 21.776,\ a_3 = 46.113,\ a_4 = 0.001$$

The mechanical property, the relationship between shear stress and shear rate, is measured according to the input current by using a viscometer and the results are presented in **Figure 1C**. It can be clearly observed that the shear stress of the MR fluid increases as the intensity of the applied magnetic field increases.

In order to achieve a high actuating torque that satisfies the design constraints of a small-sized actuator, a drum-type MR brake with a dual magnetic core shape is designed and fabricated in this work. The exploded view of the proposed MR brake is presented in **Figure 2A**. The proposed MR brake consists of a stator, magnetic core, rotor, shaft, outer case, upper case, and lower case. The copper wire is wound on the magnetic core without bobbin to generate a magnetic field. The MR fluid is filled in the gap between the rotor and stator. The MR effect, which is a torque resistant to the rotation of the rotor, can be achieved by generating a magnetic field across the rotor and stator. A section view with geometrical dimensions is presented in **Figure 2B**. The outer radius of the proposed MR brake is 25 mm, which is similar to the size of a slim beverage can. The height and gap size are 54 and 1 mm, respectively. A photograph of the manufactured MR brake is presented in **Figure 2C**. The total magnitude of the braking torque of the MR brake can be estimated from the following equation.

$$T_{total} = T_{MR} + T_\eta + T_f \quad (3)$$

Where T_{MR} is the controllable toque from the MR effect, T_η is the torque generated from the viscosity of the MR fluid, and T_f is the torque generated from the mechanical friction of the device. The controllable torque, T_{MR}, is expressed as a function of the yield stress of the MR fluid by the following equation.

$$T_{MR} = 4\pi d R^2 \tau_y(B) \quad (4)$$

TABLE 1 | Material properties of MRF-132DG.

Appearance	Dark gray liquid	Solids content by weight, %	80.98
Viscosity, Pa @ 40°C	0.092 ± 0.015	Flash Point, °C	>150
Density (g/cm^3)	2.98 − 3.18	Operating Temperature, °C	−40 to +130

Where d is the total length of the area where a magnetic force is generated in the gap and R is the radius of the rotor. The torque generating performance of the manufactured MR brake is experimentally evaluated and the results are shown in **Figure 2D**. The maximum torque is 2.2 Nm at an input current of 2 A, and that is enough to prevent rotational motion with the human hand.

Master Device

A photograph of the manufactured master device is shown in **Figure 3**. In order to realize human wrist motion exactly, the three axes of 3-DOF rotation meet at a point on the proposed master device. In addition, it is important for the master device to provide a precise reaction force or resistance torque, so it is important to design the device as a lightweight structure. For the proposed master device, the structural weight is reduced by applying an aluminum frame, and the haptic actuator is also manufactured in a small size. The weight of each element of the master device is shown in **Table 2**. The total weight of the moving part is about 1,600 g, including two MR brakes. To reduce the operator's work fatigue, a power grip that uses a stick instead of a finger grip is applied. Three MR brakes are installed on each rotary axis to produce a resistance torque for each of the three rotary directions. The MR brakes generating the torque in the pitch and roll directions are mounted to the master device frame and the MR brake generating the torque in the yaw direction is mounted on the base to reduce the weight of the master device. There are many studies that use electric motors as haptic actuators. In this case, reducers and encoders are indispensable. However, the use of MR brakes reduces the complexity and weight of the system by eliminating the need for a gear reducer, that is essential when using an electric motor. The braking force is transmitted without loss due to backlash while the actuator is directly engaged with the instrument so that the transmissibility of the haptic effect can be improved. In addition, in the proposed master device, a chip-type MEMS gyro sensor (Model MPU9250, InvenSense) is inserted into the grip stick without using an encoder on the rotating shaft, and the rotation angle is measured so that the position of the master device can be transmitted to the slave robot.

Slave Robot

The structural configuration and a photograph of the manufactured slave robot are presented in **Figures 4A,B** respectively. In order to enhance intuitive usability, the slave robot is designed to be able to rotate in 3-DOF to correspond to the degrees of freedom of the master device. The slave robot

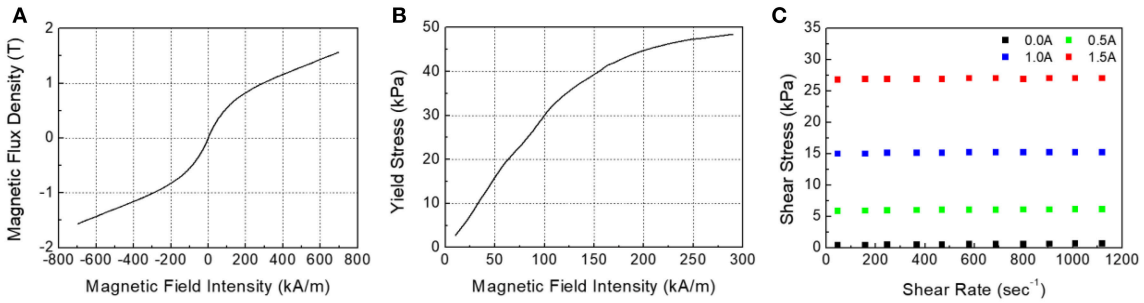

FIGURE 1 | Material characteristics of MRF-132DG. **(A)** Magnetic property, magnetic flux density vs. magnetic field intensity. **(B)** Yield stress vs. magnetic field intensity. **(C)** Shear stress vs. shear rate according to applied current.

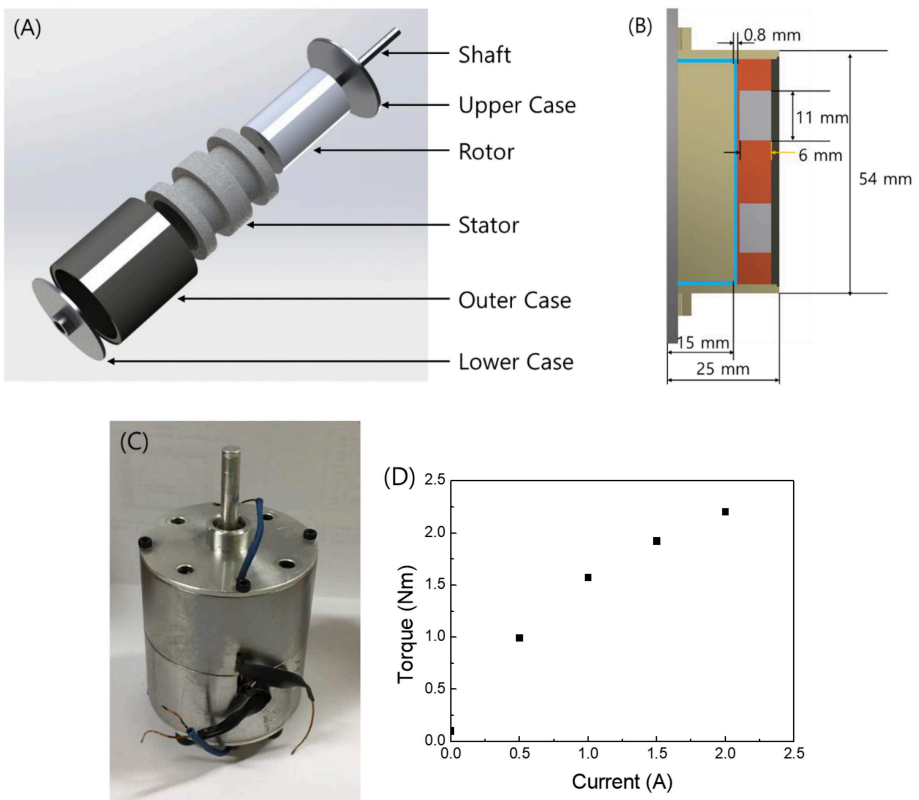

FIGURE 2 | The proposed MR brake. **(A)** Configuration. **(B)** Section view. **(C)** Photograph. **(D)** Measured torque.

is based on the manipulator type used in robot surgery, and the diameter of the arm is designed to be less than 2 mm in consideration of practical usability. The proposed slave robot is able to generate pitch and yaw motions using two servomotors, a five-bar linkage mechanism with planar motion, and a pivot point. The roll motion is generated using a separate servo motor. A schematic diagram of the slave robot for calculating the angle to be generated in the servo motor is shown in **Figure 5**. Since a pivot point is used in the proposed slave robot, the position of the slave robot end effector in the pitch and yaw directions is determined by the position of joint P of the five-bar linkage. The position of joint P can be expressed by the following equation.

$$P_x = b\sin\Phi_y,\ P_y = b\sin\Phi_p + e \tag{5}$$

Where b is the length of the robot manipulator from the five-bar linkage to the pivot point, Φ_y is the desired input angle in the yaw direction, Φ_p is the desired input angle in the pitch direction, d is the length of fixed link and e is the distance of joint P in the y-direction from the x-axis. Finally, the required angle that should be generated by the servomotor can be calculated from the following equation.

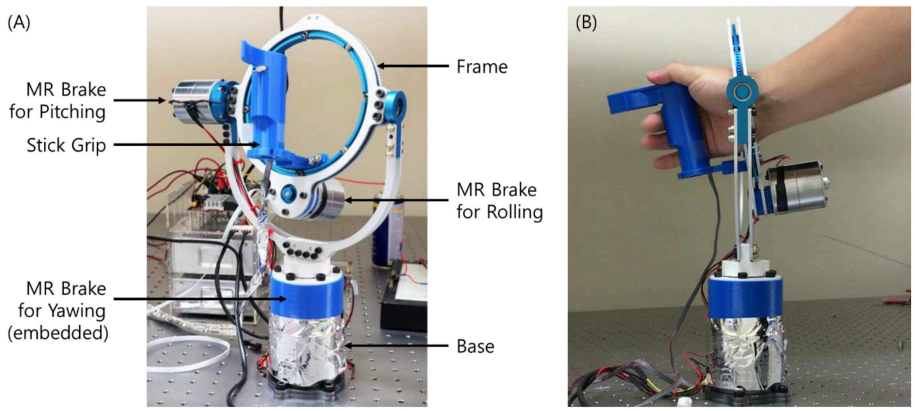

FIGURE 3 | Photograph of the manufactured master device. **(A)** Front view. **(B)** Side view.

TABLE 2 | Components of the MR Brake and their weights.

Parts	Materials	Weight
Frame	Aluminum	200 g
Grip stick	ABS	24 g
Base mount	Stainless steel	900 g
MR brake	Carbon steel (S45C), etc.	700 g

$$\theta_i = 2^{*}arctan\left\{\gamma_1+\sqrt{\frac{\gamma_1^2-(a_i^2-b_i^2)}{a_i+b_i}}\right\}, i = 1,2 \quad (6)$$

$$a_1 = P_x^2+P_y^2+P_xd+\frac{d}{2}+l_1^2-l_2^2, b_1 = 2l_1P_x+l_1d, \gamma_1 = 2P_xl_1$$

$$a_2 = P_x^2+P_y^2-P_xd+\frac{d}{2}+l_1^2-l_2^2, b_2 = 2l_1P_x-l_1d$$

For haptic feedback, the slave robot should be equipped with a sensor capable of measuring force or torque. However, since a general torque sensor is bulky, it is difficult to apply to the proposed slave robot. It is possible to apply this sensor temporarily for the experiment, but it is difficult to apply it in an actual use environment. In this study, a new type of sensor capable of measuring torque in three directions is proposed and applied. The structural configuration of the proposed torque sensor is presented in **Figure 6**. The proposed torque sensor consists of three symmetrically-arranged force sensors (Model FSS015WNSX Honeywell) and a steel ball in contact with them. The end effector of the slave robot can be inserted into one end of the proposed torque sensor, so that various end effectors capable of various operations can be utilized. If the end effector of the slave robot has a resistance force against the direction in which it is intended to operate, the steel ball is brought into contact with the force sensors and a force is generated. The resistance torque for each direction of rotation from the measurement data of the three force sensors can be calculated using the following equations.

$$T = P^{*}l_e \quad (7)$$

Where T is the resistance torque of the end effector, P is the resistance force of the end effector, and l_e is the length of the end effector. The force P can be expressed as follows using the measured forces from the three force sensors (Xu et al., 2014).

$$P = F_1 + F_2 + F_3 \quad (8)$$

The force P can be decomposed in x, y, and z directions as follows:

$$\begin{bmatrix} P_x \\ P_y \\ P_z \end{bmatrix} = \begin{bmatrix} P\cos\alpha\cos\beta \\ P\cos\alpha\sin\beta \\ P\sin\alpha \end{bmatrix} \quad (9)$$

Where α and β are the angles between the end effector and the slave robot rod in the x-z and x-y planes, respectively. The measured forces from the force sensors can be expressed by the following equations.

$$F_1 = \left[0 \; -\cos45^\circ \sin45^\circ\right]^T * k_1 * S_1$$
$$F_2 = \left[\cos45^\circ * \cos30^\circ \cos45^\circ * \sin30^\circ \sin45^\circ\right]^T * k_2 * S_2$$
$$F_3 = \left[-\cos45^\circ * \cos30^\circ \cos45^\circ * \sin30^\circ \sin45^\circ\right]^T * k_3 * S_3 \quad (10)$$

Where k_1, k_2, and k_3 are calibration coefficients and S_1, S_2, and S_3 are measured sensor values.

HAPTIC SYSTEM

The configuration of the proposed haptic system is presented in **Figure 7**. In this study, the master system and slave robot are independently controlled through the control box without configuring the PC-based control system. UART serial communication is used between the master device and slave robot to transmit the required position and torque. The control box for the master device consists of a main processor [Model.

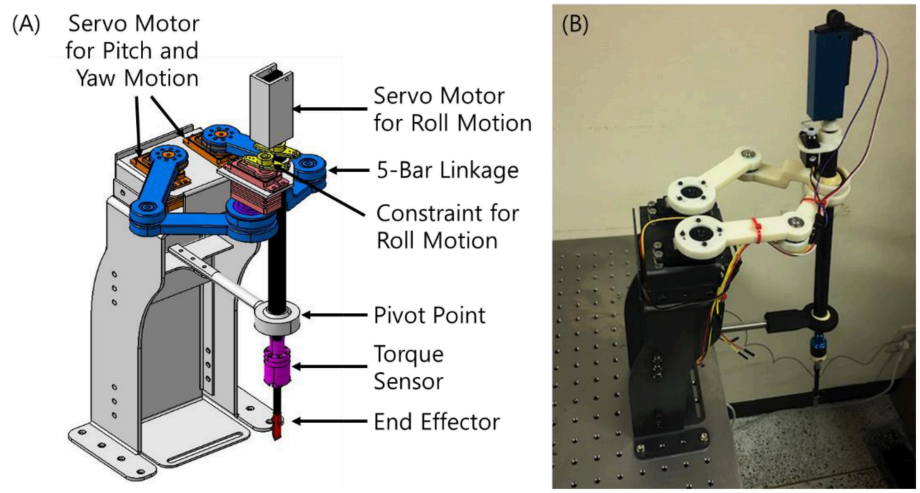

FIGURE 4 | The proposed slave robot. **(A)** Structural configuration. **(B)** Photograph.

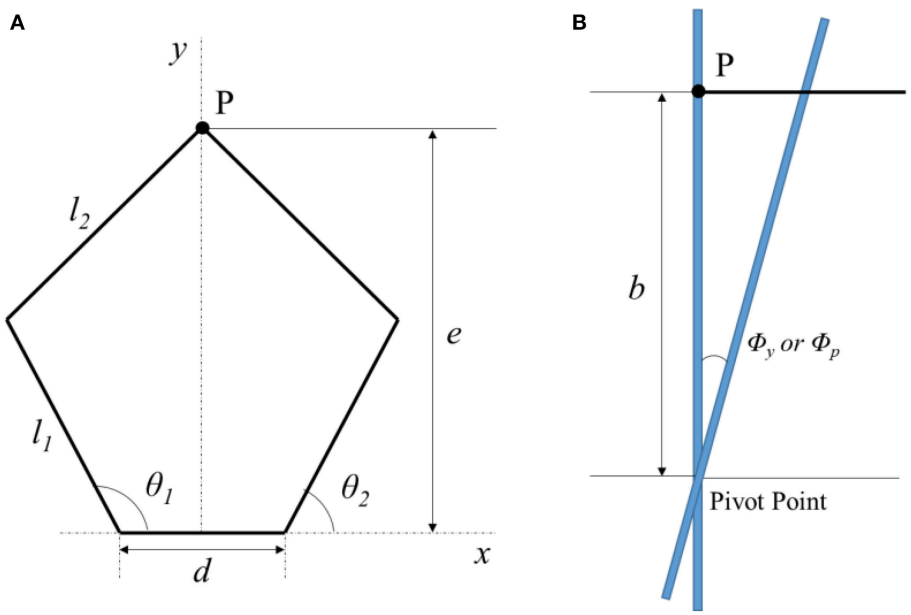

FIGURE 5 | Configuration for slave robot position determination. **(A)** Top view. **(B)** Side view.

Arduino Due (84 Mhz)], SMPS for power supply, current amplifier, and current sensor. The control box for the slave robot consists of a main processor [Model. Arduino Due (84 Mhz)], SMPS for power supply, and motor drivers for the servomotors. However, in this study, each control box and the PC are connected to be able to store measured data. Before the control experiment, the workspaces of the master device and slave robot are confirmed through experiments. The data are measured using MEMS gyro sensors attached to the master device and slave robot, and the actual wrist motion is measured by attaching the gyro sensor to the hand. The measured workspaces in the pitch and yaw directions are shown in **Figure 8**. Although the workspaces are slightly different, it can be seen that the workspace of the master device and the slave device effectively cover the workspace of the wrist.

Generally, PID control has advantages of easy configuration and application. However, since the control gain cannot be continuously changed, there is a disadvantage that control performance is limited when the external environment changes. In this study, a fuzzy-PID control algorithm is applied to control the haptic system and the PID control gain is determined using a fuzzy algorithm. A block diagram of the fuzzy-PID control algorithm is shown in **Figure 9**. The control input of the proposed fuzzy-PID control algorithm can be expressed as

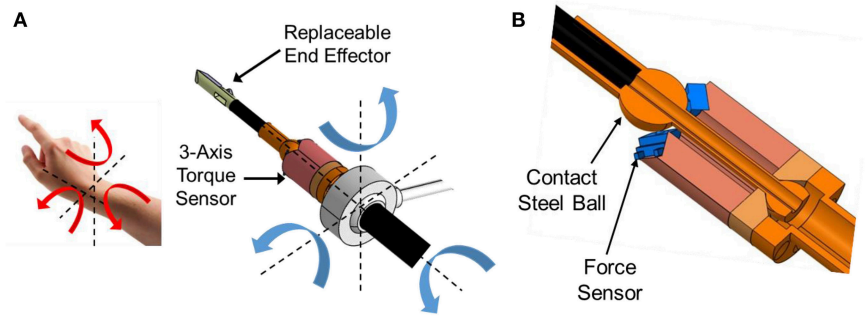

FIGURE 6 | The proposed torque sensor. **(A)** Configuration. **(B)** Section view.

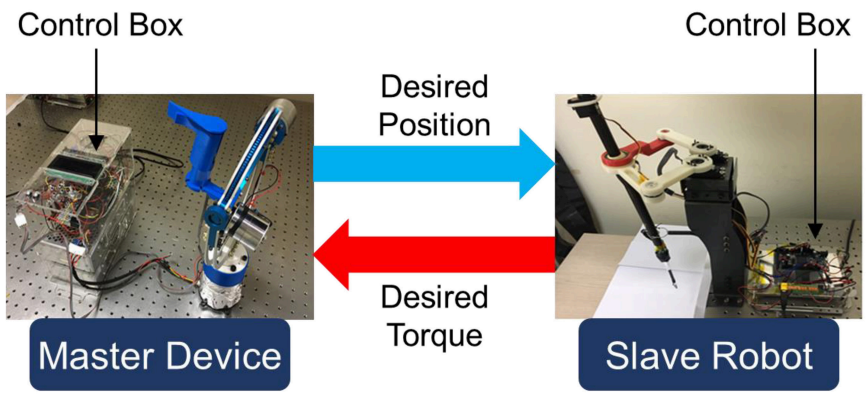

FIGURE 7 | Schematic diagram of the proposed master-slave haptic system.

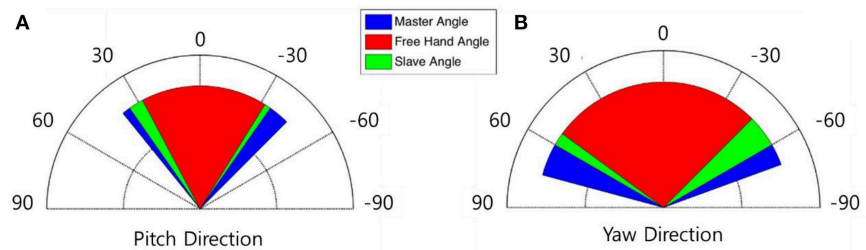

FIGURE 8 | Comparison of the measured workspaces. **(A)** Pitch motion. **(B)** Yaw motion.

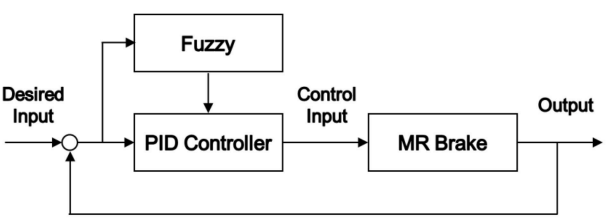

FIGURE 9 | Block diagram of the fuzzy-PID control algorithm.

follows (Ziegler and Nichols, 1942).

$$u(k) = K_P e(k) + K_I \sum_{i=1}^{n} e(i) + K_D \Delta e(k) \quad (11)$$

Where $e(k)$ is the error between the reference input and actual output, $\Delta e(k)$ is the rate of change of error. K_P, K_I, and K_D are the proportional, integral, and derivative control gains, respectively. It is assumed that the ranges of K_P and K_D are limited as follows.

$$K_{P,\,min} \leq K_P \leq K_{P,\,max},\ K_{P,\,min} = 0.32k_u,\ K_{P,\,max} = 0.6k_u \quad (12)$$

$$K_{D,\,min} \leq K_D \leq K_{D,\,max},\ K_{D,\,min} = 0.08k_u T_u,\ K_{D,\,max} = 0.15k_u T_u \quad (13)$$

Where k_u and T_u are the gain and the period of oscillation, respectively, at the stability limit under P-control. The parameters K_P', K_D' and α are determined by a fuzzy operation with $e(k)$ and $e(k)$ as input values, and the control gain of the PID controller is

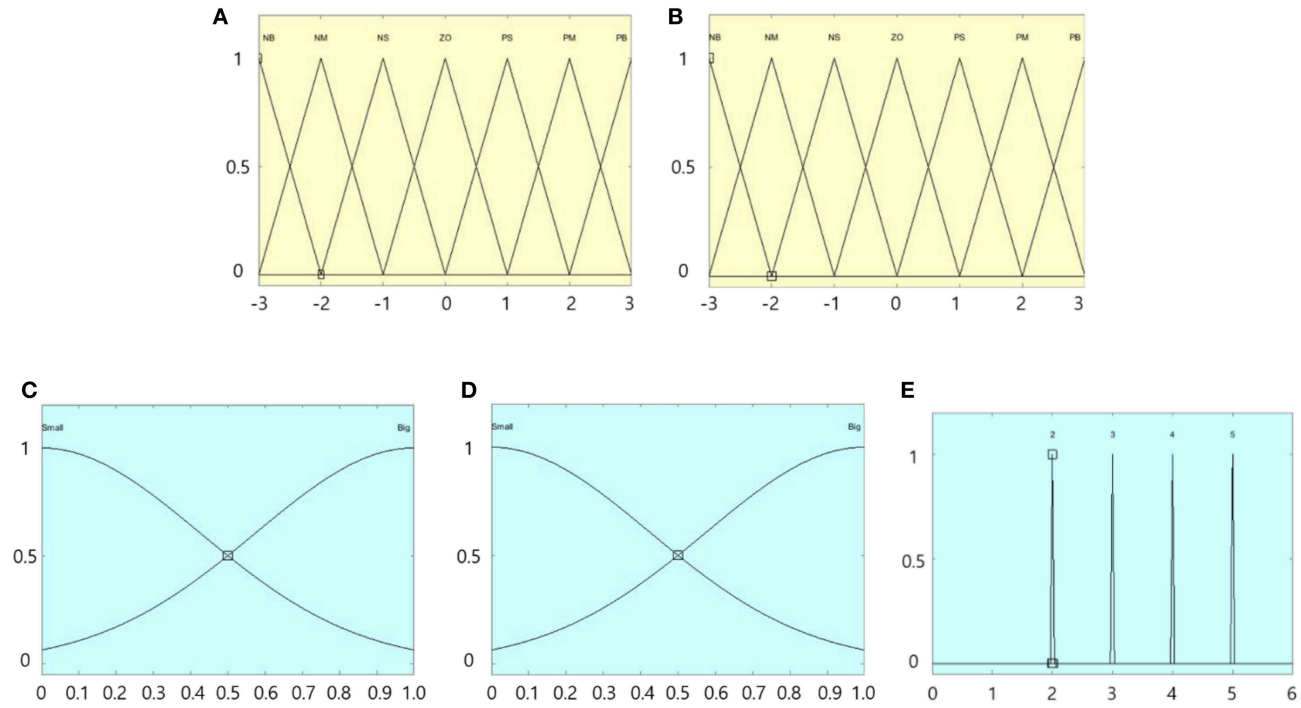

FIGURE 10 | Membership function of the fuzzy algorithm. **(A)** Input $e(k)$. **(B)** Input $\Delta e(k)$. **(C)** Output K_P. **(D)** Output K_D. **(E)** Output α.

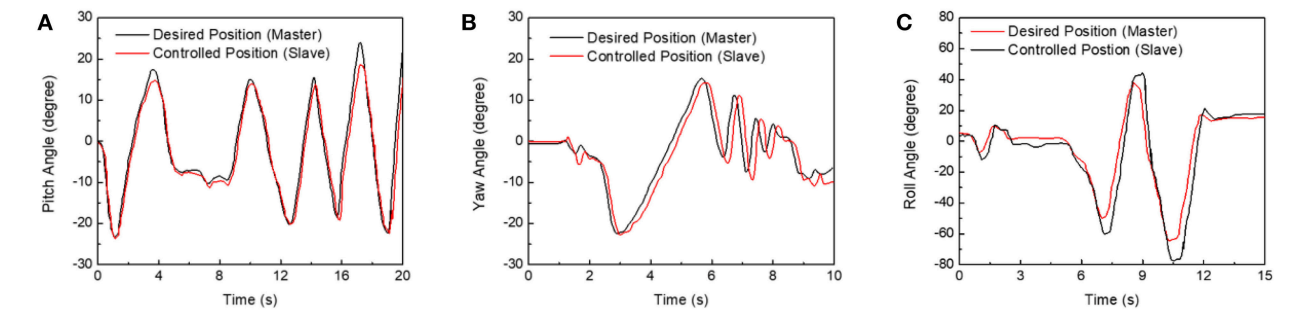

FIGURE 11 | Position tracking control results. **(A)** Pitch motion. **(B)** Yaw motion. **(C)** Roll Motion.

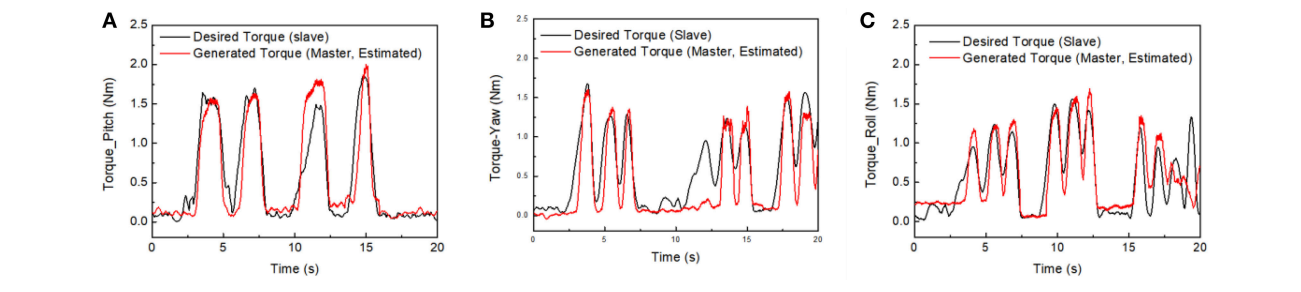

FIGURE 12 | Repulsive torque tracking control results. **(A)** Pitch motion. **(B)** Yaw motion. **(C)** Roll Motion.

TABLE 3 | Recognition test results.

Participants	Objects				
	Sponge	Fabric	Silicone	Plastic barrel	Steel rod
A	1	2	2	5	5
B	1	3	2	4	4
C	1	2	3	5	4
D	2	1	2	4	4
Average	1.25	2.00	2.25	4.50	4.25

determined from the following equations.

$$\begin{aligned} K_P &= \left(K_{P,\,max} - K_{P,\,\min}\right) K_P' + K_{P,\,min} \\ K_D &= \left(K_{D,\,max} - K_{D,\,min}\right) K_D' + K_{D,\,min} \\ K_I &= K_P^2/(\alpha K_D) \end{aligned} \tag{14}$$

The input and output membership functions used in the fuzzy algorithm are shown in **Figure 10**. Experiments are performed to confirm the performance of the proposed slave robot at tracking the position of the master device, which is changed by the hand movements of the operator. The results are shown in **Figure 11**. Only the MEMS gyro sensor is used without additional sensors such as encoders. As shown in this figure, it can be seen that the slave robot keeps track of the required position measured from the master device. Experiments are conducted to confirm that the resistance torque generated from the end effector of the slave robot is transmitted to the operator through the haptic actuator of the master device. The results are shown in **Figure 12**. In the slave robot, the resistance torque is measured by the built-in torque sensor. In the master device, which does not include an additional torque sensor, the current value applied to the MR brake is monitored and the magnitude of the generated torque estimated using results from **Figure 2D**. As shown in the results of **Figures 11**, **12**, it can be confirmed that the torque generated by the haptic actuator of the master device follows the torque generated in the slave robot substantially well. Finally, it can be concluded that the proposed low-cost haptic system has excellent control performance.

In order to confirm the applicability of the proposed haptic system, experiments are carried out to determine if a person can recognize the difference in resistance torque generated by the MR brake and transmitted to the user. Five different materials, including sponge, fabric, silicone, plastic barrel, and steel rod, are brought into contact with the end effector. When the end effector comes into contact with an object, a low resistance torque is generated. If a participant can freely perform the hand operation they give a score of 0. Conversely, if a participant feels that they cannot move their hand due to the large resistance torque, a score of 5 is given. Four participants performed the experiment, and they are prevented from seeing the objects they are touching to remove bias. The type of object contacting the end effector is selected at random. The results of the cognitive experiments are summarized in **Table 3**. From the experimental results, it can be seen that the participants could not recognize the torque value continuously, but could recognize the difference in torque transmitted in three stages. Although the experiment could have been improved by increasing the number of participants and applied objects, it is considered that it is possible for the operator of the master device to distinguish the difference in torque through several stages with the proposed MR brake-based haptic system.

CONCLUSIONS

In this study, a master device and slave robot, that can implement the same motion as a human wrist, have been proposed. In addition, a haptic system was constructed that can transmit the resistance torque generated when the end effector of the slave robot hits an object to the user of the master device. In order to improve the haptic effect, the master device was designed to be lightweight structure and a semi-active actuator was constructed using a miniaturized MR brake as a haptic actuator. Considering the possibility of its use in an actual system, the position tracking control of the master device and the slave robot was performed by replacing the commercial encoder, which has a large volume and weight, with a MEMS gyro sensor. In addition, a small sensor capable of measuring the torque of the slave robot was built and torque tracking control was performed. From the experimental results, it is confirmed that the proposed haptic system has a low-cost but excellent control performance. Finally, a cognitive characteristics experiment with four participants was performed and it was confirmed that the operator can distinguish between different magnitudes of torque by about three different levels using the proposed system. Generally, it takes more than 7-DOF to implement human arm and wrist motion. In this study, 3-DOF required for human wrist motion were considered and excellent experimental results were obtained. Based on these results, it is expected that it will be possible to extend the proposed system more than 7-DOF system.

AUTHOR CONTRIBUTIONS

HG set up experimental apparatus, conducted experiments, and collected all measured data. S-BC contributed to the conception and design of the study and analyzed the experimental results. JS wrote the first draft of the manuscript. All authors contributed to manuscript revision and read and approved the submitted version.

FUNDING

This research was supported by the National Research Foundation (NRF) of Korea funded by Ministry of Science and ICT (NRF-2017R1C1B2012207).

REFERENCES

An, J., and Kwon, D. (2009). Five-bar linkage haptic device with DC motors and MR brakes. *J. Intel. Mater. Syst. Struct.* 20, 97–107. doi: 10.1177/1045389X07086690

Imaduddin, F., Mazlan, S. A., and Zamzuri, H. (2013). A design and modelling review of rotary magnetorheological damper. *Mater Des.* 51, 575–591. doi: 10.1016/j.matdes.2013.04.042

Li, W. H., Liu, B., Kosasih, P. B., and Zhang, X. Z. (2007). A 2-DOF MR joystick for virtual reality applications. *Sens. Actuat. A Phys.* 137, 308–320. doi: 10.1016/j.sna.2007.03.015

Liu, B., Li, W. H., Kosasih, P. B., and Zhang, X. Z. (2006). Development of an MR-brake-based haptic device. *Smart Mater. Struct.* 15, 1960–1966. doi: 10.1088/0964-1726/15/6/052

Nguyen, P. B., and Choi, S. B. (2012a). A bi-directional magneto-rheological brake for medical haptic system: optimal design and experimental investigation. *Adv Sci Lett*. 13, 165–172. doi: 10.1166/asl.2012.3843

Nguyen, P. B., and Choi, S. B. (2013). Accurate torque control of a bi-directional magneto-rheological actuator considering hysteresis and friction effects. *Smart Mater. Struct*. 22:055002. doi: 10.1088/0964-1726/22/5/055002

Nguyen, Q. H., and Choi, S. B. (2012b). Selection of magnetorheological brake types via optimal design considering maximum torque and constrained volume. *Smart Mater. Struct*. 21:015012. doi: 10.1088/0964-1726/21/1/015012

Nguyen, Q. H., Choi, S. B., Lee, Y. S., and Han, M. S. (2013). Optimal design of a new 3D haptic gripper for telemanipulation featuring magnetorheological fluid brakes. *Smart Mater. Struct*. 22:015009. doi: 10.1088/0964-1726/22/1/015009

Senkal, D., and Gurocak, H. (2009). Spherical brake with MR fluid as multi degree of freedom actuator for haptics. *J. Intel. Mater. Syst. Struct.* 20, 2149–2160. doi: 10.1177/1045389X09348925

Sohn, J. W., Gang, H. G., and Choi, S. B. (2018). An experimental study on torque characteristics of magnetorheological brake with modified magnetic core shape. *Adv. Mech. Eng.* 10, 1–10. doi: 10.1177/1687814017752222

Sohn, J. W., Jeon, J., Nguyen, Q. H., and Choi, S. B. (2015). Optimal design of disc-type magneto-rheological brake for mid-sized motorcycle: experimental evaluation. *Smart Mater. Struct.* 24:085009. doi: 10.1088/0964-1726/24/8/085009

Wang, D. H., and Liao, W. H. (2011). Magnetorheological fluid dampers: a review of parametric modelling. *Smart Mater. Struct.* 20:023001. doi: 10.1088/0964-1726/20/2/023001

Wu, J., Jiang, X., Yao, J., Ki, H., and Li, Z. (2016). Design and modeling of a multi-pole and dual-gap magnetorheological brake with individual currents. *Adv. Mech. Eng.* 8, 1–15. doi: 10.1177/1687814016659182

Xu, Z., Kolev, S., and Todorov, E. (2014). "Design, optimization, calibration, and a case study of a 3D-printed, low-cost fingertip sensor for robotic manipulation," in *IEEE International Conference on Robotics and Automation (ICRA)* (Hong Kong).

Ziegler, J. G., and Nichols, N. B. (1942). Optimum settings for automatic controller. *Tran. ASME* 64, 759–768

Conflict of Interest Statement: The authors declare that the research was conducted in the absence of any commercial or financial relationships that could be construed as a potential conflict of interest.

frontiers in Materials

ORIGINAL RESEARCH
published: 19 February 2019
doi: 10.3389/fmats.2019.00017

Principle Study of a Semi-active Inerter Featuring Magnetorheological Effect

Wei-Min Zhong, Xian-Xu Bai, Chao Tang and An-Ding Zhu*

Laboratory for Adaptive Structures and Intelligent Systems (LASIS), Department of Vehicle Engineering, Hefei University of Technology, Hefei, China

Inerters are two-terminal mass elements in which the forces applied at the terminals are proportional to relative acceleration between the nodes. The volume and weight of inerters are much smaller than those of any conventional mass element for the same force, which is beneficial for engineering applications. The inerter in mechanical systems corresponds completely to the capacitor in electrical systems, which makes it more convenient to do related investigations based on mechanical-electrical analogies. A semi-active inerter (SAI) featuring a magnetorheological (MR) effect with tunable inertance is proposed, designed, and investigated to enhance the performance of the passive inerters. The proposed SAI consists of a flywheel, a flywheel housing, a ball screw, a connection sleeve, bearings, upper and lower covers, excitation coils, and MR fluid. MR fluid fulfilled in the flywheel housing of the SAI is energized by the excitation coils with applied current, and correspondingly the mechanical characteristics of the SAI are tunable via the applied current. The mathematical model and the mechanical performance of the SAI are established and tested, respectively. The nonlinearity of the experimental results is analyzed and the non-linear model of the SAI is further established. The preliminary principle verification of the continuous adjustment of the equivalent inertance of the SAI is conducted using the non-linear model. Moreover, a compensator is proposed to address the problem of the phase difference between the controllable force and the real output force of the SAI, and continuous inertance adjustment of the SAI with a compensator is realized.

Keywords: semi-active inerter, magnetorheological (MR) effect, magnetorheological (MR) fluids, continuously tunable inertance, nonlinearity

OPEN ACCESS

Edited by:
Seung-Bok Choi,
Inha University, South Korea

Reviewed by:
Xiaomin Dong,
Chongqing University, China
Xufeng Dong,
Dalian University of Technology (DUT), China
JinHyeong Yoo,
Naval Surface Warfare Center Carderock Division, United States

****Correspondence:***
Xian-Xu Bai
bai@hfut.edu.cn;
www.lasiser.com

Specialty section:
This article was submitted to Smart Materials, a section of the journal Frontiers in Materials

Received: *30 October 2018*
Accepted: *28 January 2019*
Published: *19 February 2019*

Citation:
Zhong W-M, Bai X-X, Tang C and Zhu A-D (2019) Principle Study of a Semi-active Inerter Featuring Magnetorheological Effect. Front. Mater. 6:17. doi: 10.3389/fmats.2019.00017

INTRODUCTION

In Smith (2002) introduced the concept of the inerter based on the mechanical-electrical analogy. A new inertial element in mechanical systems completely corresponding to the capacitor in electrical systems has been proposed since then. The generated forces of the conventional inertial element (i.e., the mass element) are relative to the absolute acceleration, which means that it corresponds only to the capacitor grounded in the circuit. Therefore, the degree of freedom of design of mechanical network and further vibration isolation performance are limited. The two terminals of the new inertial element (i.e., the inerter) move freely, and the forces applied at its two terminals are proportional to the relative acceleration between them. In other words, there is no "grounded"

restriction. Inerters with a small weight can be used to simulate an extremely large "virtual mass." Relative to the conventional mass element, smaller volume and weight make the inerter easier to be used in engineering applications (Smith, 2002). Inerters will not only be used to possibly improve the performance of vibration control systems of the mechanical network, they will also provide a new idea for analysis and design of the mechanical system via applying the network synthesis theory in the electrical systems.

At present, four inerter types can be found: rack pinion type (Smith, 2002), ball screw type (Smith, 2008), hydraulic motor type (Wang et al., 2011), and fluid type (Swift et al., 2013). In 2005, an inerter was first applied on an F1 racing car, and the handling and tire grip performance were much improved (Chen et al., 2009). In 2006, a steering compensation device with an inerter was applied on a high-performance motorcycle (Papageorgiou et al., 2007). The application research of inerters also involves the train suspensions (Wang et al., 2009), vehicle suspensions (Shen et al., 2016), and civil structures (Giaralis and Peteini, 2017).

The inertance of the conventional inerter is not tunable and the bandwidth of vibration suppression of the conventional inerter-based system is narrow in turn, which would be a restriction for inerter applications. Hu et al. (2017) proposed a mechanical semi-active inerter that adjusts the inertia of the flywheel by adjusting the position of the mass. Yu (2015) proposed a hydraulic semi-active inerter with hierarchically adjustable inertance by controlling the hydraulic valve. Zhang et al. (2018) simulated and analyzed a modified skyhook control for 1/4 vehicle suspension using a hydraulic continuously adjustable inerter. The new suspension shows an over 28% improvement in ride comfort compared to the conventional one. Although the proposed mechanical semi-active inerters will provide (hierarchically) controllable inertance, the response time of the inerter is too long, or the continuously adjustable inertance cannot be achieved. In order to realize a semi-active inerter with properties of simple configurations, fast response, and continuously adjustable inertance, Bai et al. (2018) and Tipuric et al. (2018) introduced the rapid and continuously controllable MR effect of the smart material—MR fluid (Tang et al., 2000; Chen et al., 2016, 2017, 2018) for adjusting the inertance of inerter. Bai et al. (2018) extended a ball screw-type inerter concept using MR fluid, but they have not yet demonstrated its feasibility. Tipuric et al. (2018) studied the feasibility of a semi-active inerter (SAI) but no experimentally verified prototype could be referred. Inspired by the concept study of Bai et al. and Tipuric et al. this paper proposes a structural principle of a SAI. The proposed SAI consists of a flywheel, a flywheel housing, a ball screw, a connection sleeve, bearings, upper, and lower covers, excitation coils and MR fluid. The MR fluid working in the pure shear mode is fulfilled in the flywheel housing, and the output force of the inerter is tuned by adjusting the applied current in the excitation coils, so that the adjustment of the inertance can be realized. The mathematical model of the SAI is established and the prototype is manufactured and tested. The concept of a compensator is further proposed to realize the continuous adjustment of the inertance of the SAI, and the corresponding analysis is conducted.

THE STRUCTURAL PRINCIPLE OF THE SAI

Figure 1 presents the structural principle of the SAI. As shown in **Figure 1**, the proposed SAI is composed of a flywheel, a flywheel housing, a ball screw, a connection sleeve, bearings, upper and lower covers, excitation coils, and MR fluid. As indicated by the arrows in **Figure 1**, according to the mechanical principle of the ball screw, the generated torque of the nut on the screw is translated to the linear force at the ends of the SAI. Thence, the output force of the SAI depends on the generated torque of the nut. The contributing factors of the generated torque include the moment of inertia of the flywheel and the viscosity of the MR fluid. An annular gap fulfilled with MR fluid is formed between the flywheel and the flywheel housing. The viscosity of the MR fluid in the annular gap is controlled by the electromagnetic field to realize the controllable force of the SAI. That is to say, the adjustment of the inertance would be achieved by tuning the applied current in the excitation coils, as shown in **Figure 1**. Specifically, the desired inertance will be achieved as long as the appropriate excitation current is applied to the excitation coils according to the relative acceleration through the two ends of the SAI. The advantage of using the ball screw mechanism to realize the SAI is that the structure is simple and the backlash can be eliminated by preloading.

MATHEMATICAL MODEL OF THE SAI

Mechanical Model

Figures 2A,B are the ideal models for the conventional inerter and the SAI, respectively. The inertance and the output force of the conventional ball screw type inerter can be expressed as:

$$b = J\left(\frac{2\pi}{p}\right)^2 \tag{1}$$

$$F_b = J\left(\frac{2\pi}{p}\right)^2(\ddot{x}_1 - \ddot{x}_2) \tag{2}$$

where b is the inertance of the inerter; F_b is the output force of the conventional inerter; J is the moment of inertia of the flywheel; p is the lead of the screw shaft of the ball screw; and x_1 and x_2 are the displacements at the two ends of the inerter.

According to equations (1) and (2), the ideal model of the conventional ball screw-type inerter is only related to the characteristics of the flywheel and the ball screw. The output force of the proposed SAI is dependent on the controllable force due to the viscosity change of the MR fluid. It can be expressed as:

$$F = F_b + F_{MR} \tag{3}$$

where F is the output force of the SAI; F_{MR} is the controllable force due to the viscosity change of the MR fluid.

F_{MR} is expressed as:

$$F_{MR} = \left(\frac{2\pi}{p}\right)(T_{vis} + T_{MR}) \tag{4}$$

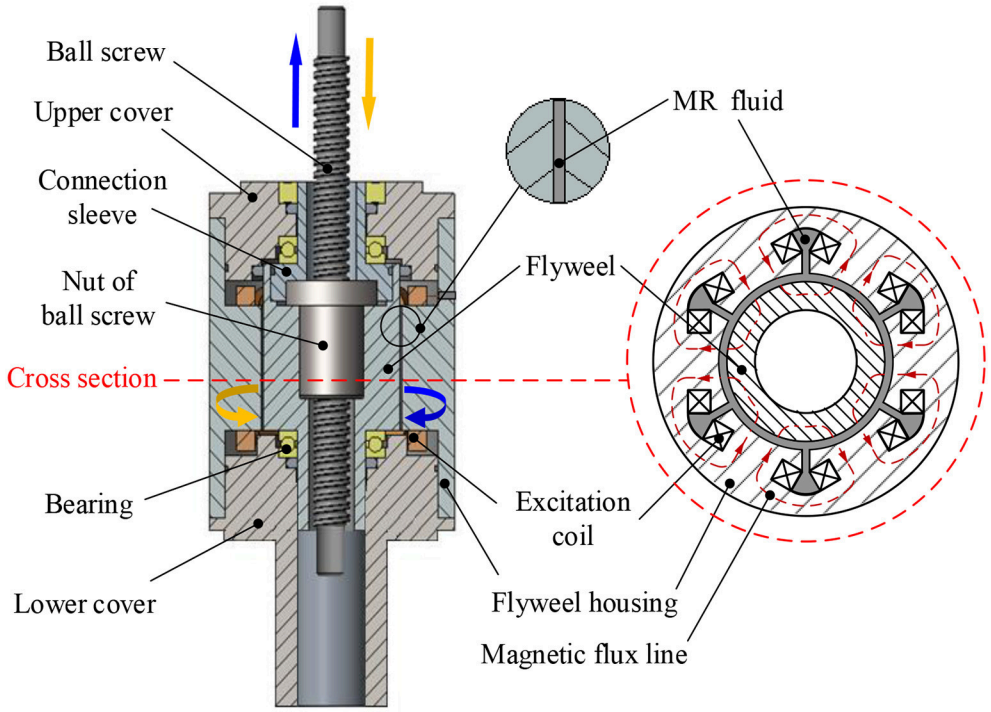

FIGURE 1 | Structural principle of the SAI.

where T_{vis} is the viscous torque produced by the MR fluid in field-off state (i.e., no applied current in the excitation coils) and T_{MR} is the field-dependent torque. T_{vis} and T_{MR} are respectively given by:

$$T_{vis} = \frac{4\pi^2 L_d \eta R_1^3 n_d}{s_d} \tag{5a}$$

$$T_{MR} = \frac{\pi \left(R_1^2 + R_2^2\right) L_d \tau_y \xi \delta}{2} \tag{5b}$$

where η is the viscosity of the MR fluid in field-off state; τ_y is the shear yield stress of the MR fluid; R_1 is the outer radius of the flywheel; R_2 is the inner radius of the flywheel housing; n_d is the rotational speed of the flywheel; s_d is the width of the annular gap; L_d is the axial length of the flywheel; δ is the correction coefficient with consideration of the influence of the magnetic leakage and ξ is the coefficient of the effective area (i.e., the ratio of the effective area to the ideal area) (Bai et al., 2018).

Equivalent Inertance

The inertance is defined by the ratio of the output force of the inerter to the relative acceleration between its two ends. That is, the corresponding inertance can be obtained by the relationship between the output force and the relative acceleration of the inerter. The output force of the proposed SAI is controllable and related to the applied current. When under a certain relative acceleration, the desired inertance can be achieved by adjusting the applied current. The inertance obtained by adjusting the applied current is defined as the equivalent inertance b' in this study.

Practically, the movement of the inerter should overcome a certain amount of inherent friction. Therefore, the output force F of the SAI in equation (3) and the equivalent inertance b' can be rewritten as:

$$\begin{cases} F = F_b + F_{MR} + f \\ b' = \frac{F}{\Delta a} \end{cases} \tag{6}$$

where f is the inherent friction force of the SAI and Δa is the relative acceleration at the two ends of the SAI.

RESULTS, ANALYSES AND INSIGHTS

Controllable Force Performance of the SAI

The prototype of the SAI is fabricated to verify the objective mechanical properties. As shown in **Figure 3**, an experimental setup based on the servo hydraulic test equipment (Type: LFH-LFV3068, SAGINOMIYA Inc.) is established to test the mechanical properties of the SAI.

Figures 4A,B show the comparisons between the theoretical and the experimental results of the mechanical response of the SAI, when a 0.5 A excitation current and sinusoidal displacement excitations with a frequency of 0.25 Hz and the excitation amplitudes of 10 mm and 20 mm are applied, respectively. As shown in **Figure 4A**, the theoretical value of the output force of the SAI is larger than the experimental results. When the

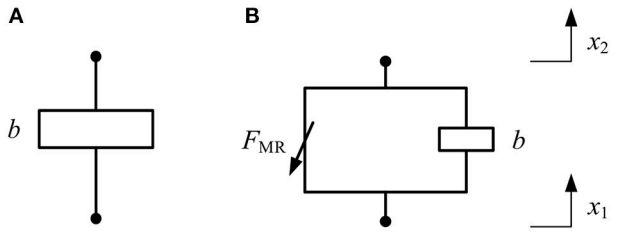

FIGURE 2 | Ideal model: **(A)** the conventional inerter and **(B)** the SAI.

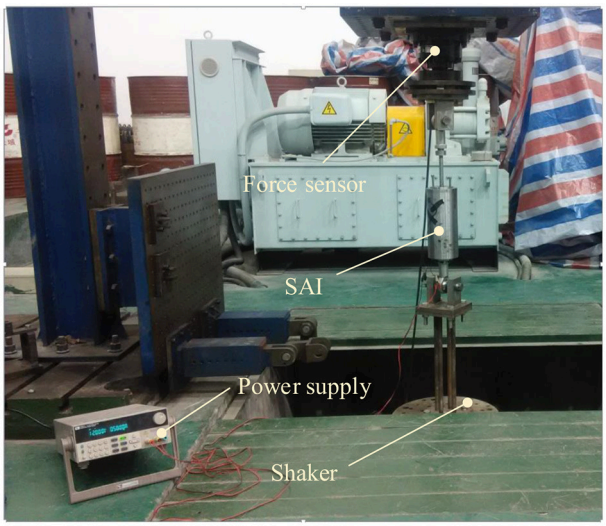

FIGURE 3 | Experimental setup for the SAI.

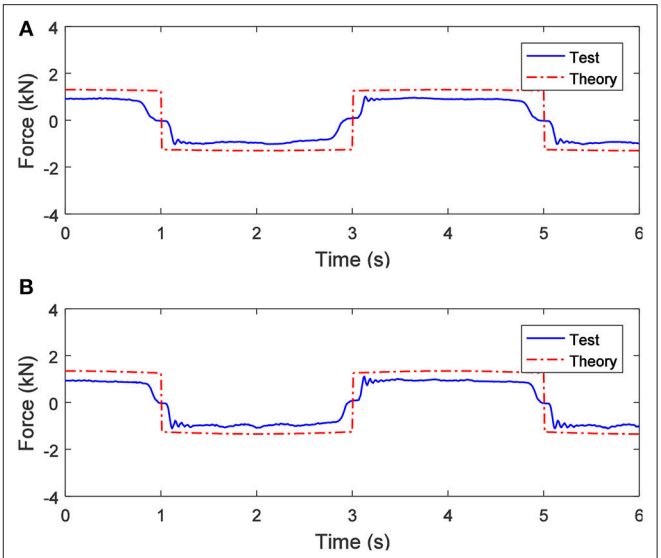

FIGURE 4 | When the applied current is 0.5 A, the output force of the SAI under sinusoidal displacement excitations with a frequency of 0.25 Hz and different amplitudes: **(A)** 10 mm and **(B)** 20 mm.

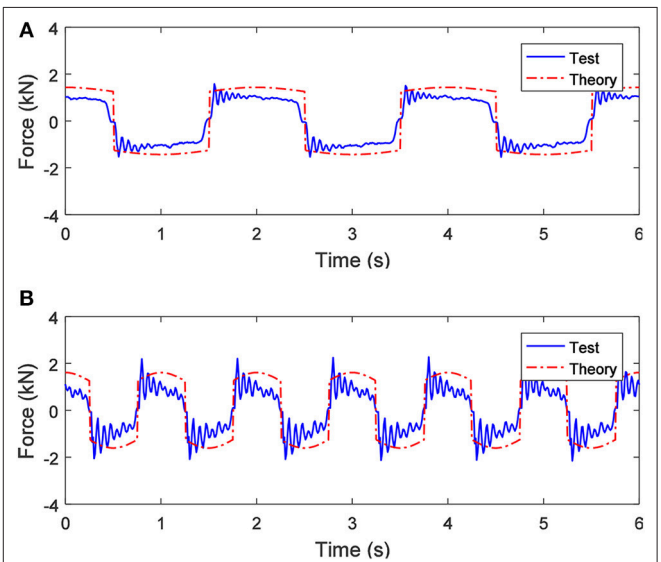

FIGURE 5 | When the applied current is 0.5 A, the output force of the SAI under sinusoidal displacement excitations with an amplitude of 20 mm and different frequencies: **(A)** 0.5 Hz and **(B)** 1.0 Hz.

direction of the force changes, the experimental result presents a certain hysteresis and slight fluctuations. The generated hysteresis is due to the MR effect and the gap between the mechanical structures, including the gap between the screw and the nut and the gap between the SAI and the mounting fixture. The reason for the slight fluctuations is the elastic effect of the ball screw itself. Comparing **Figures 4A,B**, when the amplitudes of the displacement excitations are different, the output forces of the SAI are substantially the same, indicating that the amplitude of the displacement excitation exerts little influence on the output force of the SAI.

Figures 5A,B show the comparisons between the theoretical and the experimental results of the mechanical response of the SAI, when a 0.5 A current and sinusoidal displacement excitations with an amplitude of 20 mm and the different excitation frequencies of 0.5 Hz and 1.0 Hz are applied, respectively. As shown in **Figure 5A**, the theoretical value of the output force of the SAI is larger than the experimental value, but the peak experimental value is slightly larger than the theoretical one due to the elastic effect of the ball screw. Comparing **Figures 5A,B**, when the frequency of the displacement excitation is different, the output force of the SAI is almost constant, which indicates that the frequency of the displacement excitation has little effect on the output force of the SAI. However, the fluctuation phenomenon becomes more apparent as the frequency of the displacement excitation increases.

Figures 6A,B show the comparisons between the theoretical and the experimental results of the mechanical response of the SAI, when 0 A and 1.0 A currents and a sinusoidal displacement excitation with a frequency of 1.0 Hz and an amplitude of 20 mm are applied, respectively. As shown in **Figure 6A**, the theoretical value of the output force is basically the same as the change trend

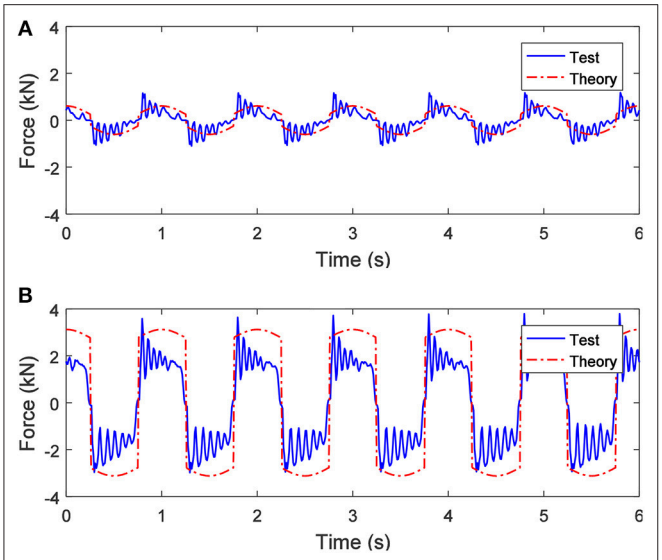

FIGURE 6 | When the applied current is different, the output force of the SAI under a sinusoidal displacement excitation with a frequency of 1.0 Hz and an amplitude of 20 mm: **(A)** 0 A and **(B)** 1.0 A.

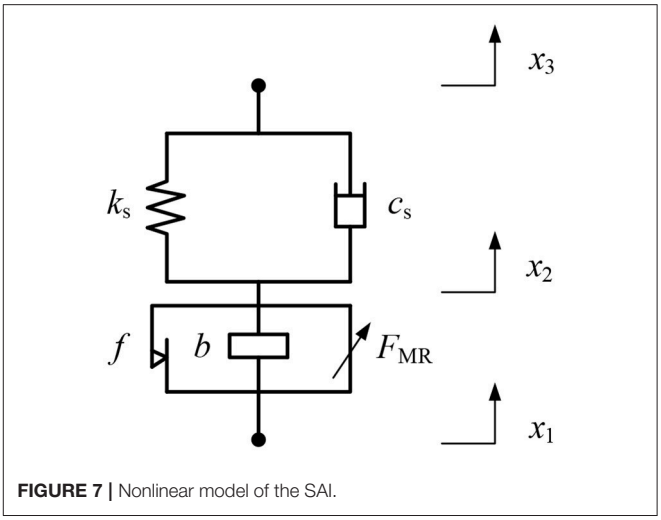

FIGURE 7 | Nonlinear model of the SAI.

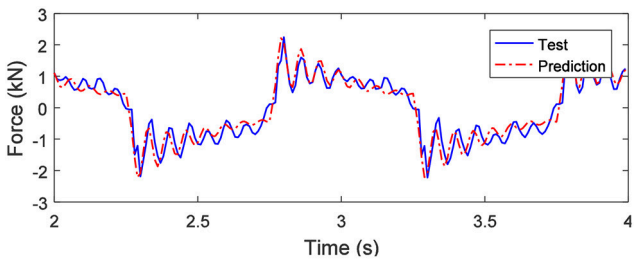

FIGURE 8 | Comparison between the experimental and predicted results when under a sinusoidal displacement excitation with an amplitude of 20 mm and a frequency of 1.0 Hz and a 0.5 A applied current.

of the experimental result, but the fluctuation of the experimental result is obvious and covers almost the entire cycle of the motion. Comparing **Figures 6A,B**, the output force of the SAI is obviously affected by the applied current and increases with the increase of the applied current. Besides, the larger the applied current is, the larger the difference between the theoretical and the experimental results.

Based on the comparison of **Figures 4–6**, when under different amplitudes and frequencies of sinusoidal displacement excitations (i.e., the different excitation speeds), the maximal output force of the SAI is nearly unchanged, which is because of the pure shear working mode of the MR fluid in the SAI.

Nonlinear Realization of the SAI

As shown in **Figures 4–6**, as the frequency of the sinusoidal displacement excitation increases, the fluctuation of the experimental result of the SAI increases, and the difference between the experimental and the theoretical values expands. Therefore, it can be deduced that the mechanical performance of the SAI is affected by nonlinear factors. The nonlinear factors affecting the output force of the SAI are mainly derived from the gap and the elastic effect of the ball screw and the inherent friction force, including the friction between the screw and the nut and the friction inside the bearing. The gap of the ball screw could be eliminated by preloading, so the effect of the gap will not be taken into account when establishing the nonlinear model. **Figure 7** shows the nonlinear model of the SAI containing inherent friction force and the elastic effects of the ball screw (Wang and Su, 2008).

In the experimental tests, one end of the SAI is fixed, as shown in **Figure 3**, so $x_3 = 0$. According to **Figure 7**, the dynamic model of the SAI with nonlinearities is expressed by:

$$b\left(\ddot{x}_1 - \ddot{x}_2\right) + \left(f + F_{\mathrm{MR}}\right) \cdot \mathrm{sign}\left(\dot{x}_1 - \dot{x}_2\right) = k_s x_2 + c_s \dot{x}_2 \qquad (7)$$

where k_s and c_s are the stiffness and damping of the ball screw, respectively.

The minimal inertance of the proposed SAI is set to 600 kg (i.e., the inherent inertance is 600 kg when the applied current is 0 A). When the SAI is excited by sinusoidal displacement excitations with low frequencies and no current is applied, the output force is dominated by the inherent friction force, and the inertia of the flywheel can be ignored. In this case, the output force of the SAI can be approximately regarded as the inherent friction force. In this study, a sinusoidal displacement excitation with a frequency of 0.1 Hz and an amplitude of 10 mm is applied to the SAI in field-off state and the inherent friction force f of the SAI is about 310 N.

Parameter identification of the nonlinear model of the SAI is conducted using experimental data under different operating conditions. The parameters k_s, c_s and F_{MR} are selected to be identified using the following criterion function with the least square method:

$$\min_{k_s,\, c_s,\, F_{\mathrm{MR}}} \left[f_{\mathrm{th}}\left(k_s, c_s, F_{\mathrm{MR}}\right) - f_{\mathrm{exp}}\right]^2 \qquad (8)$$

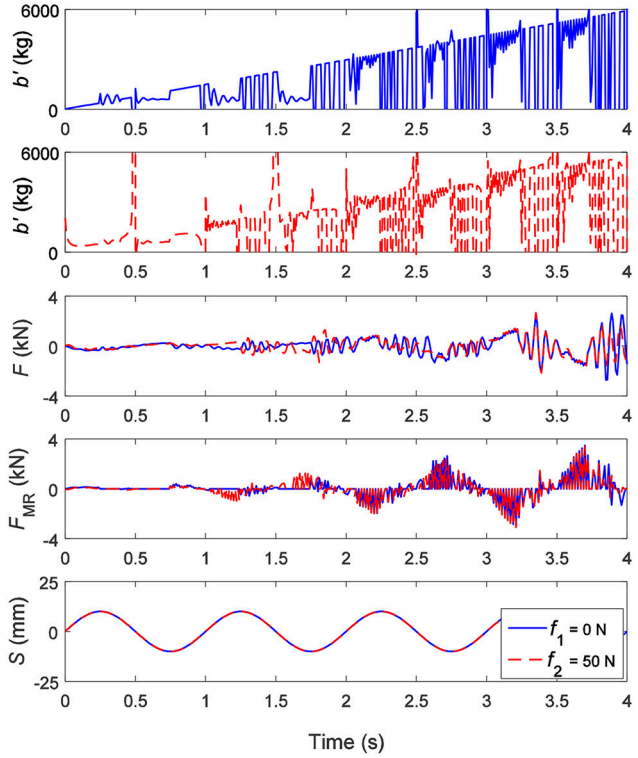

FIGURE 9 | The equivalent inertance b', the output force F, the controllable force F_{MR} under a sinusoidal displacement excitation S with an amplitude of 20 mm and a frequency of 1.0 Hz when the expected inertance is from 0 kg to 6,000 kg.

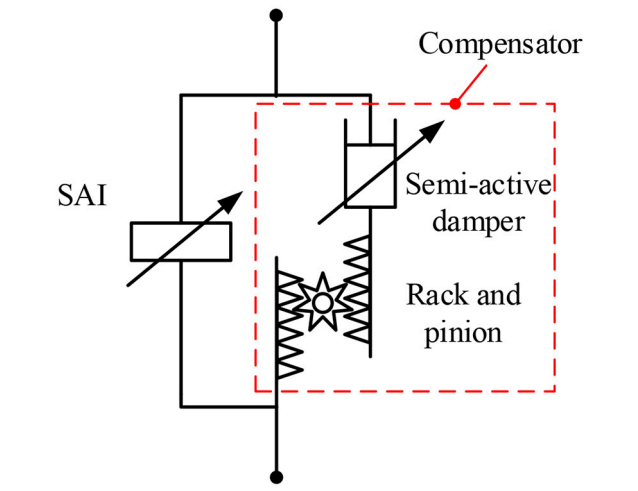

FIGURE 10 | Schematic of the SAI with a compensator.

where f_{th} is the predicted value of the output force calculated by the nonlinear model of the SAI and f_{exp} is the experimental value of the output force of the SAI.

The stiffness k_s of the ball screw is 5,500 kN/m and the damping c_s is 7,000 Ns/m according to the parameter identification. The controllable force F_{MR} changes with the applied current, which is consistent with the actual situation. **Figure 8** shows the comparison of the predicted value with the experimental value of the output force under the sinusoidal displacement excitation with an amplitude of 20 mm and a frequency of 1.0 Hz when the applied current is 0.5 A. It can be seen from **Figure 8** that the predicted value of the output force agrees well with the experimental value. The effectiveness of the established nonlinear model of the SAI is therefore verified.

The established nonlinear model of the SAI can be used to achieve adjustment of the inertance. The SAI is separately subjected to an adjustment simulation of the 0–6,000 kg inertance under the condition of the lower and upper bound force (about 0–4 kN according to the test results) of the SAI. **Figure 9** shows the simulation results under a sinusoidal displacement excitation with an amplitude of 20 mm and a frequency of 1.0 Hz when the expected inertance is from 0 to 6,000 kg. Since the friction factor must be considered, the inherent friction force is set to 0 N and 50 N, respectively. As shown in **Figure 9**, when the inherent friction force is 0 N, the adjustment of the equivalent inertance exhibits a segmented characteristic due to the existence of the phase difference between the velocity and the acceleration. The continuous adjustment of the equivalent inertance can be achieved when the controllable force works. When the controllable force fails, the equivalent inertance oscillates. In addition, both the output force and the controllable force of the SAI fluctuate at the corresponding positions, and the fluctuations are more intense as the equivalent inertance increases. When the friction force is 50 N, the fluctuation of the equivalent inertance is more obvious than that of the friction force of 0 N, but the influence on the controllable force and the output force is not very large.

Continuous Inertance Adjustment of the SAI

The output force (inertance) of the SAI is related to the acceleration, while the controllable force is related to the velocity (according to Equations 4, 5). There is a 90° phase difference between the output force and the controllable force of the SAI, which may result in failure to achieve the desired inertance when adjusting the controllable force. However, the continuous adjustment of the equivalent inertance would be achieved if a force compensator (i.e., phase adjustment mechanism) could be provided.

The SAI with a compensator is proposed and shown in **Figure 10**. As shown in **Figure 10**, the compensator is composed of a semi-active damper in series with the rack pinion mechanism and in parallel with the SAI. Taking the case under sinusoidal displacement excitation as an example, the adjustment principle of the equivalent inertance is shown in **Figure 11**. It can be seen from the areas ① and ② in **Figure 11** that the output force of the SAI cannot be continuously adjusted due to the phase difference between the relative velocity and the relative acceleration. The area ③ shows that the force generated by the compensator is always opposite to the direction of the controllable force, so that the controllable force that could not be achieved is compensated. As shown in the area ④, the output force of the SAI can be

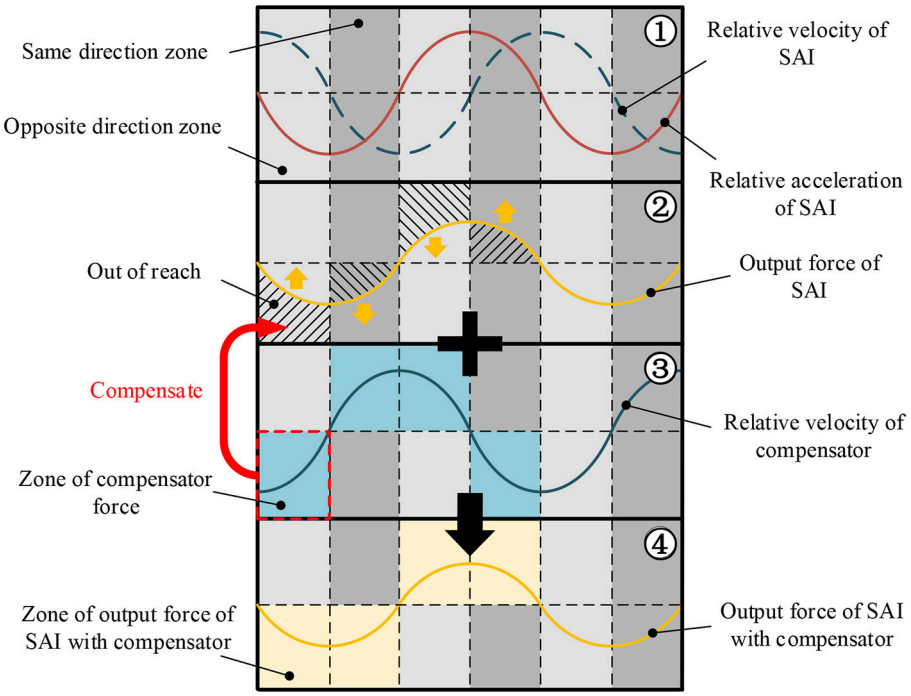

FIGURE 11 | Adjustment principle of the equivalent inertance.

continuously adjusted to achieve continuous adjustment of the equivalent inertance.

The output force of the SAI with a compensator can be expressed as:

$$F = F_b + F_{MR} + f - F_{com} \tag{9}$$

where F_{com} is the force generated by the compensator.

Figure 12 presents the simulation results under a sinusoidal displacement excitation with an amplitude of 20 mm and a frequency of 1.0 Hz when the expected inertance of the SAI with a compensator is from 0 to 6,000 kg. Since the friction could be offset by the compensator, the contrast under different inherent friction forces is not considered. It can be seen from **Figure 12** that the continuous and steady adjustment of 0–6,000 kg of the equivalent inertance can be achieved. The controllable force, the force generated by the compensator and the output force produce fluctuations, and the fluctuations are more intense as the equivalent inertance increases. This is similar to the case whereby there is no compensator, as with **Figure 9**.

An Application Case

The equivalent inertance of the ball screw-type SAI, as shown in **Figure 9**, is segmented, and the inherent friction of the ball screw set will influence the controllability. To study the influence of the segmented equivalent inertance of the SAI and the inherent friction force on the vibration control, a single-degree-of-freedom vibration control system as shown in **Figure 13** is established. The system model is given by:

$$m\ddot{z}_2 + b'(\ddot{z}_2 - \ddot{z}_1) + c(\dot{z}_2 - \dot{z}_1) + k(z_2 - z_1) = 0 \tag{10}$$

where z_1 is the input displacement of the payload m; z_2 is the displacement of the payload m; k is the stiffness of the spring and c is the damping of the passive damper.

Figure 14 shows the acceleration response of the system under a sinusoidal displacement excitation with an amplitude of 50 mm and a frequency of 1.0 Hz (the resonant frequency of the passive spring-mass-damper system). The payload m, the stiffness k, and the damping c are 557 kg, 22 kN/m and 1,500 Ns/m, respectively. The inherent friction force is set as: $f_1 = 310$ N, $f_2 = 110$ N and $f_3 = 10$ N when the SAI has no compensator. As shown in **Figure 14**, the single-degree-of-freedom vibration system with the SAI has an over 4 times smaller acceleration amplitude than the conventional vibration system (i.e., the spring-mass-damper system). When the SAI is not connected to the compensator, the acceleration fluctuates due to the inherent friction force. The greater the inherent friction force, the more serious the fluctuation of the acceleration will be. However, the acceleration is still much smaller than the conventional vibration system. The acceleration of the payload of the system when the friction is 10 N basically agrees with the system with a compensator. In other words, the segmented equivalent inertance of the SAI will not influence the control performance of the SAI-based vibration control very much. This is similar to the analysis in reference (Wang and Su, 2008); the friction force of the inerter does have an adverse effect on the vibration control performance, but when

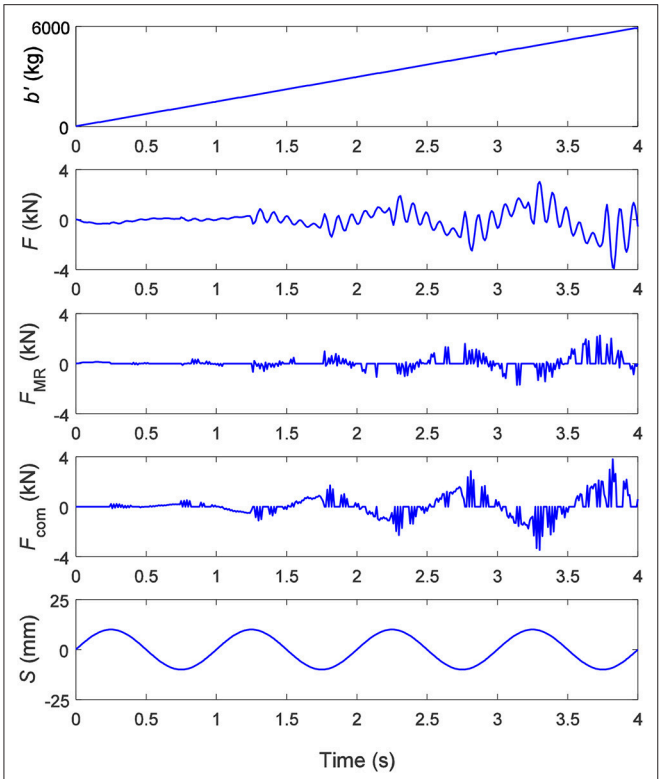

FIGURE 12 | The equivalent inertance b', the output force F, the controllable force F_{MR} and the generated force of the compensator F_{com} under a sinusoidal displacement excitation S with an amplitude of 20 mm and a frequency of 1.0 Hz when the expected inertance of the SAI with a compensator is from 0 kg to 6,000 kg.

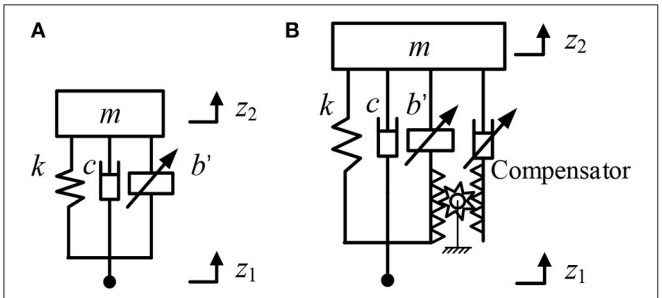

FIGURE 13 | A single-degree-of-freedom vibration control system with a SAI: **(A)** with no compensator and **(B)** with a compensator.

the stiffness of the suspension is great, the overall performance of the system using the inerter with friction force is still superior to the conventional ones.

CONCLUSIONS

In order to enhance the performance of the conventional passive inerter, the structural principle of an SAI was proposed and studied in this paper. It is composed of a flywheel, a flywheel housing, a ball screw, a connection sleeve, bearings, upper, and lower covers, excitation coils, and MR fluid. The proposed SAI

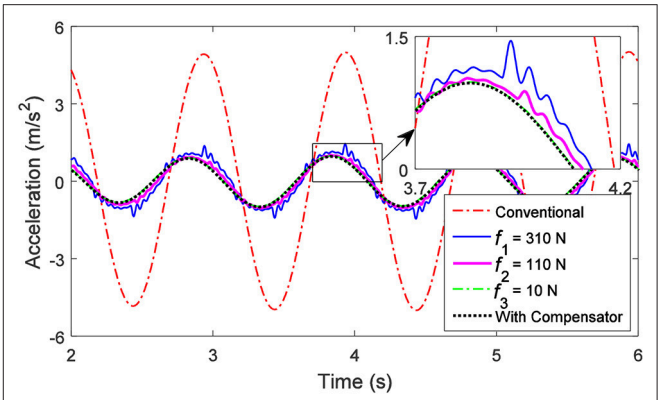

FIGURE 14 | Acceleration response of the single-degree-of-freedom vibration system under a sinusoidal displacement excitation with an amplitude of 50 mm and a frequency of 1.0 Hz.

achieves adjustment of the inertance by adjusting the applied current in the excitation coils and has the advantages of a simple structure and wide adjustable range. The mathematical model of the SAI was established and the mechanical properties of the SAI were tested based on the experimental setup. The test results indicate that the nonlinear factors of the ball screw cannot be ignored for mechanical performance description of the SAI. A nonlinear model of the SAI was established and the parameters were identified by the least squares method. The continuous adjustment of the equivalent inertance was realized by integrating a compensator to overcome the phase difference between the controllable force and the output force. Vibration attenuation performances of a single-degree-of-freedom vibration system based on the SAI with and without a compensator, as a very preliminary application case, are analyzed and compared. Based on the research of this paper, the conclusions are summarized as follows.

(i) The established nonlinear model of the SAI can effectively describe and predict the mechanical properties of the SAI.

(ii) The problem of the phase difference between the controllable force and the output force can be solved via a compensator. The continuous adjustment of an equivalent inertance with a range of 0–6000 kg could be achieved by adjusting the applied current. The proposed and employed compensator presents a helpful approach for the phase control of force in mechanical systems.

(iii) For a single-degree-of-freedom vibration system, the SAI with no compensator still provides a better vibration isolation performance than the conventional system, and the smaller the inherent friction force is, the better the performance will be.

AUTHOR CONTRIBUTIONS

W-MZ carried out the modeling, computation and experimental work, and helped draft the manuscript. X-XB conceived the

conception, investigated the technical background, designed, and coordinated the study, and drafted and revised the manuscript. CT helped do modeling and experimental work and draft the manuscript. A-DZ helped draft and revise the manuscript.

ACKNOWLEDGMENTS

The authors wish to acknowledge the Key Research and Development Projects of Anhui Province (Grant No. 1704E1002211) for her support of this research.

REFERENCES

Bai, X. X., Zhong, W. M., Zou, Q., Zhu, A. D., and Sun, J. (2018). Principle, design and validation of a power-generated magnetorheological energy absorber with velocity self-sensing capability. *Smart Mater. Struct*. 27:075041. doi: 10.1088/1361-665X/aac7ef

Chen, M. Z. Q., Papageorgiou, C., Scheibe, F., Wang, F. C., and Smith, M. C. (2009). The missing mechanical circuit element. *IEEE Circuits Syst. Magazine* 9:1. doi: 10.1109/MCAS.2008.931738

Chen, P., Bai, X. X., and Qian, L. J. (2016). Magnetorheological fluid behavior in high-frequency oscillatory squeeze mode: experimental tests and modelling. *J. Appl. Phys*. 119:105101. doi: 10.1063/1.4943168

Chen, P., Bai, X. X., Qian, L. J., and Choi, S. B. (2018). An approach for hysteresis modeling based on shape function and memory mechanism. *IEEE/ASME Transact. Mechatro.* 23, 1270–1278. doi: 10.1109/TMECH.2018.2833459

Chen, P., Qian, L. J., Bai, X. X., and Choi, S. B. (2017). Velocity-dependent characteristics of magnetorheological fluids in squeeze mode considering the hydrodynamic and the magnetic field interactions. *J. Rheol*. 61, 455–465. doi: 10.1122/1.4978594

Giaralis, A., and Peteini, F. (2017). Wind-induced vibration mitigation in tall buildings using the tuned mass-damper-inerter. *J. Struct. Eng.* 143:04017127. doi: 10.1061/(ASCE)ST.1943-541X.0001863

Hu, Y., Chen, M. Z. Q., Xu, S., and Liu, Y. (2017). Semiactive inerter and its application in adaptive tuned vibration absorbers. *IEEE Transact. Control Syst. Technol.* 25, 294–300. doi: 10.1109/TCST.2016.2552460

Papageorgiou, C., Lockwood, O. G., Houghton, N. E., and Smith, M. C. (2007). "Experimental testing and modelling of a passive mechanical steering compensator for high-performance motorcycles," in *Control Conference (ECC)* (European, IEEE), 3592–3599. doi: 10.23919/ECC.2007.7068739

Shen, Y., Chen, L., Yang, X., Shi, D., and Yang, J. (2016). Improved design of dynamic vibration absorber by using the inerter and its application in vehicle suspension. *J. Sound Vibrat*. 361, 148–158. doi: 10.1016/j.jsv.2015.06.045

Smith, M. C. (2002). Synthesis of mechanical networks: the inerter. *IEEE Transact. Automat. Control* 47, 1648–1662. doi: 10.1109/TAC.2002.803532

Smith, M. C. (2008). *Force-Controlling Mechanical Device*. U.S. Patent 7, 316–303. US 2005/0034943 A1.

Swift, S. J., Smith, M. C., Glover, A. R., Papageorgiou, C., Gartner, B., et al. (2013). Design and modelling of a fluid inerter. *Int. J. Control* 86, 2035–2051. doi: 10.1080/00207179.2013.842263

Tang, X., Zhang, X., Tao, R., and Rong, Y. (2000). Structure-enhanced yield stress of magnetorheological fluids. *J. Appl. Phys*. 87, 2634–2638. doi: 10.1063/1.372229

Tipuric, M., Deastra, P., Wagg, D., and Sims, N. (2018). "Semi-active inerters using magnetorheological fluid: a feasibility study," in *Active and Passive Smart Structures and Integrated Systems, X. I. I.* (Denver, CO), 10595.

Wang, F. C., Hong, M. F., and Lin, T. C. (2011). Designing and testing a hydraulic inerter. Proceedings of the institution of mechanical engineers, Part, C. *J. Mech. Eng. Sci*. 225, 66–72. doi: 10.1243/09544062JMES2199

Wang, F. C., Liao, M. K., Liao, B. H., Su, W. J., and Chan, H. A. (2009). The performance improvements of train suspension systems with mechanical networks employing inerters. *Vehicle Syst. Dynam*. 47, 805–830. doi: 10.1080/00423110802385951

Wang, F. C., and Su, W. J. (2008). Impact of inerter nonlinearities on vehicle suspension control. *Vehicle Syst. Dynam*. 46, 575–595. doi: 10.1080/00423110701519031

Yu, P. (2015). *Study on Some Key Technologies of Suspension Changeable Inerter*. Master Thesis of Zhejiang University, Hangzhou, China.

Zhang, X. L., Zhang, T., Nie, J., and Chen, L. (2018). A semiactive skyhook-inertance control strategy based on continuously adjustable inerter. *Shock Vibrat.* 2018:6828621. doi: 10.1155/2018/6828621

Conflict of Interest Statement: The authors declare that the research was conducted in the absence of any commercial or financial relationships that could be construed as a potential conflict of interest.

frontiers in Materials

REVIEW
published: 19 February 2019
doi: 10.3389/fmats.2019.00019

Magnetorheological Fluid Based Devices Reported in 2013–2018: Mini-Review and Comment on Structural Configurations

Do Xuan Phu[1]* *and Seung-Bok Choi*[2]*

[1] MediRobotics Laboratory, Department of Mechatronics and Sensor Systems Technology, Vietnamese-German University, Ho Chi Minh City, Vietnam, [2] Smart Structures and Systems Laboratory, Department of Mechanical Engineering, Inha University, Incheon, South Korea

This paper presents a mini-review of magnetorheological (MRF) fluid-based devices (MRF devices in short) including the brake, clutch, damper, and the mount reported from 2013 to 2018. MRF devices are usually designed based on three operating modes of MRF: flow mode, shear mode and squeeze mode. Each mode has its own characteristics for the high performance of application systems. Therefore, numerous design configurations of MRF devices have been proposed by many researchers. In this article, among many different MRF devices such as MRF brake, clutch, damper and MRF mount proposed over the last 6 years are examined in the sense of their structural configuration and operating principles. Certain advantages and demerits of each MRF device are also discussed. In addition, some useful design guidelines of MRF devices, which are absolutely different from developed MRF devices so far, are provided to enhance design simplicity and control performance.

Keywords: magnetorheological fluid (MRF), MRF devices, design configuration, MRF mount, MRF brake, MRF clutch, MRF damper

OPEN ACCESS

Edited by:
Heung Soo Kim,
Dongguk University Seoul,
South Korea

Reviewed by:
Xianzhou Zhang,
G.H. Varley Pty Ltd, Australia
Yancheng Li,
University of Technology Sydney,
Australia
Seunghwa Yang,
Chung-Ang University, South Korea

***Correspondence:**
Do Xuan Phu
phu.dx@vgu.edu.vn
Seung-Bok Choi
seungbok@inha.ac.kr

Specialty section:
This article was submitted to Smart Materials, a section of the journal Frontiers in Materials

Received: *23 October 2018*
Accepted: *30 January 2019*
Published: *19 February 2019*

Citation:
Phu DX and Choi S-B (2019) Magnetorheological Fluid Based Devices Reported in 2013–2018: Mini-Review and Comment on Structural Configurations. Front. Mater. 6:19. doi: 10.3389/fmats.2019.00019

INTRODUCTION

Magnetorheological fluid (MRF) is known as an attractive smart material which can be widely utilized to develop devices in various industries including automotive engineering, aerospace engineering, the manufacturing industry and medical fields. Specific application devices are the damper (or shock absorber), brake, clutch, mount, the prosthetic leg, and lower-limb exoskeleton. The first device which was commercialized is the shock absorber for a vehicle suspension system which can adaptively control unwanted vibrations induced by road conditions. There are several reasons why MRF devices are attractive to many different researchers. Those include reversible property between liquid phase and solid phase, low power consumption (around 2–5 Watt for the vehicle damper), fast response time (<10 *ms*) and design simplicity with the magnetic core only. In terms of the rheological characteristics, the magnitude of the storage and loss modulus are controlled by the intensity of the magnetic field to be applied to the fluid domain. In addition, one unique merit of an MRF device, which does not exist in conventional devices such as servomotor and hydraulic devices, is the fail-safe function. In other words, MRF devices can provide passive device performance, even when it fails during control action. This is possible since an MRF device has a carrier liquid which is equivalent to the viscous oil frequently used in passive devices. This unique feature is attractive for numerous application and systems utilizing MRF devices.

Among numerous MRF device-based mechanisms, in this review article MRF brake, clutch, damper, and MRF mount are examined in terms of their design configurations and operating principles. These MRF devices are chosen since they can apply to many different systems such as the vibration control of an automobile, vibration control of seismic, and several different rehabilitation prosthetics. An MRF brake and clutch can be applied to vehicles, automatic conveyer tables, vibration control cables, prosthetic legs, and rotation mechanisms such as a robot joint. An MRF damper can be applied to an automotive suspension system, the vibration control of seismic, the vibration control of a washing machine, the vibration control of flexible structures and the vibration control of mechanisms of the civil engineering field such as a vibration absorber of a very tall building or a long bridge. An MRF mount is very useful to control unwanted vibrations which occur in most dynamic systems in which an MRF damper cannot be installed due to the lack of space. For example, a mount for a vehicle engine, a wheel loader, a precision stage and a mount for a compact disk rom.

In this review article, newly developed MRF devices, in their third stage of practical application is examined by focusing on the design configuration and showing principal components. Some advantages and disadvantages of each MRF device are discussed in terms of design and control. Moreover, some drawbacks of sedimentation, leakage and durability of MRF filled in the devices are also reviewed. Prior to concluding the article, some advanced MRF devices, which can avoid existing impediments, are suggested by drawing a conceptual design configuration. This article will be very helpful to understand the specific design methods of major MRF devices and provide very useful guidelines for MRF devices which can be practically realized in the field.

TABLE 1 | Studies of MRF brake and MRF clutch in 2013–2018.

No.	Type of brake/clutch	References
1	Double-plate MRF clutch	Kavlicoglu et al., 2013
2	Linear MRF brake with multi-coil piston	Alkan et al., 2013
3	Concentric cylinder-brake	Rossa et al., 2014b
4	Disc-cylinder type MRF clutch	Dai et al., 2013
5	Two-layer multi-plate MRF clutch	Wang et al., 2013
6	Multi-gap MRF clutch	Bucchi et al., 2013
7	Multi-coil MRF brake	Shiao and Nguyen, 2013
8	Disc-type MRF brake with flexible envelope	Nguyen et al., 2014
9	Multi-layered MRF brake	Rossa et al., 2014a
10	Multi-pole MRF brake	Shiao et al., 2014
11	Multi-layered MRF brake	Rossa et al., 2014b
12	Multi-disc MRF brake	Bucchi et al., 2014
13	Outside coil MRF brake with flexible envelope	Nguyen et al., 2015
14	Multi-pole bilayer MRF brake	Shiao et al., 2016
15	Disc-type MRF brake	Wang et al., 2016
16	Multi-pole MRF brake	Wu et al., 2016
17	Disc-type MRF brake with adjustable gap	Song et al., 2017
18	Multi-gap MRF clutch	Rizzo, 2017
19	Multi-pole MRF brake	Yu et al., 2017
20	Helix MRF brake	Mars and Gurocak, 2017
21	Disc-type MRF brake and Cylinder-type MRF clutch	Cha et al., 2018

MRF BRAKE AND MRF CLUTCH

Design of an MRF brake/clutch uses two modes of MRF: flow mode and shear mode. If the core is rotated and the housing is fixed, the design is called an MRF brake, and inversely its name is n MRF clutch. The torque level of the brake and clutch is controlled by controlling the input current (or magnetic field intensity). Therefore, very accurate torque transmission and stopping can be achieved by a simple, but very effective MRF device. The MRF brake and clutch, developed during 2013–2018, is summarized in **Table 1**. In 2013, most design types of the MRF brake and clutch were classified by four configurations: multi-disc, multi-plate, multi-gap and multi-coil (pole). Basically, these design methods are easy to fabricate because it only includes the disc or the coil. In 2014, a different design for the MRF brake was presented (Nguyen et al., 2014) in which the housing structure was modified to optimize the magnetic line. This design methodology was breakthrough in the design of MRF devices in the sense of the minimization of housing material. In this design method, the torque level is similar to the conventional one, but the manufacturing cost is reduced substantially. In 2015, a new model of the MRF brake was proposed based on the changeable structure of the electric or/and magnetic coil (Nguyen et al., 2015). This was made possible by placing the electric coil at the outside of the housing. In 2016, a new combination of permanent magnetic and MRF for MRF brake design has been reported in Yu et al. (2017). It has been shown that the torque control performance of this design method is good, but the practical realization is difficult due to the large size of the permanent magnet and the housing. Moreover, the assembly and maintenance of each components is not easy. In 2017, a new design method for the MRF clutch was reported (Rizzo, 2017). In this design method, the permanent

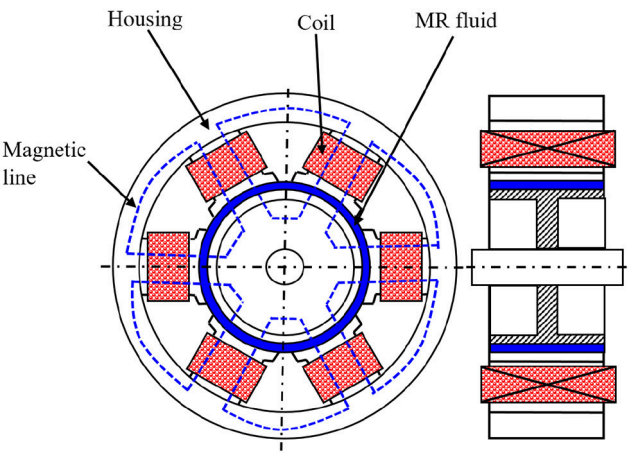

FIGURE 1 | Design of multi-coil MRF brake (Shiao and Nguyen, 2013).

magnet was used to control the magnetic field of the clutch. The magnitude of torque varied following the position of the magnet. In the off-state, the position of the magnet does not contact the MRF area using the spring. In the on-state, the position of the magnet is moved to the MRF area by the expansion of the spring. It is therefore efficient to control the rotational motion of the connected MRF devices. One unique feature of this design method is the increase of the torque level with the same magnetic field and also the prevention of the block-up phenomenon, in which the flow motion of the MRF does not occur. In 2018, no new design configuration of the MR brake and clutch has been proposed. However, the research work on the reduction of the saturation problem of the magnetic materials was actively undertaken.

In this review article, two specific design configurations of the MRF brake device are examined in more detail. **Figure 1** shows the design schematic of the MRF brake with multi-coils (Shiao and Nguyen, 2013). In this design, the multi-coil housing is used and the design concept was inspired from the configuration of the electric motor. The magnetic field in the coils control the state of the MRF from the liquid phase to solid phase, or vice versa, which is arranged in the central rod of the brake. In this brake design, the housing with the coils is always fixed. The advantages of the multi-coil brake include the increase of efficiency of the magnetic line and the separated control of every coil. However, this design may increase the manufacturing costs associated with its relatively large size. Moreover, the collision of magnetic lines among electrical coils may occur and making the torque level similar to the conventional disc type of the brake. **Figure 2** shows a type of MRF brake called a helix cylinder (Mars and Gurocak, 2017). The unique feature of this design is to shape the core of the MRF brake to the helix cylinder. By doing this, the volume of the MRF can be reduced, while also maintaining the high levels of the braking torque in the presence of a magnetic field. In fact, in this design method, the core plays an important role in the MRF brake. The air is used as an accumulator which prevents the shock vibration and supports the damping coefficient of the MRF device. This design configuration has a simple structure, but several problems need to be resolved. The first disadvantage of this design is the need for accurate manufacturing of the core part which subsequently increases the cost. Another demerit is that the flow motion of the MRF is not smooth, due to the shape of the helix gap. Moreover, high performance devices are required to maintain air pressure.

MRF DAMPER

When designing a damper, three modes of MRF is used such as flow, shear and squeeze modes. The specific design configurations of the MRF damper are summarized in **Table 2**. It can be seen from the table that the piston-type MRF damper has a structural design, in which the flow mode predominantly occurs to generate the field-dependent damping force. It can be noted here that the damping force subjected to the shear mode is smaller than that operated with the flow mode under the same design constraints. However, the MRF damper operated with the squeeze mode, can provide a larger damping force than when operated with the flow mode, due to the small stroke. The multi-coil type damper is also very effective in terms of the magnitude of the field-dependent damping force, since the magnetic coils can easily be optimized to have maximum magnetic field distribution. In 2014, three different features of the MRF damper were introduced. The first design configuration was proposed in McLaughlin et al. (2014) where the MRF valve, associated with the spiral core, to manage the flow of MRF was used. One of the merits of this structural configuration is to have a smooth flow motion of MRF in the gap since there is no obstruction in the flow path. The second type of MRF damper was fabricated on the basis of the squeeze mode (Yazid et al., 2014). One salient property of this type, is to have a high damping force compared with the type of the flow mode. However, the squeeze mode MRF damper type cannot be applied to dynamic systems, which have a large moving stroke due to the difficulty of the sealing. The third type of MRF damper was devised considering both the permanent magnetic and electrical coil (Sapinski, 2014). This type is a special device for energy harvesting purposes instead of vibration control. One drawback of this type is the design complexity, due to many parts of both the housing and the core. In 2015, a new damper using metal foams embedded MRF was introduced to save the volume of MRF (Liu et al., 2015). The design configuration is unique, but its performance is poor, due to the high friction between the core and the foam. In 2016, a new MRF damper consisting of a mechanical spring, in combination with the damper was

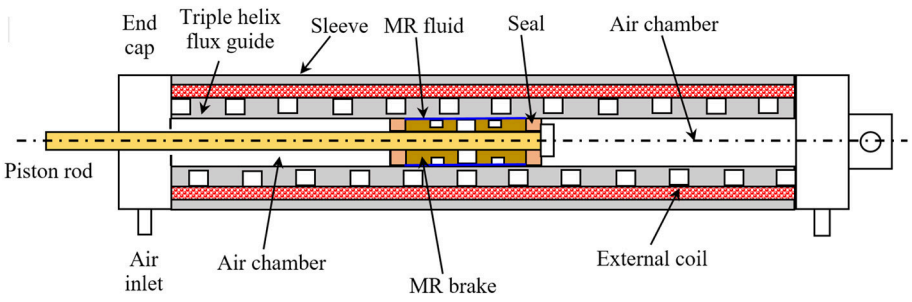

FIGURE 2 | MRF brake with helix housing design (Mars and Gurocak, 2017).

TABLE 2 | Studies of MRF damper in 2013-2018.

No.	Type of damper	References
1	Piston-type damper with single coil (flow mode)	Case et al., 2013
2	Piston-type with multi-coil (flow mode)	Bai et al., 2013
3	Piston-type with single coil (flow mode)	Goldasz and Sapinski, 2013
4	Piston-type with multi-coil (flow mode)	Ding et al., 2013
5	MRF valve with multi-coil (shear mode)	Zhou and Zhang, 2013
6	Piston-type damper with single coil (flow mode)	Hadadian et al., 2013
7	Spiral channel bypass valve (shear mode)	McLaughlin et al., 2014
8	Piston-type with multi-coil (shear and squeeze modes)	Yazid et al., 2014
9	Piston-type with multi-coil (flow mode)	Sapinski, 2014
10	Piston-type with multi-coil (flow mode)	Singh and Wereley, 2014
11	Piston-type with multi-coil (flow mode)	Zemp et al., 2014
12	Piston-type with multi-coil (flow mode)	Singh et al., 2014
13	Piston-type with single coil (flow mode)	Hu et al., 2014a
14	MRF valve with single coil (flow mode)	Chae and Choi, 2015
15	Piston-type with single coil (flow mode)	Kim et al., 2015
16	Piston-type with single coil (flow mode)	Zheng et al., 2014
17	Piston-type with single coil (flow mode)	Hu et al., 2014b
18	Piston-type with single coil (squeeze mode)	Gong et al., 2014
19	Piston-type with single coil (flow mode)	Wang et al., 2014
20	Piston-type with multi-coil (flow mode)	Mughni et al., 2015
21	Piston-type with single coil (flow mode)	Sohn et al., 2015
22	Piston-type with single coil (flow mode)	Liu et al., 2015
23	Piston-type with single coil (flow mode)	Hu et al., 2015
24	Piston-type with multi-coil (flow mode)	Powell et al., 2016
25	Piston-type with single coil (flow mode)	Kim et al., 2016
26	Piston-type with single coil (flow mode)	Park et al., 2016
27	Piston-type with permanent magnet (flow mode)	Kim et al., 2017
28	Piston-type with multi-coil (flow mode)	Zhang et al., 2017
29	Piston-type with single coil (flow mode)	Dominguez et al., 2017
30	Piston-type with single coil (flow mode)	Gao et al., 2017
31	Piston-type with multi-coil (flow mode)	Kubik et al., 2017
32	Piston-type with multi-coil (flow mode)	Zheng et al., 2017
33	Piston-type with permanent magnet (flow mode)	Maddah et al., 2018

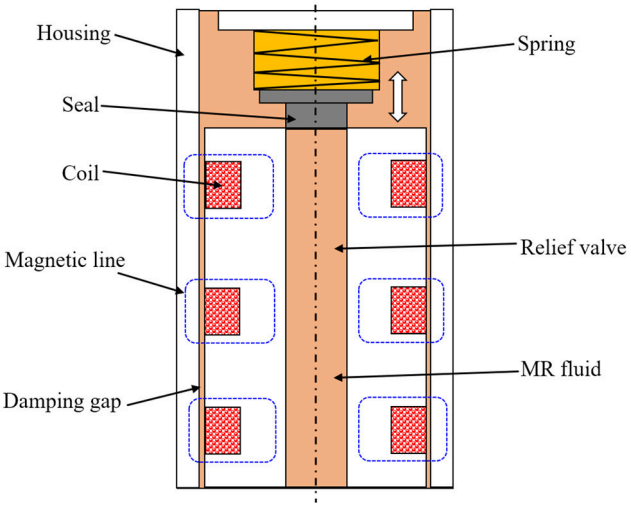

FIGURE 3 | MRF damper with valve and multi-coils (Powell et al., 2016).

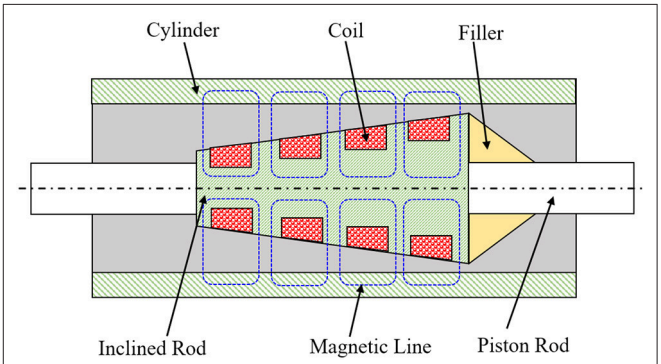

FIGURE 4 | MRF damper with inclined gap and multi-coils (Zheng et al., 2017).

proposed, to support the required static force in vibration control (Powell et al., 2016). The main function of the spring is to act as a door to open or close the valve embedded in the center of the core piston. In 2017, a new MRF damper, activated by the permanent magnets instead of the magnetic coils was introduced (Kim et al., 2017). In this damper, the capability of the field-dependent damping force control is achieved through a special arrangement of the permanent magnets. In other words, the damping force can be controlled by moving the position of the permanent magnets, to magnetize different areas. It should be noted that the MRF damper, activated by the permanent magnets, can be manufactured with a cheaper cost compared with the magnetic coil operated MRF damper, but the damping force induced from the magnetic field is lower than the conventional MRF damper. Therefore, optimizing the shape of the permanent magnets needs to be researched in order to increase the field-dependent damping force.

In this review article, two different types of MRF dampers are specifically examined with regards to their design structures. **Figure 3** presents a hybrid damper (Powell et al., 2016). This design uses a combination of a valve and a multi-coil core. The difference of upper pressure and lower pressure of the damper is adjusted by the valve with the mechanical spring. The flow of MRF is not blocked, which is an advantage of the design. When the core damper is moved up, the valve will be closed. In this case, the pressure of the upper chamber is larger than the lower chamber. The damping force is also increased to control vibration. After that, the core of the damper is moved down, the valve is opened, and the pressure of both chambers is balanced. The force in this time is smaller than the former. **Figure 4** shows the MRF damper, in which the

TABLE 3 | Studies of MRF mount in 2013–2018.

No.	Type of damper	References
1	MRF valve (flow and shear modes)	Kang et al., 2013
2	MRF valve (flow and squeeze modes)	Farjoud et al., 2013
3	MRF valve (flow and shear modes)	Nguyen et al., 2013
4	MRF valve (flow, shear, and squeeze mode)	Do et al., 2014
5	MRF valve (squeeze mode)	Li et al., 2016
6	MR elastomer	Yarra et al., 2018

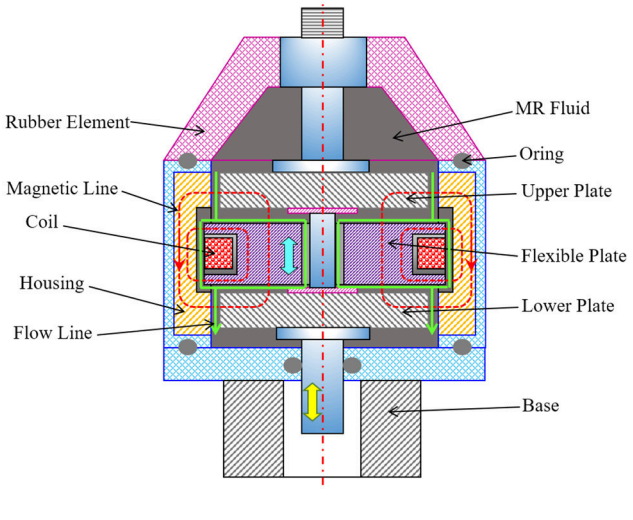

FIGURE 5 | MRF mount with the flexible plate for changeable gap (Do et al., 2014).

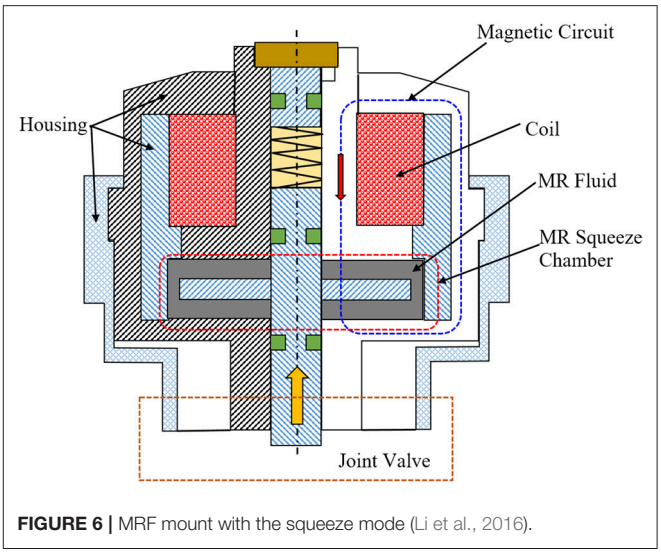

FIGURE 6 | MRF mount with the squeeze mode (Li et al., 2016).

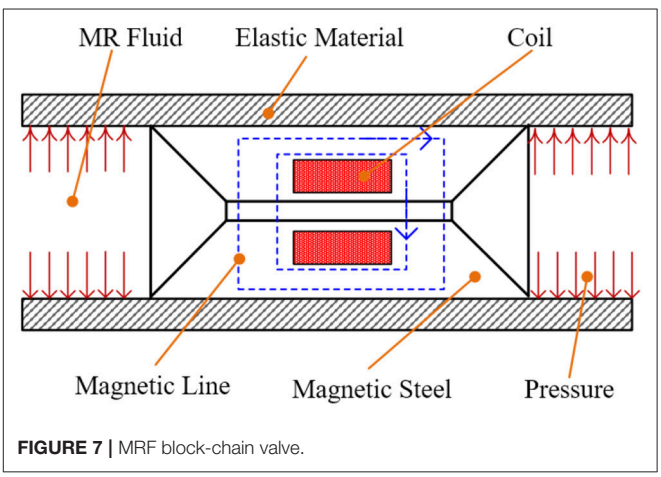

FIGURE 7 | MRF block-chain valve.

magnetic distribution can be adjusted by making an inclined gap (Zheng et al., 2017). When the core is moved, the damping force is also changed. When the core is moved to the left, the damping force obtains the maximum value to control vibration. The pressure of the left chamber is larger than the right chamber. Inversely, the force is smaller than the above movement. It has been shown that the block up phenomenon can be prevented by the inclined gap of the core damper. However, the general force for both designs, (Powell et al., 2016) and (Zheng et al., 2017), is not larger than the conventional design. In addition, the size of the proposed structure is also bigger than the conventional device.

MRF MOUNT

It is known that the MRF mount is very effective in attenuating a small magnitude and a high frequency of vibrations in many dynamic systems such engine excitation. The flow motion of the MRF mount is the same as that of the MRF damper: flow mode, shear mode and squeeze mode. For the past 6 years, many research works on the MRF mount have been undertaken and some studies are summarized in **Table 3**. Most design configurations of the MRF mount reported during 2013–2017 feature valve types with more than one operating mode. The main structure used in these years were designed to have the MRF valve type in which the H-gap is the most significant design parameter. The pressure difference between the upper and lower chambers, which is directly related to the field-dependent damping force, is determined by the H-gap. However, these types of MRF mounts have a bottle neck when the H-gap is designed with a very narrow scale. More specifically, the flow motion is stopped in the narrow gap and hence the controllability of the damping force is no longer possible. This is called the block-up phenomenon. In 2014, a breakthrough design of the MRF mount was proposed to avoid the block-up phenomenon (Do et al., 2014) as shown in **Figure 5**. It is seen from the schematic configuration that a flexible plate is positioned between the upper and lower plates which can change the glow gap depending upon the vibration or excitation magnitudes. In other words, the gap size can be enlarged when the vibration magnitude is large while it can be smaller when the vibration magnitude is very small. By activating this principle, the block-up phenomenon, which appeared in almost all conventional MRF mounts, can effectively be avoided. In addition, a simple design with a low

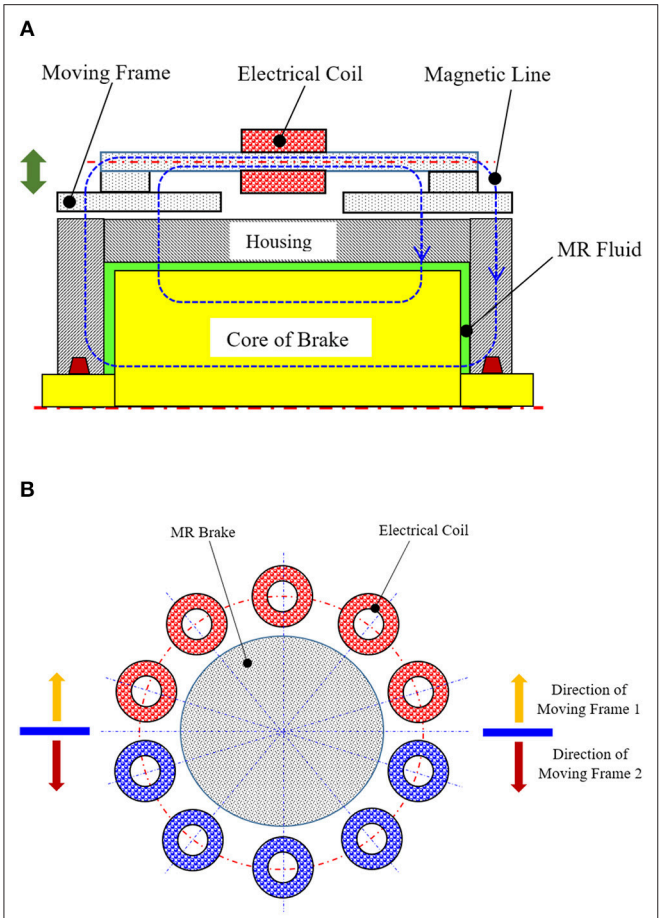

FIGURE 8 | MRF damper with multi-outside coils, **(A)** general view, **(B)** view of multi-coils.

manufacturing cost is possible to meet a certain requirement in many different applications such as an engine mount, bridge mount and an electronic appliance mount. In 2016, a squeeze mount shown in **Figure 6** was proposed in (Li et al., 2016). The core component of this type of MRF mount is the chamber containing MRF, in which the squeeze motion (or up and down motions) occurs to produce the field-dependent damping force. In order to achieve an appropriate damping force, the height (or gap) of the chamber needs to be optimized. In general, the gap size of the squeeze mode MRF mount is around 1–2 mm for the application to vehicle engine mount. One drawback of this type is the difficulty in vibration control, with relatively large magnitudes, due to the sealing issue preventing leakage in its practical use, which becomes more serious. Therefore, this type of MRF mount is effective in controlling small excitations with relatively high frequency components. Recently, a new design structure, to avoid the block-up behavior, was proposed (Sakai and Stramigioli Visuali, 2018). In this design, the cores have been modified to balance the pressure of both the upper and lower chamber. In addition, two pistons connected to the vibration plate was used to balance the pressure between the two pistons. Therefore, the block-up behavior can be avoided by properly controlling the pressure difference (or the field-dependent actuating force) through the servo valve system. It is remarked here that recently, a new kind of high-loaded mount using MR elastomer was introduced in Yarra et al. (2018). The mount based on the MR elastomer does not require any fluid reservoir, but the response time is relatively slow.

CONCLUSION WITH SUGGESTIONS

In this review article, MR devices reported over the last 6 years (2013–2018) were examined in terms of their design configuration. It was identified that many different structural configurations for the brake, clutch, damper and mount can be devised, when considering the principal operating models: flow, shear and squeeze. Several problems that need to be resolved, for successful practical use, despite some MRF dampers that are commercially available now, still remain. Among these many problems, two of the most significant issues that need to be resolved, for the practical application in many fields, are the avoidance or minimization of the block-up phenomenon and the maximization of the field-dependent actuating force with certain design constraints.

Figure 7 presents a possible design of an MRF device which can produce a high damping force without any block-up phenomenon. In this design structure, the main component is an opened block-chain of the MRF valve. The elastic housing is deformed and then the non-valve elastic joint becomes infinitely stiff in order to absorb the vibrations. Thus, the stiffness of the elastic material will be optimized to control vibrations without causing block-up behavior, by implementing an appropriate controller. Another effective design configuration for the MRF device is to place the magnetic coils on the outside of the housing as shown in **Figure 8**. Advantages of this design include the independent control of each magnetic line, the adaptiveness to the change of the vibration (or excitation) and the possibility of several segments of different actuating forces to meet the corresponding external disturbances such as unwanted vibrations or noise. It is noted here that successful development of this MRF device type requires both the reliable hardware and accurate software associated with an appropriate controller.

AUTHOR CONTRIBUTIONS

DP conceived and wrote the paper. S-BC analyzed the references and wrote the future directions of the research.

ACKNOWLEDGMENTS

This research was funded by the Vietnam National Foundation for Science and Technology Development (NAFOSTED) under grant number 107.01-2017.28. This financial support is gratefully acknowledged.

REFERENCES

Alkan, M. S., Gurocak, H., and Gonen, B. (2013). Linear magnetorheological brake with serpentine flux path as a high force and low off-state friction actuator for haptics. *J. Intell. Mater. Syst. Struct.* 24, 1699–1713. doi: 10.1177/1045389X13484098

Bai, X. X., Hu, W., and Wereley, N. M. (2013). Magnetorheological damper utilizing an inner bypass for ground vehicle suspensions. *IEEE Trans. Magn.* 49, 3422–3425. doi: 10.1109/TMAG.2013.2241402

Bucchi, F., Forte, P., Franceschini, A., and Frendo, F. (2013). Analysis of differently sized prototypes of an MR clutch by performance indices. *Smart Mater. Struct.* 22:105009. doi: 10.1088/0964-1726/22/10/105009

Bucchi, F., Forte, P., Frendo, F., Musolino, A., and Rizzo, R. (2014). A fail-safe magnetorheological clutch excited by permanent magnets for the disengagement of automotive auxiliaries. *J. Intell. Mater. Syst. Struct.* 25, 2102–2114. doi: 10.1177/1045389X13517313

Case, D., Taheri, B., and Richer, E. (2013). Design and characterization of a small-scale magnetorheological damper for tremor suppression. *IEEE/ASME Trans. Mechatron.* 18, 96–103. doi: 10.1109/TMECH.2011.2151204

Cha, S. W., Kang, S. R., Hwang, Y. H., Choi, S. B., Lee, Y. S., and Han, M. S. (2018). Design and control of a parallel mechanism haptic master for robot surgery using magneto-rheological clutches and brakes. *J. Intell. Mater. Syst. Struct.* 29, 3829–3844. doi: 10.1177/1045389X18799477

Chae, H. D., and Choi, S. B. (2015). A new vibration isolation bed stage with magnetorheological dampers for ambulance vehicles. *Smart Mater. Struct.* 24:017001. doi: 10.1088/0964-1726/24/1/017001

Dai, S. Q., Du, C. B., and Yu, G. J. (2013). Design, testing and analysis of a novel composite magnetorheological fluid clutch. *J. Intell. Mater. Syst. Struct.* 24, 1675–1682. doi: 10.1177/1045389X13483026

Ding, Y., Zhang, L., Zhu, H. T., and Li, Z. X. (2013). A new magnetorheological damper for seismic control. *Smart Mater. Struct.* 22:115003. doi: 10.1088/0964-1726/22/11/115003

Do, X. P., Shah, K., and Choi, S. B. (2014). A new magnetorheological mount featured by changeable damping gaps using a moved-plate valve structure. *Smart Mater. Struct.* 23:125022. doi: 10.1088/0964-1726/23/12/125022

Dominguez, G. A., Kamezaki, M., and Sugano, S. (2017). Proposal and preliminary feasibility study of a novel toroidal magnetorheological piston. *IEEE/ASME Trans. Mechatron.* 22, 657–668. doi: 10.1109/TMECH.2016.2622287

Farjoud, A., Taylor, R., Schumann, E., and Schlangen, T. (2013). Advanced semi-active engine and transmission mounts: tools for modelling, analysis, design, and tuning. *Vehicle Syst. Dyn.* 52, 218–243. doi: 10.1080/00423114.2013.870345

Gao, F., Liu, Y. N., and Liao, W. H. (2017). Optimal design of a magnetorheological damper used in smart prosthetic knees. *Smart Mater. Struct.* 26:035034. doi: 10.1088/1361-665X/aa5494

Goldasz, J., and Sapinski, B. (2013). Verification of magnetorheological shock absorber models with various piston configurations. *J. Intell. Mater. Syst. Struct.* 24, 1846–1864. doi: 10.1177/1045389X13479684

Gong, X. L., Ruan, X. H., Xuan, S. H., Yan, Q. F., and Deng, H. X. (2014). Magnetorheological damper working in squeeze mode. *Adv. Mech. Eng.* 2014:410158. doi: 10.1155/2014/410158

Hadadian, A., Sedaghati, R., and Esmailzadeh, E. (2013). Design optimization of magnetorheological fluid valves using response surface method. *J. Intell. Mater. Syst. Struct.* 25, 1352–1371. doi: 10.1177/1045389X13504478

Hu, G. L., Long, M., Huang, M., and Li, W. H. (2014a). Design, analysis, prototyping, and experimental evaluation of an efficient double coil magnetorheological valve. *Adv. Mech. Eng.* 2014:403410. doi: 10.1155/2014/403410

Hu, G. L., Long, M., Yu, L., and Li, W. H. (2014b). Design and performance evaluation of a novel magnetorheological valve with a tunable resistance gap. *Smart Mater. Struct.* 23:127001. doi: 10.1088/0964-1726/23/12/127001

Hu, G. L., Ru, Y., and Li, W. H. (2015). Design and development of a novel displacement differential self-induced magnetorheological damper. *J. Intell. Mater. Syst. Struct.* 26, 527–540. doi: 10.1177/1045389X14533429

Kang, O. H., Kim, W. H., Joo, W. H., and Park, J. H. (2013). "Design of the magnetorheological mount with high damping force for medium speed diesel generators," in *Active and Passive Smart Structures and Integrated Systems Proc. of SPIE 8688:86881E* (San Diego, CA). doi: 10.1117/12.2012831

Kavlicoglu, B. M., Gordaninejad, F., and Wang, X. (2013). Study of a magnetorheological grease clutch. *Smart Mater. Struct.* 22:125030. doi: 10.1088/0964-1726/22/12/125030

Kim, H. C., Oh, J. S., and Choi, S. B. (2015). The field-dependent shock profiles of a magnetorheological damper due to high impact: an experimental investigation. *Smart Mater. Struct.* 24:025008. doi: 10.1088/0964-1726/24/2/025008

Kim, K. S., Chen, Z. B., Yu, D., and Rim, C. H. (2016). Design and experiments of a novel magnetorheological damper featuring bifold flow mode. *Smart Mater. Struct.* 25:075004. doi: 10.1088/0964-1726/25/7/075004

Kim, W. H., Park, J. H., Kaluvan, S., Lee, Y. S., and Choi, S. B. (2017). A novel type of tunable magnetorheological dampers operated by permanent magnets. *Sens. Actu. A Phys.* 255, 104–117. doi: 10.1016/j.sna.2017.01.012

Kubik, M., Machacek, O., Strecker, Z., Roupec, J., and Mazurek, I. (2017). Design and testing of magnetorheological valve with fast force response time and great dynamic force range. *Smart Mater. Struct.* 26:047002. doi: 10.1088/1361-665X/aa6066

Li, Z. H., Zhang, X. J., Guo, K. H., Ahmadian, M., and Liu,. Y. (2016). A novel squeeze mode based magnetorheological valve: design, test and evaluation. *Smart Mater. Struct.* 25:127003. doi: 10.1088/0964-1726/25/12/127003

Liu, X. H., Gao, X. L., Li, F., Yu, H., and Ye, D. (2015). Shear performance of a metal foam magnetorheological fluid damper. *IEEE Trans. Magn.* 51:4600107. doi: 10.1109/TMAG.2014.2343938

Maddah, A. A., Hojjat, Y., Karafi, M. R., and Ashory, M. R. (2018). Reduction of magnetorheological dampers stiffness by incorporating of an eddy current damper. *J. Sound Vib.* 396, 51–68. doi: 10.1016/j.jsv.2017.02.011

Mars, M. C., and Gurocak, H. (2017). Pneumatic cylinder with magnetorheological brake using serpentine and helix flux guide as a linear hybrid actuator for haptics. *J. Intell. Mater. Syst. Struct.* 28, 1303–1321. doi: 10.1177/1045389X16667562

McLaughlin, G., Hu, W., and Wereley, N. M. (2014). Advanced magnetorheological damper with a spiral channel bypass valve. *J. Appl. Phys.* 115:17B532. doi: 10.1063/1.4869278

Mughni, M. J., Zeinali, M., Mazlan, S. A., Zamzuri, H., and Rahman, M. A. A. (2015). Experiments and modeling of a new magnetorheological cell under combination of flow and shear-flow modes. *J. Nonnewton. Fluid Mech.* 215, 70–79. doi: 10.1016/j.jnnfm.2014.11.005

Nguyen, Q. H., Do, X. P., Park, J. H., Choi, S. B., and Kang, O. H. (2013). Development of high damping magneto-rheological mount for ship engines. *Appl. Mech. Mater.* 336–338, 953–959. doi: 10.4028/www.scientific.net/AMM.336-338.953

Nguyen, Q. H., Lang, V. T., Nguyen, N. D., and Choi, S. B. (2014). Geometric optimal design of a magnetorheological brake considering different shapes for the brake envelope. *Smart Mater. Struct.* 23:015020. doi: 10.1088/0964-1726/23/1/015020

Nguyen, Q. H., Nguyen, N. D., and Choi, S. B. (2015). Design and evaluation of a novel magnetorheological brake with coils placed on the side housings. *Smart Mater. Struct.* 24:047001. doi: 10.1088/0964-1726/24/4/047001

Park, J. H., Yoon, G. H., Kang, J. W., and Choi, S. B. (2016). Design and control of a prosthetic leg for above-knee amputees operated in semiactive and active modes. *Smart Mater. Struct.* 25:085009. doi: 10.1088/0964-1726/25/8/085009

Powell, L. A. A., Choi, Y. T., Hu, W., and Wereley, N. M. (2016). Nonlinear modeling of adaptive magnetorheological landing gear dampers under impact conditions. *Smart Mater. Struct.* 25:115011. doi: 10.1088/0964-1726/25/11/115011

Rizzo, R. (2017). An innovative multi-gap clutch based on magneto-rheological fluids and electrodynamic effects: magnetic design and experimental characterization. *Smart Mater. Struct.* 26:015007. doi: 10.1088/0964-1726/26/1/015007

Rossa, C., Jaegy, A., Lozada, J., and Micaelli, A. (2014a). Design considerations for magnetorheological brakes. *IEEE/ASME Trans. Mechatron.* 19, 1669–1680. doi: 10.1109/TMECH.2013.2291966

Rossa, C., Jaegy, A., Micaelli, A., and Lozada, J. (2014b). Development of a multilayered wideranged torque magnetorheological brake. *Smart Mater. Struct.* 23:025028. doi: 10.1088/0964-1726/23/2/025028

Sakai, S., and Stramigioli Visuali, S. (2018). Visualization of hydraulic cylinder dynamics by a structure preserving nondimensionalization. *IEEE/ASME Trans. Mechatron.* 23, 2196–2206. doi: 10.1109/TMECH.2018.2854751

Sapinski, B. (2014). Energy-harvesting linear MR damper: prototyping and testing. *Smart Mater. Struct.* 23:035021. doi: 10.1088/0964-1726/23/3/035021

Shiao, Y. J., Nguyen, A. N., and Lai, C. H. (2016). Optimal design of a new multipole bilayer magnetorheological brake. *Smart Mater. Struct.* 25:115015. doi: 10.1088/0964-1726/25/11/115015

Shiao, Y. J., and Nguyen, Q. A. (2013). Development of a multi-pole magnetorheological brake. *Smart Mater. Struct.* 22:065008. doi: 10.1088/0964-1726/22/6/065008

Shiao, Y. J., Nguyen, Q. A., and Lin, J. W. (2014). A study of novel hybrid antilock braking system employing magnetorheological brake. *Adv. Mech. Eng.* 2014:617584. doi: 10.1155/2014/617584

Singh, H. J., Hu, W., Wereley, N. M., and Glass, W. (2014). Experimental validation of a magnetorheological energy absorber design optimized for shock and impact loads. *Smart Mater. Struct.* 23:125033. doi: 10.1088/0964-1726/23/12/125033

Singh, H. J., and Wereley, N. M. (2014). Optimal control of gun recoil in direct fire using magnetorheological absorbers. *Smart Mater. Struct.* 23:055009. doi: 10.1088/0964-1726/23/5/055009

Sohn, J. W., Oh, J. S., and Choi, S. B. (2015). Design and novel type of a magnetorheological damper featuring piston bypass hole. *Smart Mater. Struct.* 24:035013. doi: 10.1088/0964-1726/24/3/035013

Song, W. L., Li, D. H., Tao, Y., Wang, N., and Xiu, S. C. (2017). Simulation and experimentation of a magnetorheological brake with adjustable gap. *J. Intell. Mater. Syst. Struct.* 28, 1614–1626. doi: 10.1177/1045389X16679022

Wang, D. M., Tian, Z. Z., Meng, Q. R., and Hou, Y. F. (2013). Development of a novel two-layer multiplate magnetorheological clutch for high-power applications. *Smart Mater. Struct.* 22:085018. doi: 10.1088/0964-1726/22/8/085018

Wang, N., Li,. D. H., Song, W. L., Xiu, S. C., and Meng, X. Z. (2016). Effect of surface texture and working gap on the braking performance of the magnetorheological fluid brake. *Smart Mater. Struct.* 25:105026. doi: 10.1088/0964-1726/25/10/105026

Wang, Q., Ahmadian, M., and Chen, Z. B. (2014). A novel double-piston magnetorheological damper for space truss structures vibration suppression. *Shock Vibrat.* 2014:864765. doi: 10.1155/2014/864765

Wu, J., Jiang, X. Z., Yao, J., Li, H., and Li, Z. C. (2016). Design and modeling of a multi-pole and dual-gap magnetorheological brake with individual currents. *Adv. Mech. Eng.* 8, 1–15. doi: 10.1177/1687814016659182

Yarra, S., Gordaninejad, F., Behrooz, M., Pekcan, G., Itani, A. M., and Publicover, N. (2018). Performance of a large-scale magnetorheological elastomer-based vibration isolator for highway bridges. *J. Intell. Mater. Syst. Struct.* 29, 3890–3901. doi: 10.1177/1045389X18799493

Yazid, I. I. M., Mazlan, S. A., Kikuchi, T., Zamzuri, H., and Imaduddin, F. (2014). Design of magnetorheological damper with a combination of shear and squeeze modes. *Mater. Design* 54, 87–95. doi: 10.1016/j.matdes.2013.07.090

Yu, L. Y., Ma, L. X., and Song, J. A. (2017). Design, testing and analysis of a novel automotive magnetorheological braking system. *Proc. Inst. Mech. Eng. D* 231, 1402–1413. doi: 10.1177/0954407016674394

Zemp, R., Llera, J. C., and Weber, F. (2014). Experimental analysis of large capacity MR dampers with short- and long-stroke. *Smart Mater. Struct.* 23:125028. doi: 10.1088/0964-1726/23/12/125028

Zhang, X. J., Li, Z. H., Guo, K. H., Zheng,. F. M., and Wang, Z. (2017). A novel pumping magnetorheological damper: design, optimization, and evaluation. *J. Intell. Mater. Syst. Struct.* 28, 2339–2348. doi: 10.1177/1045389X17689937

Zheng, J., Li, Z. C., Koo, J. H., and Wang, J. (2014). Magnetic circuit design and multiphysics analysis of a novel MR damper for applications under high velocity. *Adv. Mech. Eng.* 2014:402501. doi: 10.1155/2014/402501

Zheng, J. J., Li, Y. C., and Wang, J. (2017). Design and multi-physics optimization of a novel magnetorheological damper with a variable resistance gap. *Proc IMechE Part C: J Mech. Eng. Sci.* 231, 3152–3168. doi: 10.1177/0954406216643109

Zhou, Y., and Zhang, Y. L. (2013). Optimal design of a shear magnetorheological damper for turning vibration suppression. *Smart Mater. Struct.* 22:095012. doi: 10.1088/0964-1726/22/9/095012

Conflict of Interest Statement: The authors declare that the research was conducted in the absence of any commercial or financial relationships that could be construed as a potential conflict of interest.

frontiers in Materials

PERSPECTIVE
published: 08 February 2019
doi: 10.3389/fmats.2019.00004

The Role of Volume Fraction and Additives on the Rheology of Suspensions of Micron Sized Iron Particles

Georges Bossis[1]*, *Olga Volkova*[1], *Yan Grasselli*[1,2] and *Alain Ciffreo*[1]

[1] Laboratory Inphyni, Institute of Physics of Nice, CNRS, University of Nice Sophia-Antipolis, Nice, France, [2] SKEMA Business School, Université Côte d'Azur, Sophia Antipolis, France

The increase of the yield stress vs. the magnetic field is the most important quantity characterizing the efficiency of a magnetorheological suspension. The theory based on the formation of columnar aggregates predicts a linear variation with the volume fraction of magnetic particles. In this paper we review previous models used to calculate forces and yield stress and will introduce a new model based on rupture at zero strain. Predictions of these models are compared with the experimental data obtained for carbonyl iron particles, by different authors. Whereas, previous analytical prediction strongly overestimates experimental yield stress, those calculated using the Finite Element Method (FEM), together with affine trajectories, reproduce the experiments well and show a linear dependence with the volume fraction and a $H^{3/2}$ behavior between 50 and 200 kA/m. Nevertheless, at very high-volume fractions (>55%), where the suspension can only flow in the presence of specific additives, the dependence of the yield stress vs. the volume fraction and the magnetic field is dramatically changed. We observed a jamming transition, which is triggered by the application of a low magnetic field and which depends strongly on the volume of the fraction. Here, we will discuss new perspectives arising from the use of these very high-volume fractions.

Keywords: carbonyl iron, yield stress, discontinuous shear thickening, jamming, magnetorheology

OPEN ACCESS

Edited by:
Seung-Bok Choi,
Inha University, South Korea

Reviewed by:
Xufeng Dong,
Dalian University of Technology (DUT), China
Evguenia Korobko,
A.V. Luikov Heat and Mass Transfer Institute (NASB), Belarus

***Correspondence:**
Georges Bossis
bossis@unice.fr

Specialty section:
This article was submitted to Smart Materials, a section of the journal Frontiers in Materials

Received: *29 October 2018*
Accepted: *10 January 2019*
Published: *08 February 2019*

Citation:
Bossis G, Volkova O, Grasselli Y and Ciffreo A (2019) The Role of Volume Fraction and Additives on the Rheology of Suspensions of Micron Sized Iron Particles. Front. Mater. 6:4. doi: 10.3389/fmats.2019.00004

INTRODUCTION

Magnetorheological (MR) suspensions are smart fluids made of magnetizable particles, with a typical size varying between 100 nm and a few microns dispersed in a carrier liquid, which can be mineral oil, silicone oil, ethylene glycol, etc. The interest of these fluids is their rapid and reversible transformation in a solid when they are submitted to a magnetic field. This transformation occurs due to the attractive interaction of a dipolar nature, generated by the magnetization of the particles. The solid phase is characterized by its resistance to a shear strain, namely the yield stress, over which the solid begins to creep. Most applications look for fluids that present the highest possible yield. Of course, the higher the magnetic field, the higher the yield stress, with the limit of the full magnetization of the particles as well as the inconvenience of weight and place that are necessary for the coils to produce a high magnetic field. Besides the importance of a high yield stress, other requisites are also important for industrial uses such as easy resuspension after sedimentation and a low off state viscosity. In order to obtain a high yield stress and a reversible magnetization,

very few materials are available, and in practice industrial MR fluids are based on carbonyl iron particles as they present a high saturation magnetization and are synthesized in large quantities to produce sintered magnetic circuits. Iron particles have the inconvenience of high density and therefore of rapid sedimentation; furthermore, due to the pressure generated by their weight and the attractive Van der Waals forces, they easily aggregate irreversibly. In order to prevent this irreversible aggregation, coating of the particles by some molecules (surfactant, polymer, even ions) is necessary. Many papers and patents describe these formulations and their effects in reducing sedimentation and aggregation [for a recent review see reference (Ashtiani et al., 2015)]. This coating, which prevents the particles to come into close contact can also present the inconvenience of lowering the magnetic force, which strongly depends on the distance between the particles. Ultimately however, despite decades of research, the maximum yield stress of commercial fluids remains in the 40–60 kPa range for a 0.3–0.5 Tesla magnetic field induction. We first take a look at the yield stresses predicted by the available models and compare these predictions with the experimental data, then, in light of recent experimental results involving frictional stresses, we will focus on the performance of these fluids and how they can be improved.

PREDICTION OF THE YIELD STRESS

The cohesion of the solid phase, and therefore its yield stress, depends first on the strength of the magnetic forces developed between the particles, and second on the structure and its evolution under combined magnetic and hydrodynamic forces. We briefly review the main models and then compare their prediction, both for the forces between the particles and for the yield stress. To do this analysis we take a look at the magnetic properties of the carbonyl iron particles, those currently used in practical applications. The magnetization curve is described by the Frolish Kennelly equation: $M{=}M_s\ \chi_i\ H/(M_s + \chi_i\ H)$ Where M_s is the saturation magnetization and χ_i the initial permeability. For the saturation magnetization we have taken the pure iron: M_s = 1,680 kA/m and the initial permeability $\chi_i = 70$ (De Vicente et al., 2002).

Magnetic Forces Between Two Particles

Contrary to well-known dipolar approximation, a multipolar approach for two particles, first presented by Klingenberg (Klingenberg and Zukoski, 1990) and then for several particles described in subsequent works (Clercx and Bossis, 1993), gives an exact prediction of the force for a linear magnetization. The result for two particles reads:

$$F_m(\vec{r}) = 12\pi\mu_0 a^2\beta^2 H^2\left(\frac{a}{r}\right)^4\left[\left(2f_{//}\cos^2(\theta) - f_\perp\sin^2(\theta)\right)\vec{e}_r + f_\Gamma\sin(2\theta)\vec{e}_\theta\right] \quad \text{with } \beta = \frac{\mu_p - 1}{\mu_p + 2} \tag{1}$$

In Equation (1) a is the radius of the particles, μ_p their relative permeability given by $\mu_p = 1{+}M/H$ and $f_{//}$, $f_\perp$, f_Γ are functions of the initial permeability: $\mu_i = \chi_i + 1$ and of the normalized separation between the surfaces of the two particles $\varepsilon = r/a\text{-}2$ (cf **Figure S1**). A **Table S2** of these functions for different separations and different values of χ_i is provided in the **Supplementary Material**.

A popular model derived in Ginder et al. (1996) uses, on the contrary, the approximation that the pole of the particles is completely saturated (cf **Figure S1**) in a zone defined by $\rho = \delta$ where ρ is the polar coordinate. The interparticle force coming from the integral of the magnetic stress tensor is then given by:

$$F_r = \frac{\mu_0}{2}\int_0^W \left(H(\rho) - H\right)^2 2\pi\rho d\rho \quad \text{with } H(\rho) = H\frac{(2+\varepsilon)}{\varepsilon + \rho^2}$$
$$\text{for } \rho > \delta \text{ and } H(\rho) = M_s \text{ for } \rho < \delta \tag{2}$$

The value of δ is obtained from the equality between the two expressions for $\rho = \delta$ which gives: $\delta = \sqrt{2H/M_s - \varepsilon}$

In these expressions the distances are normalized by the radius of the sphere and W is of order unity. In the limit where $\varepsilon/2 < H/M_s << 1$, the upper bound of the integral is negligible and we obtain:

$$F_{ra} = \pi\mu_0 a^2 M_s^2\left(\frac{2H}{M_s} - \frac{\varepsilon}{2}\right) \tag{3}$$

It is possible to check the validity of this approximation, using a finite element method (FEM) for the calculation of the magnetic field. We have used the FEMM software to calculate the force between two spheres placed in a constant magnetic field H:

$$F_{rFEM} = 2\pi a^2\int_0^\pi \left[\sigma_{rr}\cos(\theta) - \sigma_{r\theta}\sin(\theta)\right]\sin(\theta)d\theta \tag{4}$$
$$\text{with } \sigma_{rr} = \mu_0(\mu_f H_r^2 - 0.5H^2) \quad \sigma_{r\theta} = \mu_0\mu_f H_r H_\theta$$

In our case the carrier liquid was non-magnetic and so $\mu_f = 1$. The fields H_r and H_θ are the field normal and tangential to the internal surface of the particle, respectively. In **Figure S2**, we have compared the dependence of these three models on the amplitude of the magnetic field for a separation distance of 0.01a and a radius of 1 mm. As shown in this figure, the multipolar force (Equation 1) and the FEM calculation (Equation 4) gave the same result at low field as expected but above H = 25 kA/m, the multipolar model overestimates the force. The analytical model (Equation 3) largely overestimates the force. This force calculation is necessary to predict the yield stress, but we also need to know the structure and its deformation under strain.

Models for the Yield Stress

Affine Trajectories

In the standard model the particles are supposed to follow trajectories which are affine with the imposed shear flow. The magnetic field is perpendicular to the imposed flow (cf **Figure S1**). The equilibrium position of the particles is obtained by balancing the shear stress on the top particle with the magnetic restoring force. When the two representative particles are aligned with the magnetic field ($\theta = 0$ on **Figure S1**) the gap between the

surfaces is given by the thickness of the coating layer, typically of the order of a few nanometers. When particle 2 moves along the stream line, the gap increases with the strain: $\gamma = \mathrm{tg}(\theta)$ as: $\boldsymbol{\varepsilon - \varepsilon_0 = 2(\sqrt{1+\gamma^2} - 1)}$. On the other hand, the magnetic force along the x axis is $F_r \sin\theta \cos^2\theta$ where F_r is the radial force calculated in the preceding section for particles aligned in the direction of the field. In a model where all particles form chains spanning the gap with a surface density $n_c/S = 2a\ N/V = (3/2)\Phi/(\pi a^2)$, with Φ the volume fraction, the shear stress is given by:

$$\tau(\gamma) = \frac{3}{2}\Phi\ max(\frac{F_r}{\pi a^2}\sin\theta\cos^2\theta) = \frac{3}{2}\Phi\ max\left(\frac{F_r(\gamma)}{\pi a^2}\frac{\gamma}{(1+\gamma^2)^{3/2}}\right) \quad (5)$$

For the analytical expression of the force Equation (3), we get, (always for $\varepsilon/2 < H/Ms << 1$):

$$\tau_{ya} = \sqrt{16/3}\ \Phi\ \mu_0 M_s H^{3/2} \quad (6)$$

Equation (6) differs slightly from that given in Ginder et al. (1996) where the prefactor is $\sqrt{6}$. It is worth noting that when the magnetization of the particles is saturated, the force between the particles is obtained from interactions between rigid dipoles $m = M_s.v$, where v is the volume of the particle. The results for the yield stress is readily derived, for non-interacting particle chains (Ginder et al., 1996) as: $\tau_{ymax} = 0.086\ \Phi.\mu_0.M_s^2$.

For the multipolar force we need to interpolate the tables $f_{//}$, $f_\perp$, f_Γ as a function of the separation and, in the non-linear case derived by FEM, it is also needed to do this interpolation for each value of the field; the data used are given in **Table S3**. The results are presented in **Figure 1A** but, before discussing them, it is worth introducing another model, which to our knowledge, has never been used for MR (or ER) fluids.

Rupture at Zero Strain

Here we suppose that the particles are packed in some disordered way, and that the solid phase will yield suddenly when the shear stress is high enough to separate the particles on a given "cutting" plane which, in a simple shear, is perpendicular to the velocity gradient. This kind of model is used to predict the yield stress of suspensions of particles aggregated in the presence of Van der Waals forces (Scales et al., 1998). The only difference in our case is that the interparticle force is proportional to $(H\cos\theta)^2$ instead of being independent of θ. Otherwise the interparticle distances are supposed to be distributed isotropically, which is mainly true at a high-volume fraction. Following the same steps as in Scales et al. (1998) we obtain:

$$\tau_y = \frac{3\Phi\ K(\Phi)}{20\pi R^2}F_r(\varepsilon_0) \quad \text{with} \quad K(\Phi) = 36\Phi/\pi \quad (7)$$

The factor 3/20 comes from the $\cos^2\theta$ instead of 1/4 for an isotropic force. The function $K(\Phi)$ is the coordination number taken from Suzuki et al. (1981) and ε_0 is the minimum gap between two particles.

Comparison of the Different Models

The predictions of the different models are reported in **Figure 1A**. Firstly if we compare, in the affine model, the predictions related to the 3 different approximations of forces: Equations (1, 3, 4),we recover the fact that the multipolar model gives a rather good prediction for low fields but, due to the linear magnetization hypothesis, highly overestimates the yield stress at high fields. The analytic expression overestimates the yield stress given by FEM, by about one order of a magnitude. Lastly, the model of rupture at zero strain (Equation 7), is calculated with the force F_r obtained by FEM for $\varepsilon = 0.002$, which is a reasonable value considering a coating layer of 2 nm and a radius of 1 μm. The corresponding prediction is well-above the FEM prediction and is, by chance, quite close to that of the analytical model. It should also be noted that the fit of the yield stress by a power law: $\tau_y = K.H^n$ provides a good fit with $n = 1.94$ ($R^2 = 0.9997$) only for $H \leq 50$ kA/m (**Figure S3**) which is three times smaller than the field used for the transition from H^2 to $H^{3/2}$ ($H_c = 151$ kA/m) in Fang et al. (2009). It is also worth noting that the radial force, at contact between two particles, increases steadily in the range of $\varepsilon = 0$–0.01(cf **Table S2**), which may explain, at least in the rupture model, the decrease of the yield stress in the presence of a coating layer (Cvek et al., 2018). This comparison of the models was done for two spheres in a given field, which

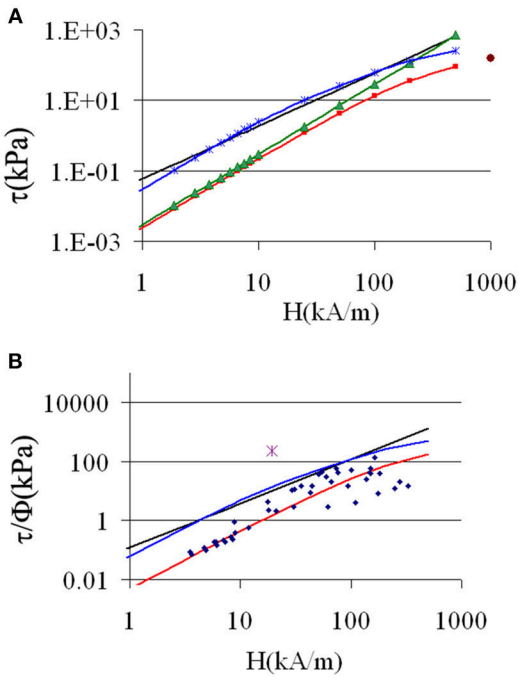

FIGURE 1 | (A) Theoretical yield stress vs. the field acting on the particles. Red squares: calculated from FEMM; green triangles calculated from multipolar forces; black solid line: Equation (6); blue crosses: Equation (7) with F_r calculated with FEM. The red dot corresponds to the saturation of the magnetization. **(B)** Comparison theory-experiment for τ_y/Φ. Blue diamonds: experimental points taken from **Table S1**. Red line, FEM result; black line, Equation (6); Blue line, Equation (7); Purple star, jamming transition.

we consider as the average field, in order to compare with the experiments in the next section. Some numerical results for the yield stress of a set of particles can be obtained with a good precision in a multipolar approach, even for high permeability, but for particles distributed on a periodic network (Clercx and Bossis, 1993) with an affine deformation. In this case all the particles are separated by the same gap, which is an unphysical and unstable structure. It is also possible to use a double chain structure so that it can deform and still keep contacts and stability, but it underestimates the yield stress (López-López et al., 2012) and also can't be used in numerical simulations. In fact, almost all numerical simulations of MR suspensions use the dipolar approximation, which largely underestimates the magnetic force (Clercx and Bossis, 1993). We have found one paper (Lacis and Gosko, 2009) using an expression similar to Equation (1), with some tables derived from FEM simulations for two particles and another based on FEM simulations between several particles in a single chain (Kang et al., 2012). A simulation method, called smooth particle dynamics (Hashemi et al., 2016, 2018), can also be used to solve the magnetostatics equation between several particles, but is restricted to a few particles with a rather small (<10) susceptibility. As discussed in the next section, the use of a magnetic force derived from FEM, calculated with a very fine mesh for two particles, is quite realistic and certainly much more efficient in terms of computing time.

COMPARISON WITH EXPERIMENTS

Comparing these predictions with experimental data is not so simple as, very often, the knowledge of the experimental conditions is incomplete. We have selected data concerning carbonyl iron particles (CI) whose magnetization curve of the powder is rather well-established with a saturation magnetization of 200 emu/g. Usually the experiments are made in plate-plate geometry, with the field perpendicular to the plate. In order to compare with the theory, we must first consider that the field inside the suspension is $H=H_0/\mu(H)$, where H_0 is the external field measured in the absence of suspension and $\mu(H)$ the permeability of the suspension. We have deduced the magnetization curve of CI particles from a measurement of M(H) at a volume fraction: $\Phi = 64\%$. This magnetization curve of CI particles is well-fitted in the range 0–400 kA/m by a Langevin curve:$M_1(H)=(\coth(c.H)-1/c.H)M_{sr}$ with $c = 0.014$ and $M_{sr} = 1750$ kA/m. This last value is slightly higher than the saturation magnetization of CI ($M_s \approx 1600$ kA/m) due to a shift of the fit for H>400 kA/m. The magnetization at any volume fraction of the suspension is obtained by replacing M_{sr} by $M_{sr}.\Phi$ and we have checked that it works well-even at low Φ, for instance for $\Phi = 0.2$ and $\Phi = 0.32$ BASF. The permeability for any given volume fraction is then: $\mu(H) = 1+M_1(H).\Phi/H$ The second point we need to take into account is that, in the plate-plate configuration, the yield stress provided by the software is overestimated by a factor of 4/3 (Bossis et al., 2002; Laun et al., 2010). The data collected in different publications (Kordonski and Golini, 1999; Chin et al., 2001; Lim et al., 2004; Jang et al., 2005; Cheng et al., 2009; Ierardi and Bombard, 2009; Laun et al., 2010; Kim et al., 2012; Bombard et al., 2015; Esmaeilnezhad et al., 2017; Dong et al., 2018; Plachy et al., 2018) are reported in **Table S1** and plotted in **Figure 1B** (blue diamonds). There is a considerable scatter of the data, but it appears clearly that the affine model with the calculation of forces through FEM (red curve), provides the best prediction compared to both Equation (6) and Equation (7). Now, we draw the attention on the single point (purple cross) above all the curves in **Figure 1B** which is the result of a jamming transition.

JAMMING TRANSITION AT HIGH VOLUME FRACTION

Jamming transition, also known as discontinuous shear thickening (DST), was observed in highly concentrated suspensions of solid non-Brownian particles like ceramics (Bergström, 1998), cornstarch (Fall et al., 2008, 2015) and also in model suspensions made of PMMA (Pan et al., 2015) or silica particles (Lootens et al., 2003) and calcium carbonate (Bossis et al., 2017). In the two last systems, superplasticizer molecules, common in the cement industry, were used as surfactants. We have recently found that by using, for instance, a polyoxyethylene polyphosphonate (Bossis et al., 2017), we can reach volume fractions of CI particles in water larger than 60%, still keeping a low yield stress and a viscosity of 1-2Pa.s. Now the rheogram at the zero field presents a singularity at a critical stress, where the shear rate abruptly decreases during a ramp of stress (**Figure 2A**). This DST phenomenon is due to the transition of a lubricated regime to a frictional one (Mari et al., 2014; Wyart and Cates, 2014). Above this point the shear rate fluctuates around some low values. We also see on this graph that, by increasing the volume fraction, the critical stress increases and the critical shear rate decreases. These critical values are obtained at zero magnetic field, but when the field is increased for a given volume fraction, the critical shear rate will continuously decrease to zero in a field range typically of 0–20 kA/m (Bossis et al., 2016). If instead of applying a ramp of stress we apply a ramp of shear rate, at the critical point we then obtain a jump of stress to very high values which overcomes the range of conventional rheometers. This is the purple point in **Figure 1B**. which was obtained in the presence of a field of 19.2 kA/m. The corresponding evolution of stress is plotted in **Figure 2B** vs. the strain. It was obtained in a cylindrical Couette flow with a vane tool and a homemade rheometer to be able to measure high torques (Bossis et al., 2016). The shear rate was increased from 0 to 1.6 s^{-1} in 2 s then kept constant for 25 s. The stress does not grow until the strain reaches a value around one and then increases up to 150 kPa where it remains constant afterwards. The interesting point is that this transition from a normal regime to this frictional regime can be controlled by the application of a low magnetic field (a few kA/m), thus opening the door for new applications of MR fluids. It is worth noting that a very high value of yield stress in a MR fluid was previously attained in another way, which also mobilizes the friction between particles, but with the help of a lateral pressure obtained by the compression of the suspension of the initial volume fraction $\Phi = 45\%$ by sliding wedges (Tao,

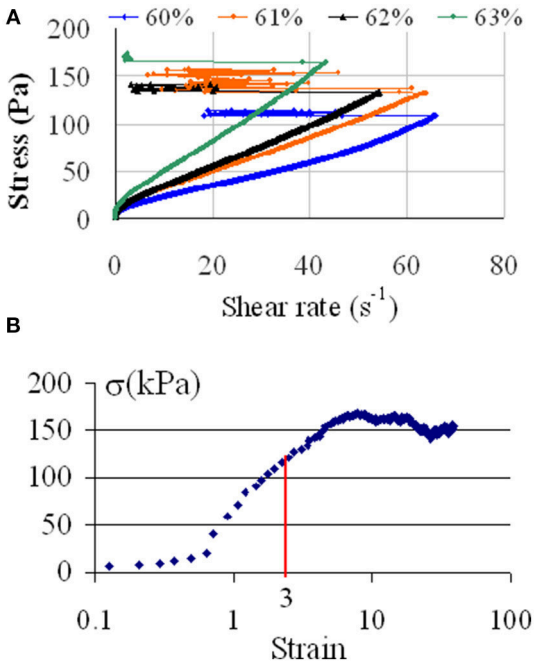

FIGURE 2 | (A) Rheogram of carbonyl iron suspensions with 0.2% of superplasticizer at high-volume fraction (blue:60%, orange 61%, black 62%,green 63%). **(B)** Stress vs. strain in cylindrical Couette geometry with vane tool, $\Phi = 0.61$;$H_0 = 19.2$ kA/m, The vertical red line corresponds to a time of 2 s where the shear rate has reached its final value of 1.6 s^{-1}.

2001). As reported in numerous previous works, [for instance (Ashtiani et al., 2015; Cvek et al., 2018)] the additives are used to stabilize the particles against corrosion and sedimentation; they can either increase the yield stress through a better compaction of the local structure [term K[Φ] in Equation (7)], or decrease it if the coating layer is too thick [term $F_r(\varepsilon_0)$ in Equation (7)]. In our case it plays a key role due its expulsion from the surface, which provokes the jamming transition

CONCLUSION

In this paper we have briefly reviewed the models of yield stress under the hypothesis of affine displacement of the particles and have also proposed a new approach based on a rupture model. It appears that the affine motion, with a calculation of the forces through FEM simulation, provides the best agreement with the experimental data of τ_y/Φ, collected for carbonyl iron suspensions. The commonly used Equation (6) strongly overestimates the experimental results but its prediction of a regime $\tau_y \propto H^{3/2}$ is verified between ∼50 and 200 kPa. No model is able to predict the high value of stress at low field obtained in suspensions of very high-volume fractions: $\Phi > 0.6$. In this case, it is the abrupt transition toward a frictional regime after expulsion of a superplasticizer layer, which leads to very high values of stress. This transition is obtained either above a critical magnetic field or above a critical shear rate, which opens up new perspectives for applications that require a strong response with a small field.

AUTHOR CONTRIBUTIONS

GB, OV, YG, and AC contributed conception and design of the study. GB wrote the first draft of the paper. OV found and organized the references and the figures. YG filled the database of the previous works on the subject and AC contributed to the theoretical part. All authors contributed to manuscript revision, read and approved the submitted version.

FUNDING

Center National d'Etudes Spatiales (CNES, the French Space Agency).

ACKNOWLEDGMENTS

This work was supported by the Center National d'Etudes Spatiales CNES. We also thank the mechanical workshop of our institute for fabricating part of our home made rheometer.

SUPPLEMENTARY MATERIAL

The Supplementary Material for this article can be found online at: https://www.frontiersin.org/articles/10.3389/fmats.2019.00004/full#supplementary-material

Figure S1 | Schematic of the notations for two particles in a magnetic field.

Figure S2 | Force vs. magnetic field for a separation $\varepsilon = 0.01$; black line: analytic expression: Equation (3); green triangles: multipolar approach: Equation (1); red triangles: FEM, Equation (4).

Figure S3 | Power law fit of the FEM result for the normalized yield stress τ_y/Φ. Red solid line:power law with $n = 1.94$; blue solid line: power law with $n = 3/2$;red crosses: FEM result; black solid line: Equation (6).

Table S1 | Corrected experimental yield stress normalized by the volume fraction (column E) in kPa vs. the Maxwell field in the suspension (column H) in kA/m.

Table S2 | Coefficients of the force in Equation (1) for differents values of $\alpha = \mu_p/\mu_f$ vs. the gap ε.

Table S3 | Values of the force obtained with the free software FEMM for different fields and separations between two spheres. The parameters for the fit vs. the normalized separation, ξ, (<0.2) are given for each field.

REFERENCES

Ashtiani, M., Hashemabadi, S. H., and Ghaffari, A. (2015). A review on the magnetorheological fluid preparation and stabilization. *J. Magn. Magn. Mater.* 374, 716–730. doi: 10.1016/j.jmmm.2014.09.020

BASF (2010). *Technical Data Sheet MR2899.*

Bergström, L. (1998). Shear thinning and shear thickening of concentrated ceramic suspensions. *Colloids Surf. A* 133, 151–155. doi: 10.1016/S0927-7757(97)00133-7

Bombard, A. J., Gonçalves, F. R., and de Vicente, J. (2015). Magnetorheology of carbonyl iron dispersions in 1-Alkyl-3-methylimidazolium ionic

liquids. *Ind. Eng. Chem. Res.* 54, 9956–9963. doi: 10.1021/acs.iecr.5b02824

Bossis, G., Boustingorry, P., Grasselli, Y., Meunier, A., Morini, R., Zubarev, A., et al. (2017). Discontinuous shear thickening in the presence of polymers adsorbed on the surface of calcium carbonate particles. *Rheol. Acta* 56, 415–430. doi: 10.1007/s00397-017-1005-4

Bossis, G., Grasselli, Y., Meunier, A., and Volkova, O. (2016). Outstanding magnetorheological effect based on discontinuous shear thickening in the presence of a superplastifier molecule. *Appl. Phys. Lett.* 109:111902. doi: 10.1063/1.4962467

Bossis, G., Volkova, O., Lacis, S., and Meunier, A. (2002). "Magnetorheology: fluids, structures and rheology," in *Ferrofluids, Part of Lecture Notes in Physics, Vol. 594* (Springer), 202–230.

Cheng, H. B., Wang, J. M., Zhang, Q. J., and Wereley, N. M. (2009). Preparation of composite magnetic particles and aqueous magnetorheological fluids. *Smart Mater Struct.* 18:085009. doi: 10.1088/0964-1726/18/8/085009

Chin, B. D., Park, J. H., Kwon, M. H., and Park, O. O. (2001). Rheological properties and dispersion stability of magnetorheological (MR) suspensions. *Rheologica Acta* 40, 211–219. doi: 10.1007/s003970000150

Clercx, H. J. H., and Bossis, G. (1993). Electrostatic interactions in slabs of polarizable particles. *J. Chem. Phys.* 98, 8284–8293. doi: 10.1063/1.464534

Cvek, M., Mrlík, M., Moucka, R., and Sedlacik, M. (2018). A systematical study of the overall influence of carbon allotrope additives on performance, stability and redispersibility of magnetorheological fluids. *Colloids Surf. A* 543, 83–92. doi: 10.1016/j.colsurfa.2018.01.046

De Vicente, J., Bossis, G., Lacis, S., and Guyot, M. (2002). Permeability measurements in cobalt ferrite and carbonyl iron powders and suspensions. *J. Magn. Magn. Mater.* 251, 100–108. doi: 10.1016/S0304-8853(02)00484-5

Dong, Y. Z., Piao, S. H., Zhang, K., and Choi, H. J. (2018). Effect of CoFe2O4 nanoparticles on a carbonyl iron based magnetorheological suspension. *Colloids Surf. A* 537, 102–108. doi: 10.1016/j.colsurfa.2017.10.017

Esmaeilnezhad, E., Jin Choi, H., Schaffie, M., Gholizadeh, M., Ranjbar, M., and Hyuk Kwon, S. (2017). Rheological analysis of magnetite added carbonyl iron based magnetorheological fluid. *J. Magnetism Magnetic Mater.* 444, 161–167. doi: 10.1016/j.jmmm.2017.08.023

Fall, A., Bertrand, F., Hautemayou, D., Mézière, C., Moucheront, P., Lemaitre, A., et al. (2015). Macroscopic discontinuous shear thickening versus local shear jamming in cornstarch. *Phys. Rev. Lett.* 114:098301. doi: 10.1103/PhysRevLett.114.098301

Fall, A., Huang, N., Bertrand, F., Ovarlez, G., and Bonn, D. (2008). Shear thickening of cornstarch suspensions as a reentrant jamming transition. *Phys. Rev. Lett.* 100:018301. doi: 10.1103/PhysRevLett.100.018301

Fang, F. F., Choi, H. J., and Jhon, M. S. (2009). Magnetorheology of soft magnetic carbonyl iron suspension with single-walled carbon nanotube additive and its yield stress scaling function. *Colloids Surf. A* 351, 46–51. doi: 10.1016/j.colsurfa.2009.09.032

Ginder, J. M., Davis, L. C., and Elie, L. D. (1996). Rheology of magnetorheological fluids: models and measurements. *Int. J. Mod. Phys. B* 10, 3293–3303. doi: 10.1142/S0217979296001744

Hashemi, M. R., Manzari, M. T., and Fatehi, R. (2016). A SPH solver for simulating paramagnetic solid fluid interaction in the presence of an external magnetic field. *Appl. Math. Model.* 40, 4341–4369. doi: 10.1016/j.apm.2015.11.020

Hashemi, M. R., Manzari, M. T., and Fatehi, R. (2018). Direct numerical simulation of magnetic particles suspended in a Newtonian fluid exhibiting finite inertia under SAOS. *J. Non-Newtonian Fluid Mech.* 256, 8–22. doi: 10.1016/j.jnnfm.2018.03.004

Ierardi, R. F., and Bombard, A. J. (2009). Off-state viscosity and yield stress optimization of magneto-rheological fluids: a mixture design of experiments approach. *J. Phys. Conf. Series* 149:012037. doi: 10.1088/1742-6596/149/1/012037

Jang, I. B., Kim, H. B., Lee, J. Y., You, J. L., Choi, H. J., and Jhon, M. S. (2005). Role of organic coating on carbonyl iron suspended particles in magnetorheological fluids. *J. Appl. Phys.* 97:10Q912. doi: 10.1063/1.1853835

Kang, T. G., Hulsen, M. A., and den Toonder, J. M. (2012). Dynamics of magnetic chains in a shear flow under the influence of a uniform magnetic field. *Phys. Fluids* 24:042001. doi: 10.1063/1.4704822

Kim, M. S., Liu, Y. D., Park, B. J., You, C.-Y., and Choi, H. J. (2012). Carbonyl iron particles dispersed in a polymer solution and their rheological characteristics under applied magnetic field. *J. Indus. Eng. Chem.* 18, 664–667. doi: 10.1016/j.jiec.2011.11.062

Klingenberg, D. J., and Zukoski, C. F. (1990). Studies on the steady-shear behavior of electrorheological suspensions. *Langmuir* 6, 15–24. doi: 10.1021/la00091a003

Kordonski, W. I., and Golini, D. (1999). Fundamentals of Magnetorheological fluid utilization in high precision finishing. *J. Intell. Mater. Syst. Struct.* 10, 683–689. doi: 10.1106/011M-CJ25-64QC-F3A6

Lacis, S., and Gosko, D. (2009). Direct numerical simulation of MR suspension: the role of viscous and magnetic interactions between particles. *J. Phys.* 149:012066. doi: 10.1088/1742-6596/149/1/012066

Laun, H. M., Gabriel, C., and Kieburg, C. (2010). Twin gap magnetorheometer using ferromagnetic steel plates—performance and validation. *J. Rheol.* 54, 327–354. doi: 10.1122/1.3302804

Lim, S. T., Cho, M. S., Jang, I. B., and Choi, H. J. (2004). Magnetorheological characterization of carbonyl iron based suspension stabilized by fumed silica. *J. Magnetism Magnetic Mater.* 282, 170–173. doi: 10.1016/j.jmmm.2004.04.040

Lootens, D., Van Damme, H., and Hébraud, P. (2003). Giant stress fluctuations at the jamming transition. *Phys. Rev. Lett.* 90:178301. doi: 10.1103/PhysRevLett.90.178301

López-López, M. T., Kuzhir, P., Caballero-Hernandez, J., Rodríguez-Arco, L., Durán, J. D., and Bossis, G. (2012). Yield stress in magnetorheological suspensions near the limit of maximum-packing fraction. *J. Rheol.* 56:1209. doi: 10.1122/1.4731659

Mari, R., Seto, R., Morris, J. F., and Denn, M. M. (2014). Shear thickening, frictionless and frictional rheologies in non-Brownian suspensions. *J. Rheol.* 58, 1693–1724. doi: 10.1122/1.4890747

Pan, Z., de Cagny, H., Weber, B., and Bonn, D. (2015). S-shaped flow curves of shear thickening suspensions: Direct observation of frictional rheology. *Phys. Rev. E* 92:032202. doi: 10.1103/PhysRevE.92.032202

Plachy, T., Kutalkova, E., Sedlacik, M., Vesel, A., Masar, M., and Kuritka, I. (2018). Impact of corrosion process of carbonyl iron particles on magnetorheological behavior of their suspensions. *J. Indus. Eng. Chem.* 66, 362–369. doi: 10.1016/j.jiec.2018.06.002

Scales, P. J., Johnson, S. B., Healy, T. W., and Kapur, P. C. (1998). Shear yield stress of partially flocculated colloidal suspensions. *AIChE J.* 44, 538–544. doi: 10.1002/aic.690440305

Suzuki, M., Makino, K., Yamada, M., and Linoya, K. (1981). A study on the coordination number in a system of randomly packed uniform sized spheres. *Int. Chem. Eng.* 21, 482–488.

Tao, R. (2001). Super-strong magnetorheological fluids. *J. Phys.* 13, R979–R99. doi: 10.1088/0953-8984/13/50/202

Wyart, M., and Cates, M. E. (2014). Discontinuous shear thickening without inertia in dense non-Brownian suspensions. *Phys. Rev. Lett.* 112:098302. doi: 10.1103/PhysRevLett.112.098302

Conflict of Interest Statement: The authors declare that the research was conducted in the absence of any commercial or financial relationships that could be construed as a potential conflict of interest.

frontiers in Materials

ORIGINAL RESEARCH
published: 04 February 2019
doi: 10.3389/fmats.2019.00006

A Bi-Directional, Liquid-Spring-Magnetorheological-Fluid-Damper System

*Nicholas Maus and Faramarz Gordaninejad**

Composite and Intelligent Materials Laboratory, Department of Mechanical Engineering, University of Nevada, Reno, NV, United States

The goal of this study was to demonstrate the feasibility of a novel fail-safe, bi-directional liquid spring, controllable magnetorheological fluid damper (BDLS-CMRD). This research introduces a device with independently pre-set spring forces in compression and rebound combined with controllable MR fluid damping. The BDLS-CMRD can potentially replace traditional metal spring-damper suspension systems. Bulky and heavy metal spring-damper suspension systems can be upgraded to the smaller and lighter BDLS-CMRD, reducing the mass of vehicle suspensions. In this work, a BDLS-CMRD was designed, fabricated, tested, and evaluated in three phases. The first design phase demonstrates the concept of a liquid spring with different spring forces in compression and rebound. The second phase incorporates viscous fluid damping of pure silicone fluid with the first phase BDLS. The final design phase combines a controllable magnetorheological fluid (MRF) damper with the first phase BDLS. This study presents the response of the BDLS-CMRD in a wide range of preloaded conditions and frequencies. Experiments were performed for sinusoidal displacements in the quasistatic and dynamic ranges to evaluate the performance of the BDLS-CMRD under different magnetic fields. The experimental results demonstrate that the device operates with significantly different spring forces from the compression to rebound regions, while providing passive viscous fluid damping or controllable MR fluid damping. This system has successfully demonstrated that the utility of a bi-directional liquid spring can be combined with the reliability of passive viscous fluid damping and the capabilities of controllable MR fluid damping into one compact and versatile device.

Keywords: fail-safe, bi-directional, liquid spring, controllable, magnetorheological fluid damper

OPEN ACCESS

Edited by:
Weihua Li,
University of Wollongong, Australia

Reviewed by:
Xufeng Dong,
Dalian University of Technology (DUT), China
Huaxia Deng,
Hefei University of Technology, China

****Correspondence:***
Faramarz Gordaninejad
faramarz@unr.edu

Specialty section:
This article was submitted to Smart Materials, a section of the journal Frontiers in Materials

Received: *06 September 2018*
Accepted: *14 January 2019*
Published: *04 February 2019*

Citation:
Maus N and Gordaninejad F (2019) A Bi-Directional, Liquid-Spring-Magnetorheological-Fluid-Damper System. Front. Mater. 6:6. doi: 10.3389/fmats.2019.00006

INTRODUCTION

The role of vibration and shock isolation has been filled traditionally by heavy metal springs and passive dampers. These traditional suspension systems are heavy and bulky. To make vehicles lighter and more adaptable, buildings and structures more resilient, and sensitive instruments more durable, a complete suspension system upgrade and replacement is necessary. This proposed system presents such a system.

The "Double-acting liquid spring" was first introduced in 1959 (Zumwalt, 1959). Double acting or bi-directional liquid springs are devices capable of reaction forces in both compression and rebound. Similar to traditional metal springs, the reaction forces of a bi-directional liquid

spring seek to return the spring to its initial position or equilibrium. However, unlike traditional metal springs, bi-directional liquid springs can have different reaction forces in compression and rebound.

This device demonstrates a force in compression that is three times that of its force in rebound. This force can be "tuned" by setting the available volume in either chamber, making this device's performance more adaptable in a similar size system when compared to traditional suspension systems. This unique dual chamber device utilizes compressible fluid springe rates in both compression and rebound by displacing a small piston from a neutral position between the chambers. The displacement compresses the MRF and results in a spring force counter to the force causing the displacement. An MR valve is incorporated in a manner that also functions as a passive annular damping valve to result in damping in the "off" or unpowered state.

Other studies have theorized the possibility of such a bi-directional liquid spring combined with passive viscous fluid damping (Samantaray, 2009). That work seeks to theoretically analyze a liquid spring damper that works in both compression and rebound and even suggests a possible design for a test apparatus, though no prototype is developed and/or tested in that study.

Magnetorheological fluid devices use magnets to control the properties of the MRF. In most devices electromagnets are used to control the viscosity and yield stress as a function of input electric current. These devices typically incorporate the electromagnet into the valves or narrow passages of the device. Potnuru et al. (2013) modeled, developed, and tested a double-ended, but not bi-directional, controllable MRF liquid spring damper. Raja et al. (2013) presented the design and development of a compressible magnetorheological damper where a theoretical model that considers the compressibilty of a magnetorheological fluid damper is developed and verified by the testing and evaluation of a prototype device. McKee et al. (2018) explored the temperature dependency of MR fluid and includes a comprehensive study of reciprocating seals. Hong et al. (2006) investigated a double-ended automotive strut that is filled with a compressible MR fluid. Hong experimentally verified a model that considers the compressibility for both the liquid spring and the compressible flow through the MR valve. Wang and Gordaninejad (2008) compiles and reviews the current state of compressible MR technology.

In this work, a novel fail-safe, bi-directional liquid spring, controllable magnetorheological fluid damper system (BDLS-CMRD) is designed, fabricated, tested, and evaluated. This proposed system is the first to combine a bi-directional liquid spring with fail-safe passive viscous fluid damping and controllable magnetorheological fluid damping in one compact device.

DESIGN

Design Requirements

The requirements for this liquid spring device include bi-directionality, a maximum internal pressure of 41.37 MPa (6,000 psi) in order to operate the linear compressibility region (Lichtenthaler et al., 1978; Sandberg and Sundqvist, 1982), and an experimental range of 2.54 cm in each direction. As a result of this pressure range, the device is capable of a spring force of up to 437.8 N/mm (2,500 lb/in). The experimental device is ∼30 cm tall and 15 cm in outside diameter. The chambers are ∼10 cm inside diameter and 8 cm in depth.

This unique two-chamber design allows for the device to have equal or dissimilar spring rates in compression and rebound. The device can be "pre-set" with regard to spring rate and damping. The spring rate in both compression and rebound can be pre-set independently. By initially assembling the device with different solid masses in either chamber, the initial volume of the chamber was altered. By precisely designing these masses, the volume of the fluid was controlled, and the spring rate was determined. A mass that displaces ∼50% of the original initial volume was tested. This mass allows for the maximum force of 11.1 kN (2,500 lb) in order to stay within the linear compression region. **Figure 1** displays the cross-sectional view of the BDLS–CMRD tested in this study.

Figure 1 illustrates how the rod gland is held together by the bearing retainer and the internal retainer. Also, **Figure 1** shows how the spring piston is held by the piston gland which is contained within the cylinder partition. The MR piston is attached to the piston rod directly on top of the spring piston in chamber 1. To increase the spring constant in compression, the tuning mass is installed to lower the initial volume in chamber 2.

Seal Gland Design

Due to the unique design of BDLS-CMRDs, internal forces on the spring piston seek equilibrium at the displacement that was set

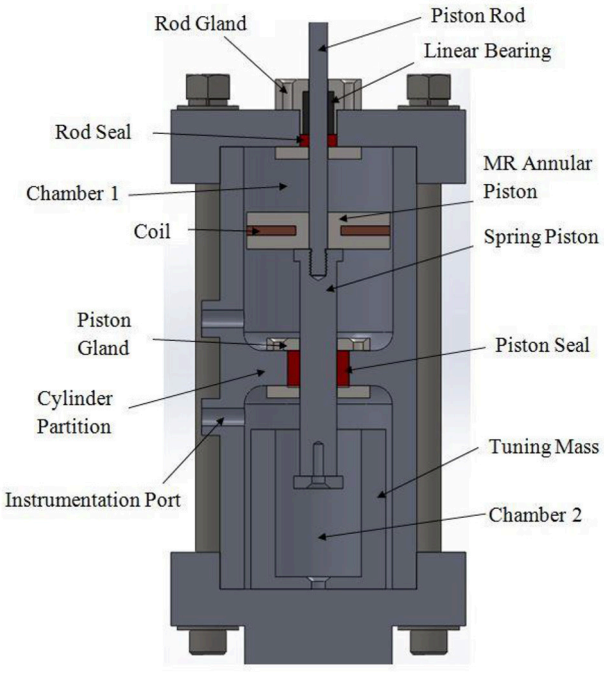

FIGURE 1 | A cross-sectional view of the BDLS-CMRD shows the general arrangement including: seals, pistons, glands, and tuning mass. Reproduced with permission from Maus and Gordaninejad (2014).

when the device was assembled and filled with the working fluid. Also, the device allowed for different spring rates in compression and rebound by changing the initial volume of the chambers. The model was constructed by first finding the pressures individually for each chamber, which can be expressed by:

$$P_n = \frac{F}{A_p} + P_i \tag{1}$$

where P_n is the pressure corresponding to a specific chamber, A_p is the area of the spring piston, and P_i is the initial pressure. Since the chambers are filled with a fluid, the pressures cannot be negative. For values ≤ 0, the pressure values are zero. An expression for the spring force of a liquid spring is (McKee et al., 2018):

$$F_{spring} = kx \tag{2}$$

$$k = \frac{\left(A_p{}^2\beta\right)}{V_n} \tag{3}$$

where x is the displacement, V_n is the volume of the same specific chamber, and β is the bulk modulus. Combining Equations (1–3), the spring force for a single chamber is:

$$F = \frac{\left(A_p{}^2\beta\right)}{V_n} x + P_i\,(x)\,A_p \tag{4}$$

Since the pressure in the opposing chambers results in opposite forces, these forces can be added to achieve a force balance. The force in chamber 1 is added to the force in chamber 2, resulting in a total spring force of F_{spring}. Internal friction is a key consideration in the modeling of a BDLS-CMRD. Due to the design requirements of the seals, friction can be a significant contribution to the total force of the device. Friction, in this model, is characterized as a constant friction and a dynamic friction. Constant friction consists of two forces and is considered to be the normal friction force of the seal against the surfaces of the rod and piston. Constant friction, F_f, is found experimentally to be 178 N (40 lb); the experimental procedure will be discussed later. The dynamic seal friction, F_{fd}, is:

$$F_{fd} = \frac{1}{2} A_s\,(P_1 - P_2) \tag{5}$$

where A_s is the area of the seals in contact with the piston and rod, and P_1 and P_2 are the pressures in the bottom and top chambers, respectively (Dixon, 2007). Since there are two seals working simultaneously in opposition, the dynamic seal friction from Equation (5) becomes:

$$F_{fd} = F_{s1} - F_{s2} \tag{6}$$

then:

$$F_{fd} = \frac{1}{2}\left(A_{s1}\,(P_1 - P_2) - A_{s2}\,(P_2 - P_a)\right) \tag{7}$$

where P_a is the ambient pressure outside the device.
Thus, the total seal friction is:

$$F_{total} = F_f \pm F_{fd} \tag{8}$$

where dynamic seal friction is subtracted from the constant friction term when velocity is positive and added when velocity is negative. The model predictions for the bi-directional liquid spring and seal friction characteristics are shown in **Figure 2**.

Buckling of the piston rod is of primary concern. Finite element analysis (FEA) is performed to ensure a gland design that limits rod buckling. In the FEA, a linear bearing, or "bushing bearing," is modeled in frictional contact with the rod. Using a single mode Euler buckling model, the reaction force between the rod and bearing is found when the rod is subjected to a compressive load. The displacement of the contact point between the rod and the bearing is found to determine the radial loading on the bearing surface. This information is crucial in bearing selection since bearings are rated by radial load. It is found that at a compressive axial load on the rod of 11.1 kN (2,500 lb), a bearing rated for 0.27 kN (60 lb) is adequate to support the radial load, restricting the buckling of the rod. **Figure 3** shows the results of the linear buckling FEA model, a solid model of the gland assembly, and the profile of the R54 seal gland assembly.

A bearing takes the shear load off of the seal while allowing the rod to travel in the axial direction. Bearings are commercially available in sizes up to 5 cm in diameter and can be custom fabricated to almost any size. These bearings are made in many different configurations and from a variety of materials. Larger bearings for higher loads are commonly made of bronze and incorporate grooves and channels for additional lubrication. Smaller linear bearings are typically made of aluminum and lined with Teflon to minimize friction on the piston rod.

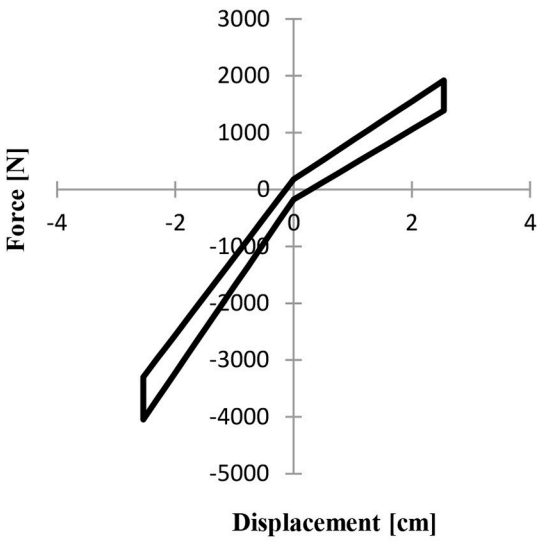

FIGURE 2 | Force displacement plot for the bi-linear liquid spring seal friction is illustrated with experimental data.

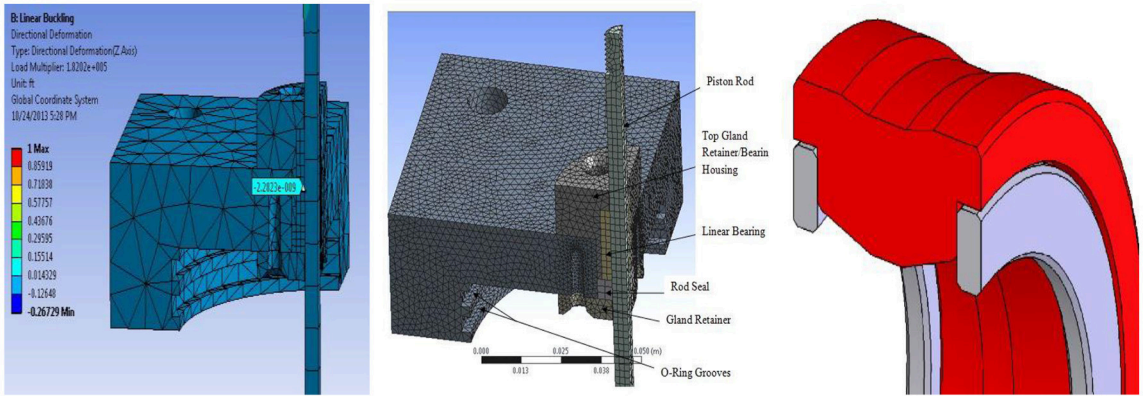

FIGURE 3 | (Left) A one quarter, three-dimensional finite element linear buckling model is used to determine radial displacement and force, **(Middle)** One quarter, three-dimensional gland assembly model showing the upper gland design. **(Right)** Custom R54 seal design.

Figure 3 shows how the piston rod is retained by the gland assembly. The gland assembly consists of a linear bearing and a rod seal. The linear bearing is pressed into the top gland retainer, and the entire assembly is held internally by the lower gland retainer. The seal between the cylinder heads and the outer cylinder wall is accomplished by compressing a pair of O-rings into the O-ring grooves.

Selection of seals for this device can be a challenge due to the pressure requirements. Other considerations are rod speed, temperature, chemical resistance, and size restrictions. Pressure is of primary concern because the seal must hold uneven pressures from either side of the gland. Conventional V-packing is one directional and leaks slowly from one chamber to the other, resulting in a change of equilibrium for the device. Standard PTFE U-seals are not well suited for low viscosity/high pressure service. These seals tend to be designed for either low viscosity or high pressure, not both. A high-performance seal is needed to meet all the requirements. High-performance seals that will not leak low viscosity fluid under high pressure are custom-made for this system. These retain uneven pressure from both sides of the gland and are capable of withstanding moderately high rod velocities and temperatures. The seals incorporate an 8% diametric compression. The seal material is Duralast 4203, and the incorporated back-up rings are Permachem 6643[1]. These materials are ideal for low and high viscosity silicone oil under high pressure. **Figure 3** shows the profile of the seal.

Shear force is a force acting perpendicular to the normal axial forces experienced by liquid springs and dampers. The foremost effect of shear loading is uneven force on the seal and gland. In standard operation the seal exerts even force all around the rod due to the seal having a smaller internal diameter than the rod's outer diameter. This interference fit compresses the seal (that is made of considerably softer material than the rod) and creates an interface to retain pressure. When the seal is loaded in shear, the force of compression is not uniform. If the non-uniformity is sufficiently large, the interface between the seal and rod may not be sufficient to retain the pressure. In extreme cases, the compression of the seal may be so high that an actual gap occurs between seal and rod. Higher shear forces can bend the rod, resulting in damage to either the gland or the rod or both. Any damage to the rod would prematurely wear the seal or possibly cause immediate failure. The most common solution to shear loading of these devices is to incorporate a linear bearing.

MR Valve Design

Damping force at given velocities and amperages can be tuned by changing the gap between the annular piston and the chamber wall. The gap for the frequency and force range selected was determined to be 1 mm. Each data point in **Figure 4** shows the maximum magnetic field at 5 Amps through the MRF at each gap width modeled and the orientation of the magnetic coil within the damping piston. The magnetic field in the MRF decreases as the annular piston gap is increased.

An electromagnet was incorporated into the damping piston. A magnetic path was developed from one end of the piston to the other when an electric current was applied. This magnetic path travels through the cylinder wall and the MR fluid because both are magnetically permeable.

The annular MR piston incorporated 22-gauge enameled copper wire. Using a staggered packing order it was determined that a 4.8 mm by 25.4 mm area can be filled with 225 windings of 22 gauge wire. These dimensions allowed for the optimal ratio of amp turns to valve length for the geometric restrictions of the device. The 22-gauge wire was optimal for this application because it produced the highest number of amp turns while operating at 5 Amps continuous current. **Table 1** shows the magnetic field as a function of amperage for the optimized geometry and wire gauge. The values for the magnetic field, B in Tesla, were determined by FEA and added to the table. **Figure 5** illustrates the magnetic field in the MR valve predicted by FEA and presented the data in **Table 1**.

Electromagnetic Finite Element Analysis

Finite element analysis was performed using Ansoft software to solve for the magnetic field through the MR valve. This model

[1]American High Performance Seals http://www.ahpseals.com/products/rod.php#2. American High Performance Seals, Inc.

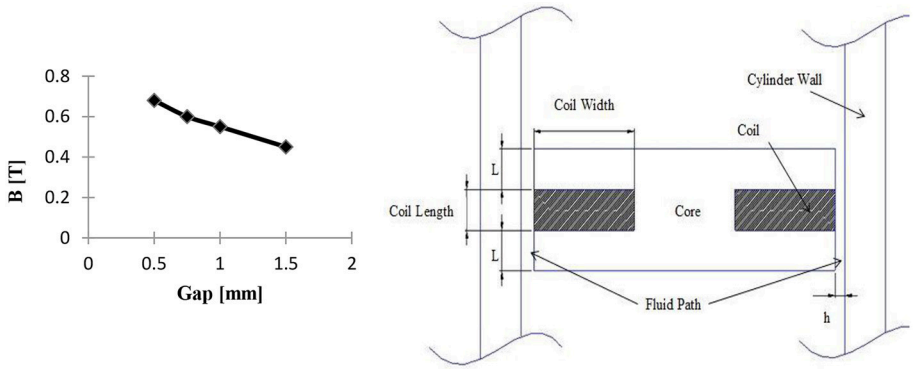

FIGURE 4 | (Left) The magnetic field density at 5 Amps decreases as the gap width increases from 0.5 to 1.5 mm. In order not to exceed the load limit of 11.1 kN (2,500 lb) at 4 Hz and 5 Amps, it is necessary to incorporate a 1mm gap. **(Right)** The diagram of electromagnetic piston and annular valve. Reproduced with permission from Maus and Gordaninejad (2014).

TABLE 1 | The magnetic field through the annular MR valve reaches saturation above 5 amps and exceeds geometric constraints near 1,100 amp turns.

I, Amps	Amp Turns	B, Tesla	V, Volts
0.1	22.5	0.00	0.07
0.2	45	0.04	0.14
0.5	112.5	0.16	0.34
1	225	0.25	0.69
2	450	0.36	1.38
3	675	0.44	2.07
4	900	0.51	2.76
5	1,125	0.57	3.45
6	1,350	0.60	4.14
7	1,575	0.62	4.83
8	1,800	0.64	5.52
9	2,025	0.65	6.20
10	2,250	0.66	6.89
13	2,925	0.68	8.96
20	4,500	0.69	13.79

assumes uniform temperature and fluid properties. **Figure 5** shows how the magnetic field through the MR valve decreases due to the lower permeability of the MR fluid compared to the high iron alloys of the piston and cylinder wall. As the gap is increased, more of the less permeable fluid separated the more permeable materials. The maximum magnetic fields of 0.57 Tesla is achieved by the 0.5 mm valve gap at 5 amps. The yellow to red regions in the figure along the edges of the coil and the perimeter of the damping piston indicate the location of the highest field strength.

EXPERIMENTAL SETUP

Rheology

A Physica MCR 300 shear rheometer with data acquisition capable of testing MRF at various temperatures and magnetic fields was used to obtain the fluid properties of yield stress and viscosity.

The carrier fluid for these tests was 5 centistokes (cSt) pure silicone fluid. For the final BDLS–CMRD test, an MR fluid was prepared in-house. The MR fluid consisted of Grade–R—2410 Micropowder Iron (Carbonyl Iron) and the 5 cSt pure silicone fluid. The MR fluid was mixed at a ratio of 80% by weight iron particles to 20% by weight silicone oil. The fluid was mixed using a variable speed mixer for 20 min at 900 rpm to ensure the particles are uniformly dispersed within the carrier fluid.

The rheometer performs tests of shear rates from 0 to 400 s^{-1} while recording values for shear stress, viscosity, and shear rate. All tests were performed with a 28 mm measuring plate set to a gap of 1 mm. A 0.3 mL test sample was used in all tests. Each test was conducted three times to ensure accuracy. A magnetic field can be induced to find these properties for various current levels used to control an MR device. Current levels were correlated to their respective magnetic field values using the Ansoft model described in the previous section. For the MR fluid tests, the magnetic field for 0, 1, and 2 Amps through the internal electromagnet correlated to 0, 0.29, and 0.56 Tesla, and values of τ (I) in Pa were 94.4, 17,247.7, and 22,555.7, respectively.

Quasistatic Test

Quasistatic tests for the bulk modulus, pressures in chambers 1 and 2, and the spring force profiles were performed on an Instron 4210 screw-drive machine. All quasistatic tests were performed at 25.4 cm/min corresponding to 0.016 Hz and were repeated three times. A LabVIEW program was written to record the data from the load cell, linear velocity and displacement transducer (LVDT), and pressure transducers, then to transcribe that data to a spreadsheet. **Figure 6** illustrates the test setup. Also shown, attached to the device, are the valves and hydraulic lines used to fill and pressurize the device.

Dynamic Test Setup

Dynamic tests were accomplished using an MTS damper testing system. The setup for dynamic testing was nearly identical to the quasistatic case, the difference being that the MTS has an internal LVDT. Tests were conducted first on the liquid spring damper configuration. Test frequencies range

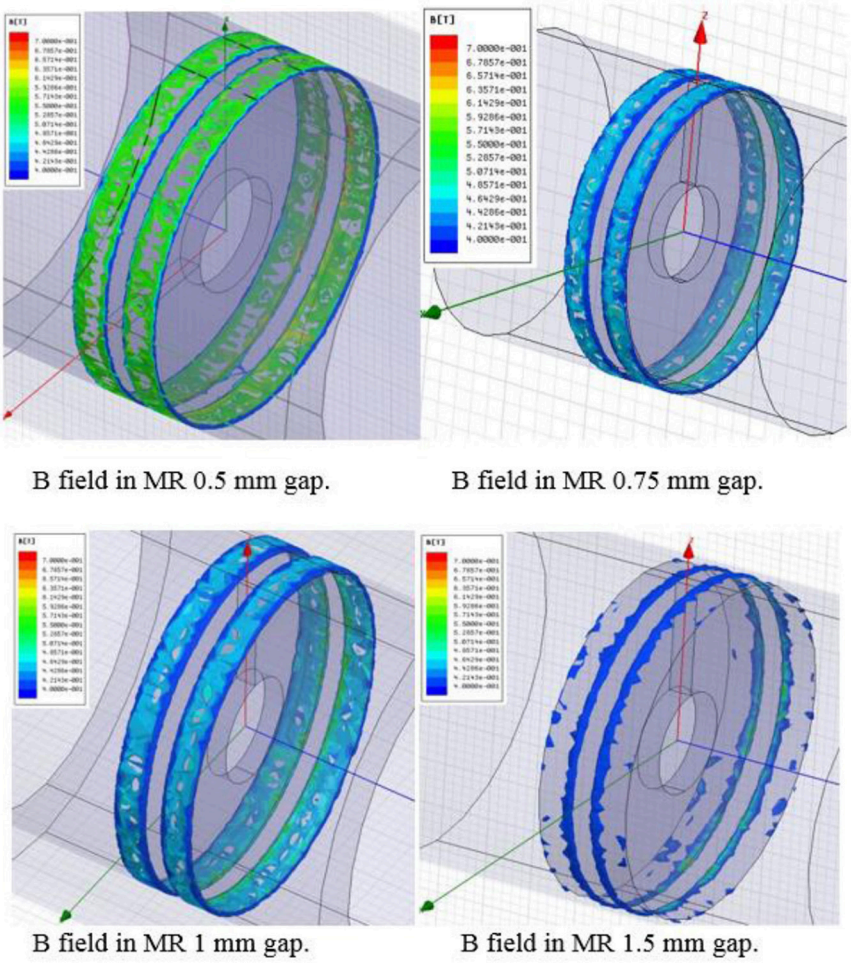

FIGURE 5 | The magnetic field in the MRF is shown to decrease as the gap is increased.

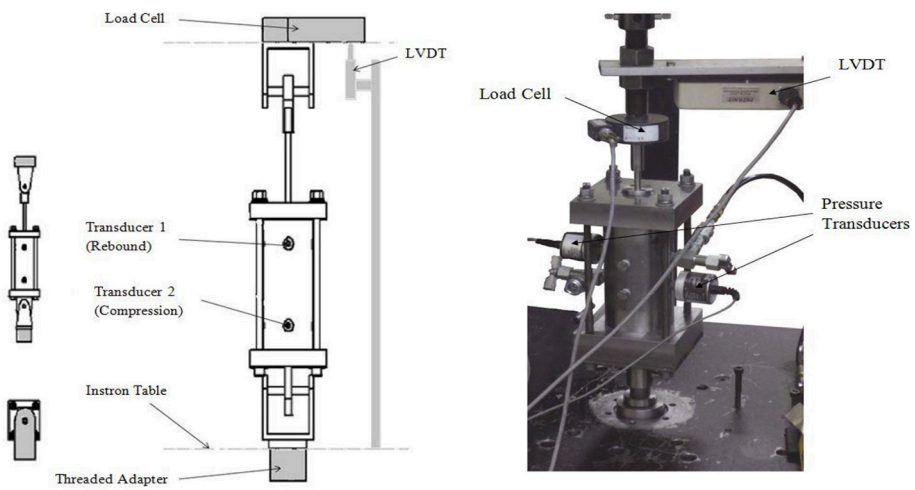

FIGURE 6 | Schematic and photograph of quasistatic test setup showing the placement of the transducers, LVDT, load cell, and attachment to the screw-drive machine.

from 0.01 to 12 Hz. All tests utilize a 2.54 cm displacement in both compression and rebound and are conducted three times. Next, BDLS–CMRD tests were accomplished on the same equipment. These tests also cover the full displacement of the device, although the frequency range was decreased to 0.01 to 4 Hz.

Experimental Study

A series of tests were conducted to characterize the BDLS–CMRD configuration. The amperage range of 1 to 5 Amps was selected because of the continuous current capacity of the 22-gauge wire used in the electromagnetic coil. The frequency range was selected to limit the maximum compressive force to 11.1 kN as predicted by the BDLS-CMRD model. The maximum external load for buckling of the piston rod was found to correspond with 4 Hz at 5 Amps for the BDLS-CMRD configuration. Tests are conducted for frequencies of 0.1, 1, 2, 3, and 4 Hz at 0, 1, 2, 3, 4, and 5 Amps. All tests are repeated three times. Tests are accomplished using an MTS damper testing system. All tests utilize a 2.54 cm displacement in both compression and rebound and are conducted three times.

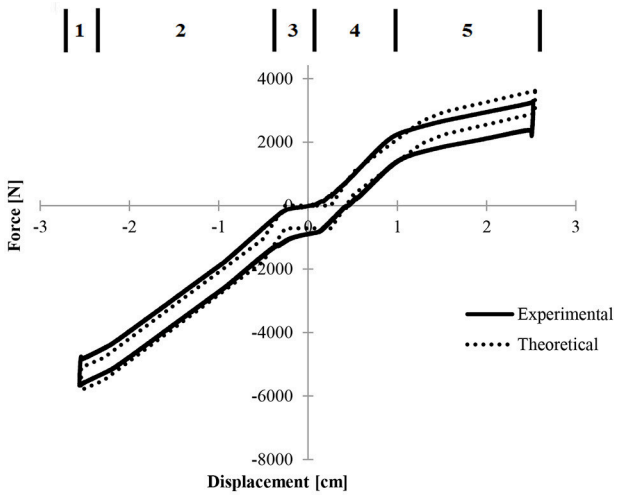

FIGURE 7 | Force displacement curves for 6.89 MPa symmetric pressure illustrating the zones of performance.

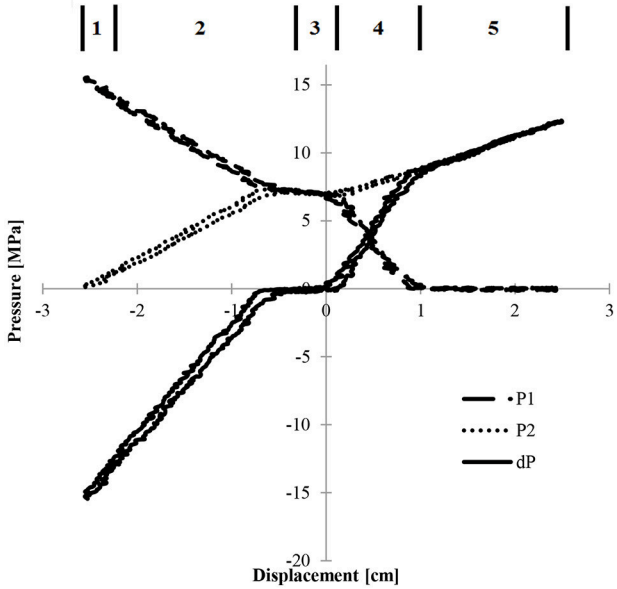

FIGURE 8 | Pressure versus displacement curves in chambers 1 and 2 (P1 and P2, respectively) and the corresponding pressure differential, dP showing the multi-linear zones of the device.

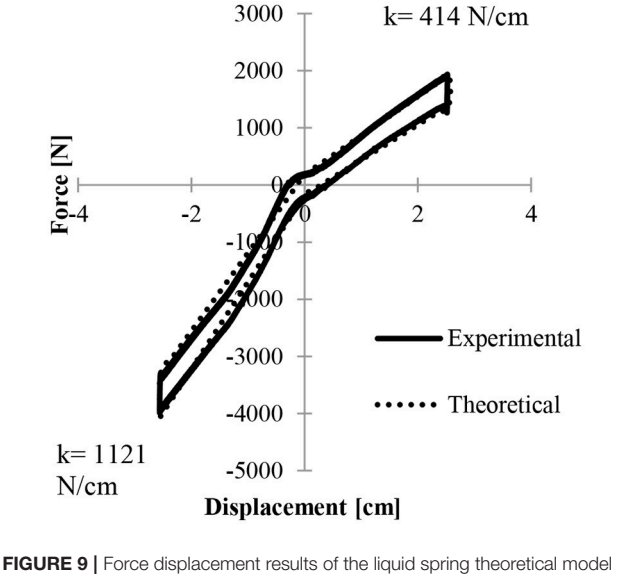

FIGURE 9 | Force displacement results of the liquid spring theoretical model with seal friction accurately predict the quasistatic experimental data.

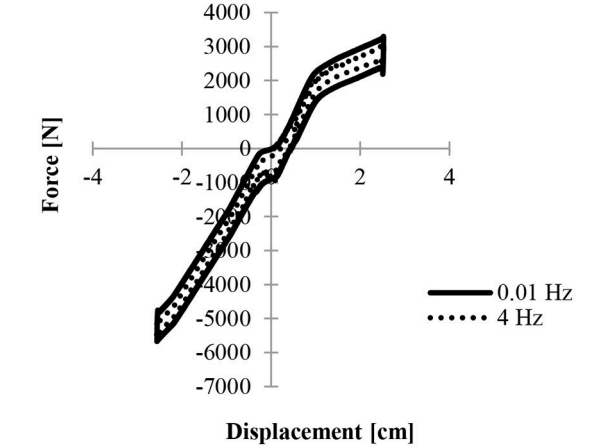

FIGURE 10 | Force displacement curves for seal friction in the quasistatic (0.01 Hz) and dynamic (4 Hz) regions indicating that seal friction does not dramatically increase with velocity.

RESULTS

Unloaded Pre-pressurizing

Pre-pressurizing this device resulted in a phenomenon of multi-linearity. "Pre-pressurizing" the device involved increasing the pressure in one or both chambers to simulate preloading without allowing the device to shift from the zero displacement or neutral position. The device was secured in the load testing machine and a hand pumped accumulator was used to increase pressure. This process was monitored with pressure transducers and verified with calibrated pressure gauges. Multi-linearity manifested in five distinct regions. **Figure 7** shows from left to right that at the most extreme compression (zone 1), there is a softening followed by a higher spring rate (zone 2) followed by a constant force (zone 3) as the device reaches its displacement equilibrium. Continuing from left to right, the force then returns to a higher spring rate (zone 4) and finally softens again as the device reaches its full displacement in rebound (zone 5). The experimental results, shown as a solid line are compared to the theoretical results as modeled by solving equations one through eight at each discrete displacement in the experimental range.

The softening regions occurred when only one chamber of the device was under pressure and there was no opposing force, resulting in a lower net force. **Figure 8** illustrates how pressure differential was affected by 6.89 MPa symmetric pressurization. Again, the multi-linear zones are shown to demonstrate how the difference in pressure relates to the total force of the device.

The net force decreased when one of the pressures approaches zero. Constant force of the central region (zone 3) was due to the seal friction being the dominant force. In this region, the pressure differential, and therefore the force differential, is less than the force due to seal friction. The softening region at the right of **curve P1** was due to the lower chamber having zero pressure (zone 5).

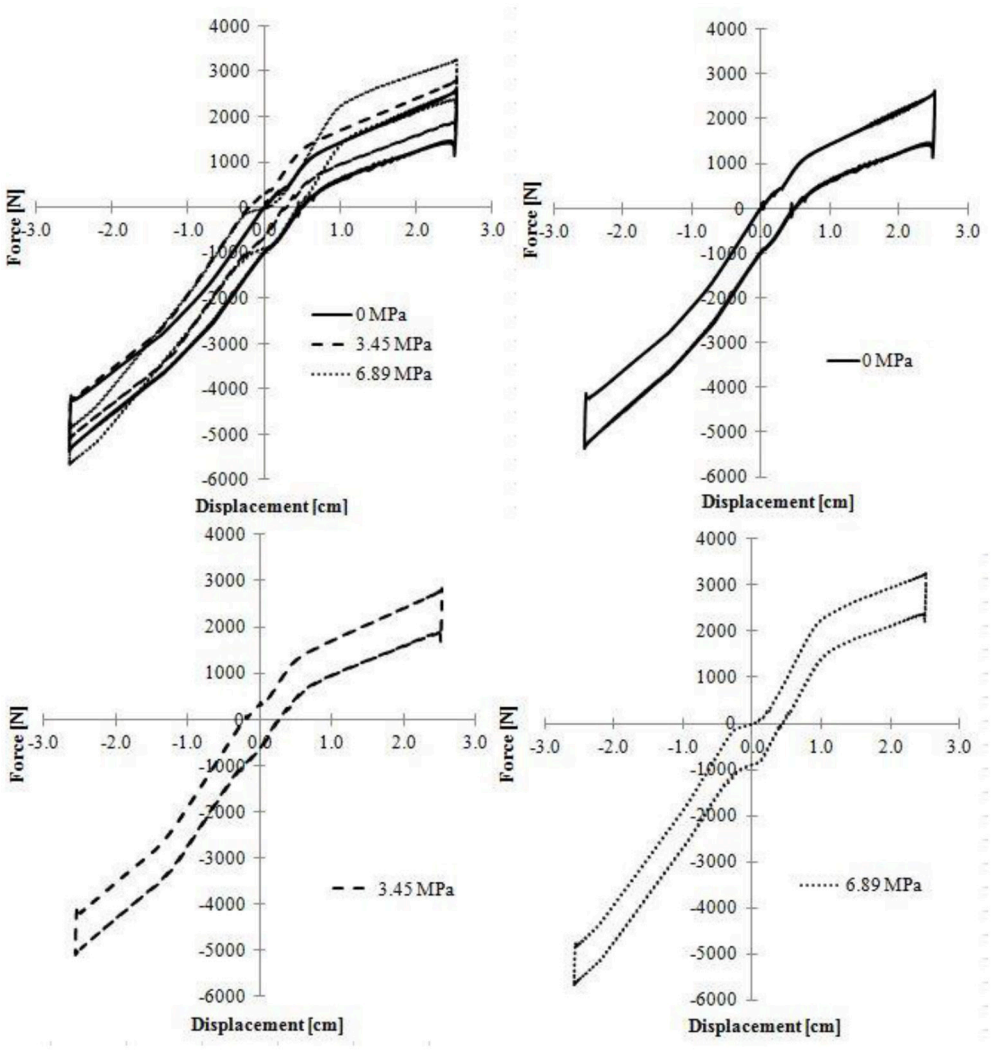

FIGURE 11 | Comparison of quasistatic symmetric, symmetrically pressurized force displacement curves at 0, 3.45, and 6.89 MPa shows the development of the multi-linear regions.

Bi-Directional Liquid Spring

Quasistatic testing is performed and compared to the liquid spring model. The model is an idealized case and does not exactly follow the curving lines of the experimental data. The discrepancy between model and experimental data is small, and maximum forces in both compression and rebound vary no more than 3% from the experimental results. **Figure 9** compares the quasistatic test results and the theoretical model.

Seal Friction Characterization

Figure 10 shows the two most extreme cases when considering hysteresis due to seal friction.

A difference of <100 N can be seen when comparing quasistatic experimental results to 4 Hz dynamic data. This difference is $<2\%$ of the maximum compressive force.

Symmetric Pressurizing

Symmetric pressurization allowed for the testing and controlling of the multi-linear regions. "Symmetric Pressurizing" was accomplished by pre-pressurizing both cylinders equally. As initial pressures were increased, the multi-linear regions become more apparent. **Figure 11** displays how the symmetric pressurization results become more multi-linear as initial pressure is increased.

Preloading

Figure 12 demonstrates how preloading shifts the multi-linear results. "Preloading" involved pre-pressurizing one chamber in order to reach an initial load or reaction force in compression or rebound. That force was measured using a load cell attached between the test machine and the connecting rod of the device. Preloading in compression shifts the curve

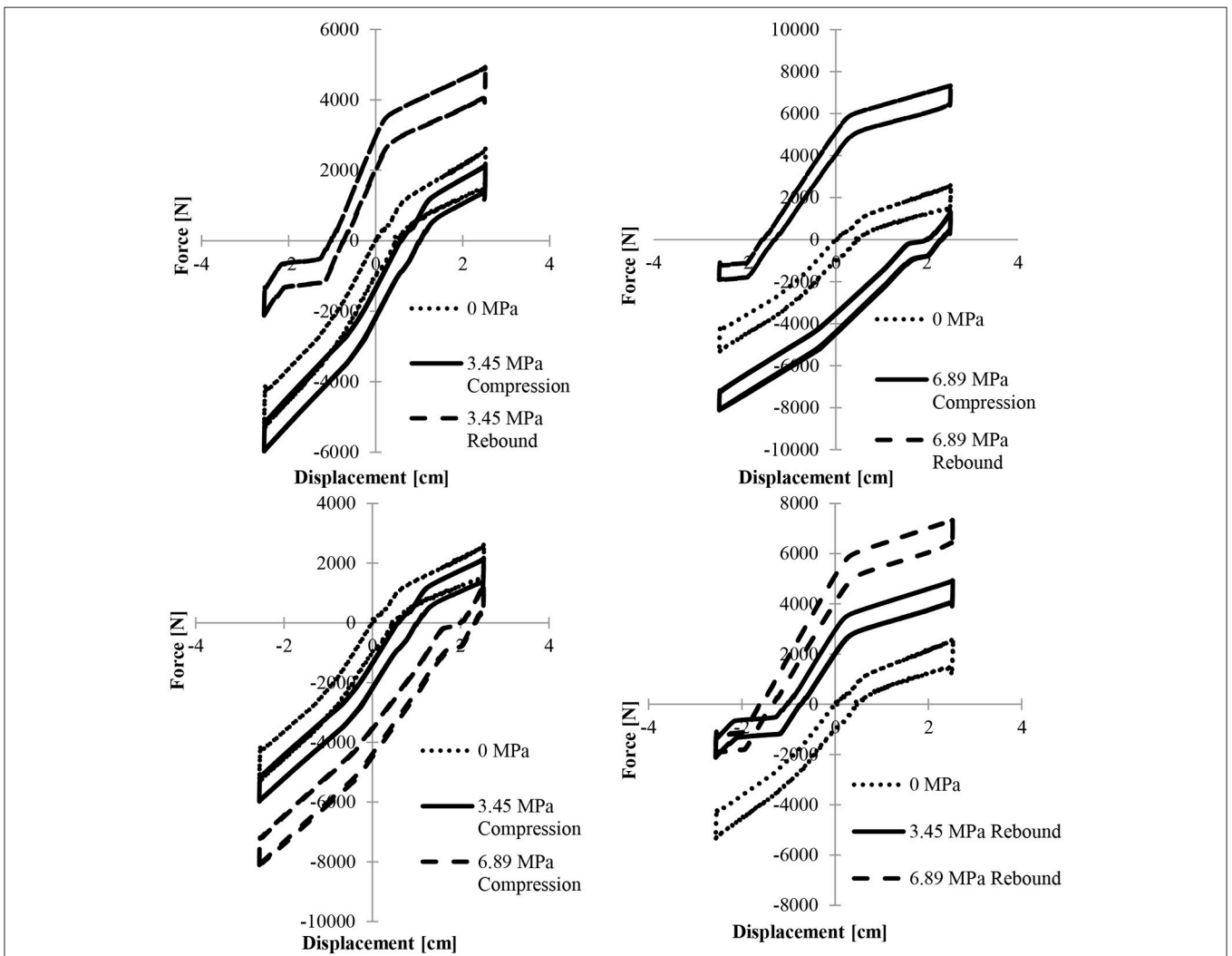

FIGURE 12 | (Top Left) Force displacement plot for quasistatic preloading in compression and rebound at 3.5 MPa compared to 0 MPa initial pressures illustrates the developing multi-linearity. **(Top Right)** Force displacement plot for quasistatic preloading in compression and rebound at 6.89 MPa. **(Bottom Left)** Comparison of quasistatic force versus displacement over the range of 0 to 6.89 MPa preloading in compression illustrates the shift in the multi-linearity. **(Bottom Right)** Comparison of quasistatic force versus displacement over the range of 0 to 6.89 MPa.

down while preloading in rebound shifts the curve up. The results are shifted proportionally; that shift can be estimated by multiplying the internal pressure of either chamber by the cross-sectional area of the spring piston. The Figures compare the unloaded results with the preloaded results in order to show the increase in multi-linearity. **Figure 12** (Bottom) also shows how the plots are shifted as preloading is increased in compression and rebound, respectively. Notice that the curves are shifted farther in their respective directions due to the increase in initial pressure. Also, the results are becoming more multi-linear due to the combination of forces.

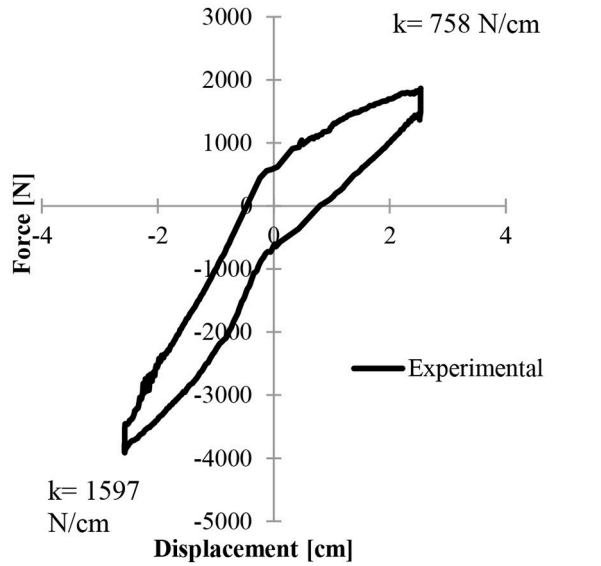

FIGURE 13 | Force displacement plots of the viscous fluid damping bi-directional liquid spring experimental results for a sinusoidal input of 2.5 cm at 6 Hz feature the different spring rates in compression and rebound.

Figure 12 demonstrates a comparison between the symmetric pressurization curve and preloading in both compression and rebound. The Figures show how symmetric pre-pressurizing and preloading result in similar multi-linearity. **Figure 12** also shows that softening regions occur when only one chamber of the device is under pressure. Since only one chamber is under pressure, there is no opposing force, resulting in a lower net force. The regions of constant force are due to the opposing forces being smaller than the constant seal friction. Since the seal friction is constant at quasistatic speeds and that constant force is dominant, the force displacement curve shows a region of constant total force.

Viscous Damping

This device can be configured as a passive liquid spring damper. A theoretical model is developed to predict the passive viscous fluid damping combined with a bi-directional liquid spring. **Figure 13** displays the model verification along with the 6 Hz experimental results.

BDLS-CMRD Full Device Demonstration

The anomalous spikes in the test data are caused by the control system of the test apparatus as the device changes from a negative reaction force to a positive reaction force. The zero force allows inertial forces to be dominant just before being damped out by the device. **Figure 14** demonstrates the bi-directional spring forces in the active MR state. The maximum spring force recorded in compression was 2,328 N/cm and the maximum in rebound was found to be 980 N/cm. Tests were conducted to show that the bi-directional liquid spring functions as a controllable liquid spring damper. In these tests it was apparent that bi-linearity is maintained even at maximum MR fluid damping. **Figure 14** (Left) shows how maximum MR fluid damping force and spring force increase as amperage increases in the BDLS–CMRD. The Figure shows an increase of damping force of more than 250% and a 200% increase in maximum spring force. The increase in damping force is due to MR fluid damping,

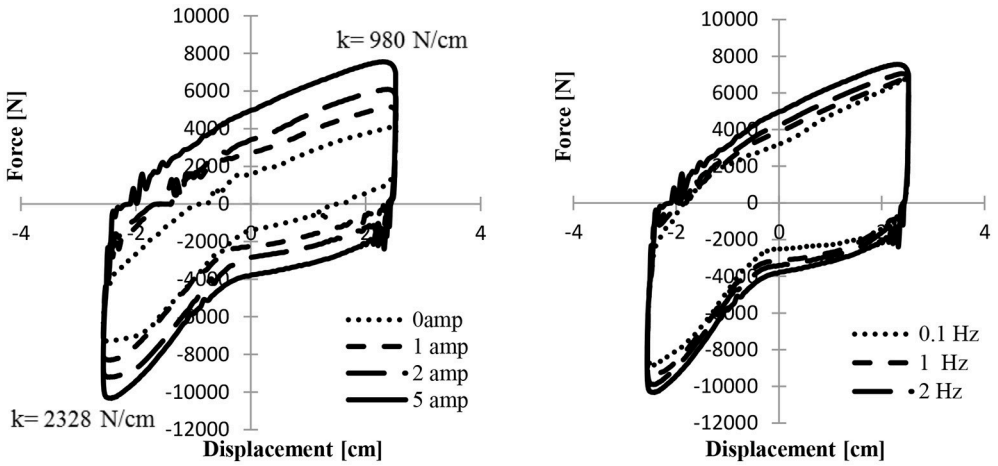

FIGURE 14 | (Left) Force displacement plots for BDLS-CMRD with a sinusoidal input of 2.5 cm at 4 Hz and 0, 1, 2, and 5 Amps illustrating the increasing MR effect. **(Right)** Force displacement plots for BDLS-CMRD with a sinusoidal input of 2.5 cm at 0.1, 1, 2, and 4 Hz.

while the increase in spring force is due to a combination of the higher shear stress and lower initial volume of compressible carrier fluid. Note that the spring rates in compression and rebound are the same for every input current. This is because spring rate is a geometric property and not a function of magnetic field. **Figure 14** (Right) compares the experimental results for the frequency range of 0.1 to 4 Hz at 5 Amps. Damping increases and frequency increases, but the spring rates stay constant with respect to frequency. Every plot has nearly the same spring rates for compression and rebound due to the spring rate being a function of initial volume.

SUMMARY AND CONCLUSIONS

A system is proposed to demonstrate the feasibility of combining a bi-directional liquid spring capable of acting independently in compression and rebound with fail-safe passive viscous fluid damping and controllable MR fluid damping. A theoretical model is developed for the design and characterization of the BDLS-CMRD. The modeling of the individual aspects of the device is broken into bi-directional liquid spring, viscous fluid damping, and MR fluid damping, then the aspects combined to present the entire modeled device. The model incorporates the compressibility and bulk modulus of a fluid, the force due to seal friction, the flow through an annular valve, and the Bingham plastic model for MR fluids. Experiments are conducted to evaluate the performance of the device for its bi-directional liquid spring, viscous fluid damping, and MR fluid damping capabilities. Model verification and experimental results cover the combination of forces, spring force, and pressure. Verification of the viscous fluid damping model is presented followed by experimental results for the complete BDLS-CMRD.

A bi-directional liquid spring can be combined with both fail-safe viscous fluid damping and controllable MR fluid damping into a compact light-weight system. This system can be designed to have different spring rates in compression and rebound that are apparent through all operating frequencies and magnetic fields.

AUTHOR CONTRIBUTIONS

All authors listed have made a substantial, direct and intellectual contribution to the work, and approved it for publication.

ACKNOWLEDGMENTS

This research was partially supported under a US Army contract number W56HZV-07-C-0459. A preliminary version of this study was published in Maus and Gordaninejad (2014).

REFERENCES

Dixon, J. (2007). *The Shock Absorber Handbook: 2nd Edn.* John Wiley & Sons Ltd.

Hong, S. R., Wang, G., Hu, W., and Wereley, N. M. (2006). Liquid spring shock absorber with controllable magnetorheological damping. Proceedings of the Institution of Mechanical Engineers, Part D. *J. Automobile Eng.* 220, 1019–1029. doi: 10.1243/09544070JAUTO74

Lichtenthaler, R. N., Liu, D. D., and Prausnitz, J. M. (1978). Specific Volumes of Dimethylsiloxane Polymers to 900 Bars. *Macromolecules* 11, 192–195.

Maus, N., and Gordaninejad, F. (2014). "A fail-safe, Bi-linear liquid spring controllable magnetorheological fluid damper," in *Proceedings of SPIE - The International Society for Optical Engineering, Vol. 9057, Smart Materials and Structures Conference*, ed Wei-Hsin Liao.

McKee, M., Wang, X., and Gordaninejad, F. (2018). Effects of temperature on performance of a compressible magnetorheological fluid damper-liquid spring suspension system. *J. Intell. Mater. Syst. Struct.* 29:1. doi: 10.1177/1045389X17705203

Potnuru, M. R., Wang, X., Mantripragada, S., and Gordaninejad, F. (2013). A compressible magneto-rheological fluid damper – liquid spring system. *Int. J. Vehicle Design* 63, 256–274. doi: 10.1504/IJVD.2013.056155

Raja, P., Wang, X., and Gordaninejad, F. (2013). A high-force controllable MR fluid damper-liquid spring suspension system. *Smart Mater. Struct.* 23:1015021. doi: 10.1088/0964-1726/23/1/015021

Samantaray, A. K. (2009). Modeling and analysis of preloaded liquid spring/damper shock absorbers. *Simulat. Model. Pract. Theory* 17, 309–325. doi: 10.1016/j.simpat.2007.07.009

Sandberg, O., and Sundqvist, B. (1982). Thermal properties of two low viscosity silicon oils as functions of temperature and pressure. *J. Appl. Phys.* 53, 8751–8755.

Wang, X., and Gordaninejad, F. (2008). Chapter 14 magnetorheological materials and their applications. *Intell. Mater.* 2008, 339–85. doi: 10.1039/9781847558008-00339

Zumwalt, R. F. (1959). *Double-Acting Liquid Spring*. US patent no. 2,899,194 August 11, 1959.

Conflict of Interest Statement: The authors declare that the research was conducted in the absence of any commercial or financial relationships that could be construed as a potential conflict of interest.

frontiers in Materials

ORIGINAL RESEARCH
published: 19 December 2018
doi: 10.3389/fmats.2018.00076

Magnetic Field Induced Surface Micro-Deformation of Magnetorheological Elastomers for Roughness Control

*Shiwei Chen[1], Rui Li[2], Xi Li[2] and Xiaojie Wang[3]**

[1] Chongqing University of Science and Technology, Academy Mathematics and Physics, Chongqing, China, [2] Chongqing University of Posts and Telecommunications, Chinese Academy of Sciences, Changzhou, China, [3] Institute of Advanced Manufacturing Technology, Hefei Institute of Physical Science, Chinese Academy of Sciences, Changzhou, China

In this work, we propose mesoscopic model to investigate the surface micro structures of magnetorheological elastomers (MREs) under a magnetic field. By comparing the surface roughness changes of MREs, we found that the surface micro-deformation of MREs, not the field-induced hardness, mainly accounts for the controllable friction characteristics of MREs. The results also demonstrate that the field-induced friction of MREs depends on the particle contents as well as the initial surface roughness. The model predicts that the maximum relative roughness change of MREs occurs when the MRE has particle volume fraction of around 9%, which is validated by experimental results.

Keywords: MRE, magnetostrictive, roughness controling, tunable interface, magneto induced deformation

OPEN ACCESS

Edited by:
Norman M. Wereley, University of Maryland, College Park, United States

Reviewed by:
Xufeng Dong, Dalian University of Technology (DUT), China
Xiaomin Dong, Chongqing University, China

****Correspondence:***
Xiaojie Wang
xjwang@iamt.ac.cn

Specialty section:
This article was submitted to Smart Materials, a section of the journal Frontiers in Materials

Received: *21 May 2018*
Accepted: *05 December 2018*
Published: *19 December 2018*

Citation:
Chen S, Li R, Li X and Wang X (2018) Magnetic Field Induced Surface Micro-Deformation of Magnetorheological Elastomers for Roughness Control. Front. Mater. 5:76. doi: 10.3389/fmats.2018.00076

INTRODUCTION

Polymers are hyperplastic materials that can be subjected to a large recoverable deformation under a relatively small loading. In taking advantage of this natural property, researchers have developed adaptive materials called magnetorheological elastomers (MREs), by embedding magnetic particles (micron size) in the polymer matrix (Jolly et al., 1996; Ginder et al., 1999). The magnetizing particles in the matrix would interact with each other under an external magnetic field, and consequently induce deformation and modulus changes of MREs. With these unique controllable properties, MREs could be possible candidates for a variety of applications, such as in soft actuators (Böse et al., 2012), vibration absorber (Menzel, 2015; Chen et al., 2016), and magnetic sensor (Sutrisno et al., 2015) etc.

Recently, several experimental studies (Lee et al., 2013; Lian et al., 2015, 2016; Li et al., 2018) have shown that the tribological properties of MREs also change with external magnetic fields, which would possibly extend the MRE's application in interfacial friction control. However, the mechanism of field-induced friction behavior of MREs is still unclear. Lee et al. (2013) employed a homemade linear sliding tester to evaluate the friction characteristics of MREs, and found that the friction coefficient of MRE decreased with the external magnetic field. Later, the same group (Lian et al., 2015, 2016) applied a reciprocating friction tester to characterize four MRE samples, which were prepared by embedded particles in different matrix materials, and found the same phenomenon for all test conditions. The authors argued that the friction reduction of MREs under

a magnetic field was due to the field-stiffening effect. According to the classic contact theory, the large stiffness of materials will result in less interfacial friction (Popov, 2010). However, in a previous study (Li et al., 2018), we observed that even though the friction coefficient of MREs increases with external magnetic fields in some cases, the MREs are getting stiffer. Accordingly, this phenomenon challenges existing theoretical interpretation.

In fact, the surface micro-scale morphology may mainly contribute to the tribological characteristics of the MREs in a magnetic field. However, few studies (Gong et al., 2012) have been carried out to investigate the surface micro-deformation of the MREs under magnetic fields.

Although theoretical modeling of the deformation behavior of MREs has been studied by many others, these models originated from either the continuum mechanics (Dorfmann and Ogden, 2004; Kankanala and Triantafyllidis, 2004), or the multiscale theories (Davis, 1999; Cremer et al., 2015) mostly focus on prediction of the magnetic induced properties of MRE in macro conditions. The models from the point of view of continuum mechanics (Allahyarov et al., 2014; Menzel, 2014) hardly take into account the surface morphology of MREs. And almost all of the representative volume unit models (Yin et al., 2002; Ivaneyko et al., 2014) based on multiscale theories ignore the surface micro profile of MREs. Therefore, all the reported theoretical work on modeling of MREs can only predict the average bulk deformation of MREs. In order to fully understand the field-induced friction behavior of MREs, it is essential to develop a new model to analyze the surface micro structures of MRE under external magnetic fields.

Meanwhile, experimental studies have been performed to measure and analyze the deformation of MREs in magnetic fields. A testing platform with a CCD camera was established by Zrínyi et al. (1996) to measure deformation of ferrogels under non-uniform magnetic fields. The effects of compress force and particle volume fraction on magnetic field induced deformation of MRE were investigated by Martin et al. (2006) and Danas et al. (2012) by using similar testing platforms. However, most experimental studies were only interested in measuring the average deformation of MRE samples. Gong et al. (2012) constructed a digital holographic interferometry to achieve so called full-field deformation of MREs. However, they did not investigate the transition of surface micro structures of MREs under magnetic fields.

To fully understand how the external magnetic field affects the surface roughness of MRE, and how the initial roughness and particle volume fractions impact on the variation of the roughness, a 2 dimension mesoscopic model is proposed in this paper. By employing the Monte-Carlo method (Tsang et al., 2004), our model could incorporate the initial surface irregularities of MRE. Based on this, the changes of MREs surface roughness in magnetic field are analyzed by utilizing magneto-mechanical coupling (FEM) algorithms. Besides, several MRE samples with different particle fractions and initial surface

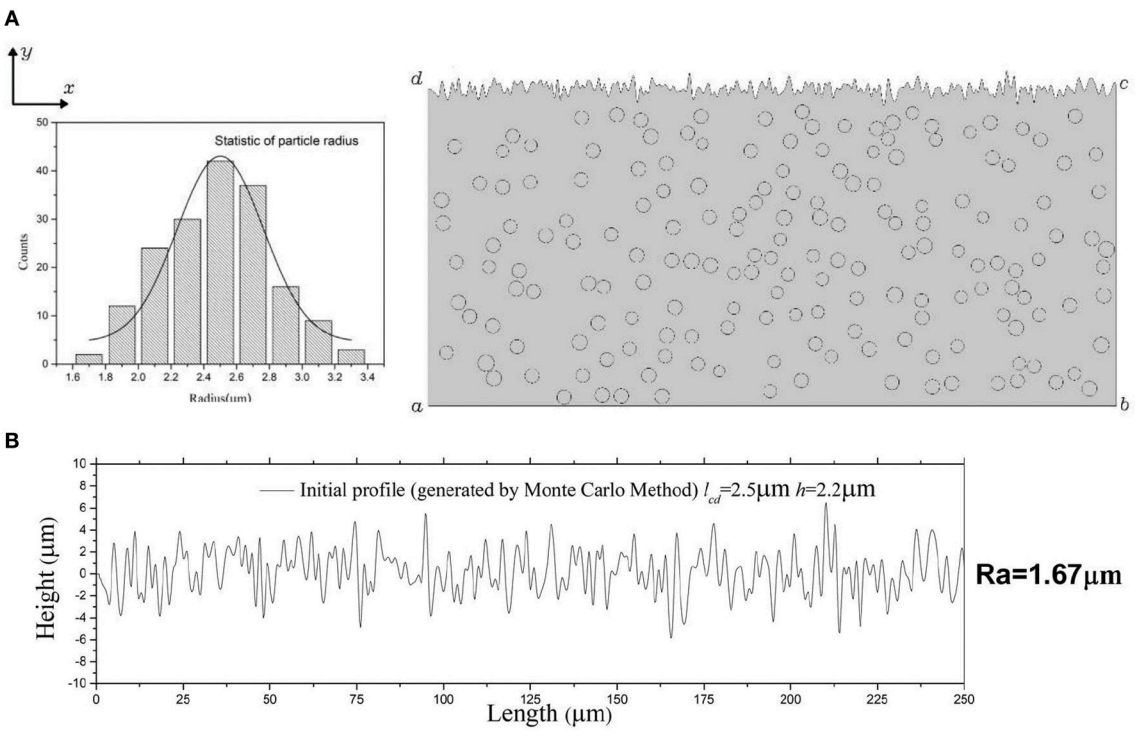

FIGURE 1 | The two dimension mesoscopic model of MRE. **(A)** Left: statistic distribution of particle sizes, the total number of particles $N = 175$ and the average of the particle radius is 2.5 μm. Right: the particles are uniform distributed in a (250 × 130 μm) matrix area, and the particles volume fraction of MRE $\phi \approx 10.5\%$. **(B)** The generated initial surface micro profile of the MRE model. The surface roughness of the MRE (*Ra*) is 1.67 μm.

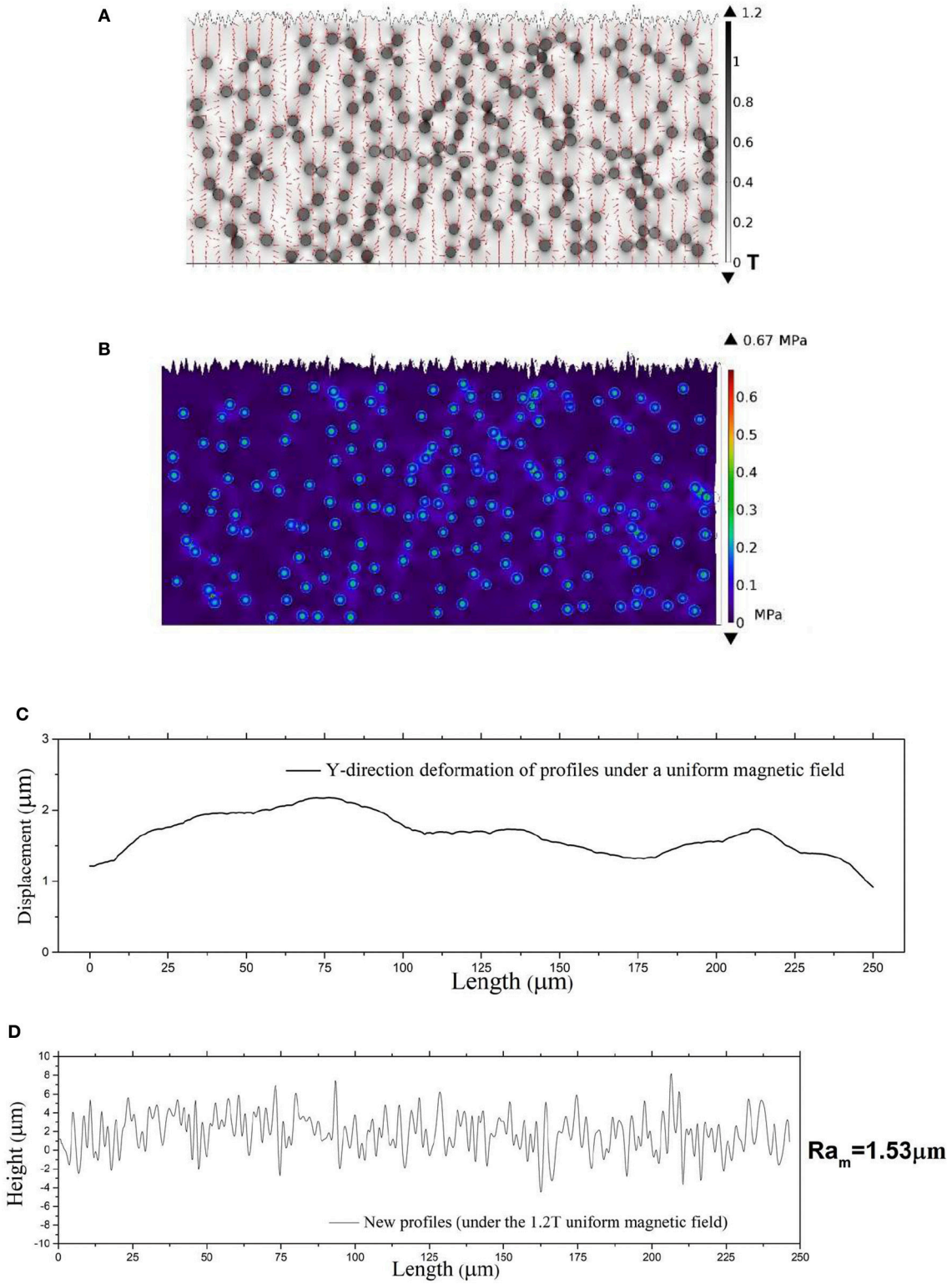

FIGURE 2 | Simulation results with proposed model **(A)** Magnetic flux density distribution. **(B)** Stress field. **(C)** Magnetic induced displacements of the surface profile in Y-direction. **(D)** The new surface profile after the magnetization of 1,000 KA/m is applied on. And the roughness of the surface is 1.53 μm.

roughness are prepared and their roughness are measured by a white light interferometer to reveal the mechanism of magneto induced roughness changes.

MODELING

In the proposed model, we assume that the radius of magnetic particle sizes follow normal distribution, and the particles are tightly bonded to the matrix. In addition, the effect of polymer networks on particle interaction is negligible in the theoretical simulation (Davis, 1999; Yin et al., 2002; Ivaneyko et al., 2014). Since the magnetic induced deformation of MRE is usually tiny (Zrínyi et al., 1996; Martin et al., 2006; Danas et al., 2012), both magnetic particles and polymer matrixes are considered as standard incompressible liner elastic materials. The Young's modulus of particles is 200Mpa, and the Young's modulus of matrixes is 1Mpa.

Figure 1A shows the statistic sizes of 175 particles which are uniformly distributed in matrix. Meanwhile, the 2D Gaussian random contour surfaces are generated by employing the Monte-Carlo method (Tsang et al., 2004) representing the initial surface micro profile of the MRE model (**Figure 1B**). In the model, the surface profiles of MRE can be linear superposed by different sinusoidal curves. The coordinate of the scatter point in the profile curve can be obtained as:

$$y_n = f(x_n) = \frac{1}{l}\sum_{j=-\frac{n}{2+1}}^{\frac{n}{2}} F(\omega_j) e^{i\omega_j x_n} \tag{1}$$

Where n is the scatter point number, (x_n,y_n) represents the coordinate of the n-th scatter point in the profile curve, $F(\omega_j)$ is the Fourier transform pair of $f(x_n)$, and can be expressed as:

$$F(\omega_j) = \frac{2\pi}{\sqrt{2\Delta x}}\sqrt{S(\omega_j)} \cdot \begin{cases} [N(0,1) + iN(0,1)] & j = -\frac{n}{2+1}, \cdots, -1 \\ N(0,1) & j = 0, \frac{n}{2} \end{cases} \tag{2}$$

Where $N(0,1)$ represents a random number of normal distribution with a mean value of 0 and a variance of 1. Δx is the distance between the nearest two scatter points in x-th direction. $S(\omega_j)$ is the power spectral density of random surface profiles, and obeys gauss distribution function. And it can be expressed as follows:

$$S(\omega) = \frac{h l_{cd}}{2\sqrt{\pi}} \exp\left(\frac{-\omega^2 l_{cd}^2}{4}\right) \tag{3}$$

Where h is the expectation of profiles' amplitudes, and l_{cd} is the expectation of distance between two peaks of profiles.

In this work, we use parameter R_a to describe the roughness of the MREs' surface micro profiles. It can be expressed as follows:

$$R_a = \frac{1}{l}\int_0^l \left| y(x) - \frac{1}{l}\int_0^l y(x)\,dx \right| dx \tag{4}$$

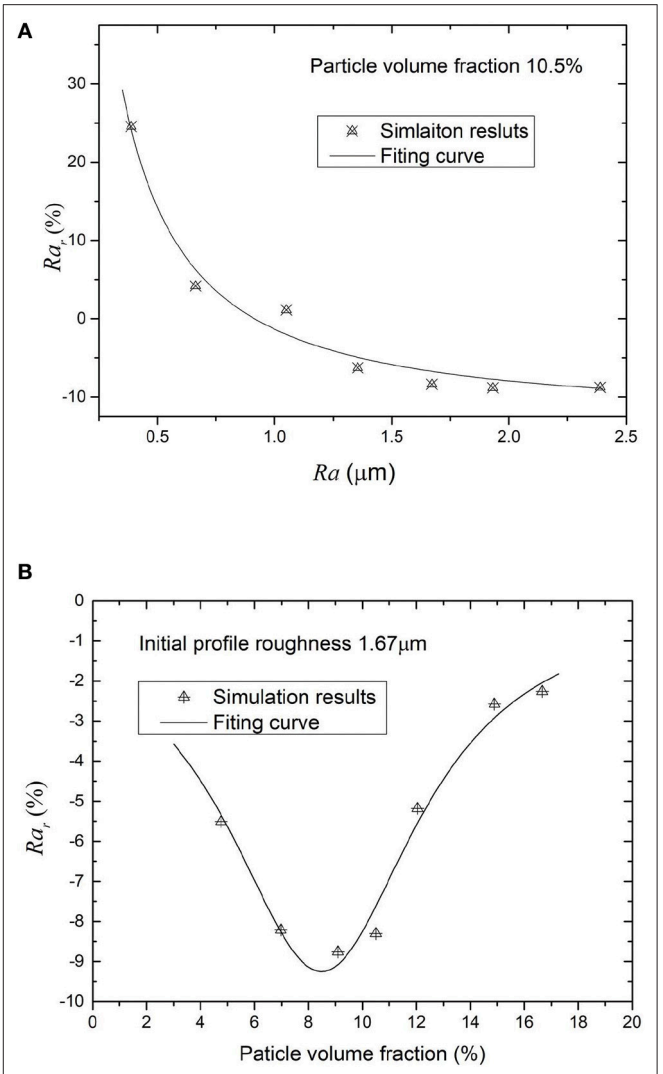

FIGURE 3 | Magnetic induced relative roughness Ra_r. **(A)** Relationship with initial roughness. **(B)** Relationship with particle volume fraction.

SIMULATION RESULTS AND DISCUSSIONS

A sequential FEM[25] is adopted in this paper to solve the magneto-mechanical coupling problem and obtain the micro deformation of MRE model in **Figure 1** by using commercial software COMSOL Multiphysics. Besides, in the mesoscopic scale, the applied magnetic field can be assumed to follow a uniform distribution. Therefore, in the magneto module (MFNC module in COMSOL), the magnetic scalar potential is equal zero on the boundary *ab*. The magnetic field applied on the MREs is in y-direction, and the particles will be magnetized in the same direction, and their magnetization is set to 1,000 kA/m. in the simulation. The other boundaries are considered as magnetic insulation. Meanwhile, in the structural mechanical module (SOLID module in COMSOL), we use $\mathbf{U}=(u,v)$ to describe the

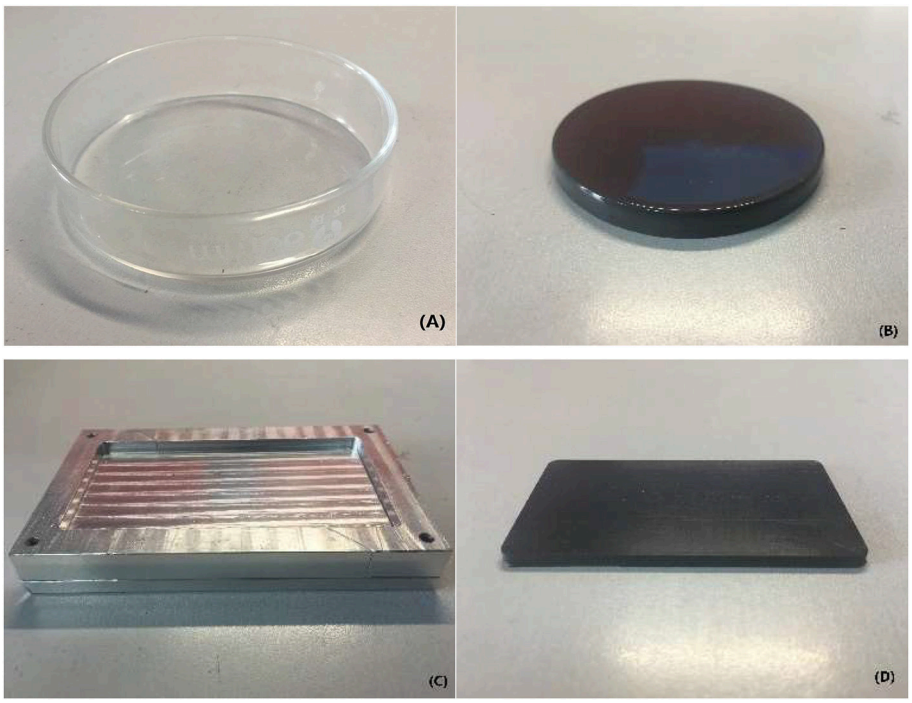

FIGURE 4 | MRE samples **(A)** the glass mold **(B)** the MRE generated in glass mold **(C)** iron mold **(D)** the MRE generated in iron mold.

displacement field of MRE. The boundary condition is chosen in such a way where u = 0 for boundary ad, and v = 0 for boundary ab, and other boundaries are free to move. Also, the magnetic force $\mathbf{F}_i$ on each particle surface $\partial\Omega_i$ can be calculated from the local field **H** with the aid of the Maxwell stress tensor $\boldsymbol{\sigma}^{\mathrm{M}}$ as follow (Ly et al., 1999):

$$\mathbf{F}_i = \frac{1}{2\pi\mu_0}\oint_{\partial\Omega_i} \sigma^M \cdot \mathbf{n}\mathrm{d}s = \frac{1}{2\pi}\oint_{\partial\Omega_i} \mu_i(\mathbf{HH} - \frac{1}{2}\|\mathbf{H}\|^2\mathbf{I})\cdot\mathbf{n}\mathrm{d}s \quad (5)$$

Where **n** is the unit normal vector on $\partial\Omega_i$, μ_i, μ_0 is the permeability for the particles and matrix, respectively, **I** is the 2th rank unit tensor.

The simulation results of the MRE model under an applied magnetic field of 1,000 kA/m are shown in **Figure 2**. **Figure 2A** gives the results of magnetic flux density distribution in the simulation domain. **Figure 2B** shows the stress field of MRE induced by the magnetic field. These results illustrate that the magnetized particles in the matrix would interact with each other though magnetic force and create the magnetic induced stress in the MRE. As a result, the MRE will deform irregularly.

Figure 2C shows the positive field-induced displacements of MRE which are consistent with previous studies is shown. However, the irregularity of the surface deformation by the magnetic field is ignored by most theoretical predictions (Davis, 1999; Yin et al., 2002; Dorfmann and Ogden, 2004; Kankanala and Triantafyllidis, 2004; Chen et al., 2013; Allahyarov et al., 2014; Andriushchenko et al., 2014; Menzel, 2014; Cremer et al., 2015). The cause of the irregular deformation of MREs can be explained by the magnetic induced stress field shown in **Figure 2B**. It can be seen that the magnetic stress is not uniformly distributed in the matrix. The stress is larger where particles are assembled, while it is smaller where the particles are scattered. **Figure 2D** shows the new surface profile of MRE after the magnetic field is applied. It is obtained by superposing the initial profile of **Figure 1B** and the magnetic induced displacement of **Figure 2C** together. **Figure 2D** shows that the roughness of the MRE is 1.53 μm. Comparing with the initial roughness Ra = 1.67 μm, the roughness of the MRE is decreased. The simulation results are consistent with previous experimental observations (Lian et al., 2015, 2016; Li et al., 2018) where the magnetic fields reduce the friction coefficient of MREs. However, when we evaluate the relative roughness changes as a function of the initial surface roughness of MREs, the magnetic fields do not always induce negative changes in surface roughness. **Figure 3A** presents the simulation results of the relative roughness changes Ra_r with initial surface roughness of MREs. The relative roughness change is defined as: Ra_r=(Ra_m-Ra)/Ra, where Ra_m, is the roughness under a magnetic field, Ra is the initial surface roughness. We can see that when the initial profile roughness Ra <1 μm, the relative roughness changes under a magnetic field are positive. This suggests that the smooth surface profiles of MREs will become rough under magnetic field; in other words, the friction coefficient of MREs will increase by an applied magnetic field. We suggested that this phenomenon is a result of that the roughness of the magnetic induced deformation itself will be the dominant role of Ra_r, When initial profile is smooth. And we can also explain it by an extreme assumption; we can imagine a MRE which has an absolute smooth surface that should become rough when superimposed on inhomogeneous deformation, which is the result of external magnetic loading.

Further, we investigate how the particle contents in MREs affect the relative roughness changes under the same applied magnetic field. We set the initial surface roughness of MREs to be 1.67 μm, and analyze the field-induced surface profiles for the MREs with different particle volume fractions. **Figure 3B** shows the simulation results of the relative roughness changes as a function of particle volume fractions of MREs.

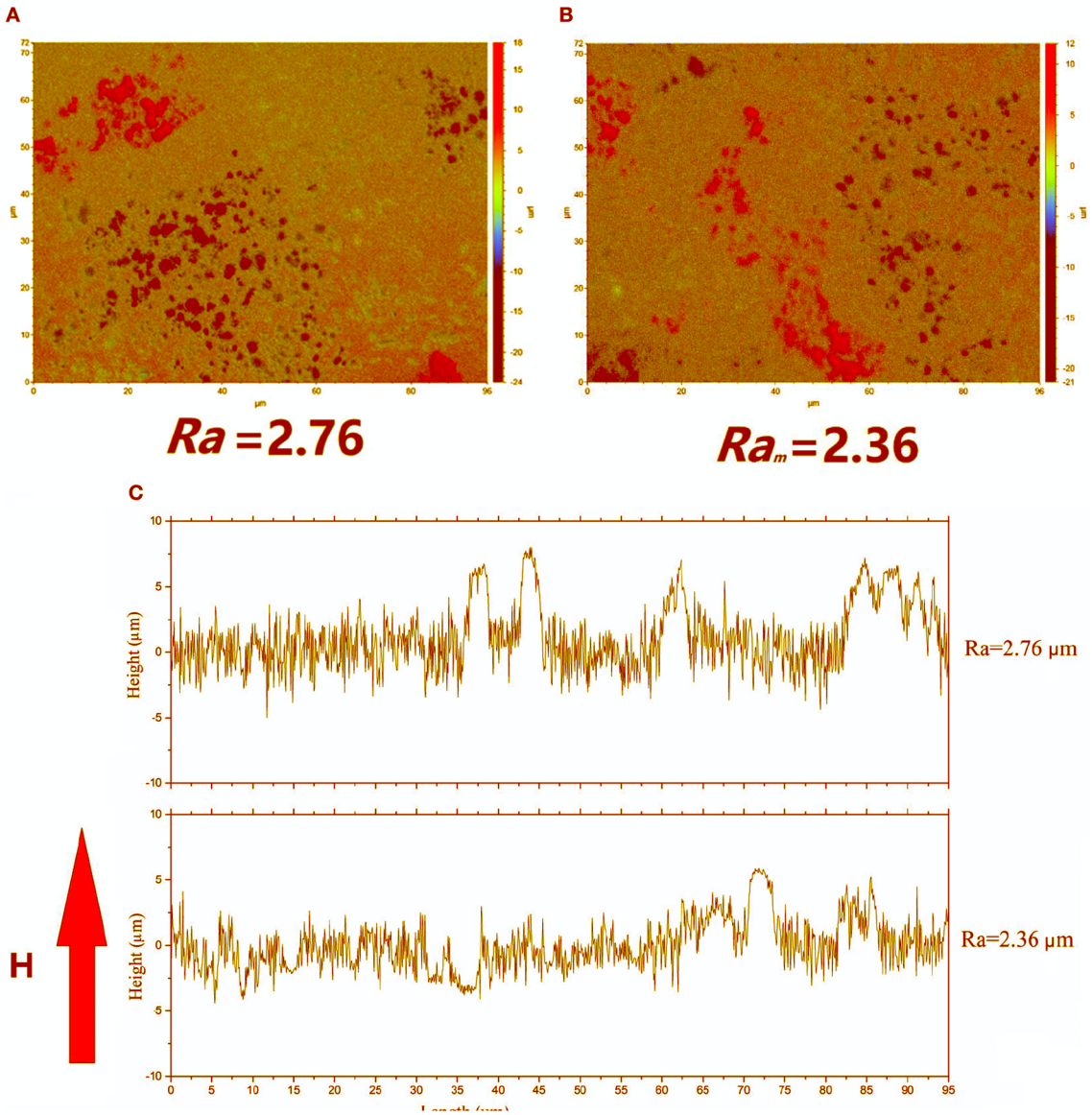

FIGURE 5 | White light interferometer test results of a typical MRE (10% particle volume fraction, generated by iron mold) **(A)** the initial surface contour, the roughness is 2.76 μm **(B)** the surface contour under a magnetic field of 450 mT, the roughness is 2.36 μm **(C)** the 2-demension profiles of MRE.

It can be seen that there is an optimal particle volume fraction for the relative roughness changes, in which the Ra_r has the maximum absolute value. It is interesting to note that optimal particle volume fraction for the Ra_r is around 9%, but is not 27%, in which the magnetorheological effect is predicted the strongest (Davis, 1999). It is suggested that it is a result of the particle distribution which varies with the particle volume fraction. When the particle volume fraction of MREs is low (<9%), the interactions between particles would be increased with its volume fraction, then the irregularity of the magnetostriction is also increased with it. However, when the particle volume fraction is higher than 9%, the distance between particles would be decreased and particle distribution becomes more uniform. Then the irregularity of the magnetostriction is reduced although the particle interactions are increasing. This finding could give an explanation as to why the MRE with 10% particle fraction has the largest tunable friction coefficients in reference Li et al. (2018)

EXPERIMENTAL VALIDATION

In this section, two kinds of isotropic MREs are manufactured by uniformly embedded magnetic particles into silicon rubber (HT-18; Shanghai Tongshuai Co., Ltd, China). As shown in **Figure 4**, One kind of MREs is the samples are prepared by using the glass mold, and the other is made by the iron mold. So, the latter has rougher surface than the former. A white light interferometer (ContourGT-K, Germany BRUKER company), of which the vertical resolution can reach 0.01 nm is used to obtain the three-dimensional morphology of all MRE samples.

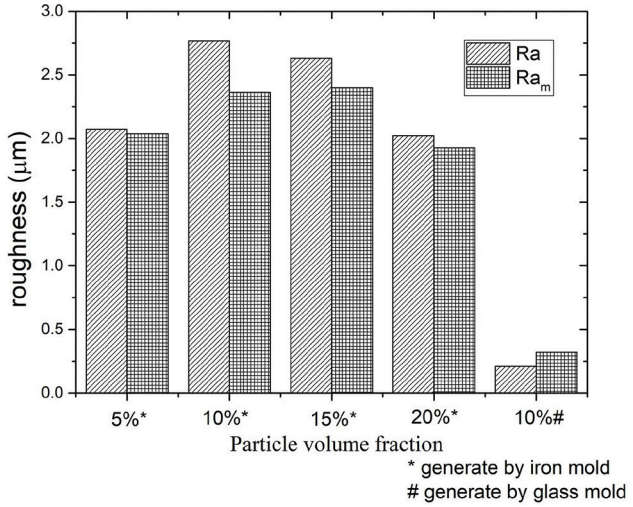

FIGURE 6 | Comparisons of roughness of MREs for different particle volume fractions with/without magnetic field.

Figure 5 gives the white light interferometer test results of a 10% particle volume fraction MRE that is generated by iron mold. **Figure 5A** gives the initial surface contour of the MRE, **Figure 5B** gives the surface contour of MRE under a uniform vertical magnetic field of 450 mT, and **Figure 5C** gives the 2 dimension picture of the MRE surface profiles with/without a uniform vertical magnetic field. It can be seen that the roughness of MRE sample decreases from 2.76 to 2.36 μm when a magnetic field is applied. However, for the MRE samples made by glass mold, the magnetic field increases the surface roughness (see **Figure 6**).

Figure 6 shows the results of surface roughness of MREs with different particle contents made by iron mold with/without magnetic field. The results of roughness of MRE samples with 10% particle volume fraction made by glass mold are also presented in the **Figure 6**. As can be seen, the initial roughness of MREs mainly depends on the roughness of corresponding molds. And MREs fabricated by the steel mold has the similar roughness. Besides, **Figure 6** shows that the MRE with 10% particle volume fraction has the largest relative roughness change, which conforms to the theoretical prediction. This is different to MREs made by iron mold, as the surface roughness of MREs generated by glass mold increases with magnetic fields.

CONCLUSION

In summary, a mesoscopic model that considers deformation of surface micro-structures of MREs has been established to predict the surface roughness of MREs under magnetic fields. The model can explain how the field-induced friction of MRE changes as a function of particle contents, and how the initial surface roughness affects the changes. In addition, the proposed model has been verified experimentally. These findings may contribute to the area of interfacial friction control, in which controllable friction surfaces or techniques are expected to apply for the design of high efficient smart devices and mechanical systems.

AUTHOR CONTRIBUTIONS

RL and XL contribute the experimental parts of this works. XW gives some advises of this manuiscript and farbricates the MRE. SC writes the paper and establishes the surface model of MRE.

FUNDING

Financial supports from the National Natural Science Foundation of China (Grant NO.11502038, NO.11572320, NO.11372366). And it also supports from China Postdoctoral Science Foundation (NO. 2017M610386).

REFERENCES

Allahyarov, E., Menzel, A. M., Zhu, L., and Löwen, H. (2014). Magnetomechanical response of bilayered magnetic elastomers. *Smart Mater. Struct.* 23:115004. doi: 10.1088/0964-1726/23/11/115004

Andriushchenko, P., Nefedev, k., and Stepanov, G. V. (2014). Calculations of magnetoactive elastomer reactions in a uniform external magnetic field. *Eur. Phys. J. B* 87:11. doi: 10.1140/epjb/e2013-31097-1

Böse, H., Rabindranath, R., and Ehrlich, J. (2012). Soft magnetorheological elastomers as new actuators for valves. *J. Intell. Mater. Syst. Struct.* 23, 989–994. doi: 10.1177/1045389

Chen, S., Wang, X., Zhang, Z., Mu, W., and Li, R. (2016). Optimal design of laminated-MRE bearings with multi-scale model. *Smart Mater. Struct.* 25:105037.doi: 10.1088/0964-1726

Chen, W., Sun, L., Li, X., and Wang, D. (2013). Numerical investigation on the magnetostrictive effect of magneto-sensitive elastomers based on a magneto-structural coupling algorithm. *Smart Mater. Struct.* 22:105012. doi: 10.1088/0964-1726/22/10/105012

Cremer, P., Löwen, H., and Menzel, A. M. (2015). Tailoring superelasticity of soft magnetic materials. *Appl. Phys. Lett.* 107:171903. doi: 10.1063/1.4934698

Danas, K., Kankanala, S. V., and Triantafyllidis, N. (2012). Experiments and modeling of iron-particle-filled magnetorheological elastomers. *J. Mech. Phys. Solids* 60, 120–138. doi: 10.1016/j.jmps.2011.09.006

Davis, L. C. (1999). Model of magnetorheological elastomers. *J. Appl. Phys.* 85, 3348–3351. doi: 10.1063/1.369682

Dorfmann, A., and Ogden, R. W. (2004). Nonlinear magnetoelastic deformations of elastomers. *Acta Mech.* 167, 13–28. doi: 10.1007/s00707-003-0061-2

Ginder, J. M., Nichols, M. E., Elie, L. D., and Tardiff, J. L. (1999). Magnetorheological elastomers: properties and applications. *Smart Struct. Mater.* 3675, 131–139. doi: 10.1117/12.352787

Gong, X., Liao, G., and Xuan, S. (2012). Full-field deformation of magnetorheological elastomer under uniform magnetic field. *Appl. Phys. Lett.* 100:211909. doi: 10.1063/1.4722789

Ivaneyko, D., Toshchevikov, V., Saphiannikova, M., and Heinrich, G. (2014). Mechanical properties of magneto-sensitive elastomers: unification of the continuum-mechanics and microscopic theoretical approaches. *Soft Matter* 10, 2213–2225. doi: 10.1039/C3SM52440J

Jolly, M. R., David Carlson, J., and Munoz, B. C. (1996). A model of the behaviour of magnetorheological materials. *Smart Mater. Struct.* 5, 607–612.

Kankanala, S. V., and Triantafyllidis, N. (2004). On finitely strained magnetorheological elastomers. *J. Mech. Phys. Solids* 52, 2869–2908. doi: 10.1016/j.jmps.2004.04.007

Lee, D. W., Lee, K., Lee, C. H., Kim, C. H., and Cho, W. O. (2013). A study on the tribological characteristics of a magneto-rheological elastomer. *J. Tribol.* 135, 014501. doi: 10.1115/1.4023080

Li, R., Ren, D., Wang, X., Chen, X., Chen, S., and Wu, X. (2018). Tunable friction performance of magneto-rheological elastomer induced by external magnetic field. *J. Intell. Mater. Syst. Struct.* 29, 160–170 doi: 10.1177/1045389X17708043

Lian, C., Lee, K. H., and Lee, C. H. (2015). Friction and wear characteristics of magneto-rheological elastomers based on silicone/polyurethane hybrid. *J. Tribol.* 137:031607. doi: 10.1115/1.4029942

Lian, C., Lee, K. H., and Lee, C. H. (2016). Friction and wear characteristics of magnetorheological elastomer under vibration conditions. *Tribol. Int.* 98, 292–298. doi: 10.1116/j.triboint.2016.02.037

Ly, H. V., Reitich, F., Jolly, M. R., Banks, H. T., and Ito, K. (1999). Simulations of particle dynamics in magnetorheological fluids. *J. Comput. Phys.* 155, 160–177. doi: 10.1006/jcph.1999.6335

Martin, J. E., Anderson, R. A., Read, D., and Gulley, G. (2006). Magnetostriction of field-structured magnetoelastomers. *Phys. Rev. E* 74:051507. doi: 10.1103/PhysRevE.74.051507

Menzel, A. M. (2014). Bridging from particle to macroscopic scales in uniaxial magnetic gels. *J. Chem. Phys.* 141, 194907. doi: 10.1063/1.4901275

Menzel, A. M. (2015). Tuned, driven, and active soft matter. *Phys. Rep.* 554, 1–45. doi: 10.1016/j.physrep.2014.10.001

Popov, V. L. (2010). *Contact Mechanics and Friction*. Berlin: Springer.

Sutrisno, J., Purwanto, A., and Mazlan, S. A. (2015). Recent progress on magnetorheological solids: materials, fabrication, testing, and applications. *Adv. Eng. Mater.* 17, 563–597. doi: 10.1002/adem.201400258

Tsang, L., Chen, D., Xu, P., Li, Q., and Jandhyala, V. (2004). Wave scattering with the UV multilevel partitioning method: 1. Two-dimensional problem of perfect electric conductor surface scattering. *Radio Sci.* 39, 1–13. doi: 10.1029/2003RS003009

Yin, H. M., Sun, L. Z., and Chen, J. S. (2002). Micromechanics-based hyperelastic constitutive modeling of magnetostrictive particle-filled elastomers. *Mech. Mater.* 34, 505–516. doi: 10.1016/S0167-6636(02)00178-3

Zrínyi, M., Barsi, L., and Büki, A. (1996). Deformation of ferrogels induced by nonuniform magnetic fields. *J. Chem. Phys.* 104, 8750–8756. doi: 10.1063/1.471564

Conflict of Interest Statement: The authors declare that the research was conducted in the absence of any commercial or financial relationships that could be construed as a potential conflict of interest.

Advantages of publishing in Frontiers

OPEN ACCESS
Articles are free to read for greatest visibility and readership

FAST PUBLICATION
Around 90 days from submission to decision

HIGH QUALITY PEER-REVIEW
Rigorous, collaborative, and constructive peer-review

TRANSPARENT PEER-REVIEW
Editors and reviewers acknowledged by name on published articles

Frontiers
Avenue du Tribunal-Fédéral 34
1005 Lausanne | Switzerland

Visit us: www.frontiersin.org
Contact us: info@frontiersin.org | +41 21 510 17 00

REPRODUCIBILITY OF RESEARCH
Support open data and methods to enhance research reproducibility

DIGITAL PUBLISHING
Articles designed for optimal readership across devices

FOLLOW US
@frontiersin

IMPACT METRICS
Advanced article metrics track visibility across digital media

EXTENSIVE PROMOTION
Marketing and promotion of impactful research

LOOP RESEARCH NETWORK
Our network increases your article's readership